UNIVERSITY
OF ICELAND

Understanding Hydrogen Sulfide Mineral Storage: Joint Geophysical Surveying and Geochemical Modeling at the Nesjavellir Geothermal Site, Iceland

Daniel Anthony Ciraula

December 2025

Ph.D. Thesis
in Geophysics

FACULTY OF EARTH SCIENCES

Understanding Hydrogen Sulfide Mineral Storage: Joint Geophysical Surveying and Geochemical Modeling at the Nesjavellir Geothermal Site, Iceland

Daniel Anthony Ciraula

Dissertation submitted in partial fulfillment of a
Philosophiae Doctor degree in Geophysics

Ph.D. Committee:
Dr. Barbara Kleine-Marshall
GeoZentrum Nordbayern, Friedrich-Alexander-Universität Erlangen-Nuremberg, Germany
Dr. Gianluca Fiandaca
Department of Earth Sciences "Ardito Desio", University of Milan, Italy
Dr. Léa Lévy
CNRS-INSU, Géosciences Rennes UMR, France
Dr. Samuel Scott
NordVulk, Institute of Earth Sciences, University of Iceland, Iceland
Dr. Halldór Geirsson
NordVulk, Institute of Earth Sciences, University of Iceland, Iceland

Opponents:
Dr. Adrian Mellage
Civil and Environmental Engineering, University of Kassel, Germany
Dr. Mariëtte Wolthers
Department of Earth Sciences, Utrecht University, The Netherlands

Faculty of Earth Sciences
School of Engineering and Natural Sciences
University of Iceland
Reykjavik, December 2025

Understanding Hydrogen Sulfide Mineral Storage: Joint Geophysical Surveying and Geochemical Modeling at the Nesjavellir Geothermal Site, Iceland
(Understanding H_2S Mineral Storage at Nesjavellir)

Dissertation submitted in partial fulfillment of a Ph.D. degree in Geophysics

Faculty of Earth Sciences
School of Engineering and Natural Sciences
University of Iceland
Askja, Sturlugata 7
102, Reykjavik Iceland

Telephone: 525-4000

Bibliographic information:
Daniel Anthony Ciraula (2025) *Understanding Hydrogen Sulfide Mineral Storage: Joint Geophysical Surveying and Geochemical Modeling at the Nesjavellir Geothermal Site, Iceland*, Ph.D. Dissertation, Faculty of Earth Sciences, University of Iceland.

Author ORCID: 0000-0003-4884-5291
ISBN: 978-9935-9772-8-1

Printing: Háskólaprent, Fálkagata 2, 107 Reykjavík

Reykjavik, Iceland, December 2025

Abstract

The physical and chemical processes that occur in the subsurface as fluids and rocks interact play a central role in shaping subsurface geochemical systems. However, capturing these fluid-rock interactions in the field is difficult, as these processes occur hidden from direct observation. Both geochemical and geophysical methods provide complementary insights into the complex fluid-rock interactions, but the disciplines are not commonly used together. This thesis aims to integrate reactive transport geochemical modeling with time-lapse geophysical surveying to better understand and monitor fluid-rock interactions associated with hydrogen sulfide (H_2S) mineral storage in basalt, focusing on the Nesjavellir geothermal site (SW Iceland). In the mineral storage approach, injected H_2S reacts with basalt-sourced iron to form the mineral pyrite. The direct current and induced polarization (DCIP) geophysical method is sensitive to pyrite abundance through the chargeability parameter and is therefore evaluated as a novel monitoring tool for H_2S mineral storage. This research integrates DCIP surveying with reactive transport models that couple fluid flow and transport with geochemical reactions to predict the fluid-rock interactions and provide insight into geochemical processes controlling the DCIP response.

Reactive transport models presented here show that H_2S mineral storage is effective under the current injection conditions, with up to 87% of the injected H_2S mineralizing as pyrite over 25 years of continuous injection. Consequently, H_2S contamination of the nearby Lake Thingvellir is expected to be minimal (<0.013 µmol/L). However, faults with high permeability pose a potential risk for contaminating the surface water. Lithologic and hydrologic controls strongly impact H_2S mineralization: it is greatest in high-permeability hyaloclastites with abundant basaltic glass and in fresh, olivine-rich lava flows; high porosity and temperature accelerate iron release and pyrite formation; and permeability governs the spatial distribution of pyrite precipitation, although high fluid flow in permeable zones can limit the fluid-rock interactions required for pyrite formation. H_2S mineralization is maximized in high-permeability hyaloclastites containing abundant basaltic glass and fresh lava flows containing abundant Fe-rich olivine. High porosity and elevated temperature accelerate basalt dissolution and iron release, enhancing H_2S mineralization. Permeability controls the spatial distribution of H_2S-rich water and subsequent pyrite precipitation. However, high fluid flow rates in permeable zones can limit fluid-rock interactions. Inversion of the 3D flow model constrained by borehole fluid temperature data reveals high permeabilities up to 9.7×10^{-11} m^2 in hyaloclastite units. The permeability values agree with estimates derived from a petrophysical relationship linking permeability, changes in electrical resistivity between 1985 and 2020, and smectite abundance, as predicted by reactive transport simulations over the same period. Multiple-porosity models indicate that slow, diffusion-dominated transport in the rock matrix enhances fluid–rock interactions, with up to 97% of the total pyrite formation occurring within the rock matrix. This highlights the importance of considering diffusive processes in multiple-porosity frameworks to accurately simulate H_2S mineral storage in fractured basalt.

Assessing DCIP monitoring capabilities at Nesjavellir shows increases in chargeability in wireline DCIP logs from injection wells injecting H_2S-rich water at rates of 12.5-149 L/s. The wireline measurements, taken 40 days apart, capture changes consistent with reactive transport model predictions of pyrite formation within 3.25 m of the borehole. In contrast, DCIP surface measurements show no significant change in chargeability following six months of continuous injection. Field-scale reactive transport models illustrate that low signal-to-noise ratios at the injection depths and small chargeability responses from dispersed pyrite mineralization limit the monitoring capability of surface DCIP. Synthetic DCIP datasets generated from reactive transport models show that cross-borehole DCIP surveying improves upon the surface DCIP approach by measuring chargeability changes at injection depths, but the method remains limited by data noise and weak chargeability signals.

Overall, this thesis provides innovative ways of integrating geochemical and geophysical approaches and provides a comprehensive, non-invasive approach to enhance hydrogeological monitoring capabilities.

Útdráttur

Eðlis- og efnafræðileg ferli sem eiga sér stað þegar vökvar og berg hvarfast hvert við annað gegna lykilhlutverki í mótun jarðefnafræðilegra kerfa í jarðskorpunni. Erfitt er að rannsaka samspil vökva og bergs með beinum athugum þar sem ferlin eiga sér stað neðanjarðar. Bæði jarðefna- og jarðeðlisfræðilegar aðferðir veita aukna innsýn í flókið samspil vökva og bergs, en þessar fræðigreinar eru almennt ekki nýttar saman. Þessi ritgerð miðar að því að samþætta jarðefnafræðileg líkön af grunnvatnsstreymi við tímaraðir jarðeðlisfræðilegra mælinga til að skilja betur og vakta víxlverkun vökva og bergs í tengslum við bindingu brennisteinsvetnis (H_2S) í steindir basalts, með áherslu á jarðhitasvæði Nesjavalla á Suðvesturlandi. Þar er dælt niður H_2S sem hvarfast við járn úr basalti og myndar pýrít. Jarðeðlisfræðilega aðferðin byggir á jafnstraumi og spanskautun bergs (e. direct current and induced polarization, DCIP) og er næm fyrir magni pýríts vegna hleðslugetu pýríts. Aðferðin gæti því verið nýstárlegt eftirlitstæki fyrir bindingu H_2S í pýrít. Í þessari rannsókn eru DCIP mælingar samþættar grunnvatnslíkönum sem tengja saman vökvaflæði og jarðefnafræðileg efnahvörf til að spá fyrir um samspil vökva og bergs og veita innsýn í þau jarðefnafræðilegu ferli sem stýra svörun DCIP-aðferðarinnar.

Grunnvatnslíkön sem hér eru sett fram sýna að binding H_2S er árangursrík, þar sem allt að 87% af niðurdældu H_2S breytist í pýrít, miðað við 25 ára samfellda niðurdælingu. Því má gera ráð fyrir að mengun Þingvallavatns af H_2S verði óveruleg ($<$0,013 µmól/L), þó að misgengi með mikla lekt geti mögulega valdið mengun yfirborðsvatns. Jarðlagagerð og grunnvatnsfræðilegar aðstæður hafa afgerandi áhrif á bindingu H_2S: Pýrítmyndun H_2S er mest í mjög gegndræpu móbergi með miklu basaltsgleri og í ferskum hraunum sem innihalda mikið af járnríku ólivíni; hátt grophlutfall og hár hiti valda hraðari uppleysingu basalts, því verður losun járns og binding H_2S hraðari; Lekt ræður dreifingu H_2S-ríks vatns og þar af leiðandi hvar pýrít fellur út; hins vegar getur mikið vatnsrennsli á lekum svæðum takmarkað samspil vökva og bergs. Kvörðun á lekt í þrívíða straumlíkaninu með tilsjón af hitagögnum úr borholum gefur allt að $9{,}7\times10^{-11}$ m^2, sem telst há lekt. Þessi lekt er í samræmi við mat sem byggir á mun viðnámsmælinga 1985–2020 og líkönum af útfellingu smektíts frá því að losun fráveituvatns hófst á Nesjavöllum. Líkan með tvenns konar gropuhlutfalli sýnir að hægt, sveimstýrt flæði í berginu auki pýrítbindingu, þar sem allt að 97% af heildarútfellingu pýríts á sér stað innan bergmassans. Þessi niðurstaða undirstrikar mikilvægi þess að taka mið af sveimi í tvígropulíkönum sem herma bindingu H_2S í brotnu basalti.

Mat á eftirlitshæfni DCIP leiðir í ljós mikilvægi borholumælinga, þar sem DCIP-borholumælingar með 40 daga millibili sýna aukna hleðslugetu, sem er í samræmi við spár grunnvatnslíkana um myndun pýríts innan 3.25 m frá borholum. Til samanburðar sýna DCIP-yfirborðsmælingar engar marktækar breytingar á hleðslugetu eftir sex mánaða niðurdælingu, sem er einnig í samræmi við niðurstöður grunnvatnslíkana og orsakast af fjarlægð mælitækja frá pýrítmynduninni. Hermd DCIP-gögn úr grunnvatnslíkönum benda til þess að DCIP-mælingar milli borhola geti umfram yfirborðs DCIP mælingar greint útfellingu H_2S, að því tilskildu að gögn séu af góðum gæðum og niðurdæling eigi sér stað yfir löng tímabil.

Í þessari ritgerð eru lagðar fram nýstárlegar leiðir til að samþætta jarðefnafræðilegar og jarðeðlisfræðilegar nálganir á heildstæðan hátt til að bæta eftirlitshæfni með bindingu H_2S.

Contents

List of Figures

List of Publications

Paper I: **Ciraula, D. A.**, Kleine-Marshall, B. I., Galeczka, I. M., Lévy, L. (2024). Advanced monitoring of H_2S injection through the coupling of reactive transport models and geophysical responses. Environmental Science and Technology. 58(25), 11128-11139, DOI: 10.1021/acs.est.3c10139

Paper II: **Ciraula, D. A.**, Scott, S. W., Sonnenthal, E. L., Gómez-Díaz, E., Kleine-Marshall, B. I. (In Prep). Quantifying H_2S Mineral Storage Processes in Fractured Basalt Using a Field-Scale Reactive Transport Model. Manuscript in Prep. for Submission to Water Resources Research.

Paper III: **Ciraula, D. A.**, Fiandaca, G., Chen, J., Scott, S. W., Lévy, L. (In Review). Constraining Time-lapse Geophysical Responses with Reactive Transport Modeling: An Approach to Monitor H_2S Mineral Storage. Manuscript Submitted to Geophysical Journal International, June 30, 2025.

Additional Publications Contributed to Outside of Thesis:

Lévy, L., **Ciraula, D. A.**, Legros, B., Martin, T., Weller, A. (2024). Understanding the fate of H_2S injected in basalts by means of time-domain induced polarization geophysical logging. Journal of Geophysical Research: Solid Earth, 129(6).
https://doi.org/10.1029/2023JB028316

Acknowledgments

I would like to first express my gratitude to my supervisors for fostering my growth as a researcher: Barbara Kleine-Marshall, Léa Lévy, Sam Scott, Gianluca Fiandaca, and Halldór Geirsson. This interdisciplinary research would not have been possible without a fully dedicated committee, contributing their expertise and providing feedback throughout the research and writing process.

Barbara, thank you for your constant patience and kindness as I began my journey into geochemistry. The technical and personal support you provided throughout my PhD, especially during the early stages, laid a solid foundation and encouraged me to broaden my academic horizons. Léa, thanks for all of your hard work, which facilitated much of this project. I am grateful for our many research discussions and for your attentive feedback, which always challenged me to think deeper and guided the project to its final form. Sam, thanks for enthusiastically becoming involved in my PhD project. I appreciate the time you always made to support me as I explored new research avenues and for the guidance you provided to improve the direction and communication of my research. Gianluca, thank you for generously agreeing to co-supervise this research and for providing expertise that extended beyond EEMverter training. I am grateful for your efforts in facilitating the summer schools, short courses, and my research trips, which allowed me to develop as a geophysicist while discovering the amazing things that Italy offers. I am grateful also to the rest of the EEMverter Team - Jian Chen, Alessandro Signora, Nicole Sullivan, Stefano Galli, Francesco Dauti, and Alice Lucchelli - for welcoming me in Milan and all of our enthusiastic hydrogeophysical discussions. Halldór, thank you for the feedback you provided on my research aims and work plans throughout the PhD process. Your support was invaluable to my progress and helped me navigate the many challenges of research.

Thanks also to the external opponents, Mariëtte Wolthers and Adrian Mellage, for their valuable time and feedback that strengthened this thesis.

I would also like to thank Rikke Pedersen for coordinating the PhD project, handling the logistics to facilitate my research, and ensuring things ran smoothly, both academically and personally.

Next, I would like to thank all of the amazing scientists who helped me, an often lost and confused geophysicist, with the geological and geochemical analyses. Rebekka Hlín Rúnarsdóttir, for help with crushing and mounting rock cutting samples. Jóhann Gunnarsson Robin, for assisting with ICP-OES analysis of fluid and rock samples. Ríkey Kjartansdóttir and Céline Mandon, for assisting with fluid sample analysis. Birgir Jóhannesson and Helga Margrét Helgadóttir for their help in analyzing the rock composition. Walt McNab, Thomas Ratouis, Jesús Carrera, Esteban Gómez-Díaz, and Sigurður Garðar Kristinsson for their discussions regarding the design of the reactive transport models. Special thanks also to Eric Sonnenthal and Iwona Galeczka for providing essential guidance and enthusiastic discussions in the development of the reactive transport models.

I am grateful to all who contributed to the fieldwork, despite the bugs and variable weather conditions, which made this research possible. To Íris Eva Einarsdóttir and Þorsteinn Ari Þorgeirsson for coordinating and assisting in collecting fluid samples. To Pradip Maurya, Muhammad Rizwan Asif, Ásdís Benediktsdóttir, Sigurður Ýmir Richter, Lydie Gailler, and Svetlana Byrdina, for their hard work installing thousands of electrodes and laying out kilometers of cables for geophysical data acquisition. Thank you to Orkuveita Reykjavíkur for providing access to the injection and groundwater wells for sampling, injection data, drill cuttings, and historical vertical electrical sounding data. Thanks to Gylfi Páll Hersir for discussions surrounding the acquisition and processing of the vertical electrical sounding data. Thanks also to Íslenskar Orkurannsóknir (ÍSOR) for collecting the wireline logging data.

To all the friends that I have made in the third-floor office who contributed to the great academic atmosphere - Nico, Jonas, Cat, Patricia, Yilin, Gabriele, Ylse, Sonja, Chiara, Greta, Nate, Daniel, Didas, and Tingting. Thanks for the spontaneous discussions during lunch and coffee breaks, watering all my plants, and our time spent away from the office that balanced PhD life. Thanks also to Jonas, Théo, and Noëmi for getting me through cold winters with our skiing adventures. Special thanks to the many adventures and memories made exploring Iceland with Nico, Ástrós, Gala, Thomas, and Una - our hiking expeditions and weekend adventures truly made Iceland special.

Thanks to my parents for their support and the strong foundation they have given me to conquer life's challenges. To my mother, for being a constant example of what selflessness and dedication looks like. To my father, for showing me that learning is cool and for the constant commitment to providing me with every opportunity to pursue my goals.

Finally, thank you to Kelsey for unintentionally becoming a fellow student of geochemistry and geophysics - tirelessly proofreading my work and discussing my research without ever complaining. I am lucky to have you by my side. Your unwavering support, strength, patience, and sacrifice are what made this PhD and our adventure together possible.

This project was graciously funded by the Nordic Volcanological Center (NordVulk), with contributions from the Icelandic Centre for Research (Rannís) to GEMGAS. Thanks also to the Landsvirkjun Energy Research Fund, the VOR-Reykjavik Energy Research and Innovation Fund, and the EEGS Foundation for providing additional funding essential to my research.

1 Introduction

1.1 Objectives and Motivation

The overarching aim behind this thesis is to integrate geochemical modeling with geophysical field surveying to enhance the application of time-lapse geophysical site investigation and to produce more accurate models that illuminate subsurface fluid-rock interactions. While not commonly utilized together, integrating geochemical and geophysical methods can provide shared mutual benefits when characterizing real-world subsurface systems (Wu et al. 2014), such as complex fluid-rock interactions.

Fluid-rock interactions describe changes in a system's geochemistry resulting from the alteration of the host rock and secondary minerals by pore fluids. These processes are fundamental to the characterization of hydrologic systems by altering fluid composition, solute transport, pore-space geometry, and geomechanical properties (e.g., Steefel et al. 2009). Yet, constraining such fluid-rock interactions in field settings is inherently challenging as they occur out of view, are often site-specific, and involve complex coupled processes. The best way to constrain fluid-rock interactions at high precision is through geochemical fluid and rock sampling (e.g., Emberley et al. 2005; McGrail et al. 2017; Polites et al. 2022), but such sampling typically provides limited spatial and temporal coverage. For example, rock samples recovered from air-lift pumping of H_2S injection wells have revealed pyrite formation, but samples were only obtained from a single well (Snæbjörnsdóttir et al. 2017).

Geophysical surveying offers an approach to improve the spatial extent and temporal resolution of subsurface monitoring efforts and provide constraints on the geochemical and hydrological heterogeneities of a system (e.g., Binley et al. 2015; Singha et al. 2015). Previous studies have utilized stochastic frameworks to estimate hydrogeologic parameters and lithologic reactive facies by linking sparsely-spaced hydrological data and densely-spaced geophysical data, collected using electromagnetic methods (Ezzedine et al. 1999), ground penetrating radar (Hubbard et al. 1997; Chen et al. 2004), seismic methods (Rubin et al. 1992; Copty et al. 1993; Wainwright et al. 2014), and joint radar-seismic approaches (Chen et al. 2001; Hubbard et al. 2001; Sassen et al. 2012). Geophysical data can also serve as calibration datasets for hydrogeophysical inversions of hydrogeological model parameters (e.g., Hinnell et al. 2010; Camporese et al. 2015; Pleasants et al. 2022). In this strategy, hydrogeological models can provide insight into the underlying systems driving geophysical signatures, such as changes in pore-fluid chemistry (Wu et al. 2011), microbial activity (Mellage et al. 2018), and biomass changes (Wu et al. 2014; Mellage et al. 2018). However, real-world noise and geologic complexities introduce ambiguity to geophysical signatures, and careful interpretation is required to distinguish the combined effects of coupled processes.

Geochemical and hydrological numerical models can serve as predictive tools to simulate subsurface fluid-rock interactions throughout subsurface systems. This provides insight into the underlying processes controlling the expected geophysical changes (e.g., Wu et al. 2014; Mellage et al. 2018), thereby serving to limit ambiguity in geophysical interpretation. However, accurately simulating real-world subsurface processes requires geochemical models with extensive spatial and temporal parameterization, including fluid flow and transport rates, geochemical reactions and rates, geologic structure, accurate model initial and boundary conditions, and geochemical time-series measurements for calibration.

This thesis explores joint geochemical-geophysical approaches for the specific case of field-scale hydrogen sulfide (H_2S) mineral storage. H_2S mineral storage aims to reduce the atmospheric emissions of H_2S gas by capturing the gas in secondary minerals in the subsurface. Release of H_2S into the atmosphere creates environmental problems, including producing odors in nearby cities (Gunnarsson et al. 2011) at concentrations as low as $\sim$1 µg/m^3. At higher concentrations, these H_2S emissions pose an environmental threat, as H_2S is toxic to humans, animals, and vegetation at concentrations exceeding 530 ppm (WHO 1981). Additionally, the oxidation of H_2S can produce sulfur dioxide and sulfuric acid, leading to acid rain (Stefánsson et al. 2011). To mitigate these impacts, European and Icelandic regulations require that the average H_2S gas concentration, based on air samples collected periodically over a 24-hour window (i.e., 24-hour moving average), remain below 50 µg/m^3 (Danzon et al. 2001; Govt. of Iceland 2010). Disposal methods such as mineral storage are explored to reduce atmospheric emissions (e.g., Matter et al. 2016).

Capturing these emissions through the mineral storage process involves injecting H_2S dissolved in water into the subsurface, where it interacts with the rock to form sulfur-bearing secondary minerals. Geochemical models and laboratory studies show that iron leached from the reservoir rock binds with the sulfur to form iron sulfides, primarily pyrite (e.g., Stefánsson et al. 2011; Přikryl et al. 2018; Schaef et al. 2013). This H_2S mineral storage process has been implemented at several Icelandic geothermal sites (Gunnarsson et al. 2018; Snæbjörnsdóttir et al. 2021; Galeczka et al. 2022; Kjeld et al. 2022). Basalt reservoirs are targeted at these sites due to their reactivity and high iron abundance (Kelemen et al. 2019), both of which are necessary components of the H_2S mineral storage approach.

While the mineral storage approach has the potential to reduce atmospheric H_2S emissions and surface hydrologic discharge, the process must be monitored to evaluate the extent of mineral precipitation, its stability over time, and possible undesirable environmental impacts. Adverse impacts of mineral storage approaches include pore clogging of the host reservoir (Callow et al. 2018), contamination and acidification of the groundwater and surface waters (Zarandi et al. 2010; Stefánsson et al. 2011; Cuoco et al. 2013; Gómez-Díaz et al. 2022), mobilization of toxic metals (Zheng et al. 2009; Floor et al. 2011; Sigfusson et al. 2011), and gas leakage to surface waters and the atmosphere (Meckel et al. 2013; Yang et al. 2013; Cameron et al. 2016).

Monitoring efforts for mineral storage in the rock formation have relied primarily on indirect quantification of mineralization (Matter et al. 2016; White et al. 2020; Gunnarsson et al. 2018; Clark et al. 2020). The monitoring methodologies have primarily been developed for CO_2 storage (e.g., Matter et al. 2016; White et al. 2020), but they apply to a large extent to H_2S storage and similar pitfalls exist for both applications. White et al. (2020) inferred CO_2 mineralization percent by calibrating gas saturation levels in numerical models to field responses of well pressure buildup. Matter et al. (2016) inferred carbonate mineralization percent by injecting CO_2 alongside a non-reactive tracer and applying mass balance calculation based on the respective concentrations measured at monitoring wells downstream. While this method indirectly quantifies mineralization percentages of injected CO_2 and H_2S (Gunnarsson et al. 2018; Clark et al. 2020), White et al. (2020) suggests that uncertainty arises due to the flow-path dependence between the injection and monitoring wells that may not represent other flow paths in the reservoir and due to complex interactions between multiple processes, including dissolution, precipitation, and adsorption. Furthermore, recent studies have shown that injected CO_2 can be stored as biomass, leading to uncertainty in the way mass balance calculations shall be interpreted (e.g., whether the lower CO_2 concentration in monitoring wells compared to tracer-based calculations may indicate carbonate precipitation or biomass formation or both) and eventually less permanent CO_2 storage than claimed (Trias et al. 2017; Daval 2018). Ultimately, each of these sampling methods has a limited spatial extent due to sparse monitoring boreholes and surface sampling sites, and they provide only indirect measurements of CO_2 and H_2S mineralization.

Electrical geophysical methods, which involve injecting current into the ground and measuring the resulting voltage differences to determine subsurface electrical properties, are particularly useful for monitoring hydrogeological processes due to their sensitivity to factors such as pore fluid conductivity, pore space geometry, and electrochemical interactions at the fluid-rock interface (Singha et al. 2015). Hydrothermal processes can significantly affect these parameters, making electrical geophysics a valuable, albeit complex, tool for imaging hydrothermal systems (see Revil et al. (2021b) and references therein). However, electrical geophysical approaches, such as induced polarization (Wu et al. 2010; Wu et al. 2011; Zhang et al. 2012; Saneiyan et al. 2018; Izumoto et al. 2020) and self-potential (Rembert 2021; Rembert et al. 2022), have primarily been applied to laboratory-scale studies of carbonate and sulfide precipitation, and their potential for monitoring field-scale systems has not been extensively investigated (Williams et al. 2009; Saneiyan et al. 2019).

Sulfides have unique electrochemical properties that produce measurable geophysical signals when imaged using the direct current and induced polarization (DCIP) method. The sulfide grains exhibit a capacitive effect, storing reversible charges at the grain-fluid interface that can be measured with DCIP (e.g., Shuey 1975; Wong 1979; Revil et al. 2015; Abdulsamad et al. 2017)(see further in Section 3.2.1). Thereby, the time-lapse DCIP surveying represents a potential tool to improve the spatial coverage and resolution of H_2S monitoring methods. However, other factors besides sulfide formation also contribute to the DCIP geophysical response, including pore space geometry, fluid conductivity, and other primary and secondary minerals (e.g., Gurin et al. 2015). This makes H_2S mineral storage an ideal target to explore the mutual benefits of integrating geochemical modeling and geophysical surveying.

Reactive transport models are well-suited for integration with field geophysical surveying because they consider the complex, coupled processes of groundwater flow, solute transport, and geochemical reactions (Steefel et al. 2005). Reactive transport more accurately models real-world systems and, in the particular case of H_2S injection systems, offers valuable insight into the fluid–rock interactions that govern and occur alongside sulfide precipitation. In general, efforts to integrate reactive transport modeling and geophysical surveying at the field-scale remain limited to parameterization of reactive transport models with geophysics (Sassen et al. 2012; Wainwright et al. 2014). At laboratory scales, applications include the assessment of biogeochemical end products (Chen et al. 2009) and carbonate precipitation for trace metal sequestration (Wu et al. 2011). The integration of geophysical surveying with reactive transport in this study provides insight into the controls of H_2S mineral storage and evaluates the performance of novel geophysical monitoring methods for mineral storage approaches.

1.2 Research Aims

The integration of DCIP geophysics and reactive transport modeling is approached through multiple avenues in this study, focusing on H_2S mineral storage. First, geophysical field measurements collected with wireline and surface survey configurations serve to improve the spatial coverage and resolution of geochemical monitoring, which has been limited to sparse borehole fluid sampling to indirectly infer H_2S mineralization. The measurements are also used to validate the geochemical model parameters and the results of the simulated fluid-rock interactions.

Next, geochemical models are used to predict the fluid-rock interactions that facilitate H_2S mineral storage and the distribution of H_2S mineralization. By providing the expected geochemical and geophysical changes, the geochemical models provide context for the measured geophysical response changes, thereby reducing the ambiguity of the interpretations. The geochemical models are also utilized a priori to evaluate the sensitivity of various geophysical surveys to H_2S mineralization.

The four specific aims addressed through the integration of DCIP with reactive transport modeling for monitoring H_2S mineral storage are as follows:

1. Understand the geochemical and hydrological factors controlling the extent of H_2S mineralization and corresponding geophysical signatures in field conditions.

2. Utilize geochemical reactive transport models alongside various time-lapse DCIP geophysical field acquisitions a priori to evaluate the sensitivity of the method to monitor H_2S mineralization.

3. Explore how geochemical reactive transport models can be used a posteriori to constrain the interpretation of time-lapse DCIP inversion results, reducing ambiguity in the geophysical interpretations.

4. Understand the long-term effectiveness of H_2S mineral storage and how to better monitor this process.

2 Background: H_2S Injection into Basalt for Geothermal Emissions Reduction

2.1 Iceland Geothermal Systems and Emissions

Geothermal energy is a key component of energy production in Iceland, providing roughly 65% of Iceland's domestic energy and 30% of the electricity demand at an installed capacity of 755.3 MWe (Ragnarsson et al. 2023). Energy demand in Iceland is forecast to increase by up to 124% in 2040, driven by increased public demand, growth in energy-intensive economic sectors, and efforts to reach climate goals (Iceland 2022). The total harnessable geothermal energy currently beneath Iceland is estimated at 59 TWh/a (Bödvarsson 1982; Pálmason et al. 1985; Stefánsson 2000), which is contained in both low and high-temperature geothermal systems. At least 250 low-temperature and 26 high-temperature geothermal fields have been identified in Iceland (Wiglusz et al. 2017).

Low-temperature systems have fluid temperatures below 200°C at depths less than 1000 m (Fridleifsson 1979). Many low-temperature systems are related to local, density-driven convection along young fractures formed by tectonic stresses in older crust (Arnórsson et al. 2008). The main gas emissions from these systems are N_2 and Ar (Arnórsson 1986). These low-temperature geothermal systems are primarily developed for district heating, supplying space heating and hot water for residential and industrial buildings (Arnórsson et al. 2008).

High-temperature systems are defined by temperatures greater than 200°C above 1000 m depth (Fridleifsson 1979), and are developed for both district heating and electricity production in Iceland (Arnórsson et al. 2008). To produce electricity, superheated geothermal water (i.e., production fluid) is brought to the surface, where a controlled pressure drop produces steam that drives turbines to generate electricity. These systems are often associated with shallow volcanic intrusions (Arnórsson 1995). Due to the magmatic heat sources, gas concentrations are higher in hig-temperature geothermal systems, and the most abundant gases are carbon dioxide (CO_2), hydrogen sulfide (H_2S), and hydrogen (H_2) (Arnórsson 1986). These gases are brought to the surface with the production fluids, resulting in geothermal emissions.

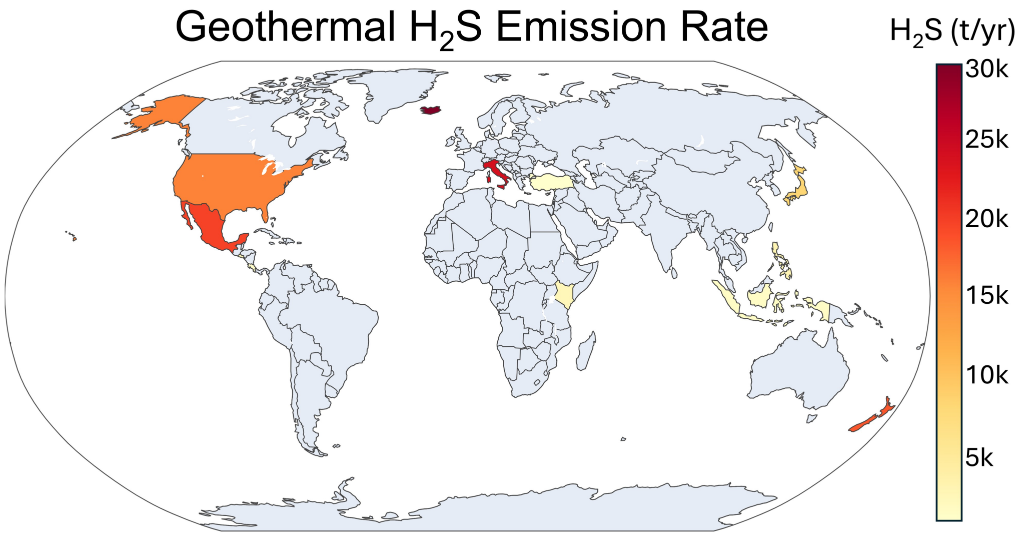

Figure 2.1: H_2S emission rates per country from geothermal energy production. Data collected from Marieni et al. (2018).

Iceland is the world's largest emitter of H_2S from geothermal energy production, estimated at 30 kt/yr (Figure 2.1). Total worldwide geothermal emissions are estimated at 9.6 Mt/yr of CO_2 and 132 kt/yr of H_2S. This study focuses on the Nesjavellir power plant (SW Iceland), which contributes up to 11,300 tons of H_2S per year (Marieni et al. 2018).

2.2 Nesjavellir Geothermal Field

Nesjavellir is a high-temperature geothermal field, producing 120 MWe and 300 MWth from 260-300 °C water sourced at 1000-1500 m depth (Snæbjörnsdóttir et al. 2021). The site is located on the northeast flank of the Hengill central volcano, which sits on a ridge-ridge-transform triple junction (Figure 2.2). Nesjavellir, and much of the faulting and recent volcanism, is situated within a 5 km-wide graben that reflects an extensional tectonic setting (Foulger 1988). The area is comprised primarily of late Quaternary and post-glacial age basalt flows and hyaloclastites (Arnason et al. 1969; Foulger et al. 1989). Basalt alteration is limited above 400 m depth, encompassing much of the injection interval explored in this study (Helgadóttir 2021). Alteration increases at greater depths, where zeolites and smectites are present closer towards the clay cap of the deep geothermal system at ~500 m depth (Franzson 1988; Helgadóttir 2021).

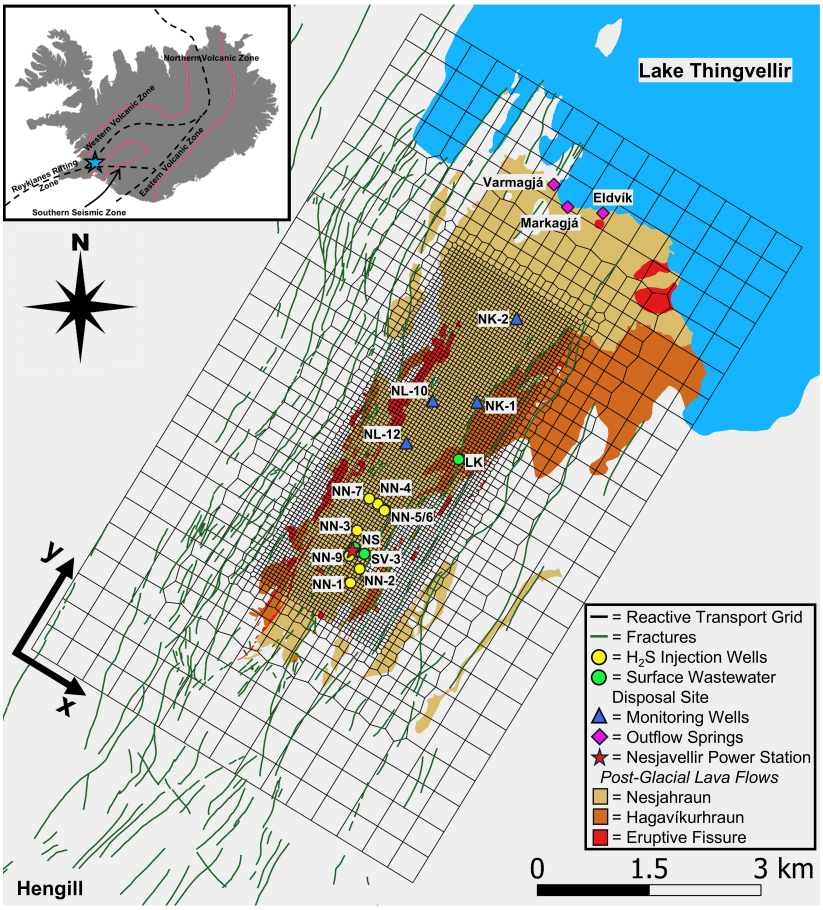

Figure 2.2: Map of the Nesjavellir site between the Hengill central volcano and Lake Thingvellir. Unmarked geology zones are hyaloclastites. The reactive transport grid (Paper II) is overlaid on the map in black. The blue star on the insert shows the location of Hengill within Iceland, located on the triple junction of the Reykjanes Peninsula Rift, South Iceland Seismic Zone, and Western Volcanic Zone (Einarsson 2008).

H_2S injection began at Nesjavellir in January 2021, where the H_2S gas is dissolved into the geothermal wastewater and injected into the shallow groundwater system (200-500 m depth). The shallow injection depth and the soft soil at the surface within the rift valley make the Nesjavellir site particularly well-suited to test the ability of the surface DCIP geophysical method to monitor field-scale H_2S mineral storage. Moreover, the site is well-suited for the development of reactive transport models, given that its geological structure is relatively well constrained by drilling, calibrated flow models already exist for the site (Gómez-Díaz et al. 2022), and thermodynamic databases have been developed explicitly for mineral storage within Icelandic basalts (Voigt et al. 2018). Lastly, monitoring wells are sparse at the Nesjavellir site and only tap into the upper ∼20-50 m of the groundwater system, so the site would greatly benefit from improved monitoring methods.

2.3 Geological Storage for Emissions Reduction

Geological storage approaches have been explored as a means to reduce atmospheric emissions of gases such as carbon dioxide (CO_2) and hydrogen sulfide (H_2S). In these approaches, gases are captured at emission sources (e.g., power plants) or directly from the atmosphere (Beuttler et al. 2019) and injected into subsurface storage reservoirs, where they are stored in the pore space. While this approach reduces atmospheric emissions, potential leakage of injected gases and brines poses a significant challenge to the emission reduction strategy (Kelemen et al. 2019). Mitigating leakage requires extensive efforts to characterize the hydrological system and to ensure the integrity of caprock units above storage reservoirs. The risk of leakage can also be reduced through secondary trapping mechanisms, including solubility trapping through dissolution of the gases (Emami-Meybodi et al. 2015), gas trapping via capillary forces (Krevor et al. 2015), and in-situ mineralization upon interaction of the pore fluids, gas, and reservoir rock (Matter et al. 2016; Zhang et al. 2017).

Trapping the gases through the precipitation of secondary mineralization (i.e., mineral storage) offers a potentially permanent (e.g., Matter et al. 2016) and cost-effective (e.g., Gunnarsson et al. 2018; Marieni et al. 2018) geological storage approach. Mineral storage involves the precipitation of secondary minerals, including carbonates (e.g., calcite, dolomite, magnesite) for CO_2 storage and iron sulfides (e.g., pyrite, pyrrhotite) for H_2S storage, upon reaction of the injected gases with the reservoir rock. Mafic and ultra-mafic rocks, including peridotite and basalt, have been explored as suitable reservoirs for mineral storage due to their reactivity and abundance of divalent cations (calcium, magnesium, and iron) required to form relevant secondary minerals (Kelemen et al. 2019).

Basalt has a major advantage for mineral storage over peridotite due to its high porosity and permeability, which increase reactivity and preserve fluid flow (Kelemen et al. 2019). Mineral storage in basalts has been implemented for H_2S and CO_2 through the Carbfix method (e.g., Matter et al. 2016) and the Wallula basalt pilot project (e.g., McGrail et al. 2011). While injection into basalts has shown promise for mineral storage at pilot sites (e.g., Matter et al. 2016; Gunnarsson et al. 2018; Clark et al. 2020), maximizing the effectiveness of mineral storage at the field-scale requires a thorough understanding of the complex fluid-rock interactions governing the mineralization of injected solutes.

2.4 Fluid-Rock Interactions

Altering the basalt reservoir is governed by complex fluid-rock interactions that are often site-specific. Basalt alteration depends on a complex interplay between factors such as lithology, temperature, fluid chemistry, and rock structure (Browne 1978; Kristmannsdóttir 1979). Temperature has a large control on basalt alteration rates and alteration mineralogy (e.g., Kristmannsdóttir 1979; Arnórsson 1983). For example, Thien et al. (2015) showed that for small basaltic glass grains, total alteration occurs after a few days at temperatures above 300°C, while hundreds of years are required at low geothermal temperatures of 50°C.

At a fixed temperature, lithology strongly controls the degree of alteration, with glass-rich hyaloclastites altering more readily than holocrystalline basalts (Kristmannsdóttir 1979). Furthermore, the rock structure of hyaloclastites, including increased initial water content, higher pore connectivity, and higher permeability, promotes higher degrees of alteration compared to lava flows (e.g., Kristmannsdóttir 1979; Thien et al. 2015; Scott et al. 2023). The lower initial porosity (i.e., initial water content) of lava flows can lead to complete pore filling by secondary minerals, thereby obstructing pore connectivity and preserving the rock from further fluid-rock interactions (Thien et al. 2015).

Fluid chemistry is also an important consideration in fluid-rock interactions, controlling factors such as alteration rates and mineral stability (e.g., Browne 1978). As related to mineral storage, Gudbrandsson et al. (2011) found in laboratory studies that Mg and Fe were preferentially removed from crystalline basalts in acidic waters compared to Ca in basic waters, thereby controlling which carbonate species precipitate. Further laboratory studies found that H_2S mineralization rates were most sensitive to the fluid's pH rather than temperature or concentration (Přikryl et al. 2018). Conversely, Franzson et al. (2008) concluded that alteration assemblages in natural systems are primarily influenced by temperature, with fluid chemistry as a secondary factor. These results illustrate the complexities of fluid-rock interactions and the complicated interplay of the factors controlling the interactions under various geochemical conditions.

Specific to mineral storage approaches, CO_2 mineralization is the subject of many studies, as detailed in the recent review by Snæbjörnsdóttir et al. (2020), while fewer studies have focused on H_2S injection (e.g., Stefánsson et al. 2011; Přikryl et al. 2018). Stefánsson et al. 2011 utilized reaction path models to show that sulfide mineralization in basalts was most affected by the availability of rock-sourced iron and the oxidation state of the iron. Their models also showed that pyrite competes with smectites and epidote for iron availability, establishing that high temperatures (>230 °C) can limit H_2S mineralization due to epidote mineralization. Laboratory flow-through column experiments presented in Přikryl et al. (2018) supported these findings, showing that iron supply controls the effectiveness of H_2S mineralization. Additionally, iron sulfide formation was greatest at the inlet side and increased with higher temperatures, indicating that H_2S mineralization is rapid and enhanced by the higher basalt alteration rates associated with elevated temperatures.

In the laboratory experiments of basalt samples that had undergone alteration with H_2S-rich water, pyrite was the main iron sulfide mineral identified by various techniques, including X-ray diffraction (XRD), electron microprobe analysis (EPMA), and energy-dispersive spectrometry (EDS) (Schaef et al. 2013; Přikryl et al. 2018). To a lesser extent, these laboratory studies also identified pyrrhotite (Přikryl et al. 2018) and marcasite (Schaef et al. 2013). XRD analysis of precipitates recovered from an airlift pump of an H_2S injection well at the nearby Hellisheiði geothermal field identified pyrite as the sole iron sulfide. However, other iron sulfides were supersaturated in the monitoring well fluid samples, including greigite, pyrrhotite, marcasite, and mackinawite, and the nanocrystalline structure of mackinawite makes it difficult to identify through XRD (Snæbjörnsdóttir et al. 2017). Furthermore, the presence of metastable iron sulfide phases, such as mackinawite, is controlled by complex processes (e.g., precipitation kinetics, nucleation, geochemical conditions) that can hinder pyrite formation (Schoonen et al. 1991; Schoonen 2004; Rickard et al. 2007). These processes are difficult to capture with geochemical models (e.g., Kaasalainen et al. 2011) and have not been fully explored in the context of H_2S mineral storage.

Ultimately, the previous studies highlight the importance of constraining fluid-rock interactions to achieve safe and effective mineral storage. Since these subsurface processes are largely hidden from view and alteration samples can be difficult to obtain, alternative monitoring approaches and predictive tools are essential.

3 Methodology

3.1 Geochemical Modeling Methods

3.1.1 Simulating Fluid-Rock Interactions

Aqueous geochemical models simulate complex fluid-rock interactions that control systems such as mineral storage approaches. The general approach of the aqueous geochemical models developed in this study is to first determine the concentrations of aqueous complexes (i.e., speciation) through mass action equations assuming local equilibrium. The saturation conditions of solid species are then calculated, and supersaturated species are allowed to precipitate and undersaturated species dissolve. Precipitation or dissolution occurs to reach equilibrium or is controlled through specific reaction rates (kinetics). Iterative procedures are utilized to solve the nonlinear system of equations and to satisfy mass and charge balances. The model inputs include the fluid chemistry, rock composition, and a thermodynamic database that provides data (e.g., equilibrium constants, species definitions, activity coefficient parameters) for the thermodynamic model (e.g., Lu et al. 2022).

In this thesis, the rock composition is constrained through whole-rock analysis of drill cuttings collected from the injection wells and milled to <150 µm (n=102). The total carbon and sulfur contents were defined utilizing a combustion infrared carbon and sulfur analyzer (www.actlabs.com/geochemistry). Inductively coupled plasma optical emission spectroscopy (ICP-OES) analysis at the University of Iceland constrained the major element composition on a subset of the samples (n=26).

ICP-OES and ion chromatography (IC) analysis at the University of Iceland constrained the fluid chemistry of the H_2S-rich waters. The waters were sampled in November 2021 at the injection wellheads and downhole at a nearby monitoring borehole using a polyvinyl chloride bailer. The CO_2 concentrations were measured through modified alkalinity titration (Jeffery et al. 1989; Arnórsson et al. 2006; Stefánsson et al. 2007) and the H_2S concentrations were measured via mercury acetate titration with dithizone as the indicator in the lab (Arnórsson et al. 2006). Additional details on the sampling and analytical methods utilized to constrain the water and rock chemistry are provided in Chapters 3 and 4 (Paper I). Lastly, the *carbfix.dat* database, developed specifically for modeling fluid-rock interactions related to mineral storage in basaltic host rocks (Voigt et al. 2018), constrains the thermodynamic conditions.

For the more complex geochemical model presented in Chapter 5, the background groundwater chemistry is defined from water samples collected near the start of geothermal production at Nesjavellir, as reported in Sigfusson et al. (2011). Additionally, more complex host rock mineralogy is included, defined by a linear least-squares fit to the average bulk rock composition.

3.1.2 Reaction Path Models

Many previous studies of H_2S mineral storage rely on batch reaction models called reaction path models (Helgeson et al. 1969; Marini 2006) that simulate progressive host rock alteration in a closed system (e.g., Galeczka et al. 2022; Gysi et al. 2008; Gysi et al. 2011; Stefánsson et al. 2001; Stefánsson et al. 2011; Schaef et al. 2013). These models output secondary minerals for a given amount of host rock dissolution, determined either by fixed user-input amounts (i.e., equilibrium-controlled) or by reaction rates and simulated time (i.e., kinetically-controlled).

At the start of the PhD, I simulated reaction path models using PHREEQC software first to constrain the expected interactions between the H_2S-rich injection water and the basalts at Nesjavellir, establish the viability of H_2S mineral storage for the specific Nesjavellir system, and to determine the expected secondary mineralogy (Figure 3.1). These simulations found similar results to models of comparable H_2S injection systems (Stefánsson et al. 2011; Schaef et al. 2013; Galeczka et al. 2022) and general basalt alteration in Iceland (e.g. Crovisier et al. 1992; Stefánsson et al. 2001; Gysi et al. 2008; Gysi et al. 2011). H_2S readily mineralizes, alongside clays and zeolites, at the Nesjavellir injection site at early stages of basalt dissolution (i.e., higher fluid/rock ratio). The degree of mineralization is limited by the iron supply at the early stages of basalt dissolution, as identified in Stefánsson et al. (2011). As the reaction progresses (i.e., lower fluid/rock ratio), carbonates and iron oxides form and iron sulfides become a smaller proportion of the alteration assemblage, suggesting that fluid-sourced H_2S has undergone near-complete mineralization. Galeczka et al. (2022) found similarly favorable conditions within the deeper injection system at the Nesjavellir site, with 100% of the injected H_2S mineralizing upon the alteration of 0.2 moles of basalt per kg of water.

While reaction path models illustrate potential fluid–rock interactions and support the feasibility of H_2S mineral storage at Nesjavellir, they do not capture the full complexity of site-specific processes. In particular, by neglecting fluid flow and solute transport, which can limit fluid-rock interactions by removing the fluids before they fully react with the rock, the reaction progress remains unconstrained and the closed-system model cannot fully characterize real-world geochemical systems (Steefel et al. 2005).

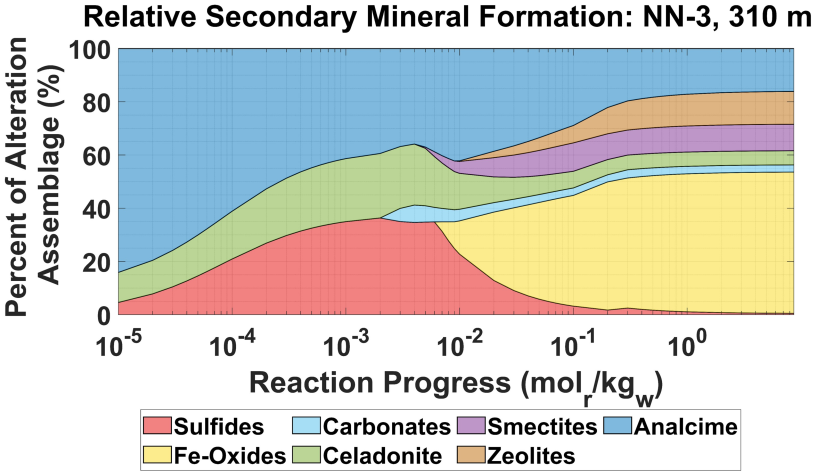

Figure 3.1: Predicted secondary mineral abundances during progressive basalt alteration, based on reaction path modeling under equilibrium conditions. Results reflect fluid-rock interactions between H_2S-rich fluid from the NN-3 injection well and basalt cuttings from 310 m depth.

3.1.3 Reactive Transport Modeling

Reactive transport models simulate both local batch geochemical reactions at each grid cell in the model and physical flow and transport processes (advection, dispersion, and diffusion). Coupling these batch reactions to physical transport at the field-scale through reactive transport modeling more accurately and quantitatively characterizes real-world geochemical systems.

At its core, reactive transport simulations satisfy the conservation of mass and momentum for reactions between the aqueous and solid phases, and for the transport of aqueous species, heat, and water. When considered as a continuum, this is accomplished by solving the advection-diffusion equation (ADE), a partial differential equation that integrates advective fluid flow ($-v \cdot \nabla c$), diffusion ($\nabla \cdot (D\nabla c)$), external sources and sinks (S), and chemical reactions (R). A generalized form of this equation can be expressed as,

$$\frac{\partial c}{\partial t} = \nabla \cdot (D\nabla c) - v \cdot \nabla c + S + R\,, \tag{3.1}$$

where c is the concentration of a single component of the system ($\mathrm{mol}_{species} \cdot \mathrm{m}^{-3}$), v is the fluid velocity field governed by Darcy's Law ($\mathrm{m} \cdot \mathrm{s}^{-1}$), D is diffusivity ($\mathrm{m}^2 \cdot \mathrm{s}^{-1}$; product of the diffusion coefficient, porosity, and tortuosity), and the terms S and R represent the source/sinks and the chemical reactions considered ($\mathrm{mol}_{species} \cdot \mathrm{m}^{-3} \cdot \mathrm{s}^{-1}$), respectively. The fluid-rock interactions described in Section 2.4 are contained in R of the ADE, considering the rock composition, fluid chemistry, and thermodynamic data.

By coupling the reactions with mass transport processes, reactive transport models describe how the chemical system changes over a flow path, thereby providing a spatial distribution of the geochemical system (Figure 3.2). The consideration of physical transport processes also captures how these processes can directly limit the geochemical reactions - a concept described by the Damkölher number, which is a ratio of the chemical reaction rates to the mass transport rate (e.g., Carrera et al. 2022).

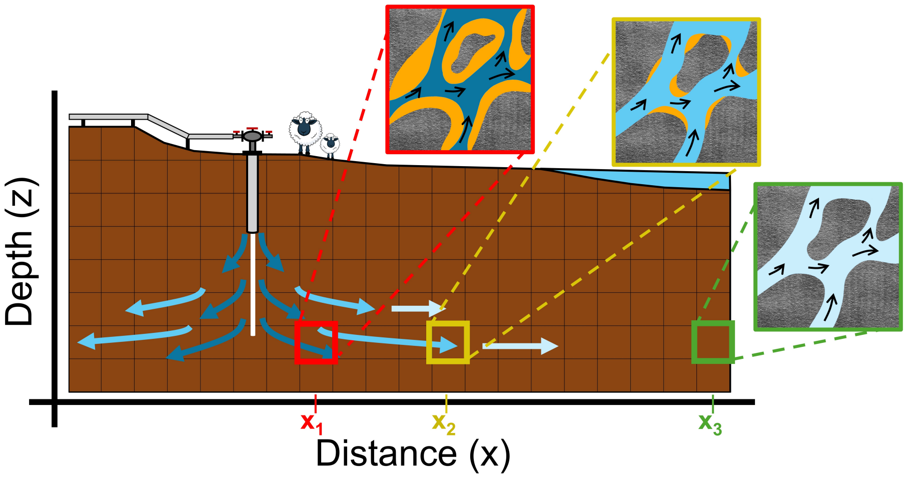

Figure 3.2: Schematic of reactive transport simulations of the injection system at Nesjavellir. The diagram highlights how reactive transport models simulate host rock alteration (gray rock) and secondary mineral precipitation (orange precipitate) resulting from fluid-rock interactions with an evolving pore fluid composition (shades of blue) along the flow path. Concentrated fluids near the injection borehole promote fluid-rock interactions, leading to increased host rock dissolution and secondary mineral precipitation.

To consider the effects of transport processes on mineral storage, I used PHREEQC software (Parkhurst et al. 2013) in Chapter 4 to develop 1D advective reactive transport models based on the mineralogy and fluid chemistry of the reaction path models discussed previously. The 1D models simulate simplified advective plug flow along a column, where each cell acts as an independent batch reactor and each transport step shifts the entire solution in a cell to the next cell without any fluid mixing. The models do not compute concentration gradients or solve advective flux equations. Instead, transport is controlled by the number of cells in the column, the number of advective shifts, the fluid residence time of each shift, and chemical reactions that occur within each cell. The total simulation time is the product of the number of shifts and the residence time per shift. The model space is defined after the simulation by assigning a fluid velocity and multiplying it by the residence time per shift, which yields an effective travel distance per shift. Because the solution in each cell is simply replaced rather than transported numerically, the model effectively reproduces the analytical solution to 1D advective flow and transport without introducing numerical dispersion. To represent radial flow from an injection well, the model uses a constant residence time while decreasing the fluid velocity as a function of radial distance r. This results in cell widths that decrease proportionally to 1/r, consistent with conservation of volumetric flow in radial geometry. Consequently, the larger cells at the start of the flow path lead to lower resolution of the steep geothermal gradients near the injection borehole.

Similar plug flow models have been developed for laboratory studies to better understand the fluid-rock interactions in flow-through column experiments (Galeczka et al. 2014; Přikryl et al. 2018). These models simplify the system to consider only 1D advective flow (Equation 3.1) and assume the host rock consists entirely of basaltic glass, a component of the host rock critical for supplying divalent cations for mineral storage. Using these models and flow-through column reactors, Přikryl et al. (2018) showed that higher temperatures and lower pH values increase the dissolution rate of basaltic glass relative to flow rate, resulting in higher percentages of H_2S mineralization. Additionally, their models characterized how porosity evolves along the flow path, with dissolution near the injection inlet driving increases in porosity. In a similar approach, Galeczka et al. (2014) used flow-through column reactors and 1D reactive transport models to illustrate how the fluid chemistry of CO_2-rich water evolves along the flow path. While the study captured fluid-rock interactions by accounting for transport processes, the simple models were unable to accurately describe the laboratory reactors. Discrepancies were found between the modeled and experimental fluid compositions, attributed to limited secondary minerals considered, simplified thermodynamic properties, and uncertainties in kinetic rates and reactive surface area constraints. Therefore, the simple 1D models I develop for the Nesjavellir injection system serve as a step towards the development of field-scale reactive transport models that consider more flow and geochemical complexities to more accurately describe the real-world H_2S mineral storage system (Chapter 5).

In the complex field system, the processes governing mass transport can vary greatly within the fractured basalt, with fast, advection-dominated transport occurring with bulk fluid motion in the fracture network and slow, diffusive-dominated processes following concentration gradients in the matrix (e.g., Berre et al. 2019). These processes can be challenging to model at the field-scale, and thus many models simplify the system to consider flow and transport through a single, effective porous medium (i.e., single-porosity). Single-porosity models use bulk-average properties to capture the average flow and transport behavior throughout the reservoir. However, Gómez-Díaz (2020) showed that these models have limited ability to reproduce tracer recovery curves in fractured basalts at the Nesjavellir site. To more accurately simulate flow and transport in complex, fractured media, such as fractured basalt (e.g., Gómez-Díaz et al. 2022; Ratouis et al. 2022), studies have developed multiple-porosity models that partition the subsurface into high-permeability fracture and low-permeability rock matrix domains (Warren et al. 1963; Pruess et al. 1985; Nelson 1987).

Laboratory models of CO_2 mineral storage approaches have also shown that mineralization occurs primarily in diffusion-dominated areas, where slow transport rates allow for sufficient fluid-rock interactions to mineralize carbonates (Giammar et al. 2014; Adeoye et al. 2017; Luhmann et al. 2017; Xiong et al. 2017). Thus, multiple-porosity reactive transport models simulating fluid-rock interactions in the distinct advection- and diffusion-dominated regions provide a means to more accurately capture the processes governing fluid flow and mineral storage.

I developed a multiple-porosity reactive transport model of the injection system using TOUGHREACT software (Xu et al. 2006). This model is built using the Multiple Interacting Continuum (MINC) multiple-porosity grid structure (Pruess et al. 1985) to account for more complex flow processes in the real-world system. In the MINC model, I subdivided the grid into three nested domains: fractures, outer rock matrix, and inner rock matrix (Figure 3.3). Flow occurs across the model domain through only the permeable fracture elements, capturing the principle that hydrological changes propagate quickly through the advection-dominated fracture network compared to the low-permeability rock matrix. I utilized PEST software (Doherty et al. 2010) to calibrate the 3D MINC flow to borehole temperature data collected after wastewater injection began at the Nesjavellir site. Local interporosity flow and transport in the MINC approach occur within each element between the fractures and the outer rock matrix, and between the outer rock matrix and the inner rock matrix. Solute transport in the rock matrix is controlled by the distance from the fracture network and by diffusion, given the concentration gradients between the fluids in the fractures and the pore space. Thus, the advective-dominated and diffusive-dominated processes are simultaneously, yet distinctly, considered by the model, resulting in a more complete simulation of real-world reactive transport processes (Warren et al. 1963; Pruess et al. 1985; Nelson 1987).

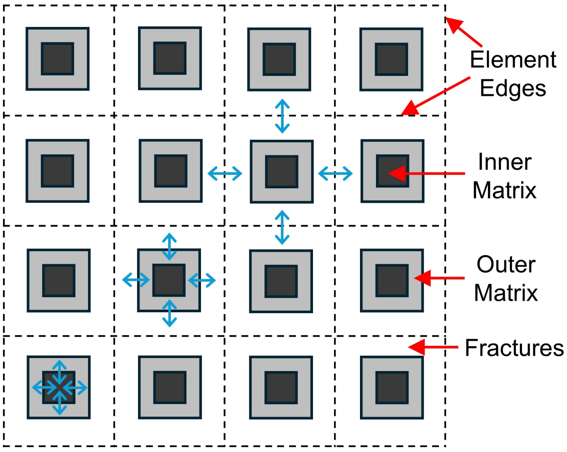

Figure 3.3: Schematic of a 2D reactive transport model with a multiple interacting continua grid (MINC). Each grid element is subdivided into three nested domains: fracture network, outer rock matrix, and inner rock matrix. The blue arrows illustrate the hydrological connections between the nested elements.

3.2 Geophysical Monitoring

3.2.1 Subsurface Electrical Properties

To apply electrical geophysical methods for mineral storage monitoring, it is essential first to understand how alteration processes in basalt affect subsurface electrical properties. This thesis utilizes the direct current and induced polarization (DCIP) electrical geophysical method, which considers both conduction (σ') and polarization (σ'') processes that contribute to the complex conductivity (σ^*) describing the electrical properties following (e.g., Vinegar et al. 1984):

$$\sigma^* = \sigma' + i\sigma'' \, . \tag{3.2}$$

Electrical Conduction:
Conduction describes how readily electrical current flows through the porous media and is the real component (σ') of complex conductivity. This bulk conductivity value is measured with the direct current (DC) resistivity geophysical method. Vinegar et al. (1984) defines the real conductivity component (σ') as the sum of the conduction through the pore fluids (σ_w, i.e., free ions in pore water) and conduction at the surface of the fluid-mineral interface (σ'_{surf}, i.e., ions exchanged with the rock matrix):

$$\sigma' = \frac{\sigma_w}{F} + \sigma'_{surf} \, , \tag{3.3}$$

where F is an electrical formation factor related to the pore architecture (i.e., tortuosity).

Processes associated with hydrothermal systems impact the pore fluid and surface conduction mechanisms:

i. Pore water salinity: Geothermal fluids are generally more saline than shallow groundwater due to processes such as phase separation (i.e., where boiling leaves behind more concentrated residual fluids), extensive fluid–rock interactions involving volcanic rocks and magmatic hydrochloric acid (HCl), enhanced rock leaching driven by elevated temperatures and lower pH from magmatic gases, and fluids mixing with deep, evolved formation waters and magmatic fluids (e.g., Arnórsson et al. 1978; Arnórsson et al. 2007; Finster et al. 2015). These processes increase the total dissolved solids and fluid salinity, leading to higher conductivities.

ii. High temperatures: Warm waters associated with hydrothermal systems are also more conductive than cold groundwater due to increased ion mobility in the less viscous fluid (Keller et al. 1966). The increase in water conductivity with increasing temperature is approximately 2% per degree C (Arps 1953; Keller et al. 1966; Hayashi 2004). As such, highly conductive responses can indicate the presence of hot water in hydrothermal systems.

iii. Reduced Porosity: Changes to the pore space geometry from hydrothermal alteration also impact the conduction mechanisms. Alteration in hydrothermal systems generally decreases the matrix porosity (e.g., Callow et al. 2018; Scott et al. 2023). Decreasing the connected porosity restricts current flow paths in the water and reduces the fluid-mineral interface, thereby decreasing the electrical conduction.

iv. Alteration Minerals: Mineralogical changes from host rock alteration in hydrothermal systems can also impact how current behaves at the fluid-rock interface (σ'_{surf}). Alteration minerals such as smectite clays and zeolites can have large cation-exchange capacities, a physiochemical property that defines the amount of exchangeable electrical charges on a mineral's surface (e.g., Weisenberger et al. 2020). Higher abundances of these alteration minerals result in increased conduction mechanisms along the surface of the rock matrix (e.g., Waxman et al. 1968; Vinegar et al. 1984). Furthermore, recent studies found that current flow through smectite clay minerals themselves (i.e., interfoliar current paths) can further contribute to the conduction mechanisms in altered basalts (Lévy et al. 2018; Lévy et al. 2019a).

Electrical Polarization:
Polarization describes the reversible storage of electrical charges in a porous material when subjected to an electric field, and it is the imaginary component (σ'') of the complex conductivity (i.e., dependent on current injection duration or frequency). This is measured through the induced polarization (IP) geophysical method (e.g., Sumner 1978; Chelidze et al. 1999). Similar to the surface conduction (σ'_{surf}) from Equation 3.3, the polarization process occurs at the surface of the fluid-mineral interface and is defined as:

$$\sigma'' = \sigma''_{surf} \,. \tag{3.4}$$

In the presence of disseminated metallic particles, the polarization mechanisms (σ'') are primarily driven by the metallic particle abundance (e.g. Wong 1979; Abdulsamad et al. 2017; Gurin et al. 2013; Gurin et al. 2015; Hupfer et al. 2016; Revil et al. 2015). Metallic particles encompass semiconducting materials, including ores, metals, and graphite (Martin et al. 2023). At the Nesjavellir site, metallic particles are primary iron oxides (e.g., magnetite, ilmenite) and secondary iron sulfides (e.g., pyrite, pyrrhotite). The semiconducting properties of metallic minerals allow for electron mobility within the minerals themselves, causing charge accumulation at the fluid-mineral interface when current flow is induced (Revil et al. 2015; Martin et al. 2023).

The degree of polarization can be described as the chargeability (m), a parameter describing the capacitive effect of the material (Sumner 1978). The chargeability is directly related to the volume fraction of metallic particles in the subsurface (Equation 3.11), with larger chargeability measurements indicating more abundant metallic particles (e.g., Wong 1979; Gurin et al. 2015; Revil et al. 2015). Lévy et al. (2019a) verified this direct relationship in laboratory studies on altered Icelandic basalts with varying abundances of metallic particles. Thus, mineralization of H_2S upon basalt alteration to iron sulfides increases the chargeability response, which is measured using the DCIP geophysical method. Although the IP response of each iron sulfide mineral are only beginning to be constrained (e.g., Gurin et al. 2015), laboratory measurements on altered volcanic samples show that pyrrhotite exhibits an IP response comparable to, or even greater than, that of pyrite (Lévy et al. 2019a).

While the volume fraction of metallic particles represents a primary control on the chargeability response, studies have also suggested a dependency on other factors such as the grain size of the metallic particles, mineral type, and surface characteristics (e.g., Martin et al. 2023; Lévy et al. 2019a; Gurin et al. 2019; Izumoto 2023). Additionally, in the absence of metallic particles, other mechanisms are believed to contribute to the polarization, including the ion exchange at the surface of smectite clays (Revil et al. 2017b; Revil et al. 2018; Ghorbani et al. 2018) and charge build-up in constricted pore spaces associated with clays called membrane polarization (Marshall et al. 1959). However, laboratory studies have also found that smectite clays diminish polarization responses (Lévy et al. 2019a), highlighting ongoing uncertainty in this relationship.

3.2.2 DCIP Methodology

This thesis focuses on the time-domain IP method, where a direct current square wave is injected into the subsurface through a pair of grounded electrodes (A and B), and the resulting voltage is measured at two additional electrodes (M and N) (Figure 3.4). The A-B-M-N electrodes make up a single quadrupole and provide a single geoelectrical measurement called the complex resistivity ($\rho_a^* = 1/\sigma_a^*$) (Martin et al. 2021):

$$\rho^* = \frac{1}{\sigma^*} = k \times \frac{2\pi \Delta V_{MN}^*}{I_{AB}^*} \,, \tag{3.5}$$

where ΔV_{MN}^* is the measured time-varying voltage difference between the M and N electrodes and I_{AB}^* is the current injected between the A and B electrodes. The term k is a geometric factor related to the distances between the various electrodes (AM, AM, BM, BN), defined as:

$$k = \frac{1}{\frac{1}{AM} - \frac{1}{AN} - \frac{1}{BM} + \frac{1}{BN}} \,. \tag{3.6}$$

The voltage response between the M and N electrodes (ΔV_{MN}^*) contains the DC electrical conduction response and the IP electrical polarization response, which

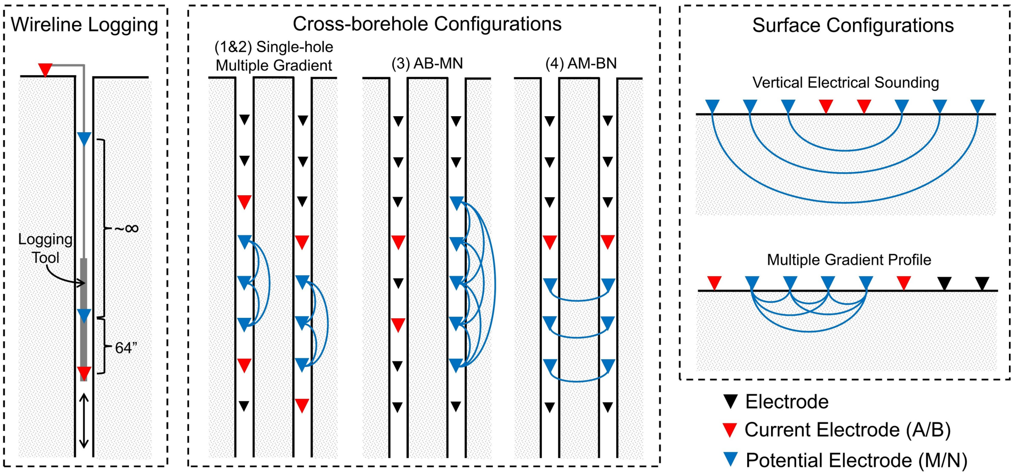

Figure 3.4: Electrode configurations for the galvanic geophysical methods utilized in this thesis. The cross-borehole data acquisition is the combination of the four configurations shown. Blue lines indicate the voltage dipole pairs.

arises when residual charges, accumulated during current injection, return to equilibrium (voltage decay). A simple schematic of the injection current and measured voltage for a 50% duty cycle is shown in Figure 3.5. Data can also be collected in a 100% duty cycle, which is implemented in the surface DCIP survey in this study to improve signal strength and reduce data acquisition time (Olsson et al. 2015). The measurement of the DC voltage (V$_{DC}$) is made near the end of the current injection (I_{on}). The voltage build-up, sometimes referred to as overvoltage, occurs during current injection due to polarization processes. Following the termination of the current, the voltage drops (V$_{IP,0}$) and decays with time as the residual charges, built-up during the current injection, relax to equilibrium (i.e., IP decay). This decay is the IP decay and contains information on the polarization of the subsurface.

There are multiple ways to quantify the IP effect from the decay curve. The intrinsic chargeability (V$_{DC}$/V$_{IP,0}$) is defined as the ratio between the DC voltage and the voltage measured just after the current is terminated (V$_{IP,0}$) (Sumner 1978). However, this term cannot be measured in the field due to electromagnetic induction at early times in the IP decay (e.g., Fiandaca et al. 2012; Maurya et al. 2018).

In field surveys, a common approach is to integrate over the entire decay curve for a given time-window (t$_1$ to t$_2$) and normalize by the DC voltage (e.g., Sumner 1978). This provides an integral chargeability term (M_{int}):

$$M_{int} = \frac{\int_{t_1}^{t_2} V_{IP}(t)\,dt}{t_1 - t_2}\frac{1}{V_{DC}} \, . \tag{3.7}$$

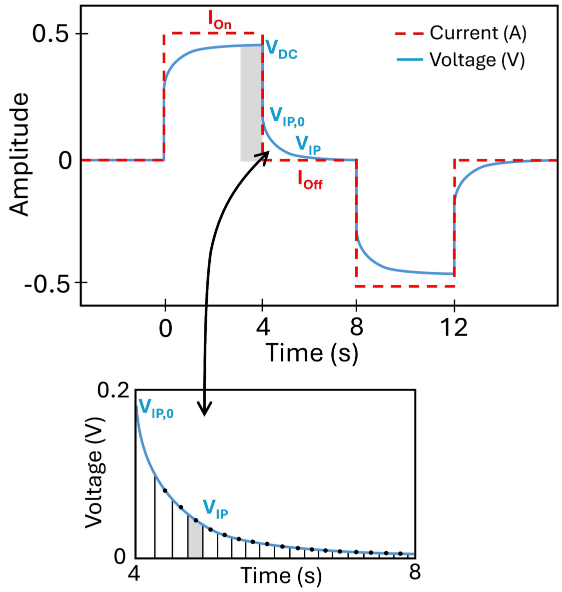

Figure 3.5: Schematic of the time-domain DCIP survey with current injection (dashed red line) for 4 seconds (I_{On}) and measured voltage response (blue line) after the current termination (I_{Off}). The voltage decay curve (V_{IP}) associated with the IP effect is shown in the bottom plot, measured at select time-gates (black dots).

The integral chargeability is a simple and convenient measure of the IP effect, and this measure is used to indicate the polarization response in Chapter 4 of this thesis because it is effective in smoothing out data noise (Lévy et al. 2024). However, it does not contain spectral information that is needed to inform petrophysical and hydrological properties (Madsen 2019). For time-domain IP data, these properties are recovered by considering the full IP decay. In the full-decay approach, the IP decay is divided into time-gates and an apparent chargeability term (m_a) is calculated for each gate i:

$$m_{a,i} = \frac{\int_{t_i}^{t_i+1} V_{IP}(t)\,dt}{t_i + 1 - t_i} \frac{1}{V_{DC}} \,. \tag{3.8}$$

The IP decay curve, defined in the time-domain by apparent chargeability measurements and contained in the complex resistivity of Equation 3.5, is often described by phenomenological models. One such model is the Cole-Cole model (Pelton et al. 1978):

$$\rho^* = \rho_0 \left[1 - m\left(1 - \frac{1}{1 + (i\omega\tau_\rho)^C}\right)\right] \,, \tag{3.9}$$

where ρ_0 is the DC resistivity (inverse of electrical conductivity, σ), m is the chargeability, τ_ρ is the relaxation time, and C is a dimensionless frequency exponent. In Chapter 6 of this thesis, a re-parameterization of the Cole-Cole model is used to describe the IP response (Fiandaca et al. 2018).

A petrophysical relationship exists between the chargeability (m) and the volume fraction of metallic particles with respect to the total porous media ($\theta_{metallic}$) (Wong 1979; Revil et al. 2015):

$$m = \frac{9}{2} \times \theta_{metallic} \, . \tag{3.10}$$

Utilizing this relationship, changes in the chargeability response can indicate changes in the sulfide abundance following H_2S injection:

$$\Delta m = \frac{9}{2} \times \Delta\theta_{metallic} \, . \tag{3.11}$$

3.2.3 DCIP Data Acquisition and Processing

There are multiple approaches to collecting galvanic electrical geophysics data in the field. In this study, I utilize four methods of data acquisition (based on synthetic and/or observed data) at the Nesjavellir geothermal site (Figure 3.4); (i) wireline DCIP logging down the injection borehole, (ii) surface DCIP profiling with a multiple gradient array, (iii) cross-borehole DCIP where electrodes are placed down the injection and nearby monitoring boreholes, and (iv) vertical electrical sounding (VES) along the surface. Each DCIP survey includes a dataset collected prior to H_2S injection and a second dataset collected after a period of continuous H_2S injection. The VES data were collected in 1985 before geothermal development at Nesjavellir, and the soundings provide only the DC resistivity parameter (no IP).

Wireline Logging:
Wireline logging data used in this study (Paper I) were collected in two of the injection boreholes, NN-3 and NN-4 (Figure 3.6), in September 2020 (prior to H_2S injection) and March 2021 (1.5 months following continuous H_2S injection). The wells were logged with the 16/64 QL40-ELOG/IP probing tool (www.alt.lu/downhole-probes/) using a 50% duty cycle, 2 s injection pulse, and 2 s release for a total cycle of 8 s and a sampling frequency of 450 Hz, which was the maximum possible with this tool. The logging instrument utilizes the "normal" configuration with a current (A) and potential electrode (N) spaced 64 inches apart, and the second potential electrode (M) located at the surface (Helander 1983). Wireline IP logging provides electrical data with a high vertical resolution within a few meters of the borehole (Roy et al. 1971).

The data were processed following the procedure outlined in Lévy et al. (2024). First, background time-invariant self-potential voltages and 50 Hz harmonic noise from a nearby buried powerline were removed from the data. The data were re-gated into 37 log-spaced windows to describe the full waveform decay signal. The first time gate was removed due to noise from electromagnetic coupling. Next, the data were normalized by the DC voltage (Equation 3.8) and the decays were stacked using an arithmetic mean of the positive and negative decays to improve the signal-to-noise ratio. The decays were averaged over 2 m-thick intervals to further smooth noise and facilitate an easier comparison between the logging campaigns. Lastly, the decay curves were integrated to obtain the integral chargeability value at each depth (Equation 3.8).

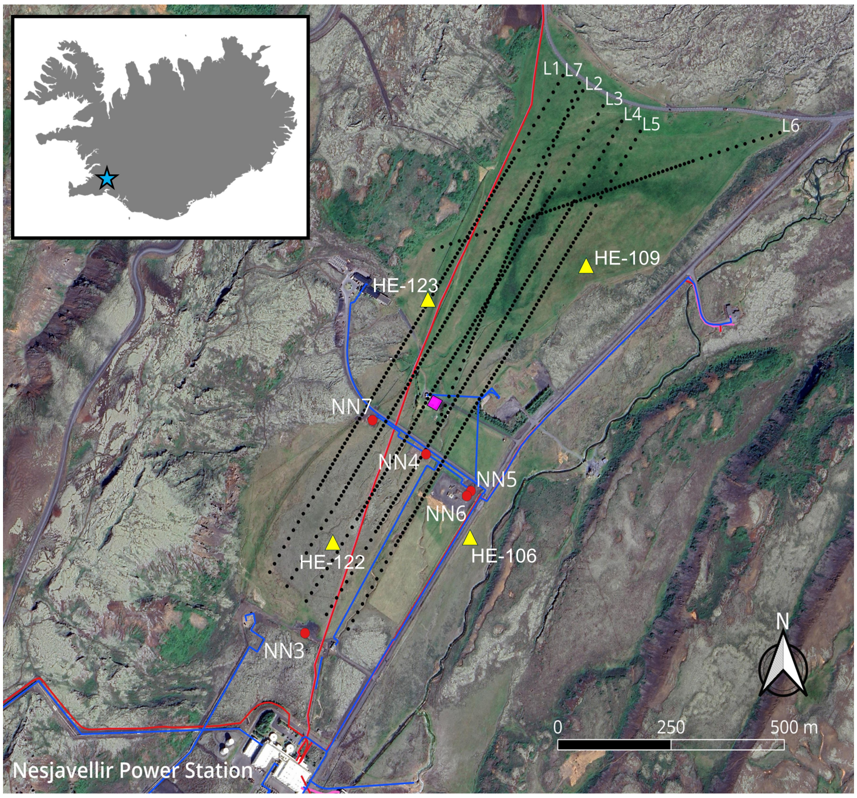

Figure 3.6: Map of the Nesjavellir geothermal field site. The H_2S injection wells are shown as red circles. The approximate electrode locations along the DCIP survey lines are displayed as black dots, and the locations of the vertical electrical soundings collected in 1985 are shown as yellow triangles. Red lines indicate buried power lines, the pink square is the location of a residential building, and the blue lines indicate hot water and steam pipes.

Surface DCIP:
Surface DCIP data is used in Paper III of this thesis (Chapter 6). The data were collected in the summers of 2019, 2020, and 2021. However, the 2019 survey served to inform the acquisition strategy for the following years, and this data is not utilized in this thesis. The time-domain, full waveform data were collected using the ABEM Terrameter LS2 with a 100% duty cycle, varying injection and decay measurement durations ranging from 4 s to 8.2 s, and a sampling frequency of 3.75 kHz. The data were collected along seven lines using a multiple gradient array configuration (Figure 3.6). Lines 1-5 were 1200 m long and were oriented parallel to the rift valley in the direction of groundwater flow. These 1200 m-long lines consisted of 101 electrodes, with 10 m spacing at the center of the line (200-1000 m) and 20 m spacing at the edges (0-200 m and 1000-1200 m). Lines 6-7 were 800 m long and transected Lines 1-5. These 800 m-long lines consisted of 81 electrodes with 10 m spacing in the center of the line (200-600 m) and 20 m spacing at the line edges (0-200 m and 600-800 m).

The data were processed by first removing the 50 Hz powerline noise following the algorithm presented in Olsson et al. (2016). I then manually processed the gated decays using EEMstudio software (Sullivan et al. 2023) to remove data outliers. I utilized EEMverter software (Fiandaca et al. 2023) to invert the processed data for subsurface electrical parameters, as detailed in Chapter 6. The 2D inversions implemented a time-lapse scheme in which the 2020 and 2021 datasets were inverted simultaneously, penalizing large time-lapse changes between the models to balance compact time-lapse model changes with data fit (Fiandaca et al. 2015). Topography was considered in the inversions utilizing a digital elevation model over the survey area. Additionally, I implemented a multi-mesh inversion approach that solves for the time-lapse model parameters on a shared mesh geometry that minimizes the distance between the field electrode positions. This process reduced inversion artifacts resulting from surface electrode misplacement between the 2020 and 2021 surveys. After the inversions, I further processed the decay curves to remove data with large misfits to the optimized model and re-ran the inversions.

Synthetic surface DCIP data were also generated along the survey lines using predictions from reactive transport simulations of H_2S injection for 0.5 and 25 years, respectively, to assess the sensitivity of the surface DCIP method to monitor H_2S mineral storage. The IP response associated with the predicted pyrite formation was calculated utilizing Equation 3.11 and added to the 2020 baseline DCIP data. Time-lapse inversions were then performed using the baseline and synthetic datasets to determine whether the pyrite mineralization could be detected.

Synthetic Cross-hole DCIP:
Cross-hole surveys involve placing electrodes in neighboring boreholes. This allows for electrical imaging between the boreholes, thereby providing high-resolution DCIP data at greater depths compared to surface DCIP surveying (e.g., Lévy et al. 2022). The boreholes each have 31 electrodes spaced at 10 m apart throughout the injection zone (150-450 m depth). The survey design utilizes two boreholes spaced 100 m apart. Quadrupoles are constructed by selecting A-B current electrode pairs and M-N potential electrode pairs between the two boreholes, and four different acquisition geometries are combined to maximize the survey resolution between the boreholes (Lévy et al. 2022).

In this thesis (Paper III), I use synthetic data to test the sensitivity of cross-hole DCIP surveying to H_2S mineralization at the Nesjavellir injection site and evaluate the potential of this method for future monitoring. I construct the expected geophysical anomaly using Equation 3.11, with the sulfide mineralization predicted by 2D-radial reactive transport simulations of H_2S injection for 5 and 25 years. The anomaly is added to baseline models defined by the 2020 baseline dataset. Additionally, random Gaussian noise with a standard deviation of 2% of the data values was added to the synthetic DCIP to better represent field conditions. This dataset is inverted using the previously discussed EEMverter time-lapse inversion scheme to assess the method's ability to monitor H_2S injection.

Vertical Electrical Sounding Method:
In addition to the DCIP field data, I utilize historical vertical electrical sounding (VES) data (Paper III) collected at the Nesjavellir site in 1985 (Figure 3.6) to characterize the subsurface electrical properties prior to geothermal production and wastewater disposal (Árnason et al. 1986). VES measures the DC voltage (V_{DC} in Figure 3.5) to provide the bulk conductivity component (σ' in Equation 3.3). This bulk conductivity is acquired in a similar approach to the surface DCIP method, in which voltage is measured across the M-N dipole electrodes following a current injection through the A-B electrodes.

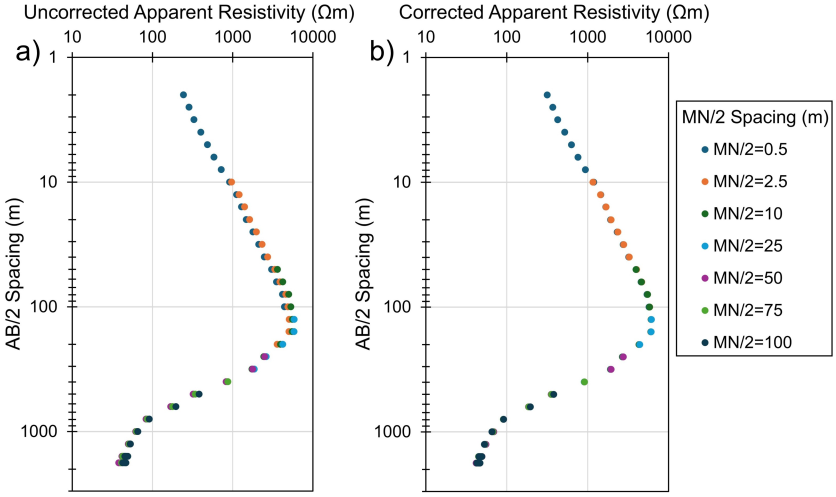

Figure 3.7: Vertical electrical sounding data collected at the Nesjavellir geothermal site in 1985 (Sounding HE-122 in Árnason et al. (1986)). The left plot (a) shows the uncorrected data, and the right plot (b) shows the corrected data, tied in together through multiplication factors.

Compared to the DCIP profiles, the VES provides a 1D sounding of subsurface resistivity (inverse of conductivity), utilizing a Schlumberger array configuration. To obtain the soundings at the Nesjavellir site, the current electrodes remained fixed around the central sounding location, and their spacing was gradually increased from 4 to 3560 m, with larger spacings measuring deeper into the subsurface. The M-N potential electrodes also remained centered at the sounding location, and their spacing was increased from 1 to 200 m (Árnason et al. 1986).

I processed the VES data to remove local, near-surface heterogeneities that impact measurements made at varying M-N potential electrode spacings (Figure 3.7). This involved correcting the resistivity curves with a multiplication factor to force the segments, measured at various M-N spacings, to tie into the measurements made at the largest M-N spacings, as these are less affected by local heterogeneities (Hersir et al. 2022). The processed data were inverted using the pyGIMLi software (Rücker et al. 2017) to obtain a 1D resistivity model of the Nesjavellir system in 1985.

3.2.4 DCIP Monitoring at a Geothermal Site

The DCIP method has been historically used for mineral exploration due to its sensitivity to ore deposits and other metallic particles (e.g., Bleil 1953; Dusabemariya et al. 2020). However, recent studies have explored the potential of the DCIP method to image hydrothermal and volcanic systems (e.g. Revil et al. 2021b). These systems have traditionally been imaged using electrical and electromagnetic resistivity methods that measure the conduction mechanisms of the subsurface (i.e., σ') associated with warm water and geothermal clay caps (e.g., Árnason et al. 2010; Hersir et al. 2022). However, these measurements of the bulk electrical conduction are controlled by both the pore fluid conductivity (σ_w) and the surface conductivity (σ'_{surf}). Therefore, the method cannot identify the individual contributions from pore fluids and mineral alteration (Equation 3.3). Conversely, polarization mechanisms are only dependent on the surface charge accumulation at the fluid-mineral interface (Equation 3.4), thereby providing information uniquely related to the mineralogy itself (e.g., texture, pore architecture, and alteration) (e.g., Singha et al. 2015; Revil et al. 2017b; Lévy et al. 2019b).

Ghorbani et al. (2018) showed that alteration strongly impacts IP parameters in core samples of volcanic rocks and utilized synthetic modeling to show how IP can be used for geohazard mapping in hydrothermal areas by indicating out-gassing and slope instabilities associated with alteration. Additional studies have utilized IP to characterize the pore size and permeability characteristics of basaltic reservoirs (Revil et al. 2017a; Zhang et al. 2023), map temperature distributions associated with the degree of alteration (Revil et al. 2021a; Zhang et al. 2023), and independently map lithological, mineralogical, and hydrogeological structures of geothermal systems (Lévy et al. 2019b; Piolat et al. 2023).

While the use of DCIP to identify alteration processes has been explored previously, the method has not been developed to monitor mineral storage approaches. However, Lévy et al. (2019a) and Lévy et al. (2019b) utilized the electrical conduction responses alongside the polarization responses in field data to establish the ability of the DCIP method to uniquely identify pyrite within alteration of Icelandic basalts. Building on these results, a recent study associated with this thesis research began to explore this methodology by testing the DCIP method's sensitivity and exploring processing techniques (Lévy et al. 2024). The results identified complexities in the methodology and, in particular, the need for future studies to address ambiguity in interpreting the IP response, given the combination of multiple processes contributing to the response.

3.3 Conceptual Model: Geochemistry-Geophysics of H_2S Mineralization

Insights from the thesis presented here, alongside reaction path modeling (Stefánsson et al. 2011; Clark et al. 2018; Galeczka et al. 2022) and laboratory experiments (Marieni et al. 2018; Přikryl et al. 2018), aid in the development of a conceptual model detailing the relevant processes of H_2S mineralization in the H_2S-water-basalt system at Nesjavellir. Basaltic rocks are targeted for mineral storage due to their reactivity and abundance of cations, particularly Ca^{2+} for CO_2 mineralization and Fe^{2+} for H_2S mineralization (e.g., Stefánsson et al. 2011; Matter et al. 2016). During low temperature basalt alteration, such as in the shallow injection system at Nesjavellir (< 100 °C), these cations are released to form secondary minerals, including amorphous silica, zeolites, smectite clays, iron oxides, carbonates, sulfides, and sulfates. The specific assemblage of secondary minerals is controlled by the basalt and fluid composition, thermodynamic conditions (e.g., temperature, redox state, pH, kinetic rates), and transport processes (e.g., advection, diffusion, dispersion, fluid mixing, fluid residence time), among other factors.

For the case of H_2S injection for mineral storage, the release of Fe^{2+} from the primary minerals (i.e., basaltic glass, iron-rich olivine, iron oxides, and pyroxene) promotes the formation of iron sulfides, including pyrite and potentially pyrrhotite. As related to the IP geophysical response, primary iron oxide minerals (magnetite/titanomagnetite) and iron sulfides have similar chargeability responses dependent on their volumetric abundance (e.g., Wong 1979; Gurin et al. 2015; Revil et al. 2015). Thus, the dissolution of the primary iron oxides can reduce the overall chargeability response while iron sulfide mineralization works to increase the chargeability (Equation 3.11).

The formation of pyrite upon H_2S injection is controlled by the pH conditions, redox state, and fluid-sourced SO_4^{2-}, Fe^{2+}, and HS^-, following the reaction:

$$4FeS_2 + 4H_2O = H^+ + SO_4^{2-} + 4Fe^{2+} + 7HS^- \, . \tag{3.12}$$

Pyrite is supersaturated in the injection fluids prior to injection, promoting rapid mineralization. To maintain pyrite formation, Fe^{2+} must be supplied from the alteration of the basaltic rock. The availability of Fe^{2+} is the largest limitation for H_2S mineral storage at the injection conditions, which can be limited by the rate of basalt dissolution, redox state of the aqueous Fe, and the uptake of Fe^{2+} from competing secondary minerals. Smectite clay formation is the most competitive secondary mineral for Fe^{2+} supply, forming alongside pyrite as the basalt rock begins to alter. However, as the basalt begins to alter, pyrite is the only Fe(II)-bearing alteration mineral, and smectites are limited to Fe(III)-bearing phases. The impact of smectite clay mineralization on the IP response is uncertain, and there is no agreed-upon model for polarization (e.g., Revil et al. 2017b; Ghorbani et al. 2018; Lévy et al. 2019a). However, smectites increase the electrical conduction along the surface of the rock matrix due to their cation exchange capacity (e.g., Waxman et al. 1968; Revil et al. 2017b; Weisenberger et al. 2020) and the additional electrical conduction pathways within the smectite minerals (intra-solid conduction) (Lévy et al. 2018). Higher conductivities can reduce the magnitude of the IP signal, thus impacting the ability to resolve small-magnitude IP responses (e.g., Lévy et al. 2019b). The higher salinity and temperature of the injected geothermal wastewater compared to fresh groundwater can also increase total conductivity, further weakening IP responses.

Under conditions of more intense host rock alteration, more basalt-sourced Fe^{2+} is supplied. The degree of alteration can be increased through faster basalt dissolution rates driven by temperature and pH conditions, or through increased fluid residence times in lower-permeability zones or within the rock matrix, which allow for more fluid-rock interactions. The increased alteration can promote pyrrhotite (FeS) and Fe(II)-smectite mineralization. Under reduced conditions, higher pH values, and with more abundant Fe^{2+}, pyrrhotite becomes the stoichiometrically-favored sulfide, following:

$$FeS + H^+ = Fe^{2+} + HS^- \ . \tag{3.13}$$

Similar to pyrite mineralization, pyrrhotite will increase the chargeabilitiy response as a function of its volumetric abundance (Lévy et al. 2019a). Laboratory results in Lévy et al. (2019a) have even shown that pyrrhotite may increase the IP response more sharply than pyrite. Increased Fe^{2+} supply from increased alteration also promotes Fe(II)-smectite formation, which can impede sulfide formation, reducing total H_2S mineralization and the IP chargeability response changes.

Ultimately, this conceptual model of the H_2S-water-basalt geochemical system provides insight into the underlying processes driving DCIP changes. These processes are complex and occur concurrently, adding ambiguity to the interpretation of the DCIP response, especially in field settings. The field-scale modeling pursued in this study seeks to quantify the individual contributions of these underlying geochemical processes to better understand the field DCIP response from H_2S mineralization.

3.4 Present Work

The first paper (Chapter 4) investigates H_2S mineral storage in the vicinity of the injection boreholes using both reactive transport modeling and wireline DCIP. Simple geochemical reactive transport models are constructed to provide insight into the geochemical and hydrological processes controlling H_2S mineralization. Additionally, the models are compared with geophysical wireline measurements taken in the borehole to establish links between geochemical processes and changes in the measured geophysical response. The near-borehole models serve as a first step into understanding H_2S mineral storage under field conditions from geochemical and geophysical perspectives.

The second paper (Chapter 5) expands upon the geochemical model presented in Chapter 4 through the development of a multiple-porosity reactive transport geochemical model of the entire injection reservoir at Nesjavellir. The improved geochemical model incorporates complex hydrological and geochemical processes to better characterize H_2S mineral storage under natural field conditions and provide insights into the risks associated with long-term H_2S injection at the Nesjavellir site. The model is further used to evaluate how effective borehole fluid sampling, a current monitoring approach, is in quantifying the degree of H_2S mineralization.

The third paper (Chapter 6) investigates the use of the direct current/induced polarization (DCIP) geophysical method to improve the spatial extent of H_2S mineral storage monitoring. The paper presents time-lapse DCIP data collected at the Nesjavellir injection site, and utilizes advanced time-lapse inversion software to resolve subsurface changes associated with H_2S injection. The results of the field-scale reactive transport model presented in Chapter 5 (Paper II) inform interpretations of the time-lapse DCIP results. Additionally, the reactive transport results are used to inform synthetic geophysical models that test the applicability of DCIP as a monitoring method across various field implementations. Lastly, the historical electrical resistivity values collected in 1985 are compared to resistivity values measured in 2020 to identify subsurface changes resulting from geothermal production at Nesjavellir and to validate the reactive transport models.

4 Wireline DCIP and 1D Reactive Transport - Paper 1

Ciraula, D. A., Kleine-Marshall, B. I., Galeczka, I. M., Lévy, L. (2024). Advanced monitoring of H_2S injection through the coupling of reactive transport models and geophysical responses. *Environmental Science and Technology.* 58(25), 11128-11139, https://pubs.acs.org/doi/10.1021/acs.est.3c10139

4.1 Summary

The first paper of this thesis sets the foundation for the joint application of DCIP geophysics and reactive transport modeling to explore field-scale H_2S mineralization. In this work, simple 1D reactive transport models are developed in PHREEQC (Parkhurst et al. 2013), representing the first geochemical models of H_2S mineralization developed for the Nesjavellir field site that account for flow processes. The study focuses on the near-borehole environment, characterizing changes in the wireline IP response measured in injection wells following H_2S injection. This study aims to couple wireline geophysical surveying with geochemical reactive transport models to better understand the processes and physicochemical parameters impacting H_2S mineralization at the Nesjavellir site. Additionally, this paper, and the related work presented in Lévy et al. (2024), are the first to apply geophysics to monitor mineral storage approaches in the field. I develop geochemical models to better understand the wireline DCIP time-lapse changes.

The reactive transport models provide insight into the fluid-rock interactions between the injection fluids of NN-3 and NN-4 and the basaltic glass at Nesjavellir. Fluid chemical parameters, including H_2S concentration, temperature, and pH, are varied to understand their impact on mineralization in the near-borehole environment. Physical parameters of flow rate, porosity, and permeability are defined using additional wireline logging methods (i.e., resistivity, neutron, and temperature pump-tests). These physical parameters are varied along the flow path to illustrate how they impact the distribution of H_2S mineralization (Figure 4.1).

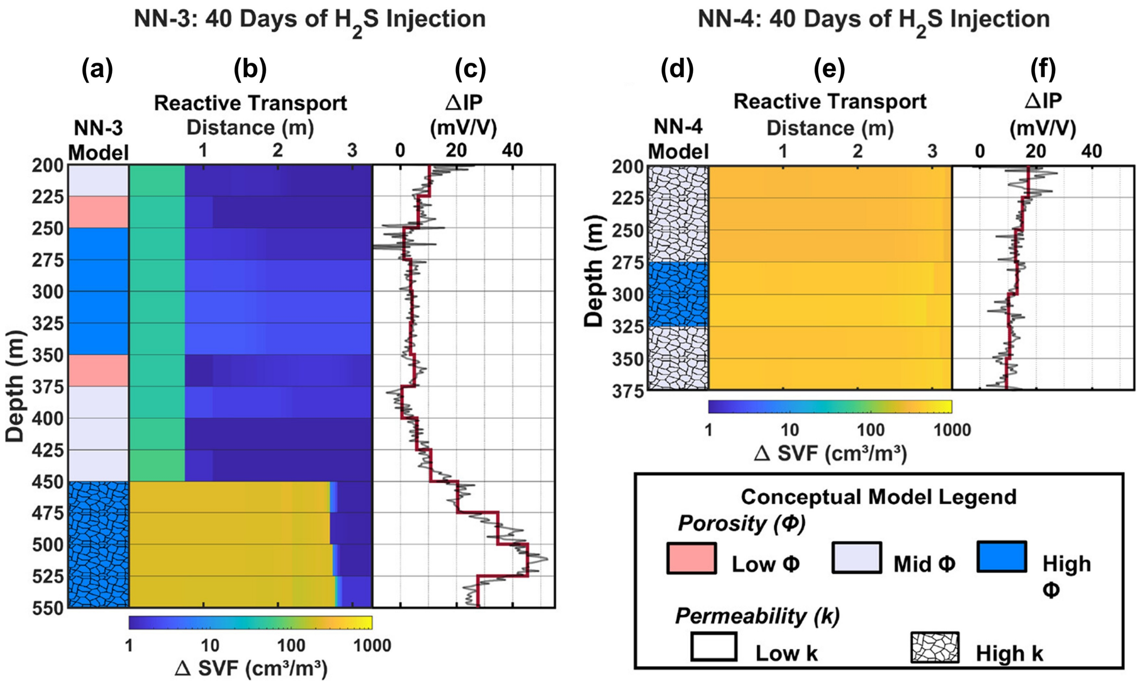

Figure 4.1: Results are shown for injection wells NN-3 (a-c) and NN-4 (d-f): (a) and (d) correspond to the relative porosity and permeability used in the reactive transport model; (b) and (e) show the predicted sulfide mineralization from reactive transport simulations of 40 days of the H_2S injection, displayed as sulfide volume fraction (SVF, ratio of volume sulfides to the total volume); (c) and (f) correspond to the measured change in integral chargeability (mV/V) after 40 days of H_2S injection.

The wireline logging recovers an increase in the integral chargeability IP response after 40 days of continuous H_2S injection (Figure 4.1). In NN-3, the integral chargeability increases are greatest at deeper depths along the model, with 0-10 mV/V increases at shallow depths and 50 mV/V near the bottom of the well. NN-4 recovers more uniform increases in integral chargeability, ranging from 10-17 mV/V over the entire well. Joint interpretation of these changes alongside the reactive transport models reveals a complex relationship between the IP response change and both the magnitude and distribution of H_2S mineralization.

Among both the NN-3 and NN-4 models, H_2S mineralization is rapid, with sulfide formation greatest near the borehole. However, the distribution of sulfide formation along the borehole is controlled largely by the permeability distribution along the borehole. This is particularly evident in NN-3, where high permeability values near the bottom of the borehole, identified by the temperature logs, result in larger amounts of H_2S-rich fluid supply and, thus, increased sulfide mineralization. Increased sulfide mineralization in the bottom third of the injection well, recovered

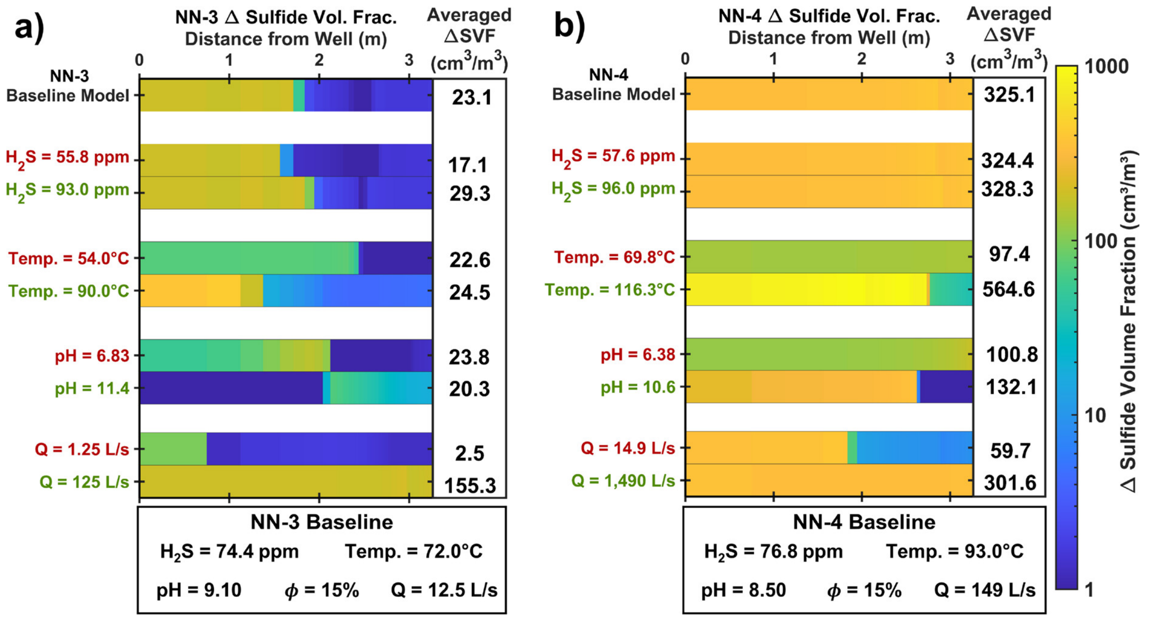

Figure 4.2: Row 1 of each figure illustrates changes in sulfide volume fraction (SVF) predicted in the reactive transport model of NN-3 and NN-4 with input data defined in the legend below the plots (measured dissolved H_2S, pH, and injection water temperature, average basaltic glass composition across the entire borehole, midestimate porosity, and the well injection rates with even allocation of the injection water to each model layer). The additional rows show the change in sulfide volume fraction predicted by reactive transport models with a single parameter varied, as displayed along the y-axis. The chemical parameters are varied by -25% (red) and +25% (green) of the measured values.

by the reactive transport models, aligns with the trends observed in the measured IP increase. NN-4 recovers a uniform distribution of IP changes, suggesting sulfide mineralization throughout the borehole. This is captured through a uniform distribution of high permeability along the borehole.

The magnitude of sulfide formation is impacted by multiple parameters, including the porosity, temperature, pH, and injection rate (Figure 4.2). Larger porosities increase the reactive surface area of the basaltic glass host rock, promoting fluid-rock interactions that supply Fe for H_2S mineralization. Larger porosities also increase the fluid-rock ratio, thereby increasing the H_2S available for sulfide precipitation. The temperature and pH impact H_2S mineralization through their impact on the dissolution rate of basaltic glass (Figure 4.2). Particularly for NN-4, increasing the temperature by 25% increases the averaged sulfide volume fraction by $\sim$ 75%, maximizing sulfide mineralization. The increased fluid-rock interactions at higher temperatures, coupled with the ample H_2S-rich fluid supply from large injection rates in NN-4, facilitate the large increase in sulfide formation. Conversely, increasing the fluid temperature in NN-3 by 25% only increases the averaged sulfide volume fraction by $\sim 6\%$ as the sulfide mineralization is ultimately limited by the H_2S supply from lower injection rates. This underscores the complex interplay of processes that control the magnitude of H_2S mineralization in the field.

Overall, this first study of the thesis establishes the potential for H_2S mineralization at the Nesjavellir site and helps to identify processes that impact the magnitude and distribution of H_2S mineralization in the field setting. Furthermore, the study lays the foundation for subsequent studies to apply joint IP geophysical and reactive transport geochemical investigations to monitor H_2S mineralization and optimize the implementation of mineral storage.

4.2 Main Results

- Increases in the induced polarization response following 40 days of H_2S injection suggest that H_2S mineralizes in the near-borehole basalt.

- The permeability controls the supply of H_2S-rich injection fluid, thereby controlling the vertical distribution of sulfide mineralization identified in the wireline logs.

- The magnitude of H_2S mineralization is controlled by the release of Fe from the host rock and thus by the factors that impact the Fe release, mainly porosity and temperature. Larger porosities increase reactive surface areas and promote H_2S mineralization. Higher temperatures increase the rate of basaltic glass dissolution, increasing H_2S mineralization.

- While elevated flow rates can increase the supply of H_2S-rich fluid and promote increased sulfide mineralization, large flow rates can also reduce the residence time for fluid-rock interactions, thereby reducing the Fe supply and sulfide mineralization.

- Improved coupling of the IP field measurements and the geochemical models requires more complex reactive transport models and stronger quantitative links between the IP response and predicted sulfide mineralization.

5 3D Reactive Transport Model of the Nesjavellir H_2S Injection System - Paper 2

Ciraula, D. A., Scott, S. W., Sonnenthal, E. L., Gómez-Díaz, E., Kleine-Marshall, B. I. (*In Prep*). Quantifying H_2S Mineral Storage Processes in Fractured Basalt Using a Field-Scale Reactive Transport Model. Manuscript in Prep. for Submission to Water Resources Research.

5.1 Summary

In the second paper of this thesis, I develop a 3D field-scale reactive transport model of the injection system at Nesjavellir (grid in Figure 2.2). This paper builds on the reactive transport models produced in the first paper by adding more complexities to model the real-world injection system. This includes increased dimensionality to three dimensions, integration of field-measured temperature and injection rates, secondary mineral precipitation and dissolution kinetics, complete primary mineral assemblage, interactions with the ambient groundwater system, hydrogeologic heterogeneities, non-isothermal fluid flow, and a multiple-porosity model framework. The main objectives of the study are to (i) predict H_2S mineralization over long-duration injections for further evaluation of DCIP monitoring sensitivity (Chapter 6), (ii) constrain the field-scale geological controls on H_2S mineralization, (iii) assess the risk associated with H_2S injection at the Nesjavellir site, and (iv) validate fluid mass balance monitoring methods commonly utilized to evaluate the effectiveness of mineral storage approaches.

The field-scale reactive transport model recovers effective H_2S mineralization, with 87% of the injected H_2S mineralization within the model domain bounded by Lake Thingvellir (Figure 5.1). Similar to the findings of the first paper, high permeabilities transfer H_2S outside the model domain, thereby lowering the percentage of H_2S mineralized within the specified modeled volume. The high permeabilities of the fracture network, ranging from 1.01×10^{-12} to 9.71×10^{-11} m^2, are identified through calibration to temperature data and align with values

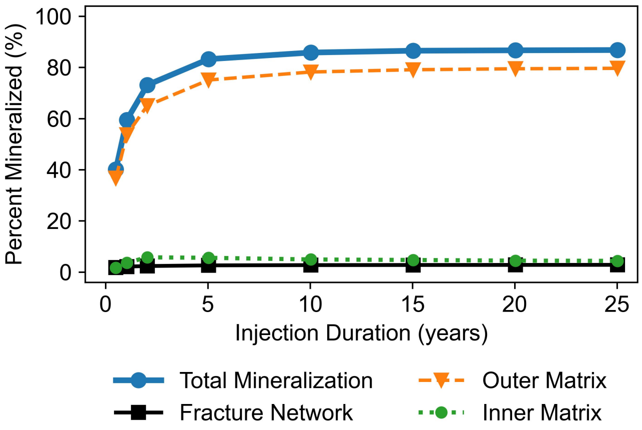

Figure 5.1: Percentage of the injected H_2S that mineralizes within the model domain and the proportion of H_2S mineralization occurring in each MINC domain (fracture, outer matrix, and inner matrix).

observed in fresh Icelandic basalts (Scott et al. 2023) and through previously calibrated flow models at Nesjavellir (Gómez-Díaz et al. 2022). Moreover, the permeability distribution controls the spatial distribution of aqueous H_2S and the resulting sulfide precipitation, which occurs within the rift valley. While the highly permeable fractured basalt transports H_2S efficiently, contamination of Lake Thingvellir is expected to be minimal (<0.013 µmol/L). However, high vertical permeabilities along faulted zones and density-driven flow result in the upwelling of the warm injection fluid, which has the potential to contaminate the surface waters.

Mineralization occurs as pyrite, and no elemental sulfur or sulfates form, suggesting that the redox conditions remain favorable for sulfide mineralization. Additionally, after 25 years of H_2S injection, aqueous sulfate concentrations remain low (<0.17 mmol/L) and the pH remains basic (>7.5), indicating that the injected H_2S does not oxidize to sulfuric acid and that groundwater acidification is unlikely under the current injection conditions. Most of the H_2S mineralization ($\sim 90\%$) occurs in the outer matrix of the reservoir rock (Figure 5.1), where transport is slow and controlled by diffusive processes. Compared to the fracture domain, the slow transport provides sufficient time for fluid-rock interactions to occur, supplying Fe for pyrite mineralization. Fe is supplied from basaltic glass in hyaloclastites and Fe-rich olivines in the lava flows and hyaloclastites; therefore, H_2S mineralization is greatest when basaltic glass and olivine are abundant. With sufficient Fe supply, pyrite mineralization is rapid and only 4-8% of the injected H_2S reaches the inner rock matrix and mineralizes to pyrite. These results suggest that diffusive processes are essential for H_2S mineral storage and must therefore be accounted for in modeling to accurately capture mineralization processes.

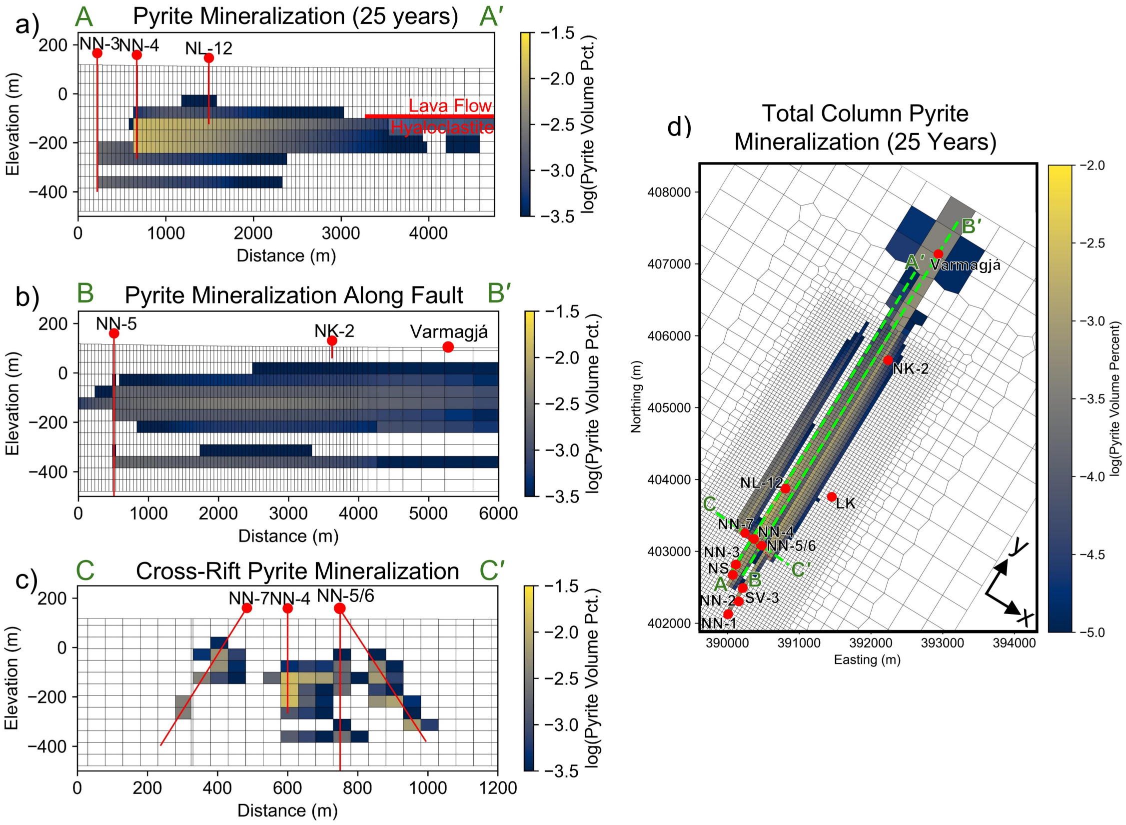

Figure 5.2: (a-c) Profiles of the volume of sulfide mineralized following 25 years of H_2S injection. The red dashed arrows highlight the trends of pyrite mineralization away from the injection wells, with a larger vertical distribution of pyrite in the fault zone. (d) Sum of the sulfide volume in each column of the reactive transport grid. Wastewater disposal sites, injection wells, and key monitoring boreholes are displayed as red dots. The dashed green indicates the locations of the profiles shown in the left subplots (A-A', B-B', and C-C').

Overall, the pyrite mineralization is distributed throughout the host rock reservoir (Figure 5.2) and comprises only a minor fraction of the total reservoir rock volume. In fact, total host rock alteration remains minimal on the yearly-decadal time-scales investigated in this study; after 25 years of injection, secondary minerals comprise just 0.034% of the volume in hyaloclastites near the injection boreholes. Although the extent of alteration is small, extrapolation to longer durations can provide context for the short engineering timescales investigated for mineral storage. For example, secondary minerals scale to about 7% of the hyaloclastite volume if alteration occurs over the duration since the most recent heating episode of the Nesjavellir system (~5,000 years), and 100% when extrapolating to the age of the oldest heating episode (~73,000 years). This illustrates the importance of considering the timescale of mineralogical changes when monitoring field systems.

Finally, I utilize the field-scale reactive transport model to provide insight into the capability of the fluid mass balance method, as presented in Matter et al. (2016), to accurately quantify mineralization. Using their calculations, I confirm the speculation of White et al. (2020) that the method only quantifies mineralization that occurs along the flow path between the injection and sampling wells. For example, in the reactive transport model, a monitoring well sampling 1000 m away from the NN-4 injection well and situated along a highly permeable flow path suggests 51% H_2S mineralization. In contrast, a monitoring well at the same distance but outside a primary flow path shows 83% mineralization. In comparison of these two cases, the more permeable flow path supplies abundant H_2S-rich water but limits fluid-rock interactions along the flow path (e.g., Chapter 4) leading to lower H_2S mineralization percentages.

5.2 Main Results

- 3D reactive transport models predict that H_2S mineral storage at the Nesjavellir site is effective and contamination of Lake Thingvellir is expected to be minimal, with 87% mineralizing to pyrite before reaching the lake's extent.
- The risk of contaminating Lake Thingvellir is greatest when injection occurs into fault zones that allow for the vertical migration of H_2S-rich water.
- Acidification of the shallow groundwater system at Nesjavellir is not expected under the current injection conditions as H_2S oxidation to sulfuric acid is not observed.
- Diffusive transport within the rock matrix is essential to H_2S mineralization, since the slow transport rate provides sufficient time for fluid–rock interactions to occur.
- Fe-rich olivine and basaltic glass make both lava flows and hyaloclastites suitable for H_2S mineral storage.
- Total host rock alteration is minimal over the 25-year injection duration studied here, and permeability is expected to decrease by only 4.5% over 100 years of injection. However, future studies should develop finer-scale models to explore the porosity and permeability evolution at finer spatial resolution.
- Fluid mass balance monitoring methods do not indicate mineralization over the entire reservoir as they are flow path dependent, only providing quantitative information regarding H_2S mineralization between the injection and monitoring wells.

6 Field DCIP Monitoring of H_2S Injection at Nesjavellir - Paper 3

Ciraula, D. A., Fiandaca, G., Chen, J., Scott, S. W., Lévy, L. (*In Review*). Constraining Time-lapse Geophysical Responses with Reactive Transport Modeling: An Approach to Monitor H_2S Mineral Storage. Manuscript submitted to Geophysical Journal International (June 30, 2025) and received back after review with moderate revisions (September 8, 2025).

6.1 Summary

The third and final paper of this thesis explores the use of surface and cross-hole DCIP geophysics to monitor H_2S mineralization at the Nesjavellir site. Building on the reactive transport model produced in Chapter 5 (Paper II), this study aims to (i) evaluate the ability of the DCIP method to monitor H_2S mineral storage at the field-scale, (ii) couple geochemical models with the geophysical data to reduce ambiguity in the interpretations of time-lapse DCIP changes, and (iii) explore how time-lapse electrical geophysical methods (i.e., DCIP and VES) can be used to validate reactive transport model parameters.

Surface DCIP data were collected in 2020 prior to H_2S injection and in 2021 following six months of H_2S injection. A time-lapse inversion scheme with a flexible gridding structure is introduced in order to handle complexities in the data arising from electrode misplacement between the 2020 and 2021 surface DCIP surveys. The gridding structure, called the mid-point model mesh, is shown to reduce time-lapse anomalies introduced by electrode misplacement. Ultimately, the time-lapse IP surveying does not recover any significant changes that could be attributed to H_2S mineralization (Figure 6.1). Instead, all IP changes are isolated to local infrastructure (i.e., a residential building, buried powerline, injection wells), illustrating the strong impact noise has on the inversion outcomes. Additionally, a sensitivity analysis shows that the inversion models have limited sensitivity with depth, and pyrite anomalies are not well resolved at the 200 m injection depth.

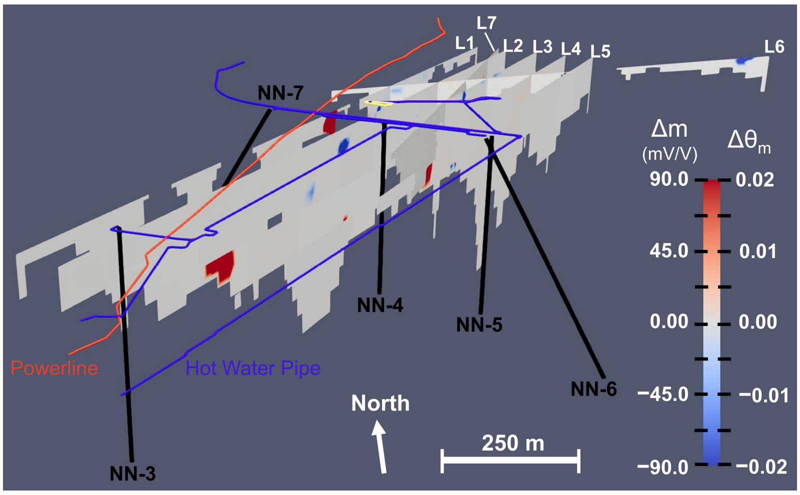

Figure 6.1: Results of the time-lapse IP inversion recovering changes in chargeability (m) and pyrite volume fraction (θ_m) following six months of H_2S injection. The casings of the NN injection wells (∼200 m depth) are displayed as black lines and indicate the minimum depth that H_2S-charged water enters the subsurface. Beneath the casing, the wells are open and extend another 200-350 m. The results are trimmed to the water table at ∼110 m depth and to the depth of investigation. Infrastructure in the survey area is displayed along the ground surface (yellow outline = house, blue line = hot water/steam pipes, red line = buried power line).

To constrain the underlying processes impacting the geophysical responses and aid in the interpretation of surface DCIP field data, I utilize the reactive transport model developed in the second paper (Chapter 5). As discussed in Chapter 5, the RTM was calibrated using data independent from the time-lapse geophysical surveys analyzed here, namely: permeability estimations from temperature logs, porosity from logging and core samples (Stefánsson 1991; Muñoz 1996), and reaction rates from model calibration to the fluid chemistry of samples of monitoring boreholes. The predicted mineralogical changes in the system provided by the RTM, combined with state-of-the-art petrophysical relations linking mineral volume and IP response, indicate that secondary pyrite mineralization is driving IP changes, while iron oxide and smectite minerals have minimal influence on IP changes. Nevertheless, the reactive transport model confirms the lack of change observed in the surface DCIP data, as pyrite mineralization occurs too deep (>200 m) and too spread out to be resolved with the surface DCIP method. Since chargeability is related to the pyrite volume fraction, dispersed pyrite mineralization results in small chargeability changes, predicted to be <0.02 mV/V.

Since these results indicate that surface DCIP monitoring would not work at the Nesjavellir site, I explore the expected response of cross-borehole DCIP monitoring using synthetic data derived from 2D radial reactive transport predictions. This allows investigating whether cross-borehole DCIP could be a reliable monitoring method in future experiments. The 2D radial model is developed to simulate injection into the NN-4 borehole using the same geochemical parameterization as the 3D model. However, the 2D model has cells refined to 5×5 m around the NN-4 injection borehole to enhance the simulation's resolution of the near-borehole processes that the cross-hole DCIP seeks to image. The refined radial geometry captures the flow and transport near the injection boreholes while ensuring computational efficiency. The 2D radial model improves upon the radial model presented in Chapter 4 in similar ways as the 3D model developed in Chapter 5 (i.e., more complex basalt mineralogy, kinetic dissolution and precipitation, field injection rates and temperature, mixing with groundwater, MINC grid with hydrogeological heterogeneities, diffusive transport, and non-isothermal fluid flow). While the 2D radial model represents a major improvement to capturing the field H_2S-basalt-water system compared to the 1D models in Chapter 4, ultimately both models reveal similar changes in the sulfide volume fractions ($\sim 1 \times 10^{-4}$).

The sulfide mineralization predicted by the 2D radial reactive transport models results in IP chargeability changes up to 1.9 mV/V after injection of highly concentrated H_2S-rich fluids for 25 years (Figure 6.2). Cross-hole DCIP surveying is shown to be sensitive to these changes, particularly between the two boreholes. Long-term injection of fluids with lower H_2S concentrations produces smaller chargeability changes of 0.6 mV/V, which are not as well recovered by the inversions and would be difficult to interpret given the expected noise level. H_2S mineralization from short-term injection (5 years) is poorly recovered for the highly concentrated injection fluid and is not recovered for the lower-concentration injection fluids.

The change of IP response after 40 days, measured by the wireline logging tool and expressed as integral chargeability, is in the range 10-20 mV/V (Chapter 4). While these values appear much larger than the IP chargeability response predicted for 25 years of injection in the 2D radial model (chargeability change of 1.9 mV/V), the wireline integral chargeability (Equation 3.8) cannot be directly compared to the RCC chargeability (Equation 3.9) calculated by applying a Cole-Cole model to the predictions of the RTM. The integral chargeability used in Chapter 4 cannot be interpreted quantitatively because (i) there is no petrophysical relationship between pyrite volume fraction and integral chargeability, and (ii) the integral chargeability calculated here does not account for the current waveform and is thus not an intrinsic parameter of the medium. The RCC chargeability accounts for the waveform through the inversion process, thereby providing an intrinsic parameter that can be quantitatively related to the volume fraction of metallic particles (Equation 3.10).

While the integral chargeability presented in Chapter 4 does not quantify H_2S mineralization from the wireline response, Lévy et al. (2024) utilized Debye decomposition of the wireline IP response to quantify the H_2S mineralization. The pyrite volume fraction changes after long injection durations (> 270 days) are found

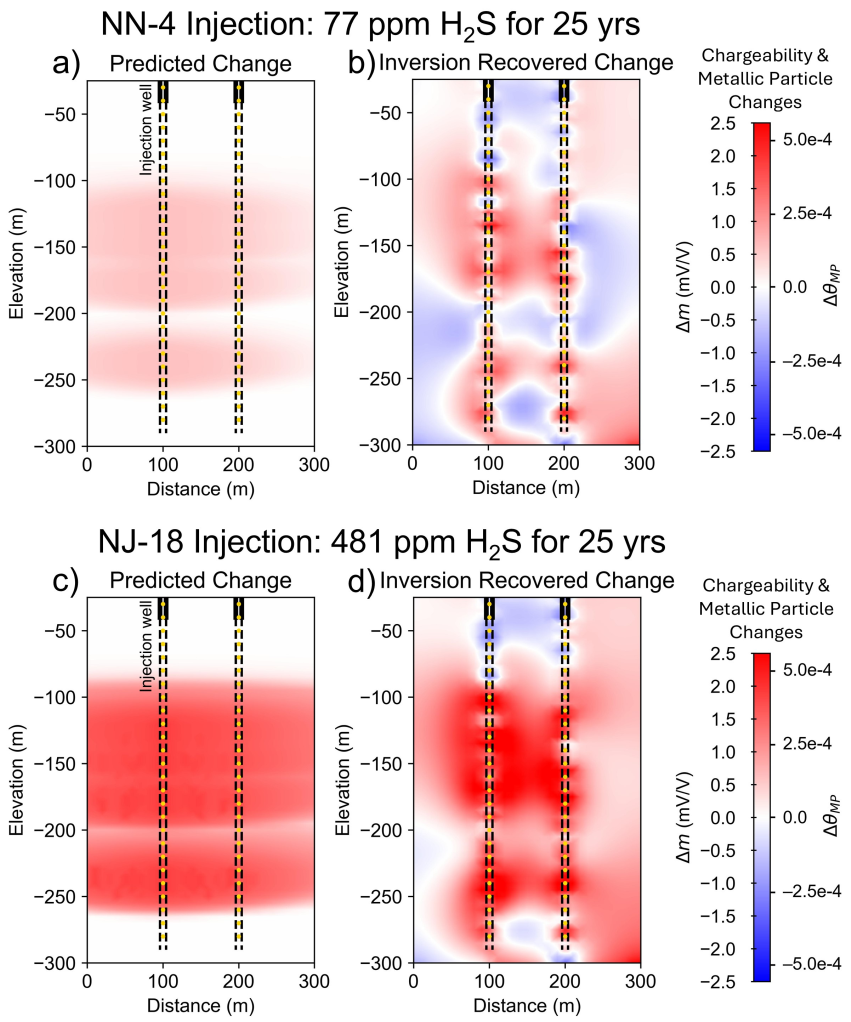

Figure 6.2: Results of the synthetic cross-hole modeling showing expected chargeability (m) change and the corresponding change in volume fraction of metallic particles (θ_{MP}) following 25 years of injection into NN-4 (top row) and NJ-18 (bottom row). The right plots show the time-lapse inversion results of the predicted synthetic data with 2% Gaussian noise added to the IP decays and the DC voltages. Solid black lines indicate borehole casing, dashed black lines indicate the open boreholes, and yellow dots indicate the electrode locations.

to remain near zero throughout most of the borehole, with few isolated intervals with pyrite volume fractions near 5×10^{-3}. However, these low values follow an initial increase in the wireline response after 40 days of injection, recovering volume fractions approaching 2×10^{-2}, suggesting possible re-dissolution of the pyrite after 40 days. The author's speculate a few areas of uncertainty in interpreting these findings of decreases response, including passivation of the pyrite minerals due to formation of other secondary minerals (e.g., Gurin et al. 2019), corrosion of the pyrite surfaces (e.g., Placencia-Gómez et al. 2013), connectivity of pyrite grains (e.g., Izumoto 2023), or the oxidation of sulfides due to microbial blooms (e.g., Zettlitzer et al. 2010; Lavalleur et al. 2013; Trias et al. 2017). Furthermore, the Debye decomposition analysis carried out by Lévy et al. (2024) serves as a first-order estimate for H_2S mineralization since it does not account for the current waveform, and the data were collected with a truncated injection pulse (2-second injection duration), adding additional uncertainty to the pyrite volume fraction estimates.

Expanding beyond the IP response, I used historical vertical electrical sounding (VES) data collected in 1985 (before the Nesjavellir powerplant began operations) and available in the archives to reveal how subsurface electrical properties have changed due to geothermal wastewater disposal at Nesjavellir. I compared resistivity inversion models obtained from the 1985 data to those from DCIP data from 2020 (before the start of H_2S injection but after 30 years of geothermal wastewater disposal into the reservoir from Nesjavallir powerplant operation). Clear decreases in electrical resistivity from 1925 Ωm to 325 Ωm are observed down-gradient from the injection wells. Analysis of the individual current-conduction pathways contributing to the total conductivity reveals that the increase in pore-fluid conductivity resulting from the disposal of warm, conductive geothermal wastewater is the primary cause of the decrease in resistivity between 1985 and 2020. Smectite mineralization predicted by the reactive transport simulation further contributes to the decrease in resistivity, lowering the resistivity to 330-385 Ωm, values similar to the 2020 measured resistivity (325 Ωm).

I further used reactive transport models and petrophysical relationships, linking resistivity, permeability, and smectite abundance (Lévy et al. 2020), to inform the permeability estimates used in the reactive transport models. I find that a high permeability value of 7.9×10^{-12} m^2 is required to achieve the resistivity decrease given the degree of smectite precipitation (0.06% by volume) and temperature changes (5 °C increase). This high permeability is similar to the values of 1.01×10^{-12} to 9.71×10^{-11} m^2 recovered through the inversion of the flow model to borehole temperature data in Chapter 5. However, this permeability estimate represents an upper bound because it does not account for changes in resistivity arising from differences in salinity between the geothermal wastewater and the shallow groundwater. While this assumption could be debated, it is consistent with the idea put forward by Revil et al. (1998) and Lévy et al. (2018) that, at low fluid conductivities, the primary conduction path shifts from the pore space to the mineral-water interface. This is particularly relevant given that the fluid conductivity in 2020 was only 0.07 S·m^{-1}, which lies at the lower end of fluid conductivity ranges usually investigated in the laboratory.

6.2 Main Results

- The flexible gridding approach, where the DCIP time-lapse inversion is solved on a shared model mesh, reduces inversion artifacts resulting from electrode misplacement.

- Time-lapse surface DCIP field surveys and field-scale reactive transport models both indicate that the surface DCIP method has limited ability to resolve H_2S mineralization at the Nesjavellir site due to the injection depths (>200 m), small magnitude response changes expected due to dispersed pyrite mineralization, and the external noise sources.

- Cross-hole DCIP surveying is sensitive to H_2S mineralization at the field-scale, yet the monitoring method requires low noise, highly concentrated H_2S-rich injection waters, and sufficiently long injection durations.

- Reactive transport models are used with petrophysical relationships to constrain the underlying processes impacting the IP response, suggesting that sulfide mineralization has the largest impact on IP response changes.

- Resistivity decreases from 1925 Ωm to 325 Ωm are observed between 1985 and 2020, owing primarily to the disposal of warm, conductive wastewater in the shallow groundwater system. Smectite precipitation further decreases the resistivity response.

- An independent petrophysical relationship between smectite abundance, resistivity, and permeability supports the high permeabilities recovered by model calibrations in previous studies.

7 Concluding Remarks

7.1 General Conclusions

The main objective of this thesis was to explore how geochemical reactive transport modeling could be integrated with geophysical DCIP field monitoring to better understand and capture subsurface fluid-rock interactions, with the specific application of assessing H_2S mineral storage at the Nesjavellir geothermal site.

The DCIP method on its own is sensitive to fluid-rock interactions, but the underlying processes controlling the measured response changes cannot be distinguished. The first outcome of this research addresses this gap by using reactive transport models to constrain the fluid-rock interactions that impact H_2S mineralization and the corresponding geophysical signature (Aims 1 and 3). Parameter sensitivity analysis revealed that the degree of H_2S mineralization is controlled by the rate of basalt dissolution relative to permeability. Parameters that facilitated more rapid basalt dissolution, such as pH, temperature, and porosity, increased the iron supply and led to increased H_2S mineralization. The relationship between permeability and H_2S mineralization is found to be complex, with low permeabilities limiting the supply of H_2S and high permeabilities limiting the residence time for fluid-rock interactions to occur; both resulting in less total H_2S mineralization. Conversely, increased residence times and fluid-rock interactions in the rock matrix, where diffusive processes control transport, result in the most pyrite formation.

The second outcome of this research enhances the interpretations of DCIP changes using reactive transport models (Aims 1 and 3). The reactive transport models reveal that iron oxide dissolution and smectite mineralization, two factors potentially influencing the IP response, have minimal impact on the IP response relative to pyrite mineralization. The small IP changes predicted by the reactive transport modeling also support the interpretation that large, isolated changes in the surface DCIP response are not related to pyrite mineralization but are likely due to noise.

At the start of this thesis, the use of DCIP geophysics to monitor H_2S mineral storage remained unexplored. The third outcome of this research illustrates how reactive transport models can be used, both before (Aim 2) and after (Aim 3) geophysical data collection, to evaluate the sensitivity of geophysical methods to subsurface processes and help guide the field surveying design and implementation. Increases in the measured DCIP response in wireline logs following 40 days of

H_2S injection indicate pyrite mineralization, which is further supported by reactive transport models along the borehole. Conversely, geophysical changes indicative of H_2S mineralization are not recovered by the surface DCIP surveying. Reactive transport models and DCIP sensitivity analysis indicate that the expected IP anomaly is too small to be detected by surface DCIP surveying, primarily because pyrite mineralization is too dispersed and too deep. Cross-hole data acquisition, tested with synthetic data generated by reactive transport models, is shown to be sensitive to H_2S mineralization at the injection depths when the injection duration is long, the fluid contains high H_2S concentrations, and data noise is low. These results from the synthetic geochemical-geophysical cross-hole modeling also contribute to the fourth outcome of this work: using reactive transport models to help identify how H_2S mineral storage can be better monitored (Aims 2 and 4).

The final outcome of this work establishes the long-term effectiveness of H_2S mineral storage at the Nesjavellir site (Aim 4). The field-scale reactive transport models indicate that H_2S mineralizes to pyrite upon interaction with the basalt host rock. Over long injection durations of 25 years, the majority of the injected H_2S mineralizes before reaching the extent of Lake Thingvellir, with minimal contamination of the lake predicted and no groundwater acidification expected. These results suggest that the mineral storage system implemented at the Nesjavellir geothermal site is an effective approach to reduce atmospheric emissions of H_2S.

7.2 Outlook - Geochemical-Geophysical Integration

Human activity contributes to the majority of H_2S emissions, originating from sources such as natural gas processing, paper production, petroleum refining, coal gasification, petrochemical manufacturing, and geothermal energy production (Habeeb et al. 2018). Many of these same processes also contribute significantly to atmospheric CO_2 emissions (Anwar et al. 2019). Although reducing energy usage and overall consumption could substantially lower anthropogenic emissions, completely eliminating emissions is currently unrealistic. Consequently, approaches such as mineral storage may become critical strategies to reduce atmospheric emissions while emission reductions continue to be pursued (Kelemen et al. 2019).

This research focused on mineral storage related to a part of a single geothermal field in Iceland, but the estimated field sequestration capacity of Iceland comprises only 23% and 1% and of the global field sequestration capacity for H_2S and CO_2, respectively (Marieni et al. 2018). In fact, laboratory experiments have demonstrated successful H_2S mineralization in basalt samples collected from field sites worldwide (e.g., Schaef et al. 2013; Schaef et al. 2014). However, H_2S injection in the field is yet to be implemented outside of Iceland (Gunnarsson et al. 2018; Galeczka et al. 2022; Kjeld et al. 2022). Implementing effective industrial-scale mineral storage and monitoring injection processes at field sites outside Iceland will face challenges arising from differences in reservoir host rock types, local heterogeneities, and site-specific biogeochemical processes. These complexities highlight the need to develop new, robust methods to ensure effective mineral storage.

This thesis shows that the application of reactive transport modeling and DCIP geophysical surveying is a complementary approach to better constrain and monitor fluid-rock interactions for H_2S mineral storage. However, future research is needed to advance the joint implementation – both in applying DCIP specifically for monitoring mineral storage and more broadly in the general integration of geophysics with process-based models, such as reactive transport modeling, at the field-scale.

Specific to monitoring H_2S mineralization with DCIP, continued efforts are required to refine the understanding of the electrochemical processes that govern the IP response. Although the DCIP method is sensitive to mineralogical changes associated with H_2S injection, uncertainty remains regarding other factors such as pyrite grain geometry (e.g., Gurin et al. 2013; Hupfer et al. 2016; Izumoto 2023; Martin et al. 2023), pore structure (e.g., Revil et al. 2017a; Weller et al. 2022), and smectite clay precipitation (e.g., Revil et al. 2017b; Lévy et al. 2019a; Ghorbani et al. 2018). While laboratory studies in controlled settings can help constrain these parameters, bridging the gap between these laboratory IP experiments and field IP surveys remains an important challenge (Martin et al. 2021; Orozco et al. 2022). Similar uncertainties also exist for monitoring CO_2 mineral storage with DCIP, where recent laboratory studies have cast doubt on the polarization response of carbonates (Izumoto et al. 2020; Rembert 2021) that were initially interpreted (Wu et al. 2010; Wu et al. 2011; Saneiyan et al. 2018).

DCIP survey configurations with buried or down-hole electrodes (i.e., wireline logging, cross-hole surveying) show potential in this study as a unique geophysical method to monitor H_2S mineralization directly. Surface electrode configurations with more powerful current sources and larger dipole spacing, such as the FullWaver System from IRIS Instruments (www.iris-instruments.com/v-fullwaver.html), could be explored in future studies to expand the depth of DCIP monitoring (e.g., Piolat et al. 2025). While other geophysical methods (e.g., seismic, gravity, magnetics, electromagnetics) are less suited for or are unable to directly detect mineralogical changes, they remain valuable for characterizing injection reservoirs (e.g., Junker et al. 2025) and tracking fluid-rock interactions associated with mineral storage approaches.

Beyond the specific application of monitoring H_2S mineralization, integrating process-based models, such as reactive transport models, with geophysics presents broader challenges that future studies should consider. First, the integration relies heavily on the validity of petrophysical relationships. Reducing uncertainty in these relationships and demonstrating their applicability across a range of field conditions is critical to the continued integration of these approaches. Second, discrepancies in the scale and resolution of the process-based model and the geophysical inversion models pose a difficult challenge, as pore-scale processes may differ from those controlling continuum-scale behavior. Furthermore, as shown in this thesis, fine-scale geological changes predicted by continuum-scale process-based models produce small geophysical changes, detectable with select survey configurations. Finally, all process-based models contain simplifications of the real-world system, and excluding key processes, such as biological processes, from reactive transport models (e.g., Carrera et al. 2022), risks the misinterpretation of geophysical responses.

As these challenges are addressed, joint geochemical-geophysical approaches will provide a more comprehensive framework for constraining subsurface processes. Continued development of these interdisciplinary approaches could open the door for higher orders of integration, including joint geophysical-geochemical inversions and fully coupled hydrogeophysical inversions of reactive transport models (e.g., Hinnell et al. 2010; Singha et al. 2015; Pleasants et al. 2022; Camporese et al. 2015). Such advances would ultimately enhance our ability to monitor and accurately model real-world subsurface systems.

References

Abdulsamad, F., N. Florsch, and C. Camerlynck (2017). “Spectral induced polarization in a sandy medium containing semiconductor materials: Experimental results and numerical modelling of the polarization mechanism”. In: *Near Surface Geophysics* 15 (6). ISSN: 15694445. DOI: `10.3997/1873-0604.2017052`.

Adeoye, J. T., A. H. Menefee, W. Xiong, R. K. Wells, P. Skemer, D. E. Giammar, and B. R. Ellis (2017). “Effect of transport limitations and fluid properties on reaction products in fractures of unaltered and serpentinized basalt exposed to high PCO_2 fluids”. In: *International Journal of Greenhouse Gas Control* 63. ISSN: 17505836. DOI: `10.1016/j.ijggc.2017.06.003`.

Anwar, M. N., M. Iftikhar, B. Khush Bakhat, N. F. Sohail, M. Baqar, A. Yasir, and A. S. Nizami (2019). “Sources of Carbon Dioxide and Environmental Issues”. In: *Sustainable Agriculture Reviews 37: Carbon Sequestration Vol. 1 Introduction and Biochemical Methods*. Ed. by Inamuddin, A. M. Asiri, and E. Lichtfouse. Springer International Publishing, pp. 13–36. DOI: `10.1007/978-3-030-29298-0_2`.

Arnason, B., P. Theodorsson, S. Björnsson, and K. Saemundsson (1969). “Hengill, a high temperature thermal area in Iceland”. In: *Bulletin Volcanologique* 33 (1). ISSN: 14320819. DOI: `10.1007/BF02596720`.

Árnason, K., H. Eysteinsson, and G. P. Hersir (2010). “Joint 1D inversion of TEM and MT data and 3D inversion of MT data in the Hengill area, SW Iceland”. In: *Geothermics* 39 (1). ISSN: 03756505. DOI: `10.1016/j.geothermics.2010.01.002`.

Árnason, K., G. I. Haraldsson, G. V. Johnsen, G. Thorbergsson, G. P. Hersir, K. Saemundsson, L. S. Georgsson, S. T. Rögnvaldsson, and S. P. Snorrason (1986). *Report OS-87018 (In Icelandic): Nesjavellir - Ölkelduháls Yfirbordsrannsóknir 1986*. Tech. rep. Orkustofnun.

Arnórsson, S. (1983). “Chemical equilibria in icelandic geothermal systems-Implications for chemical geothermometry investigations”. In: *Geothermics* 12 (2-3). ISSN: 03756505. DOI: `10.1016/0375-6505(83)90022-6`.

Arnórsson, S. (1986). “Chemistry of gases associated with geothermal activity and volcanism in Iceland: A review”. In: *Journal of Geophysical Research: Solid Earth* 91 (B12). ISSN: 0148-0227. DOI: `10.1029/jb091ib12p12261`.

Arnórsson, S. (1995). “Geothermal systems in Iceland: Structure and conceptual models-I. High-temperature areas”. In: *Geothermics* 24 (5-6). ISSN: 03756505. DOI: `10.1016/0375-6505(95)00025-9`.

Arnórsson, S., G. Axelsson, and K. Sæmundsson (2008). “Geothermal systems in Iceland”. In: *Jökull* 58.

Arnórsson, S., J. Ö. Bjarnason, N. Giroud, I. Gunnarsson, and A. Stefánsson (2006). “Sampling and analysis of geothermal fluids”. In: *Geofluids* 6 (3). ISSN: 14688115. DOI: `10.1111/j.1468-8123.2006.00147.x`.

Arnórsson, S., K. Grönvold, and S. Sigurdsson (1978). “Aquifer chemistry of four high-temperature geothermal systems in Iceland”. In: *Geochimica et Cosmochimica Acta* 42 (5). ISSN: 00167037. DOI: `10.1016/0016-7037(78)90202-8`.

Arnórsson, S., A. Stefánsson, and J. Ö. Bjarnason (2007). “Fluid-fluid interactions in geothermal systems”. In: *Reviews in Mineralogy and Geochemistry* 65. ISSN: 15296466. DOI: `10.2138/rmg.2007.65.9`.

Arps, J. (1953). “The Effect of Temperature on the Density and Electrical Resistivity of Sodium Chloride Solutions”. In: *Journal of Petroleum Technology* 5 (10). ISSN: 0149-2136. DOI: `10.2118/953327-g`.

Berre, I., F. Doster, and E. Keilegavlen (2019). “Flow in Fractured Porous Media: A Review of Conceptual Models and Discretization Approaches”. In: *Transport in Porous Media* 130 (1). ISSN: 15731634. DOI: `10.1007/s11242-018-1171-6`.

Beuttler, C., L. Charles, and J. Wurzbacher (2019). “The Role of Direct Air Capture in Mitigation of Anthropogenic Greenhouse Gas Emissions”. In: *Frontiers in Climate* 1. ISSN: 26249553. DOI: `10.3389/fclim.2019.00010`.

Binley, A., S. S. Hubbard, J. A. Huisman, A. Revil, D. A. Robinson, K. Singha, and L. D. Slater (2015). “The emergence of hydrogeophysics for improved understanding of subsurface processes over multiple scales”. In: *Water Resources Research* 51 (6). ISSN: 19447973. DOI: `10.1002/2015WR017016`.

Bleil, D. F. (1953). “Induced polarization: A method of geophysical prospecting”. In: *Geophysics* 18 (3). ISSN: 19422156. DOI: `10.1190/1.1437917`.

Bödvarsson, G. (1982). “Terrestrial energy currents and transfer in Iceland”. In: *Continental and Oceanic Rifts: Geodynamics Series 8*. Ed. by G. Pálmason. American Geophysical Union. DOI: `10.1029/gd008p0271`.

Browne, P. R. (1978). “Hydrothermal Alteration in Active Geothermal Fields”. In: *Annual Review of Earth and Planetary Sciences* 6. ISSN: 00846597. DOI: `10.1146/annurev.ea.06.050178.001305`.

Callow, B., I. Falcon-Suarez, S. Ahmed, and J. Matter (2018). “Assessing the carbon sequestration potential of basalt using X-ray micro-CT and rock mechanics”. In: *International Journal of Greenhouse Gas Control* 70. ISSN: 17505836. DOI: `10.1016/j.ijggc.2017.12.008`.

Cameron, D. A., L. J. Durlofsky, and S. M. Benson (2016). “Use of above-zone pressure data to locate and quantify leaks during carbon storage operations”. In: *International Journal of Greenhouse Gas Control* 52. ISSN: 17505836. DOI: `10.1016/j.ijggc.2016.06.014`.

Camporese, M., G. Cassiani, R. Deiana, P. Salandin, and A. Binley (2015). “Coupled and uncoupled hydrogeophysical inversions using ensemble Kalman filter assimilation of ERT-monitored tracer test data”. In: *Water Resources Research* 51 (5). ISSN: 19447973. DOI: `10.1002/2014WR016017`.

Carrera, J., M. W. Saaltink, J. Soler-Sagarra, W. Jingjing, and C. Valhondo (2022). "Reactive Transport: A Review of Basic Concepts with Emphasis on Biochemical Processes". In: *Energies* 15 (3). ISSN: 19961073. DOI: `10.3390/en15030925`.

Chelidze, T. L. and Y. Gueguen (1999). "Electrical spectroscopy of porous rocks: A review-I. Theoretical models". In: *Geophysical Journal International* 137 (1). ISSN: 0956540X. DOI: `10.1046/j.1365-246X.1999.00799.x`.

Chen, J., S. Hubbard, and Y. Rubin (2001). "Estimating the hydraulic conductivity at the South Oyster Site from geophysical tomographic data using Bayesian techniques based on the normal linear regression model". In: *Water Resources Research* 37 (6). ISSN: 00431397. DOI: `10.1029/2000WR900392`.

Chen, J., S. Hubbard, Y. Rubin, C. Murray, E. Roden, and E. Majer (2004). "Geochemical characterization using geophysical data and Markov Chain Monte Carlo methods: A case study at the South Oyster bacterial transport site in Virginia". In: *Water Resources Research* 40 (12). ISSN: 00431397. DOI: `10.1029/2003WR002883`.

Chen, J., S. S. Hubbard, K. H. Williams, S. Pride, L. Li, C. Steefel, and L. Slater (2009). "A state-space Bayesian framework for estimating biogeochemical transformations using time-lapse geophysical data". In: *Water Resources Research* 45 (8). ISSN: 00431397. DOI: `10.1029/2008WR007698`.

Clark, D. E., I. Gunnarsson, E. S. Aradóttir, M. Þ. Arnarson, Þ. A. Þorgeirsson, S. S. Sigurðardóttir, B. Sigfússon, S. Snæbjörnsdóttir, E. H. Oelkers, and S. R. Gíslason (2018). "The chemistry and potential reactivity of the CO_2-H_2S charged injected waters at the basaltic CarbFix2 site, Iceland". In: *Energy Procedia*. Vol. 146. DOI: `10.1016/j.egypro.2018.07.016`.

Clark, D. E., E. H. Oelkers, I. Gunnarsson, B. Sigfússon, S. Snæbjörnsdóttir, E. S. Aradóttir, and S. R. Gíslason (2020). "CarbFix2: CO_2 and H_2S mineralization during 3.5 years of continuous injection into basaltic rocks at more than 250 °C". In: *Geochimica et Cosmochimica Acta* 279. ISSN: 00167037. DOI: `10.1016/j.gca.2020.03.039`.

Copty, N., Y. Rubin, and G. Mavko (1993). "Geophysical-hydrological identification of field permeabilities through Bayesian updating". In: *Water Resources Research* 29 (8). ISSN: 19447973. DOI: `10.1029/93WR00745`.

Crovisier, J. L., J. Honnorez, B. Fritz, and J. C. Petit (1992). "Dissolution of subglacial volcanic glasses from Iceland: laboratory study and modelling". In: *Applied Geochemistry* 7. ISSN: 08832927. DOI: `10.1016/S0883-2927(09)80064-4`.

Cuoco, E., D. Tedesco, R. J. Poreda, J. C. Williams, S. D. Francesco, C. Balagizi, and T. H. Darrah (2013). "Impact of volcanic plume emissions on rain water chemistry during the January 2010 Nyamuragira eruptive event: Implications for essential potable water resources". In: *Journal of Hazardous Materials* 244-245. ISSN: 03043894. DOI: `10.1016/j.jhazmat.2012.10.055`.

Danzon, M. A., F. X. V. Leeuwen, and M. Krzyzanowski (2001). *Air quality guidelines: For Europe.* DOI: `10.1016/0269-7491(88)90163-7`.

Daval, D. (2018). “Carbon dioxide sequestration through silicate degradation and carbon mineralisation: promises and uncertainties”. In: *npj Materials Degradation* 2 (1). ISSN: 23972106. DOI: `10.1038/s41529-018-0035-4`.

Doherty, J. and R. Hunt (2010). “Approaches to highly parameterized inversion: a guide to using PEST for groundwater-model calibration”. In: *U. S. Geological Survey Scientific Investigations Report 2010-5169*.

Dusabemariya, C., W. Qian, R. Bagaragaza, A. R. Faruwa, and M. Ali (2020). “Some Experiences of Resistivity and Induced Polarization Methods on the Exploration of Sulfide: A Review”. In: *Journal of Geoscience and Environment Protection* 08 (11). ISSN: 2327-4336. DOI: `10.4236/gep.2020.811004`.

Einarsson, P. (2008). “Plate boundaries, rifts and transforms in Iceland”. In: *Jökull* 58 (1). DOI: `10.33799/jokull2008.58.035`.

Emami-Meybodi, H., H. Hassanzadeh, C. P. Green, and J. Ennis-King (2015). “Convective dissolution of CO_2 in saline aquifers: Progress in modeling and experiments”. In: *International Journal of Greenhouse Gas Control* 40. ISSN: 17505836. DOI: `10.1016/j.ijggc.2015.04.003`.

Emberley, S., I. Hutcheon, M. Shevalier, K. Durocher, B. Mayer, W. D. Gunter, and E. H. Perkins (2005). “Monitoring of fluid-rock interaction and CO_2 storage through produced fluid sampling at the Weyburn CO_2-injection enhanced oil recovery site, Saskatchewan, Canada”. In: *Applied Geochemistry* 20 (6). ISSN: 08832927. DOI: `10.1016/j.apgeochem.2005.02.007`.

Ezzedine, S., Y. Rubin, and J. Chen (1999). “Bayesian method for hydrogeological site characterization using borehole and geophysical survey data: Theory and application to the Lawrence Livermore National Laboratory Superfund site”. In: *Water Resources Research* 35 (9). ISSN: 00431397. DOI: `10.1029/1999WR900131`.

Fiandaca, G., E. Auken, A. V. Christiansen, and A. Gazoty (2012). “Time-domain-induced polarization: Full-decay forward modeling and 1D laterally constrained inversion of Cole-Cole parameters”. In: *Geophysics* 77 (3). ISSN: 00168033. DOI: `10.1190/geo2011-0217.1`.

Fiandaca, G., J. Doetsch, G. Vignoli, and E. Auken (2015). “Generalized focusing of time-lapse changes with applications to direct current and time-domain induced polarization inversions”. In: *Geophysical Journal International* 203 (2). ISSN: 1365246X. DOI: `10.1093/gji/ggv350`.

Fiandaca, G., L. M. Madsen, and P. K. Maurya (2018). “Re-parameterisations of the Cole-Cole model for improved spectral inversion of induced polarization data”. In: *Near Surface Geophysics* 16 (4). ISSN: 15694445. DOI: `10.3997/1873-0604.2017065`.

Fiandaca, G., B. Zhang, J. Chen, A. Signora, F. Dauti, S. Galli, N. A. L. Sullivan, A. Bollino, and A. Viezzoli (2023). “Closing the gap between galvanic and inductive methods: EEMverter, a new 1D/2D/3D inversion tool for electric and electromagnetic data with focus on induced polarisation”. In: *AEM 2023: Short abstracts, Preview, 2023:225*, pp. 52–66. DOI: `10.1080/14432471.2023.2236352`.

Finster, M., C. Clark, J. Schroeder, and L. Martino (2015). “Geothermal produced fluids: Characteristics, treatment technologies, and management options”. In:

Renewable and Sustainable Energy Reviews 50. ISSN: 18790690. DOI: `10.1016/j.rser.2015.05.059`.

Floor, G. H., S. Calabrese, G. Román-Ross, W. D'Alessandro, and A. Aiuppa (2011). "Selenium mobilization in soils due to volcanic derived acid rain: An example from Mt Etna volcano, Sicily". In: *Chemical Geology* 289 (3-4). ISSN: 00092541. DOI: `10.1016/j.chemgeo.2011.08.004`.

Foulger, G. R. (1988). "Hengill Triple Junction, SW Iceland: 1. Tectonic structure and the spatial and temporal distribution of local earthquakes". In: *Journal of Geophysical Research* 93 (B11). ISSN: 01480227. DOI: `10.1029/jb093ib11p13493`.

Foulger, G. R. and D. R. Toomey (1989). "Structure and evolution of the Hengill-Grensdalur volcanic complex, Iceland: geology, geophysics, and seismic tomography". In: *Journal of Geophysical Research* 94 (B12). ISSN: 01480227. DOI: `10.1029/jb094ib12p17511`.

Franzson, H. (1988). "Nesjavellir-Borholujardfrædi, vatnsgengd í jardhitageymi". In: *Orkustofnun, Report No. OS-88046/JHD-09*.

Franzson, H., R. Zierenberg, and P. Schiffman (2008). "Chemical transport in geothermal systems in Iceland. Evidence from hydrothermal alteration". In: *Journal of Volcanology and Geothermal Research* 173 (3-4). ISSN: 03770273. DOI: `10.1016/j.jvolgeores.2008.01.027`.

Fridleifsson, I. B. (1979). "Geothermal activity in Iceland". In: *Jökull*.

Galeczka, I. M., D. Wolff-Boenisch, E. H. Oelkers, and S. R. Gíslason (2014). "An experimental study of basaltic glass-H_2O-CO_2 interaction at 22 and 50°C: Implications for subsurface storage of CO_2". In: *Geochimica et Cosmochimica Acta* 126. ISSN: 00167037. DOI: `10.1016/j.gca.2013.10.044`.

Galeczka, I. M., A. Stefánsson, B. I. Kleine, J. Gunnarsson-Robin, S. Ó. Snæbjörnsdóttir, B. Sigfússon, S. H. Gunnarsdóttir, T. B. Weisenberger, and E. H. Oelkers (2022). "A pre-injection assessment of CO_2 and H_2S mineralization reactions at the Nesjavellir (Iceland) geothermal storage site". In: *International Journal of Greenhouse Gas Control* 115. ISSN: 17505836. DOI: `10.1016/j.ijggc.2022.103610`.

Ghorbani, A., A. Revil, A. Coperey, A. S. Ahmed, S. Roque, M. J. Heap, H. Grandis, and F. Viveiros (2018). "Complex conductivity of volcanic rocks and the geophysical mapping of alteration in volcanoes". In: *Journal of Volcanology and Geothermal Research* 357. ISSN: 03770273. DOI: `10.1016/j.jvolgeores.2018.04.014`.

Giammar, D. E., F. Wang, B. Guo, J. A. Surface, C. A. Peters, M. S. Conradi, and S. E. Hayes (2014). "Impacts of diffusive transport on carbonate mineral formation from magnesium silicate-CO_2-water reactions". In: *Environmental Science and Technology* 48 (24). ISSN: 15205851. DOI: `10.1021/es504047t`.

Gómez-Díaz, E. (2020). "Numerical Modelling of the Shallow Reinjection and Tracer Transport at Nesjavellir Geothermal System, Iceland. An Assessment of Heat Transfer and Fluid Flow". PhD thesis. Reykjavík University.

Gómez-Díaz, E., S. Scott, T. Ratouis, and J. Newson (2022). "Numerical modeling of reinjection and tracer transport in a shallow aquifer, Nesjavellir Geothermal

System, Iceland". In: *Geothermal Energy* 10 (7). ISSN: 2195-9706. DOI: `10.1186/s40517-022-00217-3`.

Govt. of Iceland (2010). *Iceland Ministry of the Environment, Energy and Climate, Regulation no. 514/2010.*

Gudbrandsson, S., D. Wolff-Boenisch, S. R. Gíslason, and E. H. Oelkers (2011). "An experimental study of crystalline basalt dissolution from 2<pH<11 and temperatures from 5 to 75°C". In: *Geochimica et Cosmochimica Acta* 75 (19). ISSN: 00167037. DOI: `10.1016/j.gca.2011.06.035`.

Gunnarsson, I., E. S. Aradóttir, E. H. Oelkers, D. E. Clark, M. Þ. Arnarson, B. Sigfússon, S. Snæbjörnsdóttir, J. M. Matter, M. Stute, B. M. Júlíusson, and S. R. Gíslason (2018). "The rapid and cost-effective capture and subsurface mineral storage of carbon and sulfur at the CarbFix2 site". In: *International Journal of Greenhouse Gas Control* 79. ISSN: 17505836. DOI: `10.1016/j.ijggc.2018.08.014`.

Gunnarsson, I., B. Sigfússon, A. Stefánsson, S. Arnórsson, S. W. Scott, and E. Gunnlaugsson (2011). "Injection of H2S from Hellisheidi Power Plant, Iceland". In: *Thirty-Sixth Workshop on Geothermal Reservoir Engineering.*

Gurin, G., A. Tarasov, Y. Ilyin, and K. Titov (2013). "Time domain spectral induced polarization of disseminated electronic conductors: Laboratory data analysis through the Debye decomposition approach". In: *Journal of Applied Geophysics* 98. ISSN: 09269851. DOI: `10.1016/j.jappgeo.2013.07.008`.

Gurin, G., K. Titov, and Y. Ilyin (2019). "Induced Polarization of Rocks Containing Metallic Particles: Evidence of Passivation Effect". In: *Geophysical Research Letters* 46 (2). ISSN: 19448007. DOI: `10.1029/2018GL080107`.

Gurin, G., K. Titov, Y. Ilyin, and A. Tarasov (2015). "Induced polarization of disseminated electronically conductive minerals: A semi-empirical model". In: *Geophysical Journal International* 200 (3). ISSN: 1365246X. DOI: `10.1093/gji/ggu490`.

Gysi, A. P. and A. Stefánsson (2008). "Numerical modelling of CO_2-water-basalt interaction". In: *Mineralogical Magazine* 72 (1). ISSN: 0026-461X. DOI: `10.1180/minmag.2008.072.1.55`.

Gysi, A. P. and A. Stefánsson (2011). "CO_2-water-basalt interaction. Numerical simulation of low temperature CO_2 sequestration into basalts". In: *Geochimica et Cosmochimica Acta* 75 (17). ISSN: 00167037. DOI: `10.1016/j.gca.2011.05.037`.

Habeeb, O. A., R. Kanthasamy, G. A. Ali, S. Sethupathi, and R. B. M. Yunus (2018). "Hydrogen sulfide emission sources, regulations, and removal techniques: A review". In: *Reviews in Chemical Engineering* 34 (6). ISSN: 01678299. DOI: `10.1515/revce-2017-0004`.

Hayashi, M. (2004). "Temperature-electrical conductivity relation of water for environmental monitoring and geophysical data inversion". In: *Environmental Monitoring and Assessment* 96 (1-3). ISSN: 01676369. DOI: `10.1023/B:EMAS.0000031719.83065.68`.

Helander, D. P. (1983). *Fundamentals of Formation Evaluation.* Oil & Gas Consultants Intl. ISBN: 978-0930972028.

Helgadóttir, H. M. (2021). *NN-03 and NN-04 in Nesjavellir Drill cuttings analysis.* Tech. rep. ÍSOR Short Report 21001.

Helgeson, H. C., R. M. Garrels, and F. T. MacKenzie (1969). “Evaluation of irreversible reactions in geochemical processes involving minerals and aqueous solutions-II. Applications”. In: *Geochimica et Cosmochimica Acta* 33 (4). ISSN: 00167037. DOI: `10.1016/0016-7037(69)90127-6`.

Hersir, G. P., E. Á. Gudnason, and Ó. G. Flóvenz (2022). “Geophysical Exploration Techniques”. In: *Comprehensive Renewable Energy.* Ed. by T. M. Letcher. 2nd ed. Vol. 7. Elsevier.

Hinnell, A. C., T. P. Ferré, J. A. Vrugt, J. A. Huisman, S. Moysey, J. Rings, and M. B. Kowalsky (2010). “Improved extraction of hydrologic information from geophysical data through coupled hydrogeophysical inversion”. In: *Water Resources Research* 46 (4). ISSN: 00431397. DOI: `10.1029/2008WR007060`.

Hubbard, S. S., J. Chen, J. Peterson, E. L. Majer, K. H. Williams, D. J. Swift, B. Mailloux, and Y. Rubin (2001). “Hydrogeological characterization of the South Oyster bacterial transport site using geophysical data”. In: *Water Resources Research* 37 (10). ISSN: 00431397. DOI: `10.1029/2001WR000279`.

Hubbard, S. S., Y. Rubin, and E. Majer (1997). “Ground-penetrating-radar-assisted saturation and permeability estimation in bimodal systems”. In: *Water Resources Research* 33 (5). ISSN: 00431397. DOI: `10.1029/96WR03979`.

Hupfer, S., T. Martin, A. Weller, T. Günther, K. Kuhn, V. D. N. Ngninjio, and U. Noell (2016). “Polarization effects of unconsolidated sulphide-sand-mixtures”. In: *Journal of Applied Geophysics* 135. ISSN: 09269851. DOI: `10.1016/j.jappgeo.2015.12.003`.

Iceland, G. of (Mar. 2022). *The State and Challenges of Energy Affairs with reference to the government’s climate action targets and emphases.* Iceland Ministry of the Environment, Energy and Climate.

Izumoto, S. (2023). “Induced Polarization of Metal Grains: Simulations of Three-Dimensional Electric Fields”. In: *Journal of Geophysical Research: Solid Earth* 128 (9). ISSN: 21699356. DOI: `10.1029/2023JB026757`.

Izumoto, S., J. A. Huisman, Y. Wu, and H. Vereecken (2020). “Effect of solute concentration on the spectral induced polarization response of calcite precipitation”. In: *Geophysical Journal International* 220 (2). ISSN: 1365246X. DOI: `10.1093/gji/ggz515`.

Jeffery, G. H., J. Bassett, M. J, and R. C. J. Denney (1989). *Vogel’s textbook of quantitative chemical analysis.* 5th ed. Longman Scientific and Technical. ISBN: 0-582-44693-7.

Junker, J. S., A. Obermann, M. Voigt, H. Maurer, O. E. Eruteya, A. Moscariello, S. Wiemer, and A. Zappone (2025). “Geophysical characterization of the in-situ CO_2 mineral storage pilot site in Helguvik, Iceland”. In: *International Journal of Greenhouse Gas Control* 141. DOI: `https://doi.org/10.1016/j.ijggc.2025.104320`.

Kaasalainen, H. and A. Stefánsson (2011). “Sulfur speciation in natural hydrothermal waters, Iceland”. In: *Geochimica et Cosmochimica Acta* 75 (10). ISSN: 00167037. DOI: `10.1016/j.gca.2011.02.036`.

Kelemen, P., S. M. Benson, H. Pilorgé, P. Psarras, and J. Wilcox (2019). “An Overview of the Status and Challenges of CO_2 Storage in Minerals and Geological Formations”. In: *Frontiers in Climate* 1. ISSN: 26249553. DOI: `10.3389/fclim.2019.00009`.

Keller, G. V. and F. C. Frischknecht (1966). *Electrical Methods in Geophysical Prospecting*. Pergamon Press.

Kjeld, A., H. J. Bjarnadottir, and R. Olafsdottir (2022). “Life cycle assessment of the Theistareykir geothermal power plant in Iceland”. In: *Geothermics* 105. ISSN: 03756505. DOI: `10.1016/j.geothermics.2022.102530`.

Krevor, S., M. J. Blunt, S. M. Benson, C. H. Pentland, C. Reynolds, A. Al-Menhali, and B. Niu (2015). “Capillary trapping for geologic carbon dioxide storage - From pore scale physics to field scale implications”. In: *International Journal of Greenhouse Gas Control* 40. ISSN: 17505836. DOI: `10.1016/j.ijggc.2015.04.006`.

Kristmannsdóttir, H. (1979). “Alteration of basaltic rocks by hydrothermal-activity at 100-300°C”. In: *Developments in Sedimentology* 27 (C). ISSN: 00704571. DOI: `10.1016/S0070-4571(08)70732-5`.

Lavalleur, H. J. and F. S. Colwell (2013). “Microbial characterization of basalt formation waters targeted for geological carbon sequestration”. In: *FEMS Microbiology Ecology* 85 (1). ISSN: 01686496. DOI: `10.1111/1574-6941.12098`.

Lévy, L., B. Gibert, F. Sigmundsson, D. Deldicque, F. Parat, and G. P. Hersir (2019a). “Tracking Magmatic Hydrogen Sulfur Circulations Using Electrical Impedance: Complex Electrical Properties of Core Samples at the Krafla Volcano, Iceland”. In: *Journal of Geophysical Research: Solid Earth* 124 (3). ISSN: 21699356. DOI: `10.1029/2018JB016814`.

Lévy, L., B. Gibert, F. Sigmundsson, O. G. Flóvenz, G. P. Hersir, P. Briole, and P. A. Pezard (2018). “The role of smectites in the electrical conductivity of active hydrothermal systems: Electrical properties of core samples from Krafla volcano, Iceland”. In: *Geophysical Journal International* 215 (3). ISSN: 1365246X. DOI: `10.1093/gji/ggy342`.

Lévy, L., P. K. Maurya, S. Byrdina, J. Vandemeulebrouck, F. Sigmundsson, K. Árnason, T. Ricci, D. Deldicque, M. Roger, B. Gibert, and P. Labazuy (2019b). “Electrical resistivity tomography and time-domain induced polarization field investigations of geothermal areas at Krafla, Iceland: Comparison to borehole and laboratory frequency-domain electrical observations”. In: *Geophysical Journal International* 218 (3). ISSN: 1365246X. DOI: `10.1093/gji/ggz240`.

Lévy, L., R. Thalund-Hansen, T. Bording, G. Fiandaca, A. Christiansen, K. Rügge, N. Tuxen, M. Hag, and P. L. Bjerg (2022). “Quantifying Reagent Spreading by Cross-Borehole Electrical Tomography to Assess Performance of Groundwater Remediation”. In: *Water Resources Research* 58 (9).

Lévy, L., D. Ciraula, B. Legros, T. Martin, and A. Weller (2024). “Understanding the fate of H_2S injected in basalts by means of time-domain induced polarization geophysical logging”. In: *Journal of Geophysical Research: Solid Earth* 129 (6). DOI: `10.1029/2023JB028316`.

Lévy, L., B. Gibert, D. Escobedo, P. Patrier, B. Lanson, D. Beaufort, D. Loggia, P. Pezard, and N. Marino (2020). “Relationships between Lithology, Permeability, Clay Mineralogy and Electrical Conductivity in Icelandic Altered Volcanic Rocks”. In: *World Geothermal Congress*.

Lu, P., G. Zhang, J. Apps, and C. Zhu (2022). “Comparison of thermodynamic data files for PHREEQC”. In: *Earth-Science Reviews* 225. ISSN: 00128252. DOI: `10.1016/j.earscirev.2021.103888`.

Luhmann, A. J., B. M. Tutolo, B. C. Bagley, D. F. Mildner, W. E. Seyfried, and M. O. Saar (2017). “Permeability, porosity, and mineral surface area changes in basalt cores induced by reactive transport of CO_2-rich brine”. In: *Water Resources Research* 53 (3). ISSN: 19447973. DOI: `10.1002/2016WR019216`.

Madsen, L. M. (2019). “Monte Carlo analysis and 3D spectral inversion of full-decay induced polarization data”. PhD thesis. Aarhus University.

Marieni, C., J. Přikryl, E. S. Aradóttir, I. Gunnarsson, and A. Stefánsson (2018). “Towards ‘green’ geothermal energy: Co-mineralization of carbon and sulfur in geothermal reservoirs”. In: *International Journal of Greenhouse Gas Control* 77. ISSN: 17505836. DOI: `10.1016/j.ijggc.2018.07.011`.

Marini, L. (2006). “Chapter 7: Reaction path modelling of geological CO_2 sequestration”. In: *Developments in Geochemistry*. Vol. 11. DOI: `10.1016/S0921-3198(06)80027-X`.

Marshall, D. J. and T. R. Madden (1959). “Induced polarization, a study of its causes”. In: *Geophysics* 24 (4). ISSN: 0016-8033. DOI: `10.1190/1.1438659`.

Martin, T., K. Titov, A. Tarasov, and A. Weller (2021). “Spectral induced polarization: Frequency domain versus time domain laboratory data”. In: *Geophysical Journal International* 225 (3). ISSN: 1365246X. DOI: `10.1093/gji/ggab071`.

Martin, T. and A. Weller (2023). “Superposition of induced polarization signals measured on pyrite-sand mixtures”. In: *Geophysical Journal International* 234 (1). ISSN: 1365246X. DOI: `10.1093/gji/ggad091`.

Matter, J. M., M. Stute, S. Snæbjörnsdóttir, E. H. Oelkers, S. R. Gíslason, E. S. Aradóttir, B. Sigfusson, I. Gunnarsson, H. Sigurdardóttir, E. Gunnlaugsson, G. Axelsson, H. A. Alfredsson, D. Wolff-Boenisch, K. Mesfin, D. F. D. L. R. Taya, J. Hall, K. Dideriksen, and W. S. Broecker (2016). “Rapid carbon mineralization for permanent disposal of anthropogenic carbon dioxide emissions”. In: *Science* 352 (6291). ISSN: 10959203. DOI: `10.1126/science.aad8132`.

Maurya, P. K., G. Fiandaca, A. V. Christiansen, and E. Auken (2018). “Field-scale comparison of frequency- and time-domain spectral induced polarization”. In: *Geophysical Journal International* 214 (2). ISSN: 1365246X. DOI: `10.1093/GJI/GGY218`.

McGrail, B. P., F. A. Spane, E. C. Sullivan, D. H. Bacon, and G. Hund (2011). "The Wallula basalt sequestration pilot project". In: *Energy Procedia*. Vol. 4. DOI: `10.1016/j.egypro.2011.02.557`.

McGrail, B. P., H. T. Schaef, F. A. Spane, J. B. Cliff, O. Qafoku, J. A. Horner, C. J. Thompson, A. T. Owen, and C. E. Sullivan (2017). "Field validation of supercritical CO_2 reactivity with basalts". In: *Environmental Science and Technology Letters* 4 (1). ISSN: 23288930. DOI: `10.1021/acs.estlett.6b00387`.

Meckel, T. A., M. Zeidouni, S. D. Hovorka, and S. A. Hosseini (2013). "Assessing sensitivity to well leakage from three years of continuous reservoir pressure monitoring during CO_2 injection at Cranfield, MS, USA". In: *International Journal of Greenhouse Gas Control* 18. ISSN: 17505836. DOI: `10.1016/j.ijggc.2013.01.019`.

Mellage, A., C. M. Smeaton, A. Furman, E. A. Atekwana, F. Rezanezhad, and P. V. Cappellen (2018). "Linking Spectral Induced Polarization (SIP) and Subsurface Microbial Processes: Results from Sand Column Incubation Experiments". In: *Environmental Science and Technology* 52 (4). ISSN: 15205851. DOI: `10.1021/acs.est.7b04420`.

Muñoz, A. Q. (1996). *Interpretation of Geophysical Well Logs from the Nesjavellir Geothermal Field, Iceland*. Tech. rep. The United Nations University, Geothermal Training Program (13).

Nelson, R. A. (1987). "Fractured reservoirs: turning knowledge into practice". In: *Journal of Petroleum Technology* 39 (4). ISSN: 01492136. DOI: `10.2118/16470-PA`.

Olsson, P. I., T. Dahlin, G. Fiandaca, and E. Auken (2015). "Measuring time-domain spectral induced polarization in the on-time: Decreasing acquisition time and increasing signal-to-noise ratio". In: *Journal of Applied Geophysics* 123. ISSN: 09269851. DOI: `10.1016/j.jappgeo.2015.08.009`.

Olsson, P. I., G. Fiandaca, J. J. Larsen, T. Dahlin, and E. Auken (2016). "Doubling the spectrum of time-domain induced polarization by harmonic de-noising, drift correction, spike removal, tapered gating and data uncertainty estimation". In: *Geophysical Journal International* 207 (2). ISSN: 1365246X. DOI: `10.1093/gji/ggw260`.

Orozco, A. F., M. Steiner, T. Katona, N. Roser, C. Moser, M. J. Stumvoll, and T. Glade (2022). "Application of induced polarization imaging across different scales to understand surface and groundwater flow at the Hofermuehle landslide". In: *Catena* 219. ISSN: 03418162. DOI: `10.1016/j.catena.2022.106612`.

Pálmason, G., G. V. Johnsen, H. Torfason, K. Saemundsson, K. Ragnars, G. I. Haraldsson, and G. K. Halldórsson (1985). *National Energy Authority Report OS-85076/JHD-10*. Tech. rep. Orkustofnun.

Parkhurst, D. L. and C. Appelo (2013). *Description of input and examples for PHREEQC Version 3 — A computer program for speciation, batch-reaction, one-dimensional transport, and inverse geochemical calculations*. Tech. rep.

Pelton, W. H., S. H. Ward, P. G. Hallof, W. R. Sill, and P. H. Nelson (1978). "Mineral discrimination and removal of inductive coupling with multifrequency IP". In: *Geophysics* 43 (3). ISSN: 19422156. DOI: `10.1190/1.1440839`.

Piolat, L., A. Revil, P. Cosme, Y. Géraud, T. Dupaigne, W. Wheeler, J. Tveranger, B. Lønøy, E. Turinimana, E. Karangwa, and A. Favier (2025). "Induced polarization of volcanic rocks. 9. Anatomy of a rising thermal plume". In: *Geophysical Journal International* 243.1. DOI: `10.1093/gji/ggaf307`.

Piolat, L., Y. Geraud, and A. Revil (2023). "Induced Polarization Images the Plumbing System of Hydrothermal Vents in an Intracontinental Rift, Lake Abhé, Republic of Djibouti". In: *Geophysical Research Letters* 50 (24). ISSN: 19448007. DOI: `10.1029/2023GL105145`.

Placencia-Gómez, E., L. Slater, D. Ntarlagiannis, and A. Binley (2013). "Laboratory SIP signatures associated with oxidation of disseminated metal sulfides". In: *Journal of Contaminant Hydrology* 148. ISSN: 01697722. DOI: `10.1016/j.jconhyd.2013.02.007`.

Pleasants, M. S., F. dos A. Neves, A. D. Parsekian, K. M. Befus, and T. J. Kelleners (2022). "Hydrogeophysical Inversion of Time-Lapse ERT Data to Determine Hillslope Subsurface Hydraulic Properties". In: *Water Resources Research* 58 (4). ISSN: 19447973. DOI: `10.1029/2021WR031073`.

Polites, E. G., H. T. Schaef, J. A. Horner, A. T. Owen, J. E. J. Holliman, B. P. McGrail, and Q. R. Miller (2022). "Exotic Carbonate Mineralization Recovered from a Deep Basalt Carbon Storage Demonstration". In: *Environmental Science & Technology* 56, pp. 14713–14722.

Přikryl, J., C. Marieni, S. Guðbrandsson, E. S. Aradóttir, I. Gunnarsson, and A. Stefánsson (2018). "H_2S sequestration process and sustainability in geothermal systems". In: *Geothermics* 71. ISSN: 03756505. DOI: `10.1016/j.geothermics.2017.09.010`.

Pruess, K. and T. N. Narasimhan (1985). "A Practical Method for Modeling Fluid and Heat Flow in Fractured Porous Media". In: *Society of Petroleum Engineers Journal* 25 (1). ISSN: 01977520. DOI: `10.2118/10509-pa`.

Ragnarsson, A., B. Steingrímsson, and S. Thorhallsson (2023). "Geothermal development in Iceland 2020–2022". In: *Proceedings of the World Geothermal Congress.*

Ratouis, T. M., S. Snæbjörnsdóttir, M. J. Voigt, B. Sigfússon, G. Gunnarsson, E. S. Aradóttir, and V. Hjörleifsdóttir (2022). "Carbfix 2: A transport model of long-term CO_2 and H_2S injection into basaltic rocks at Hellisheidi, SW-Iceland". In: *International Journal of Greenhouse Gas Control* 114. ISSN: 17505836. DOI: `10.1016/j.ijggc.2022.103586`.

Rembert, F. (2021). "Development of geo-electrical methods to characterize dissolution and precipitation processes in a carbonate context". PhD thesis. Sorbonne Université.

Rembert, F., D. Jougnot, L. Luquot, and R. Guérin (2022). "Interpreting Self-Potential Signal during Reactive Transport: Application to Calcite Dissolution and Precipitation". In: *Water* 14 (10). DOI: `10.3390/w14101632`.

Revil, A., M. L. Breton, Q. Niu, E. Wallin, E. Haskins, and D. M. Thomas (2017a). "Induced polarization of volcanic rocks. 2. Influence of pore size and permeability".

In: *Geophysical Journal International* 208 (2). ISSN: 1365246X. DOI: `10.1093/gji/ggw382`.

Revil, A., L. M. Cathles, S. Losh, and J. A. Nunn (1998). "Electrical conductivity in shaly sands with geophysical applications". In: *Journal of Geophysical Research: Solid Earth* 103 (10). ISSN: 21699356. DOI: `10.1029/98jb02125`.

Revil, A., A. Ghorbani, L. S. Gailler, M. Gresse, N. Cluzel, N. Panwar, and R. Sharma (2018). "Electrical conductivity and induced polarization investigations at Kilauea volcano, Hawai'i". In: *Journal of Volcanology and Geothermal Research* 368. ISSN: 03770273. DOI: `10.1016/j.jvolgeores.2018.10.014`.

Revil, A., M. Murugesu, M. Prasad, and M. L. Breton (2017b). "Alteration of volcanic rocks: A new non-intrusive indicator based on induced polarization measurements". In: *Journal of Volcanology and Geothermal Research* 341. ISSN: 03770273. DOI: `10.1016/j.jvolgeores.2017.06.016`.

Revil, A., Y. Qi, A. Ghorbani, M. Gresse, and D. M. Thomas (2021a). "Induced polarization of volcanic rocks. 5. Imaging the temperature field of shield volcanoes". In: *Geophysical Journal International* 225 (3). ISSN: 1365246X. DOI: `10.1093/gji/ggab039`.

Revil, A. and M. Gresse (2021b). "Induced polarization as a tool to assess alteration in geothermal systems: A review". In: *Minerals* 11 (9). ISSN: 2075163X. DOI: `10.3390/min11090962`.

Revil, A., N. Florsch, and D. Mao (2015). "Induced polarization response of porous media with metallic particles -Part 1: A theory for disseminated semiconductors". In: *Geophysics* 80 (5). ISSN: 19422156. DOI: `10.1190/GEO2014-0577.1`.

Rickard, D. and G. W. Luther (2007). "Chemistry of iron sulfides". In: *Chemical Reviews* 107 (2). ISSN: 00092665. DOI: `10.1021/cr0503658`.

Roy, A. and R. L. Dhar (1971). "Radius of investigation in DC resistivity well logging". In: *Geophysics* 36 (4). ISSN: 0016-8033. DOI: `10.1190/1.1440210`.

Rubin, Y., G. Mavko, and J. Harris (1992). "Mapping permeability in heterogeneous aquifers using hydrologic and seismic data". In: *Water Resources Research* 28 (7). ISSN: 19447973. DOI: `10.1029/92WR00154`.

Rücker, C., T. Günther, and F. M. Wagner (2017). "pyGIMLi: An open-source library for modelling and inversion in geophysics". In: *Computers and Geosciences* 109. ISSN: 00983004. DOI: `10.1016/j.cageo.2017.07.011`.

Saneiyan, S., D. Ntarlagiannis, J. Ohan, J. Lee, F. Colwell, and S. Burns (2019). "Induced polarization as a monitoring tool for in-situ microbial induced carbonate precipitation (MICP) processes". In: *Ecological Engineering* 127. ISSN: 09258574. DOI: `10.1016/j.ecoleng.2018.11.010`.

Saneiyan, S., D. Ntarlagiannis, D. D. Werkema, and A. Ustra (2018). "Geophysical methods for monitoring soil stabilization processes". In: *Journal of Applied Geophysics* 148. ISSN: 09269851. DOI: `10.1016/j.jappgeo.2017.12.008`.

Sassen, D. S., S. S. Hubbard, S. A. Bea, J. Chen, N. Spycher, and M. E. Denham (2012). "Reactive facies: An approach for parameterizing field-scale reactive transport models using geophysical methods". In: *Water Resources Research* 48 (10). ISSN: 00431397. DOI: `10.1029/2011WR011047`.

Schaef, H. T., B. P. McGrail, A. T. Owen, and B. W. Arey (2013). “Mineralization of basalts in the CO_2-H2O-H_2S system”. In: *International Journal of Greenhouse Gas Control* 16. ISSN: 17505836. DOI: `10.1016/j.ijggc.2013.03.020`.

Schaef, H. T., J. A. Horner, A. T. Owen, C. J. Thompson, J. S. Loring, and B. P. McGrail (2014). “Mineralization of basalts in the CO_2-H_2O-SO_2-O_2 system”. In: *Environmental Science and Technology* 48 (9). ISSN: 15205851. DOI: `10.1021/es404964j`.

Schoonen, M. A. and H. L. Barnes (1991). “Reactions forming pyrite and marcasite from solution: II. Via FeS precursors below 100°C”. In: *Geochimica et Cosmochimica Acta* 55 (6). ISSN: 00167037. DOI: `10.1016/0016-7037(91)90123-M`.

Schoonen, M. A. (Jan. 2004). “Mechanisms of sedimentary pyrite formation”. In: *Sulfur Biogeochemistry - Past and Present*. Geological Society of America. ISBN: 9780813723792. DOI: `10.1130/0-8137-2379-5.117`. URL: `https://doi.org/10.1130/0-8137-2379-5.117`.

Scott, S. W., L. Lévy, C. Covell, H. Franzson, B. Gibert, Á. Valfells, J. Newson, J. Frolova, E. Júlíusson, and M. S. Guðjónsdóttir (2023). “Valgarður: a database of the petrophysical, mineralogical, and chemical properties of Icelandic rocks”. In: *Earth System Science Data* 15 (3). ISSN: 18663516. DOI: `10.5194/essd-15-1165-2023`.

Shuey, R. T. (1975). *Semiconducting Ore Minerals*. Vol. 4. Elsevier Scientific Publishing Company.

Sigfusson, B., S. R. Gíslason, and A. A. Meharg (2011). “A field and reactive transport model study of arsenic in a basaltic rock aquifer”. In: *Applied Geochemistry* 26 (4). ISSN: 08832927. DOI: `10.1016/j.apgeochem.2011.01.013`.

Singha, K., F. D. Day-Lewis, T. Johnson, and L. D. Slater (2015). “Advances in interpretation of subsurface processes with time-lapse electrical imaging”. In: *Hydrological Processes* 29 (6). ISSN: 10991085. DOI: `10.1002/hyp.10280`.

Snæbjörnsdóttir, S. Ó., I. M. Galeczka, B. Sigfússon, and E. H. Oelkers (2021). “Injection of geothermal CO_2 and H_2S gases at the Nesjavellir site, SW Iceland: A pre-injection overview”. In: *Proceedings World Geothermal Congress 2021*.

Snæbjörnsdóttir, S. Ó., E. H. Oelkers, K. Mesfin, E. S. Aradóttir, K. Dideriksen, I. Gunnarsson, E. Gunnlaugsson, J. M. Matter, M. Stute, and S. R. Gíslason (2017). “The chemistry and saturation states of subsurface fluids during the in situ mineralisation of CO_2 and H_2S at the CarbFix site in SW-Iceland”. In: *International Journal of Greenhouse Gas Control* 58. ISSN: 17505836. DOI: `10.1016/j.ijggc.2017.01.007`.

Snæbjörnsdóttir, S. Ó., B. Sigfússon, C. Marieni, D. Goldberg, S. R. Gíslason, and E. H. Oelkers (2020). “Carbon dioxide storage through mineral carbonation”. In: *Nature Reviews Earth and Environment* 1 (2). ISSN: 2662138X. DOI: `10.1038/s43017-019-0011-8`.

Steefel, C. I., D. J. DePaolo, and P. C. Lichtner (2005). “Reactive transport modeling: An essential tool and a new research approach for the Earth sciences”.

In: *Earth and Planetary Science Letters* 240 (3-4). ISSN: 0012821X. DOI: `10.1016/j.epsl.2005.09.017`.

Steefel, C. I. and K. Mäher (2009). “Fluid-rock interaction: A reactive transport approach”. In: *Reviews in Mineralogy and Geochemistry* 70. ISSN: 15296466. DOI: `10.2138/rmg.2009.70.11`.

Stefánsson, A., S. Arnórsson, I. Gunnarsson, H. Kaasalainen, and E. Gunnlaugsson (2011). “The geochemistry and sequestration of H_2S into the geothermal system at Hellisheidi, Iceland”. In: *Journal of Volcanology and Geothermal Research* 202 (3-4). ISSN: 03770273. DOI: `10.1016/j.jvolgeores.2010.12.014`.

Stefánsson, A. and S. R. Gíslason (2001). “Chemical weathering of basalts, southwest Iceland: Effect of rock crystallinity and secondary minerals on chemical fluxes to the ocean”. In: *American Journal of Science* 301 (6). ISSN: 00029599. DOI: `10.2475/ajs.301.6.513`.

Stefánsson, A., I. Gunnarsson, and N. Giroud (2007). “New methods for the direct determination of dissolved inorganic, organic and total carbon in natural waters by Reagent-Free™ Ion Chromatography and inductively coupled plasma atomic emission spectrometry”. In: *Analytica Chimica Acta* 582 (1). ISSN: 00032670. DOI: `10.1016/j.aca.2006.09.001`.

Stefánsson, V. (2000). “The renewability of geothermal energy”. In: *Proceedings World Geothermal Congress.*

Stefánsson, V. (1991). *Forðafræðistuðlar : poruhluti bergs.* Tech. rep. Orkustofnun Report VS-91/02.

Sullivan, N. A. L., A. Viezzoli, and G. Fiandaca (2023). “EEMstudio: an open-source freeware QGIS plugin for processing, modelling and inversion of electric and electromagnetic data”. In: *AEM 2023: Short abstracts, Preview, 2023:225*, pp. 52–66. DOI: `10.1080/14432471.2023.2236352`.

Sumner, J. S. (1978). “Principles of Induced Polarization for Geophysical Exploration”. In: *Developments in Economic Geology.* Ed. by J. S. Sumner. Vol. 5. Elsevier.

Thien, B. M., G. Kosakowski, and D. A. Kulik (2015). “Differential alteration of basaltic lava flows and hyaloclastites in Icelandic hydrothermal systems”. In: *Geothermal Energy* 3 (1). ISSN: 21959706. DOI: `10.1186/s40517-015-0031-7`.

Trias, R., B. Ménez, P. L. Campion, Y. Zivanovic, L. Lecourt, A. Lecoeuvre, P. Schmitt-Kopplin, J. Uhl, S. R. Gislason, H. A. Alfreosson, K. G. Mesfin, S. O. Snæbjörnsdóttir, E. S. Aradóttir, I. Gunnarsson, J. M. Matter, M. Stute, E. H. Oelkers, and E. Gérard (2017). “High reactivity of deep biota under anthropogenic CO_2 injection into basalt”. In: *Nature Communications* 8 (1). ISSN: 20411723. DOI: `10.1038/s41467-017-01288-8`.

Vinegar, H. J. and M. H. Waxman (1984). “Induced Polarization of Shaly Sands”. In: *Geophysics* 49 (8). ISSN: 00168033. DOI: `10.1190/1.1441755`.

Voigt, M., C. Marieni, D. E. Clark, S. R. Gíslason, and E. H. Oelkers (2018). “Evaluation and refinement of thermodynamic databases for mineral carbonation”. In: *Energy Procedia.* Vol. 146. DOI: `10.1016/j.egypro.2018.07.012`.

Wainwright, H. M., J. Chen, D. S. Sassen, and S. S. Hubbard (2014). “Bayesian hierarchical approach and geophysical data sets for estimation of reactive facies over plume scales”. In: *Water Resources Research* 50 (6). ISSN: 19447973. DOI: `10.1002/2013WR013842`.

Warren, J. and P. Root (1963). “The Behavior of Naturally Fractured Reservoirs”. In: *Society of Petroleum Engineers Journal* 3 (03). ISSN: 0197-7520. DOI: `10.2118/426-pa`.

Waxman, M. H. and L. J. Smits (1968). “Electrical Conductivities in Oil-Bearing Shaly Sands”. In: *Soc. Pet. Eng. J.* (8). ISSN: 08910901. DOI: `10.2118/1863-a`.

Weisenberger, T. B., H. Ingimarsson, G. P. Hersir, and Ó. G. Flóvenz (2020). “Cation-exchange capacity distribution within hydrothermal systems and its relation to the alteration mineralogy and electrical resistivity”. In: *Energies* 13 (21). ISSN: 19961073. DOI: `10.3390/en13215730`.

Weller, A. and L. Slater (2022). “Ambiguity in induced polarization time constants and the advantage of the Pelton model”. In: *Geophysics* 87 (6). ISSN: 19422156. DOI: `10.1190/geo2022-0158.1`.

White, S. K., F. A. Spane, H. T. Schaef, Q. R. Miller, M. D. White, J. A. Horner, and B. P. McGrail (2020). “Quantification of CO_2 Mineralization at the Wallula Basalt Pilot Project”. In: *Environmental Science and Technology* 54 (22). ISSN: 15205851. DOI: `10.1021/acs.est.0c05142`.

WHO (1981). “Hydrogen sulfide”. In: *World Health Organization* (Environmental Health Criteria, No. 19).

Wiglusz, T., A. Sapińska-Śliwa, H. Tulinius, R. Wiśniowski, T. Sliwa, M. Kruszewski, and T. Kowalski (2017). “Analysis of drilling and well completion technology for geothermal wells in Poland as a result of a EEA international project in cooperation with Iceland”. In: *Geological Exploration Technology, Geothermal Energy, Sustainable Development.*

Williams, K. H., A. Kemna, M. J. Wilkins, J. Druhan, E. Arntzen, A. L. N’Guessan, P. E. Long, S. S. Hubbard, and J. F. Banfield (2009). “Geophysical monitoring of coupled microbial and geochemical processes during stimulated subsurface bioremediation”. In: *Environmental Science and Technology* 43 (17). ISSN: 0013936X. DOI: `10.1021/es900855j`.

Wong, J. (1979). “An electrochemical model of the induced-polarization phenomenon in disseminated sulfide ores.” In: *Geophysics* 44 (7). ISSN: 00168033. DOI: `10.1190/1.1441005`.

Wu, Y., J. B. Ajo-Franklin, N. Spycher, S. S. Hubbard, G. Zhang, K. H. Williams, J. Taylor, Y. Fujita, and R. Smith (2011). “Geophysical monitoring and reactive transport modeling of ureolytically-driven calcium carbonate precipitation”. In: *Geochemical Transactions* 12. ISSN: 14674866. DOI: `10.1186/1467-4866-12-7`.

Wu, Y., S. Hubbard, K. H. Williams, and J. Ajo-Franklin (2010). “On the complex conductivity signatures of calcite precipitation”. In: *Journal of Geophysical Research: Biogeosciences* 115 (G2). DOI: `10.1029/2009jg001129`.

Wu, Y., V. K. Surasani, L. Li, and S. S. Hubbard (2014). “Geophysical monitoring and reactive transport simulations of bioclogging processes induced by Leuconostoc mesenteroides". In: *Geophysics* 79 (1). ISSN: 19422156. DOI: `10.1190/GEO2013-0121.1`.

Xiong, W., R. K. Wells, A. H. Menefee, P. Skemer, B. R. Ellis, and D. E. Giammar (2017). "CO_2 mineral trapping in fractured basalt". In: *International Journal of Greenhouse Gas Control* 66. ISSN: 17505836. DOI: `10.1016/j.ijggc.2017.10.003`.

Xu, T., E. Sonnenthal, N. Spycher, and K. Pruess (2006). "TOUGHREACT - A simulation program for non-isothermal multiphase reactive geochemical transport in variably saturated geologic media: Applications to geothermal injectivity and CO_2 geological sequestration". In: *Computers and Geosciences* 32 (2). ISSN: 00983004. DOI: `10.1016/j.cageo.2005.06.014`.

Yang, C., P. J. Mickler, R. Reedy, B. R. Scanlon, K. D. Romanak, J. P. Nicot, S. D. Hovorka, R. H. Trevino, and T. Larson (2013). "Single-well push-pull test for assessing potential impacts of CO_2 leakage on groundwater quality in a shallow Gulf Coast aquifer in Cranfield, Mississippi". In: *International Journal of Greenhouse Gas Control* 18. ISSN: 17505836. DOI: `10.1016/j.ijggc.2012.12.030`.

Zarandi, S. and G. Ivarsson (2010). *A Review on Waste Water Disposal at the Nesjavellir Geothermal Power Plant.* Tech. rep.

Zettlitzer, M., F. Moeller, D. Morozova, P. Lokay, and H. Würdemann (2010). "Re-establishment of the proper injectivity of the CO2-injection well Ktzi 201 in Ketzin, Germany". In: *International Journal of Greenhouse Gas Control* 4 (6). ISSN: 17505836. DOI: `10.1016/j.ijggc.2010.05.006`.

Zhang, C., L. Slater, G. Redden, Y. Fujita, T. Johnson, and D. Fox (2012). "Spectral induced polarization signatures of hydroxide adsorption and mineral precipitation in porous media". In: *Environmental Science and Technology* 46 (8). ISSN: 0013936X. DOI: `10.1021/es204404e`.

Zhang, K., N. Chibati, A. Revil, J. Richard, M. Gresse, Y. Xue, and Y. Geraud (2023). "Induced polarization of volcanic rocks-6: Relationships with other petrophysical properties". In: *Geophysical Journal International* 234 (3). ISSN: 1365246X. DOI: `10.1093/gji/ggad246`.

Zhang, S. and D. J. DePaolo (2017). "Rates of CO_2 Mineralization in Geological Carbon Storage". In: *Accounts of Chemical Research* 50 (9). ISSN: 15204898. DOI: `10.1021/acs.accounts.7b00334`.

Zheng, L., J. A. Apps, Y. Zhang, T. Xu, and J. T. Birkholzer (2009). "On mobilization of lead and arsenic in groundwater in response to CO_2 leakage from deep geological storage". In: *Chemical Geology* 268 (3-4). ISSN: 00092541. DOI: `10.1016/j.chemgeo.2009.09.007`.

Paper 1

Environmental Science & Technology

pubs.acs.org/est

Article

Advanced Monitoring of H_2S Injection through the Coupling of Reactive Transport Models and Geophysical Responses

Daniel A. Ciraula,* Barbara I. Kleine-Marshall, Iwona M. Galeczka, and Léa Lévy

Cite This: https://doi.org/10.1021/acs.est.3c10139

Read Online

ACCESS | Metrics & More | Article Recommendations | Supporting Information

ABSTRACT: Hydrogen sulfide (H_2S), an environmentally harmful pollutant, is a byproduct of geothermal energy production. To reduce the H_2S emissions, H_2S-charged water is injected into the basaltic subsurface, where it mineralizes to iron sulfides. Here, we couple geophysical induced polarization (IP) measurements in H_2S injection wells and geochemical reactive transport models (RTM) to monitor the H_2S storage efforts in the subsurface of Nesjavellir, one of Iceland's most productive geothermal fields. An increase in the IP response after 40 days of injection indicates iron-sulfide formation near the injection well. Likewise, the RTM shows that iron sulfides readily form at circumneutral to alkaline pH conditions, and the iron supply from basalt dissolution limits its formation. Agreement in the trends of the magnitude and distribution of iron-sulfide formation between IP and RTM suggests that coupling the methods can improve the monitoring of H_2S mineralization by providing insight into the parameters influencing iron-sulfide formation. In particular, accurate fluid flow parameters in RTMs are critical to validate the predictions of the spatial distribution of subsurface iron-sulfide formation over time obtained through IP observations. This work establishes a foundation for expanding H_2S sequestration monitoring efforts and a framework for coupling geophysical and geochemical site evaluations in environmental studies.

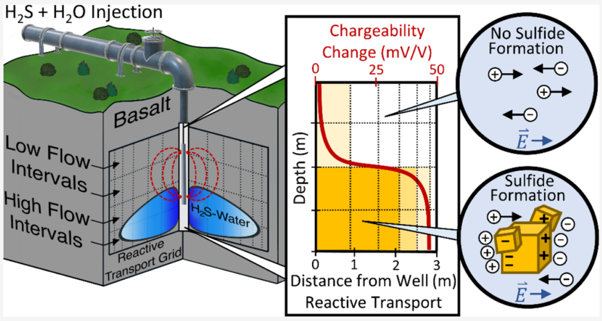

KEYWORDS: *hydrogen sulfide, induced polarization, wireline logging, mineral storage, basalt, pyrite, geothermal wastewater*

1. INTRODUCTION

Geothermal energy production offers an environmentally friendly base-load energy alternative to fossil fuels. However, as the geothermal steam contains significant H_2S content, it contributes to anthropogenic hydrogen sulfide (H_2S) emissions at a rate of ~0.2 Mt/year globally and 30 kt/year in Iceland.[1−3] The H_2S emissions are toxic to humans, causing respiratory arrest at concentrations exceeding 530 ppm.[4] They also pose a threat to the environment when reacting with the atmospheric oxygen to form acid rain.[5] Recently established air quality regulations limit the H_2S concentration to 50−150 μg/m^3 per 24 h.[6,7]

To meet emission standards at the Nesjavellir power plant in southwest Iceland, H_2S from the geothermal flue gas is captured, dissolved into geothermal wastewater, and injected into the basaltic subsurface.[8] Due to high reactivity and a high divalent cations content (up to 25 wt % Ca, Mg, Fe),[9,10] basalt has the potential to effectively mineralize H_2S through iron sulfide (e.g., pyrite, pyrrhotite) formation upon interaction with the H_2S-charged injection fluid.[1−3] This mineral storage approach is similar to the CarbFix process, which has been studied extensively for the co-capture of CO_2 and H_2S.[3,11−17] Although these studies suggest that H_2S injection and its subsequent mineralization in basalt is a viable solution to store the H_2S emissions permanently, it is crucial to establish a reservoir monitoring strategy to identify potential consequences of such injection. For example, if sulfide mineralization is sluggish, dissolved H_2S oxidation can acidify groundwater and mobilize toxic metals from the host rock.[18−23]

The most utilized method to monitor field-scale H_2S injections is to analyze the chemical composition of the injection reservoir fluid and its parameters.[15−17] Such monitoring, along with geochemical numerical models and laboratory simulations, gives insights into the processes governing the dissolved H_2S removal from the injection fluid.[1−3,11,13−16,24,25] However, verification of the mineralization requires monitoring boreholes close to the injection wells. Furthermore, the chemical composition of water from the reservoir provides only indirect evidence of such mineralization. A potential method to acquire direct information on the magnitude and spatial distribution of the H_2S mineralization in

Received: December 3, 2023
Revised: May 21, 2024
Accepted: May 22, 2024

the storage reservoir is induced polarization (IP) wireline logging. Implementing borehole IP as a monitoring technique provides benefits of high spatial resolution and repeatability over time, enabling alteration processes to be measured along the borehole.[26,27]

The magnitude of the induced polarization response and the volume of polarized material exhibit a positive relationship.[28,29] Previous studies have implemented the IP method to interpret mineral precipitation (i.e., sulfides and carbonates) in laboratory experiments[30−36] and at field sites.[37−41] Particularly for field studies, interpretation of the acquired data can be challenging due to signal noise and the presence of other IP sources that contribute to the signal, especially when dynamic processes are studied.[39,42] To aid in the interpretation of IP measurements and to constrain physiochemical parameters, the IP surveys can be investigated alongside mechanistic models, such as geochemical reactive transport modeling (RTM).[33,39,42−44] While laboratory studies have coupled electrochemical geophysics and RTM,[30,33] this coupling remains unexplored for field-scale applications of mineral precipitation.

In this study, we aim to couple wireline geophysical surveying (i.e., IP geophysics) and geochemical RTM to identify the processes and physicochemical parameters (e.g., fluid and rock chemistry, degree of basalt alteration, temperature, and reservoir porosity and permeability), controlling subsurface H_2S mineralization. The outcome of this study contributes to (1) the general understanding of engineered H_2S mineralization, (2) enhancing the monitoring methods to improve the safety of such operations, and (3) advancing the integration of joint geochemical and geophysical interpretations.

2. MATERIALS AND METHODS

2.1. Site Description. This study focuses on the geothermal power plant at the Nesjavellir high-temperature (>200 °C at <1 km depth) geothermal field (SW Iceland). Here, we provide a brief overview of the geologic setting and the H_2S injection system at Nesjavellir, which have been previously described in detail.[11,45−47] The lithology primarily comprises shallow hyaloclastite formations and lava flows (<400 m), with intrusions at greater depths.[47,48] The production fluid (260−300 °C) at Nesjavellir is sourced at 1000−1500 m depth.[12] The intensity of the subsurface basalt alteration is temperature- and depth-dependent, and it is manifested as distinct alteration zones: (1) no alteration in the upper 450 m, (2) zeolite and smectite (<200 °C), (3) mixed layer clays (200−230 °C), (4) chlorite (230−250 °C), (5) chlorite−epidote (250−280 °C), (6) epidote−actinolite (280−330 °C), and (7) amphibolite at the greatest depths (>330 °C).[46,49]

Production began at Nesjavellir in 1990, and the power plant currently outputs 120 MW_e of electricity and 290 MW_{th} as thermal energy for district heating. A byproduct of this energy production is geothermal wastewater, sourced from the high enthalpy production fluid. The majority of the wastewater is disposed of in shallow injection wells, including the NN-3 and NN-4 wells, which began injecting in 2004. These wells were drilled through minimally altered lavas down to 563 m (NN-3) and 422 m (NN-4) depth, and they tap the cold groundwater system at the outskirts of the geothermal site.[46,49] Boreholes for chemical monitoring are limited at this injection site, and the closest borehole is ∼1.5 km from the injection.

Since January 29, 2021, the power station has dissolved captured H_2S from the geothermal emissions into the wastewater (separated geothermal wastewater and condensate wastewater mixture) and has continuously injected the H_2S-charged water into the NN-3 and NN-4 wells. Injection is under reduced conditions to prevent corrosion of the infrastructure resulting from the formation of sulfuric acid following S^{2-} oxidation. The gas capture process for the Nesjavellir injection system studied here utilizes liquid ring vacuum pumps located at the condensers to dissolve CO_2 and H_2S into geothermal wastewater.[50] This varies from the CarbFix process of gas capture, which utilizes a pressurized scrubbing tower to dissolve CO_2 and H_2S gases.[17,50] Additional details on the wastewater produced at Nesjavellir, the injection system, and wells NN-3 and NN-4 are included in Supporting Information (SI) Text S1 and Table S1.

2.2. Wireline Logging. The geophysical wireline logging methods used to parametrize the reactive transport models and identify H_2S mineralization are introduced here. These geophysical methods are outlined in red on the study workflow, shown in Figure S1. Logging data (neutron, temperature, resistivity, and IP) collected in the NN-3 and NN-4 injection wells before the start of H_2S injection (September 21, 2020) define the porosity and permeability parameters used in the geochemical modeling and establish a baseline IP response. Logging measurements were repeated 40 days after the start of injection (March 10, 2021) to evaluate physicochemical changes due to H_2S injection. Before logging, cold groundwater is injected to decrease the borehole temperature to 60 °C, as required by the logging instruments.

The neutron logging tool emits neutrons from a radioactive americium−beryllium source and uses a neutron receiver to measure the number of neutrons arriving per second.[51] Values are reported to an American Petroleum Institute industrial standard unit, API. Neutron logs are primarily sensitive to the presence of hydrogen near wells, and reduced neutron responses can indicate high water contents and porosities. However, clays and other hydrous minerals can also lower the neutron response, leading to the misinterpretation of high-porosity zones.[52]

The 16/64 QL40-ELOG/IP probing tool (www.alt.lu/downhole-probes/) measures the electrical resistivity and IP response. It uses the "normal" electrode configuration with a 64-in. electrode spacing, defined as the distance between the current electrode (A) and the potential electrode (N).[53] The reference potential electrode (M) is located at the surface such that the distance between the potential electrodes (M and N) is considered infinite.

Electrical resistivity (units Ωm) is inversely related to porosity and clay content, with decreasing electrical resistivity values potentially indicating increased porosity and/or clay content. Electrical resistivity is also a function of temperature as defined by Keller and Frischknecht[54] and Revil et al.[55] We use this relationship, assuming a temperature coefficient of resistivity of 0.025 °C, to standardize the resistivities to 70 °C. This standardization removes the influence of the geothermal gradient and temperature variations between successive resistivity logs. The influence of temperature on the polarization effect is poorly understood, but it appears to be independent of temperature in samples containing metallic particles over the range of 5−50 °C.[37,55,56] Therefore, it was not accounted for in the IP data.

The QL40-ELOG/IP instrument also measures time-domain IP. Following the application of an electric field, the instrument records the discharge of polarized materials as a decaying voltage at discrete times.[57,58] In the presence of metallic particles, the IP response is generally dominated by the volume of polarizable minerals (e.g., pyrite, pyrrhotite, magnetite, and graphite), with larger chargeability responses associated with larger volumes.[29,59,60] The following IP acquisition parameters were used for each measurement campaign: square-wave current injection (positive-off-negative-off for 2 s each, 8 s total), 450 Hz sampling rate of the voltage during the whole cycle, spatial resolution of 25 cm, and wireline speed of 1.8 m/min.

A common practice is to integrate the decay curve over a definite time interval to obtain the integral chargeability.[29,57,60] Although the integral chargeability cannot be used for quantitative predictions, it has the advantage of smoothing out the noise and can be comparatively assessed along the borehole. Hereafter, we refer to the integral chargeability as chargeability, *M*, for simplicity.

2.3. RTM Chemical Parametrization. The properties of the RTM and the model parametrization are discussed here. These components are outlined in blue in the workflow shown in Figure S1. To assess the processes and physicochemical parameters that control the H_2S mineralization upon the injection of H_2S-charged water, 1D advective RTMs were constructed into the adjacent rock along the boreholes using PHREEQC[61] and the *CarbFix.dat* database.[62,63] This database is adapted from the *core10.dat* database,[64] and it includes revised mineral solubilities (including clays and sulfides) and aqueous species stabilities that are specifically tuned to improve the model accuracy of basalt systems at high temperatures (>90 °C).[62,63]

In this study, we constructed 1D RTMs that incorporate evolving water chemistry and cumulative basaltic glass dissolution along the lateral flow path, given initial water and rock chemistry representing the H_2S injection water, basaltic glass kinetic dissolution rates, host rock porosity and permeability, and reaction time step.[65] The RTM grids, shown in Figure 1, were created by discretizing the NN-3 and NN-4 injection boreholes into layers of 25 m in length. Each layer is treated as an independent 1D RTM. The size and spacing of the grid were based on the availability of chemical data of the host rock and the sensitivity radius of the IP tool (Text S2).[66,67]

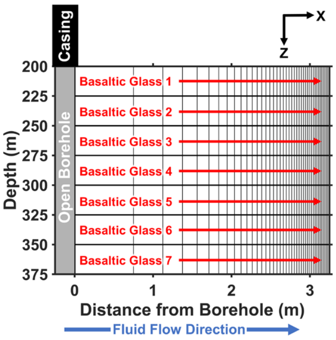

Model Domain	
Number of cells (X)	43
Number of cells (Z)	14 (NN-3), 7 (NN-4)
Fluid per cell	1 L
Basaltic glass RSA	20 cm^2/g
Percent basaltic glass	25%

Solution Compositions	Background		Injection	
	NN-3	NN-4	NN-3	NN-4
pH	9.10	8.50	9.10	8.50
Temperature (°C)	68.0	88.0	72.0	93.0
H_2S (ppm)	0.010	0.010	74.4	76.8
Rate (L/s)	-	-	12.5	149

Figure 1. Diagram of the 1D reactive transport model domain (shown for NN-4) and table of the key model parameters. Additional model parameters are listed in Tables S2 and S3. The host rock (basaltic glass) composition is defined for each of the individual flow models, labeled in red. 1D advective flow is along the *x*-direction, and mixing between the individual models is not considered in the modeling. Cell widths are scaled by 1/*r* to model decreases in the radial flow velocity.

The water flow velocities were calculated using Darcy's law and assuming uniform radial flow. The volumetric flow rate for each layer was determined by scaling the total volumetric injection rate for NN-3 and NN-4 by a mobility factor, which is the permeability of the layer normalized by the total sum of the permeability in the well (Text S3). In PHREEQC, 1D RTMs assume constant velocity along the flow path, so the radial flow velocity was achieved by scaling the cell widths by 1/*r*. These 1D RTMs are beneficial as they can simulate radial flow away from the borehole in a computationally efficient manner, capturing the processes impacting the trends of the bulk geophysical measurements along the borehole.

The basaltic glass host rocks used in the RTMs were represented by the measured bulk composition of drill cuttings collected along the NN-3 and NN-4 boreholes (Table S2). The measured rock compositions were averaged over 25 m-depth intervals (Table S3). The initial background water for each flow model was uniform and had a composition identical with the injection waters measured in NN-3 and NN-4 but with H_2S depleted (Figure 1 and Table S4). This estimate of the initial water composition represents the geothermal wastewater that has been injected since 2004 and is the same wastewater into which the H_2S is dissolved into. The H_2S-charged injection water input into each 1D RTM was assumed to be uniform across each well. The reaction temperature corresponded to an average temperature measured over 1 year for the background water and measured continuously during the 40 days of injection for the H_2S injection water. Details on sampling and analytical approaches of the bulk rock composition and injection water concentrations are given in SI Text S4.

Similar to previous studies modeling basaltic alteration processes,[1,68−70] each of the RTMs incorporated kinetically controlled stoichiometric basaltic glass dissolution with the kinetic rate given by Gíslason & Oelkers (2003).[71] Since the short time frame of H_2S injection between IP measurements is short (40 days) and basaltic glass dissolution is faster than the dissolution of crystalline minerals in basalt,[72,73] we assume that basaltic glass is the primary phase affected most by the reaction of the injection fluid and host rock. Basaltic glass is estimated to be 25% of the matrix volume based on measurements from unaltered hyaloclastites in south and southwest Iceland.[74] The saturation conditions of the dissolving basaltic glass were calculated assuming that the primary phase is a leached layer of amorphous Al-hydroxide and amorphous silica.[75−77] Its reactive surface area (RSA), a parameter generally unknown in natural settings and uncertain in reactive transport modeling,[78−80] was assumed to be 20 cm^2/g of basaltic glass, consistent with previous studies.[25,70] The RSA varies as a function of the porosity and the amount of basaltic glass dissolved, assuming the dissolution of spherical particles.[81] The molar volumes of the alteration minerals were taken from Voigt et al. (2018),[62] and basaltic glass density was assumed to be 2.9 g/cm^3.[2,76]

Alteration minerals allowed to precipitate at local equilibrium following basaltic glass dissolution were chosen based on alteration mineral assemblages from laboratory studies[1,24,82] and observations in low-temperature zones within the subsurface of Nesjavellir (Table S5). They include sulfides (pyrite, pyrrhotite), carbonates (calcite, dolomite, magnesite,

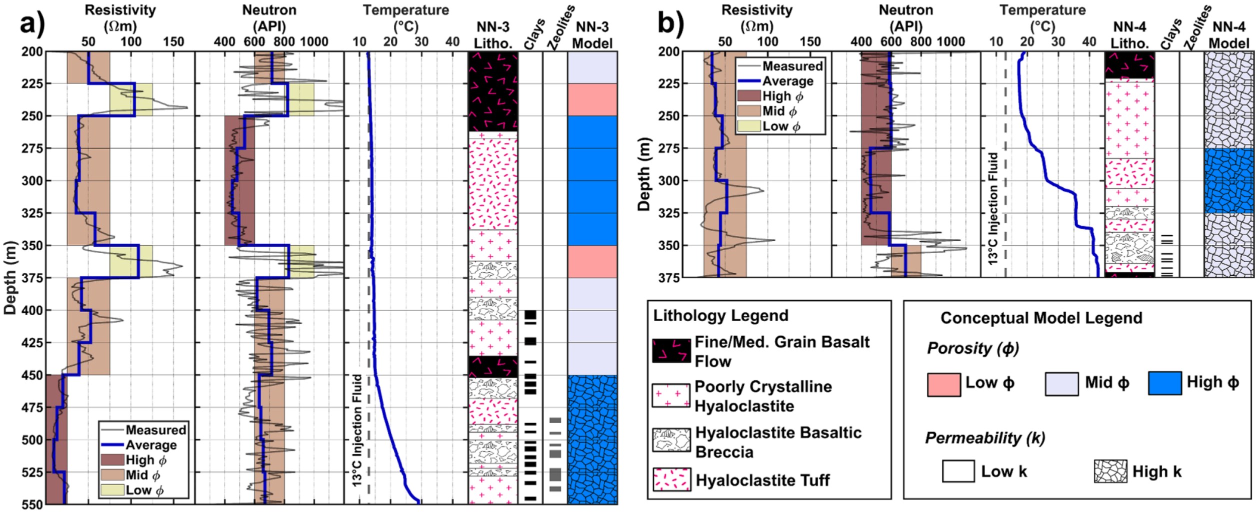

Figure 2. Wireline logging results and drill cutting analysis in NN-3 (a) and NN-4 (b). Wireline logs were collected in September 2020, prior to the start of the H_2S injection. The average resistivity and neutron response are grouped into categories of 5, 15, and 25% porosity (right columns). The temperature logs used for permeability estimates (1×10^{-13} and 1×10^{-11} m^2) were acquired after the cold injection of 13 °C water.[91]

siderite), zeolites (analcime, thomsonite), clay minerals (celadonite, Ca−K−Na−Al−Mg−Fe−vermiculite, Ca−Na−Mg−saponites), and iron hydroxides (goethite).[46,47,83−86] Precipitation kinetics for secondary minerals, which are largely unconstrained, are not incorporated into these RTMs. However, laboratory studies showed a strong correlation between the rate of H_2S mineralization in basaltic systems and the rate of basaltic glass dissolution, suggesting that the basaltic glass dissolution rate is the limiting factor for H_2S mineralization.[1,3]

To compare the results of the RTMs to the geophysical data, we calculated the volume of the secondary sulfides (pyrite and pyrrhotite) formed per unit volume of formation after the injection of H_2S-charged water for 40 days. This value is referred to as the sulfide volume fraction (SVF). We then average the change in SVF over the flow paths, weighted by the distance-dependent electric signal contribution.[67] This provides a single weighted average SVF for each RTM, indicative of the IP response. Hereafter, we refer to this as the IP-equivalent average SVF change. Details on the IP-equivalent average SVF calculations are given in SI Text S2.

2.4. RTM Physical Parametrization.

To parametrize the porosity of the RTM, we utilize the electrical resistivity and neutron wireline logs. These wireline logs provide qualitative data on the porosity[52,87] but have limited ability to define the porosity quantitatively.[87] Empirically derived relationships for porosity have limited applicability in basaltic aquifers, given their calibration to sedimentary formations and the complex relationships observed between porosity, resistivity, and clay content in basalts.[52,87] To assign the relative porosity estimates from the resistivity and neutron logs, we group the measured responses into three categories (low−mid−high) based on their average response over 25 m-depth intervals. Resistivity values are grouped as <25, 25−75, and >75 Ωm, and neutron responses are grouped as <600 API, 600−800 API, and >800 API for high, mid, and low porosities, respectively (Figure 2). We assign porosity estimates of 5, 15, and 25% based on literature values reported at Nesjavellir and in the surrounding Hengill area.[88−90]

The permeability values assigned in the RTMs were determined based on temperature logs from 2001, measured 87 and 45 days after the cold injection of 13 °C water into NN-3 and NN-4, respectively.[91] Temperature changes along the borehole indicate a loss of the cold injection water and inflow of the warmer groundwater, thus highly permeable feed zones. Zones without temperature change indicate low permeability as the injection water does not communicate with the surrounding groundwater.[92] We focus on broad temperature trends over the 25 m borehole intervals and not localized temperature increases, which may indicate fracture-dominated flow paths that facilitate rapid fluid migration outside the near-borehole model domain. Permeabilities were grouped into high (1×10^{-11} m^2) and low (1×10^{-13} m^2) categories based on values reported for basalts in the Hengill area.[1,70,74,93,94] These permeability estimates control the injection water supply to each layer in the RTM, with larger permeabilities facilitating more water flow (SI Text S3).

3. RESULTS AND DISCUSSION

3.1. Wireline Results Parametrizing RTMs.

Two zones of high porosity are defined in NN-3 from 250 to 350 m depth and 450−550 m depth. In these zones, either the average measured resistivity or neutron response falls into high-porosity grouping. Drill cuttings from these intervals agree with the high-porosity assignment as a vesicular, foam-like porous tuff is observed from 250 to 350 m depth, and secondary alteration minerals are present at the bottom of NN-3 (i.e., clays, zeolites),[49] indicative of increased water−rock interactions.[2,95] We assign mid porosity in NN-3 from 200 to 225 and 375 to 450 m depths and low porosity from 225 to 250 and 350 to 375 m depths based on the agreement between the average measured resistivity and neutron responses.

For NN-4, the average measured neutron responses over the 25 m cells are low (<600 API) in the 200−350 m depth range and moderate (∼700 API) in the 350−375 m depth range. Where neutron responses fall near the 600 API threshold value (200−275 and 325−350 m), we assign mid porosities given the moderate resistivities observed throughout the entire well (30−45 Ωm). The neutron response is particularly low from

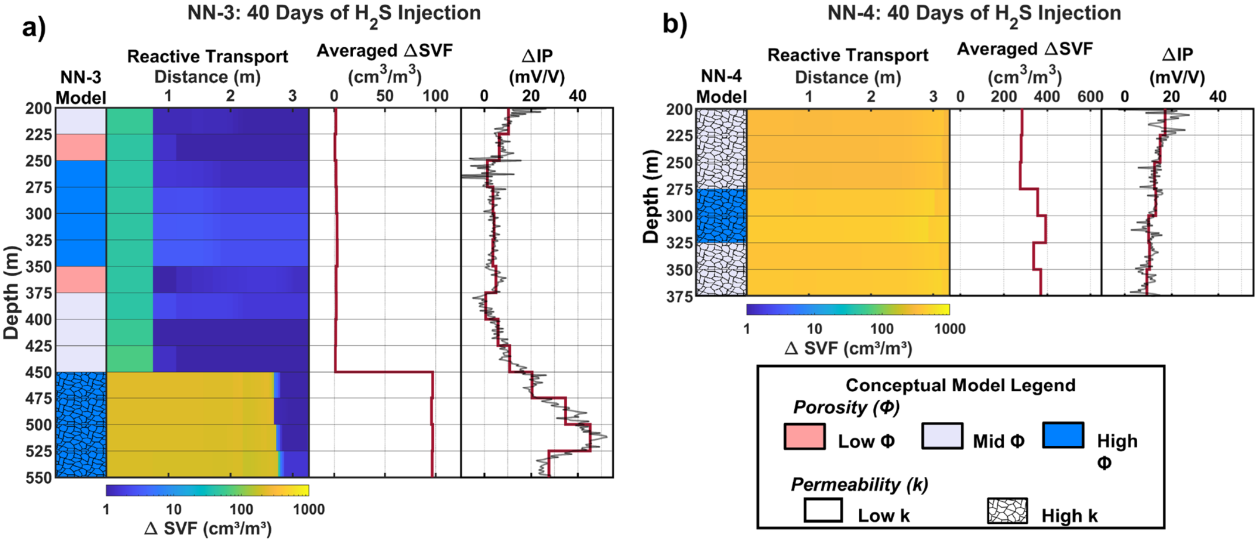

Figure 3. (Left to right) Relative porosity and permeability used in the reactive transport model, together with the change in SVF resulting from the reactive transport modeling along the flow path after 40 days of the H_2S injection. The change in the IP-equivalent average SVF over the flow path takes account of a weighted function describing the dependence of the electric field magnitude on the distance from the borehole.[67] The measured change in chargeability (mV/V) after 40 days of H_2S injection. Results are included for injection wells NN-3 (a) and NN-4 (b).

275 to 325 m depth (~460 API), so we characterize this interval as high porosity. Additionally, drill cuttings from this interval identify a vesicular, foam-like porous tuff similar to the interval from 250 to 350 m depth in NN-3.[49]

The NN-3 temperature profile is characterized by temperatures close to the injection temperature (<15 °C) down to 450 m. Temperatures start increasing beneath the 450 m depth, indicating increased water flow into the borehole (Figure 2). Therefore, low permeabilities were assigned to the depth range of 200−450 m, and high permeabilities were assigned to 450−550 m. The NN-4 temperature log shows an increase in temperature with depth throughout the entire well. A faster and greater temperature recovery in NN-4 (17−43 °C) compared to NN-3 (13−29 °C) indicates higher water flow into NN-4 compared to NN-3.[91] Based on this, high permeabilities were assigned in NN-4.

3.2. Pyrite Formation Mechanisms upon H_2S Injection Revealed by RTMs. The results of the RTM show that under the current injection conditions, pyrite, which is supersaturated in the injection water, readily forms in the first cells (Figure 3). Upon basalt dissolution in the H_2S-charged injection water, the injection-water-sourced S and basalt-sourced Fe allow pyrite formation, following eq 1:

$$\mathrm{FeS_2 + 4H_2O = H^+ + SO_4^{2-} + 4Fe^{2+} + 7HS^-} \qquad (1)$$

The solubility of pyrite is low at the modeled temperature (~70−90 °C) and pH (8.5−9.1) conditions,[96] and pyrite formation is favored over other Fe sulfides. Moreover, pyrite formation is found to be controlled by the supply of Fe (from rock leaching) to the system, which agrees with previous laboratory and modeling studies that found Fe availability to be a limiting factor of H_2S mineralization.[1,2] Pyrite formation occurs prior to Fe oxides and Fe-bearing smectites, suggesting that pyrite formation is efficient and controlled by the supply of Fe (Figure S2). Additionally, the modeled pyrite formation close to the well at the early stages of the water−rock interaction agrees with field observations of rapid pyrite formation from solids recovered from an airlift pump of an injection well during the Carbfix1 CO_2−H_2S injection.[16]

As the reactive water flows through the model, the S supply from the H_2S-charged water decreases due to pyrite precipitation (Figure S3). Continuous dissolution of basaltic glass and accompanied alteration mineral precipitation ultimately lead to an increase in pH (and decrease in redox potential) over the flow path and favorable conditions for the precipitation of Fe-smectites, goethite, and pyrrhotite. Pyrrhotite, smectite, and goethite formation are most extensive in low-permeability zones, where the water interacts with larger amounts of basaltic glass in each time step (i.e., low water−rock ratios; Figure S2). Zeolite formation is also most extensive at low water−rock ratios.

3.3. Coupling RTMs and Wireline Responses to Monitor Subsurface H_2S Mineralization. Comparing trends in the change in sulfide volume fraction observed in the RTM to the IP results of NN-3 after 40 days of H_2S injection, we observe a general agreement between the two methods across many intervals of the borehole. The largest change in SVF IP-equivalent average ~100 cm^3/m^3) and the largest increases in the chargeability response (10−50 mV/V) are observed at the bottom of NN-3, where permeability was estimated to be the highest. This suggests that under the current injection conditions of NN-3, sulfide mineralization is controlled largely by permeability, with sulfide formation occurring dominantly in intervals with an increased supply of injection water. Compared to permeability, porosity exhibits less control on sulfide formation in the NN-3 RTM.

In NN-4, the measured chargeability increases over the entire borehole, trending from ~17 mV/V at 200 m depth to ~10 mV/V at 375 m depth. The modeled change in SVF in the NN-4 RTM also shows an increase in values over the entire borehole and flow path, supporting the assumption of an evenly distributed water flow (i.e., uniform RTM permeability) throughout the NN-4 intervals. The higher injection rate into NN-4 compared to NN-3 sustains H_2S mineralization over the entire RTM flow path.

After 40 days of injection, half of the injected H_2S into NN-4 is mineralized in the near-borehole model. Lower flow rates around NN-3 result in the complete mineralization of the injected H_2S near the NN-3 borehole over 40 days of injection. This increased localization of H_2S mineralization around NN-3 relative to NN-4 could help to explain why the largest measured increase in the IP response in NN-3 is 50 mV/V compared with 17 mV/V in NN-4. While these estimates on mineralization efficiency are uncertain due to model simplifications (e.g., no groundwater mixing, single porosity medium), comparing their relative values provides insight into the IP response changes.

The modeled SVF is larger in NN-4 compared to NN-3 due to the larger fluid supply in NN-4. Additionally, higher injection water temperatures in NN-4 compared to NN-3 (93 vs 72 °C) result in faster basalt glass dissolution rates in NN-4, contributing to the higher magnitude changes in SVF near the borehole (Figure S4). The highest SVF change among the first cells is 235 cm^3/m^3 in NN-3 (450−475 m), compared to 540 cm^3/m^3 in NN-4 (300−325 m).

While agreement between the change in SVF predicted by the RTM and changes in chargeability exists in the intervals detailed above, discrepancies in other intervals illustrate the necessity to further constrain RTM parameters, particularly the porosity and permeability values along the boreholes. A moderate chargeability increase (∼10 mV/V) observed from 200 to 225 m in NN-3 could indicate higher permeability in this zone rather than the low value assigned in the RTM. This is in accordance with ambient temperature logs of NN-3 that identify an inflow of warm water at 200 m, attributed to wastewater disposed of in nearby shallow wells.[91] In NN-4, the change in IP response slightly decreases with depth while the change in the IP-equivalent average SVF slightly increases with depth. The RTM trend is partially explained by larger porosities in the RTM from 275 to 325 m depth, which increases the reactive surface areas in this interval, leading to increased basaltic glass dissolution and Fe supply. Additionally, variations in the basaltic glass composition contribute more basalt-sourced S and promote faster dissolution rates, resulting in elevated SVF changes near the bottom of NN-4 (Figure S5). However, variations in the basaltic glass compositions have little impact on the H_2S mineralization efficiency, particularly at early stages of basaltic glass alteration (high water−rock ratios) (Figure S6).

These discrepancies highlight the challenges of using simplified RTMs to quantitatively model system dynamics. First, mixing of water with ambient groundwater is not considered in these RTMs. Mixing could change the water composition and temperature along the borehole, impacting secondary minerals' kinetic rates and saturation. Next, single porosity advection flow RTMs simplify the hydrologic model and do not capture complex flow structures (e.g., isolated fracture networks and variable tortuosity). However, given the small flow path modeled here and the large fluid flow in proximity to the injection wells, advection-dispersion models are found to produce similar results to the advection-only model (Figure S7). Lastly, reaction rates are challenging to incorporate into RTMs as kinetic precipitation rates are often unconstrained and reactive surface areas are often site-specific values and difficult to determine for field studies.[79,80] In fact, RTMs utilizing kinetically controlled pyrite precipitation and a range of reactive surface areas from literature[79,97] recover similar distributions of H_2S mineralization along the flow path but a 19% difference in the IP-equivalent average SVF (Figure S8). However, we find that the IP-equivalent average SVF change of the equilibrium model used in this study falls between the range of values recovered in the kinetic models, suggesting that the equilibrium-driven precipitation of sulfides is a relevant approximation that adds computational efficiency.

Challenges with linking RTM and IP also arise from complexities in the IP response, such as variable sulfide grain size/shape and clay contributions.[37,57,98] Influences of metallic mineral grain connectivity and size/shape distributions on chargeability is the subject of ongoing research and the influences are often not considered in the final interpretation.[60,99] Smectite clay, a common secondary mineral in basaltic rocks at temperatures <100 °C,[84,85,100] is predicted to precipitate in our model (Figure S2) and can also impact the IP response. Elevated smectite content can decrease the chargeability response as interfoliar current flow increases conduction (reducing resistivity) and decreases the material's ability to build charge.[37,98] However, outside of a few isolated zones in NN-3 (225−250 m, 350−375 m, and 400−425 m depths), resistivities remain unchanged since the start of injection, suggesting the limited influence of smectites on the bulk electrical properties upon 40 days of H_2S injection (Figure S9). Clays can also decrease the neutron response,[52] and indeed, the average neutron response decreases by 81 API after 40 days of H_2S injection in NN-3 (Figure S9). However, a similar decrease is not observed in NN-4.

3.4. Parameters Influencing Sulfide Formation.

Physical Parameters and Heterogeneity. Additional RTMs were constructed to better understand how radial heterogeneity in porosity and permeability impact the H_2S mineralization along the flow path and contribute to discrepancies between the RTM results and the measured IP response changes (Figure 4). These models are based on the NN-3 model from 525 to 550 m depths (25% porosity, 1 ×

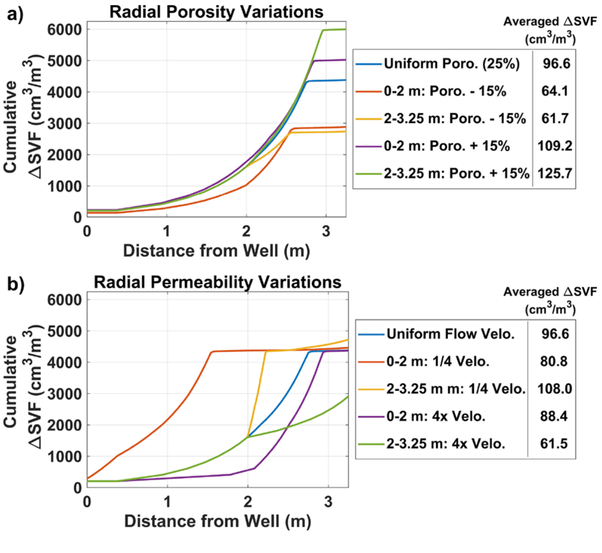

Figure 4. Effects of (a) porosity and (b) permeability heterogeneity on the cumulative change in SVF and the IP-equivalent average SVF change. The porosity and permeability values are adjusted from the 1D reactive transport model of NN-3, 525−550 m depth, which assumed uniform porosity and permeability along the flow path. Changes in the matrix permeability are modeled via the flow velocity.

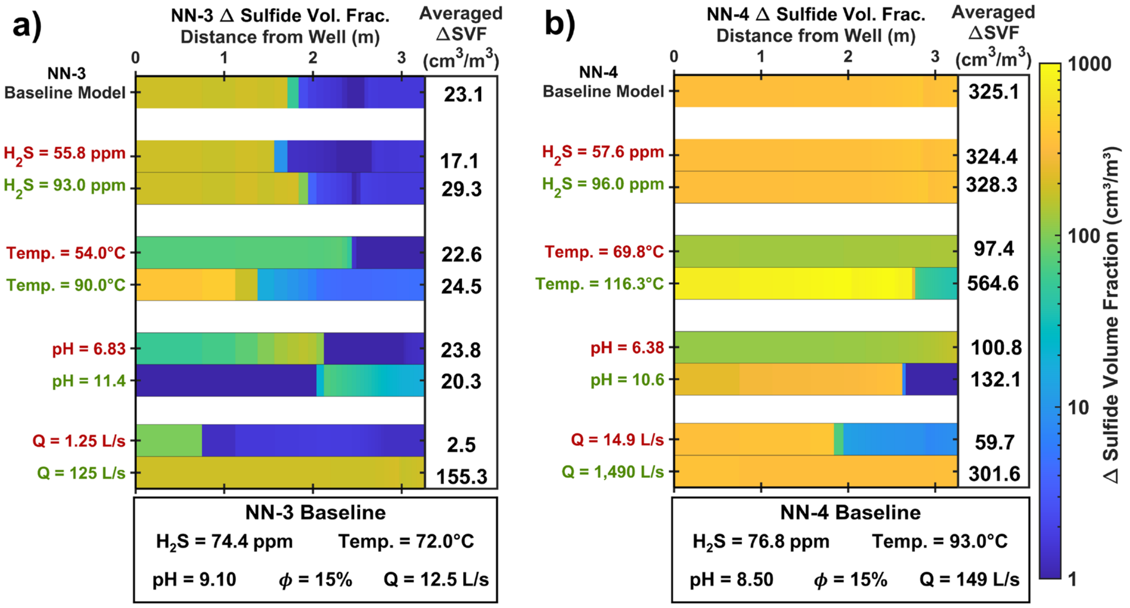

Figure 5. Row 1 of each figure illustrates changes in SVF predicted in the RTM of NN-3 and NN-4 with input data defined in the legend below the plots (measured dissolved H_2S, pH, and injection water temperature, average basaltic glass composition across the entire borehole, midestimate porosity, and the well injection rates with even allocation of the injection water to each model layer). The additional rows show the change in SVF predicted by RTMs with a single parameter varied, as displayed along the y-axis. The chemical parameters are varied by −25% (red) and +25% (green) of the measured values.

10^{-11} m^2 permeability), and they utilize different porosity or permeability values assigned from 0 to 2 m and 2 to 3.25 m along the flow path (for example, porosity = 25% from 0 to 2 m and 10% from 2 to 3.25 m).

Porosity heterogeneity was simulated by increasing or decreasing the porosity of the uniform model (25% in NN-3, 525−550 m depth) by 15% while maintaining constant flow velocities. These simulations reveal that the porosity has a minimal influence on the distribution of H_2S along the flow path (Figure 4). However, larger porosities result in larger cumulative change in SVF, particularly toward the end of the flow path as the water residence times are greater further from the well. The larger SVF changes in the high-porosity system arises from increased RSAs, thereby increasing the supply of basalt-sourced Fe in these high porosity zones. Additionally, larger porosities increase the supply of water-sourced S to the system, thus increasing the total change in SVF over the flow path.

The water flow velocity from the NN-3, 525−550 m depth model (11.7 m/day at the wellbore) is increased and decreased by a factor of 4 to simulate radial heterogeneity in the permeability along the flow path. Due to the short lateral flow path, smaller lateral permeability variations are used here compared to the variations assigned to the field model (Section 2.4) to mimic small variations that occur within the stratigraphic unit. The modeling reveals that permeability heterogeneity influences both the distribution of H_2S mineralization and the cumulative change in the SVF over the flow path. In the uniform flow velocity model (NN-3, from 525 to 550 m depth), all the water-sourced S is mineralized before 2.75 m along the flow path, indicated by the plateau in the cumulative SVF change at ∼4400 cm^3/m^3. Cumulative SVF change greater than 4400 cm^3/m^3, observed when flow velocity is low at flow distances of 2 to 3.25 m, is due to H_2S mineralization from basalt-sourced S resulting from longer water residence times. Decreasing the flow velocity also results in a more rapid H_2S mineralization along the flow path. Conversely, increasing the water flow velocity at the start of the flow path (0 to 2 m) limits H_2S mineralization in the first 2 m along the flow path. Large flow velocity from 2 to 3.25 m along the flow path decreases the cumulative change in SVF to below 3000 cm^3/m^3 as not all the water-sourced S mineralizes over the 3.25 m flow path. These results suggest that low-permeability zones near the borehole are most at risk of pore clogging due to enhanced secondary mineralization in these zones.

Permeability heterogeneity also impacts the IP-equivalent average of the SVF change and thus likely contributes to discrepancies between the RTM-predicted H_2S mineralization and the measured IP responses (Figure 3). Since ∼60% of the measured IP signal comes from distances 0.5 to 2 m (Text S2), H_2S mineralization at this distance range has the most impact on the IP-equivalent average SVF change. For example, most of the H_2S mineralization occurs at 1 to 2.25 m in the model with reduced flow velocities at 2 to 3.25 m, resulting in the largest IP-equivalent average SVF change of 126 cm^3/m^3. Comparatively, the model with reduced flow velocity from 0 to 2 m along the flow path has a lower IP-equivalent average SVF change due to larger amounts of H_2S mineralization at 0 to 0.5 m, where the IP tool is less sensitive to changes. The models with increased flow rates at 0 to 2 and 2 to 3.25 m also result in lower IP-equivalent average SVF changes as H_2S mineralization occurs further into the formation.

Chemical Parameters. To better understand the mechanisms controlling sulfide formation in our RTM, the effects of water chemical parameters (temperature, H_2S concentration, and pH) on the magnitude and distribution of sulfide formation were investigated (Figure 5). The values are compared to baseline model results, consisting of the measured injection water parameters, 15% porosity (midestimate value), and well injection rates with injection water evenly distributed to each model layer. Overall, the IP-equivalent average change in SVF in NN-3 is less sensitive to parameter changes than that in NN-4. This is because the fluid supply is less in NN-3 compared to that in NN-4, which limits the influence of the fluid chemical parameters on the system.

Variations in the basaltic glass chemical compositions have little influence on the magnitude of the SVF change in NN-3 but influence SVF changes in NN-4 (Figure S5). In NN-4, faster basaltic glass dissolution rates (primarily from higher injection water temperatures) and larger water flow than NN-3 increase the water−rock interactions over the entire flow path. This enhances the influence of basaltic glass composition on the resulting secondary mineralogy.

Changes in the H_2S concentration of the injection water do not influence sulfide mineralization near the NN-4 borehole (Figure 5). The large flow rates sustain sulfide precipitation over the entire flow path for every modeled H_2S concentration, suggesting that the basaltic glass dissolution rate (Fe supply) is the limiting factor in the magnitude of H_2S sequestration in NN-4. In NN-3, increasing the water's H_2S concentration by 25% from the baseline value results in a 29% increase in the IP-equivalent average SVF change as sulfides form further into the formation. However, at short flow distances (<1.5 m), the H_2S concentration does not influence the magnitude of sulfide precipitation. This illustrates that total sulfide mineralization near the NN-3 borehole is controlled by both the water supply and the basaltic glass dissolution rates. The H_2S itself is found to have minimal influence on the rate of basaltic glass dissolution (<2% rate change) (Figure S4).

The basaltic glass dissolution rates strongly depend on the temperature and pH of the reacting water (Figure S4).[71] Decreasing the temperature by 25% from the measured values results in slower basaltic glass dissolution and a more limited Fe supply. This decreases the IP-equivalent average sulfide mineralization by 2% in NN-3 and 70% in NN-4. Since the H_2S supply is larger in NN-4, the limited Fe supply at lower temperatures has a larger relative impact on the IP-equivalent average sulfide mineralization. These model results of decreased H_2S mineralization at lower temperatures are consistent with lab studies showing more limited H_2S mineralization at temperatures ~100 °C compared to higher temperatures (200−250 °C).[1]

The change in the injection water pH from circumneutral to alkaline results in faster basaltic glass dissolution (Figure S4). The faster dissolution reflects the pH dependence of the basaltic glass dissolution rate established in Gislason and Oelkers (2003), with progressively faster rates as pH increases and decreases from pH = 5 at temperatures near 100 °C. However, the faster basaltic glass dissolution from the increased pH does not equate to larger changes in SVF for both boreholes. In NN-3, large pH values of 11.4 (measured pH + 25%) limit sulfide mineralization at the injection inlet, as pyrite is more soluble at this high pH value.[96] A slightly lower pH of 10.4 in NN-4 enables sulfide mineralization near the injection borehole but at quantities lower than those of the baseline model. This illustrates that the influence of pH conditions on both the dissolution rate and pyrite solubility must be considered to achieve the most efficient mineralization of H_2S.

Well Injection Rate. Changes to the injection water supply greatly control the magnitude of sulfide precipitation along the flow path for both models. For NN-3, an order of magnitude increase in the injection water volumetric rate sustains sulfide precipitation over the entire flow path, thus greatly increasing the IP-equivalent average SVF change (+132 cm^3/m^3) from that of the baseline model. This aligns with the findings of the NN-3 RTM (Figure 3), where sulfide mineralization is largely controlled by the water supply (i.e., permeability of each layer and the well injection rate).

Similar to the impact of the H_2S concentration in NN-4, increasing the injection water supply by an order of magnitude does not increase the IP-equivalent average SVF change in NN-4. The increased water flow results in a slight decrease in the IP-equivalent average SVF change (325 vs 301 cm^3/m^3), attributed to slower basaltic glass dissolution from slightly lower pH values maintained over the flow path. The reduced pH results from the fast water flow, which limits the time for water−rock interactions along the flow path. These results further suggest that the Fe supply is the limiting factor in the magnitude of sulfide mineralization when injection rates are large (~hundreds of L/s).

4. IMPLICATIONS FOR IP AND RTM FIELD-SCALE MONITORING

Validation of RTM-predicted trends by IP trends observed after 40 days of H_2S injection suggests that coupling IP wireline logging with RTM can advance the monitoring of H_2S mineral storage within basaltic reservoirs in Iceland and abroad. The RTMs add spatial and temporal dimensions to the IP survey and provide valuable insight into the parameters influencing the magnitude and distribution of sulfide mineralization.

While RTMs help to understand trends in the IP response, discrepancies between the RTM and geophysical IP responses and the lack of a quantitative link between the SVF and chargeability changes highlight challenges in the current application of this joint monitoring approach. Furthermore, this study does not address the long-term stability of sulfides following H_2S injection as assessed with subsequent monitoring data presented in Lévy et al. (2024)[101] To strengthen the joint use of IP and RTM as a monitoring technique and assess the long-term stability of H_2S mineralization, more complex models are required that incorporate, e.g., measured dissolved oxygen levels to understand how leakage impacts the system, interactions with oxidizing microbes,[102,103] and retroaction between flow parameters and mineral dissolution/precipitation. Additionally, constraining water flow parameters through direct measurements would reduce uncertainty in the RTM. Lastly, joint geochemical and geophysical monitoring approaches would benefit from a data-based link between site-specific geochemical and geophysical information through direct measurements of the water composition[15,17] and rock alteration.[104,105] These measurements reduce critical RTM uncertainties and validate the geophysical responses, which can then be extrapolated over larger areas with expanded RTMs and geophysical surveying. With these additional constraints, joint IP and RTM interpretation represents a scalable, noninvasive, and cost-effective approach for monitoring H_2S mineralization.

■ ASSOCIATED CONTENT

Data Availability Statement

The data underlying this study are openly available in a Zenodo repository at doi: 10.5281/zenodo.10076311 upon publication.

Supporting Information

The Supporting Information is available free of charge at https://pubs.acs.org/doi/10.1021/acs.est.3c10139.

> (Text S1) Nesjavellir power station wastewater and injection system background; (Text S2) further details on the calculation of the sulfide volume fraction and the weighted averaging function applied to the change in sulfide volume fraction; (Text S3) derivation of the well mobility; (Text S4) complete methodology of the injection water and bulk rock chemical analysis; (Table S1) details on the NN-3 and NN-4 injection wells; (Table S2) basaltic glass whole rock composition; (Table S3) basaltic glass formulas utilized in the RTMs; (Table S4) measured injection water chemistry; (Table S5) chemical formulas of the secondary alteration minerals allowed to precipitate in the RTMs; (Figure S1) the workflow outlining the joint application of geophysical methods and reactive transport modeling to study H_2S mineralization; (Figure S2) the volume fraction of all secondary minerals from the NN-3 and NN-4 RTMs; (Figure S3) relative source of S upon progressive basaltic glass dissolution; (Figure S4) basaltic glass dissolution rates for the various RTMs; (Figure S5) sulfide formation predicted by RTMs with homogeneous basaltic glass composition; (Figure S6) percentage of total S mineralized upon basaltic glass alteration in reaction path models constructed for all measured basaltic glass compositions in NN-3 and NN-4; (Figure S7) impact of advective transport flow schemes compared to advective-dispersive transport schemes on the change in sulfide volume fraction; (Figure S8) impact of pyrite kinetic precipitation rates on the expected change in sulfide volume fraction compared to RTMs that allow pyrite to mineralize to equilibrium; (Figure S9) and changes in resistivity, neutron, and IP wireline response after 40 days of H_2S-charged water injection (PDF)

■ AUTHOR INFORMATION

Corresponding Author

Daniel A. Ciraula − *Nordic Volcanological Center, Institute of Earth Sciences, University of Iceland, Reykjavík 101, Iceland;* orcid.org/0000-0003-4884-5291; Email: danielac@hi.is

Authors

Barbara I. Kleine-Marshall − *GeoZentrum Nordbayern, Friedrich-Alexander-Universität, Erlangen-Nuremberg 91054, Germany*

Iwona M. Galeczka − *ÍSOR-Iceland Geosurvey, Kópavogur 203, Iceland; Carbfix, Reykjavík 110, Iceland*

Léa Lévy − *ÍSOR-Iceland Geosurvey, Kópavogur 203, Iceland; Engineering Geology, Lund University, Lund SE-221 00, Sweden;* orcid.org/0000-0001-5214-467X

Complete contact information is available at:
https://pubs.acs.org/10.1021/acs.est.3c10139

Notes

The authors declare no competing financial interest.

■ ACKNOWLEDGMENTS

Project funding was provided by the Nordic Volcanological Center (NordVulk) and contributions from the Icelandic Centre for Research (Rannís) to GEMGAS (grant no. 198637-0611). The authors would like to thank Orkuveita Reykjavíkur for giving access to injection wells and drill cuttings used in this study. Íris Eva Einarsdóttir (Orkuveita Reykjavíkur) is thanked for her assistance during fluid sampling at Nesjavellir. Thomas Ratouis (CarbFix) is thanked for providing information on the injection infrastructure at Nesjavellir. The authors also would like to thank Íslenskar Orkurannsóknir (ÍSOR) for collecting the logging data, in particular SigurÐur GarÐar Kristinsson for discussions on temperature log interpretations, and Helga Margrét Helgadóttir and Sveinborg Hlíf Gunnarsdóttir for organization and assistance during collection of well cuttings. The authors also thank Samuel Scott, Walt McNab, and Jesús Carrera for discussing reactive transport design and parameters. Editor Greg Lowry is thanked for careful editorial handling. The manuscript has been greatly improved by the reviews and suggestions of two anonymous reviewers.

■ ABBREVIATIONS

Al: aluminum
API: American Petroleum Institute industrial standard unit
Ca: calcium
CO_2: carbon dioxide
Fe: iron
H_2S: hydrogen sulfide
IP: induced polarization
K: potassium
M: chargeability
Mg: magnesium
Na: sodium
RSA: reactive surface area
RTM: reactive transport model
S: sulfur
SVF: sulfide volume fraction
1D: one-dimensional

■ REFERENCES

(1) Přikryl, J.; Marieni, C.; GuÐbrandsson, S.; Aradóttir, E. S.; Gunnarsson, I.; Stefánsson, A. H2S Sequestration Process and Sustainability in Geothermal Systems. *Geothermics* **2018**, *71*, 156.

(2) Stefánsson, A.; Arnórsson, S.; Gunnarsson, I.; Kaasalainen, H.; Gunnlaugsson, E. The Geochemistry and Sequestration of H2S into the Geothermal System at Hellisheidi, Iceland. *Journal of Volcanology and Geothermal Research* **2011**, *202* (3−4), 179.

(3) Marieni, C.; Přikryl, J.; Aradóttir, E. S.; Gunnarsson, I.; Stefánsson, A. Towards 'Green' Geothermal Energy: Co-Mineralization of Carbon and Sulfur in Geothermal Reservoirs. *International Journal of Greenhouse Gas Control* **2018**, *77*, 96.

(4) WHO. *Hydrogen Sulfide*. World Health Organization, Environmental Health Criteria, No. 19 1981.

(5) Greaver, T. L.; Sullivan, T. J.; Herrick, J. D.; Barber, M. C.; Baron, J. S.; Cosby, B. J.; Deerhake, M. E.; Dennis, R. L.; Dubois, J.-J. B.; Goodale, C. L.; Herlihy, A. T.; Lawrence, G. B.; Liu, L.; Lynch, J. A.; Novak, K. J. Ecological Effects of Nitrogen and Sulfur Air Pollution in the US: What Do We Know? *Front. Ecol. Environ.* **2012**, *10*, 365.

(6) Danzon, M. A.; Van Leeuwen, F. X. R.; Krzyzanowski, M. Air Quality Guidelines: For Europe. *World Health Organization Regional Publications - European Series*, **2001**.

(7) *Iceland Ministry of the Environment, Energy and Climate, Regulation No. 514/2010*; 2010.

(8) Mamrosh, D. L.; McIntush, K. E.; Douglas, A.; Fisher, K. S.; Júlíusson, B. M.; Gunnarsson, I.; Markússon, S. H.; Matthíasdóttir, K. V.; Arnarson, M. P. Removal of Hydrogen Sulfide and Recovery of Carbon Dioxide from Geothermal Non-Condensable Gas Using Water. In *Transactions - Geothermal Resources Council*; 2014; Vol. *38*.

(9) Gysi, A. P.; Stefánsson, A. Numerical Modelling of CO2-Water-Basalt Interaction. *Mineral Mag* **2008**, *72* (1), 55.

(10) Matter, J. M.; Stute, M.; Snæbjörnsdóttir, S.; Oelkers, E. H.; Gíslason, S. R.; Aradóttir, E. S.; Sigfusson, B.; Gunnarsson, I.; SigurÐardóttir, H.; Gunnlaugsson, E.; Axelsson, G.; Alfredsson, H. A.; Wolff-Boenisch, D.; Mesfin, K.; De La Reguera Taya, D. F.; Hall, J.; Dideriksen, K.; Broecker, W. S. Rapid Carbon Mineralization for Permanent Disposal of Anthropogenic Carbon Dioxide Emissions. *Science* **2016**, *352* (6291), 1312.

(11) Galeczka, I. M.; Stefánsson, A.; Kleine, B. I.; Gunnarsson-Robin, J.; Snæbjörnsdóttir, S. Ó.; Sigfússon, B.; Gunnarsdóttir, S. H.; Weisenberger, T. B.; Oelkers, E. H. A Pre-Injection Assessment of CO2 and H2S Mineralization Reactions at the Nesjavellir (Iceland) Geothermal Storage Site. *International Journal of Greenhouse Gas Control* **2022**, *115*, 103610.

(12) Snæbjörnsdóttir, S. Ó.; Galeczka, I. M.; Sigfússon, B.; Oelkers, E. H. Injection of Geothermal CO2 and H2S Gases at the Nesjavellir Site, SW Iceland: A Pre-Injection Overview. In *Proceedings World Geothermal Congress 2021*; Reykjavík, Iceland, 2021.

(13) Marieni, C.; Voigt, M.; Clark, D. E.; Gíslason, S. R.; Oelkers, E. H. Mineralization Potential of Water-Dissolved CO2 and H2S Injected into Basalts as Function of Temperature: Freshwater versus Seawater. *International Journal of Greenhouse Gas Control* **2021**, *109*, 103357.

(14) Clark, D. E.; Gunnarsson, I.; Aradóttir, E. S.; Arnarson, M. P.; Þorgeirsson, Þ. A.; SigurÐardóttir, S. S.; Sigfússon, B.; Snæbjörnsdóttir, S.; Oelkers, E. H.; Gíslason, S. R. The Chemistry and Potential Reactivity of the CO2-H2S Charged Injected Waters at the Basaltic CarbFix2 Site, Iceland. *Energy Procedia* **2018**, *146*, 121.

(15) Clark, D. E.; Oelkers, E. H.; Gunnarsson, I.; Sigfússon, B.; Snæbjörnsdóttir, S.; Aradóttir, E. S.; Gíslason, S. R. CarbFix2: CO2 and H2S Mineralization during 3.5 years of Continuous Injection into Basaltic Rocks at More than 250 °C. *Geochim. Cosmochim. Acta* **2020**, *279*, 45.

(16) Snæbjörnsdóttir, S. Ó.; Oelkers, E. H.; Mesfin, K.; Aradóttir, E. S.; Dideriksen, K.; Gunnarsson, I.; Gunnlaugsson, E.; Matter, J. M.; Stute, M.; Gíslason, S. R. The Chemistry and Saturation States of Subsurface Fluids during the in Situ Mineralisation of CO2 and H2S at the CarbFix Site in SW-Iceland. *International Journal of Greenhouse Gas Control* **2017**, *58*, 87.

(17) Gunnarsson, I.; Aradóttir, E. S.; Oelkers, E. H.; Clark, D. E.; Arnarson, M. P.; Sigfússon, B.; Snæbjörnsdóttir, S.; Matter, J. M.; Stute, M.; Júlíusson, B. M.; Gíslason, S. R. The Rapid and Cost-Effective Capture and Subsurface Mineral Storage of Carbon and Sulfur at the CarbFix2 Site. *International Journal of Greenhouse Gas Control* **2018**, *79*, 117.

(18) Galeczka, I. M.; SigurÐsson, G.; Eiríksdóttir, E. S.; Oelkers, E. H.; Gíslason, S. R. The Chemical Composition of Rivers and Snow Affected by the 2014/2015 BárÐarbunga Eruption, Iceland. *J. Volcanol. Geotherm. Res.* **2016**, *316*, 101−119.

(19) Flaathen, T. K.; Gíslason, S. R. The Effect of Volcanic Eruptions on the Chemistry of Surface Waters: The 1991 and 2000 Eruptions of Mt. Hekla, Iceland. *Journal of Volcanology and Geothermal Research* **2007**, *164* (4), 293.

(20) Floor, G. H.; Calabrese, S.; Román-Ross, G.; D'Alessandro, W.; Aiuppa, A. Selenium Mobilization in Soils Due to Volcanic Derived Acid Rain: An Example from Mt Etna Volcano, Sicily. *Chem. Geol.* **2011**, *289* (3−4), 235.

(21) Delmelle, P.; Maters, E.; Oppenheimer, C. Chapter 50 - Volcanic Influences on the Carbon, Sulfur, and Halogen Biogeochemical Cycles. In *The Encyclopedia of Volcanoes*, 2015.

(22) Cuoco, E.; Tedesco, D.; Poreda, R. J.; Williams, J. C.; De Francesco, S.; Balagizi, C.; Darrah, T. H. Impact of Volcanic Plume Emissions on Rain Water Chemistry during the January 2010 Nyamuragira Eruptive Event: Implications for Essential Potable Water Resources. *J. Hazard Mater.* **2013**, *244−245*, 570.

(23) Aiuppa, A.; Bellomo, S.; Brusca, L.; D'Alessandro, W.; Di Paola, R.; Longo, M. Major-Ion Bulk Deposition around an Active Volcano (Mt. Etna, Italy). *Bull. Volcanol* **2006**, *68* (3), 255.

(24) Schaef, H. T.; McGrail, B. P.; Owen, A. T.; Arey, B. W. Mineralization of Basalts in the CO2-H2O-H2S System. *International Journal of Greenhouse Gas Control* **2013**, *16*, 187.

(25) Bacon, D. H.; Ramanathan, R.; Schaef, H. T.; McGrail, B. P. Simulating Geologic Co-Sequestration of Carbon Dioxide and Hydrogen Sulfide in a Basalt Formation. *International Journal of Greenhouse Gas Control* **2014**, *21*, 165.

(26) Lévy, L.; Thalund-Hansen, R.; Bording, T.; Fiandaca, G.; Christiansen, A. V.; Rügge, K.; Tuxen, N.; Hag, M.; Bjerg, P. L. Quantifying Reagent Spreading by Cross-Borehole Electrical Tomography to Assess Performance of Groundwater Remediation. *Water Resour. Res.* **2022**, *58* (9), No. e2022WR032218.

(27) Falzone, S.; Robinson, J.; Slater, L. Characterization and Monitoring of Porous Media with Electrical Imaging: A Review. *Transp Porous Media* **2019**, *130* (1), 251.

(28) Wong, J. An Electrochemical Model of the Induced-Polarization Phenomenon in Disseminated Sulfide Ores. *Geophysics* **1979**, *44* (7), 1245.

(29) Revil, A.; Florsch, N.; Mao, D.; et al. Induced polarization response of porous media with metallic particles — Part 1: A theory for disseminated semiconductors. *Geophysics* **2015**, *80* (5), D525.

(30) Ntarlagiannis, D.; Williams, K. H.; Slater, L.; Hubbard, S. Low-Frequency Electrical Response to Microbial Induced Sulfide Precipitation. *J. Geophys. Res.: Biogeosci.* **2005**, *110* (G2), G02009.

(31) Williams, K. H.; Ntarlagiannis, D.; Slater, L. D.; Dohnalkova, A.; Hubbard, S. S.; Banfield, J. F. Geophysical Imaging of Stimulated Microbial Biomineralization. *Environ. Sci. Technol.* **2005**, *39* (19), 7592.

(32) Saneiyan, S.; Ntarlagiannis, D.; Werkema, D. D.; Ustra, A. Geophysical Methods for Monitoring Soil Stabilization Processes. *J. Appl. Geophy* **2018**, *148*, 234.

(33) Wu, Y.; Ajo-Franklin, J. B.; Spycher, N.; Hubbard, S. S.; Zhang, G.; Williams, K. H.; Taylor, J.; Fujita, Y.; Smith, R. Geophysical Monitoring and Reactive Transport Modeling of Ureolytically-Driven Calcium Carbonate Precipitation. *Geochem. Trans.* **2011**, *12*, 7.

(34) Wu, Y.; Hubbard, S.; Williams, K. H., Ajo-Franklin, J.; On the complex conductivity signatures of calcite precipitation. *J. Geophys. Res.: Biogeosci.* **2010**, *115* (G2).

(35) Wu, Y.; Slater, L.; Versteeg, R.; LaBrecque, D. A Comparison of the Low Frequency Electrical Signatures of Iron Oxide versus Calcite Precipitation in Granular Zero Valent Iron Columns. *J. Contam Hydrol* **2008**, *95* (3−4), 154.

(36) Wu, Y.; Versteeg, R.; Slater, L.; LaBrecque, D. Calcite Precipitation Dominates the Electrical Signatures of Zero Valent Iron Columns under Simulated Field Conditions. *J. Contam Hydrol* **2009**, *106* (3−4), 131.

(37) Lévy, L.; Maurya, P. K.; Byrdina, S.; Vandemeulebrouck, J.; Sigmundsson, F.; Árnason, K.; Ricci, T.; Deldicque, D.; Roger, M.; Gibert, B.; Labazuy, P. Electrical Resistivity Tomography and Time-Domain Induced Polarization Field Investigations of Geothermal Areas at Krafla, Iceland: Comparison to Borehole and Laboratory Frequency-Domain Electrical Observations. *Geophys J. Int.* **2019**, *218* (3), 1469.

(38) Flores-Orozco, A.; Williams, K. H.; Long, P. E.; Hubbard, S. S.; Kemna, A. Using Complex Resistivity Imaging to Infer Biogeochemical Processes Associated with Bioremediation of an Uranium-Contaminated Aquifer. *J. Geophys. Res.: Biogeosci.* **2011**, *116* (3).

(39) Saneiyan, S.; Ntarlagiannis, D.; Ohan, J.; Lee, J.; Colwell, F.; Burns, S. Induced Polarization as a Monitoring Tool for In-Situ Microbial Induced Carbonate Precipitation (MICP) Processes. *Ecol Eng.* **2019**, *127*, 36.

(40) Flores-Orozco, A.; Williams, K. H.; Kemna, A. Time-Lapse Spectral Induced Polarization Imaging of Stimulated Uranium Bioremediation. *Near Surface Geophysics* **2013**, *11* (5), 531.

(41) Williams, K. H.; Kemna, A.; Wilkins, M. J.; Druhan, J.; Arntzen, E.; N'Guessan, A. L.; Long, P. E.; Hubbard, S. S.; Banfield, J. F. Geophysical Monitoring of Coupled Microbial and Geochemical Processes during Stimulated Subsurface Bioremediation. *Environ. Sci. Technol.* **2009**, *43* (17), 6717.

(42) Kessouri, P.; Furman, A.; Huisman, J. A.; Martin, T.; Mellage, A.; Ntarlagiannis, D.; Bücker, M.; Ehosioke, S.; Fernandez, P.; Flores-Orozco, A.; Kemna, A.; Nguyen, F.; Pilawski, T.; Saneiyan, S.; Schmutz, M.; Schwartz, N.; Weigand, M.; Wu, Y.; Zhang, C.; Placencia-Gomez, E. Induced Polarization Applied to Biogeophysics: Recent Advances and Future Prospects. *Near Surface Geophysics* **2019**, *17* (6), 595.

(43) Sassen, D. S.; Hubbard, S. S.; Bea, S. A.; Chen, J.; Spycher, N.; Denham, M. E. Reactive Facies: An Approach for Parameterizing Field-Scale Reactive Transport Models Using Geophysical Methods. *Water Resour. Res.* **2012**, *48* (10).

(44) Chen, J.; Hubbard, S. S.; Williams, K. H.; Pride, S.; Li, L.; Steefel, C.; Slater, L. A State-Space Bayesian Framework for Estimating Biogeochemical Transformations Using Time-Lapse Geophysical Data. *Water Resour. Res.* **2009**, *45* (8).

(45) Gómez-Díaz, E.; Scott, S.; Ratouis, T.; Newson, J. Numerical Modeling of Reinjection and Tracer Transport in a Shallow Aquifer, Nesjavellir Geothermal System, Iceland. *Geotherm. Energy* **2022**, *10* (7), 7.

(46) Franzson, H. *Nesjavellir-BorholujarÐfræÐi, Vatnsgengd í JarÐhitageymi. Orkustofnun, Report No. OS-88046/JHD-09* 1988.

(47) Franzson, H. Hydrothermal Evolution of the Nesjavellir High-Temperature System, Iceland. In *World Geothermal Congress 2000*; 2000.

(48) Arnórsson, S.; Axelsson, G.; Sæmundsson, K. Geothermal Systems in Iceland. *Jökull* **2008**, *58*, 269−302.

(49) Helgadóttir, H. M. *NN-03 and NN-04 in Nesjavellir Drill Cuttings Analysis*; Reykjavík, 2021.

(50) Sigfússon, B.; Arnarson, M. P.; Snæbjörnsdóttir, S. Ó.; Karlsdóttir, M. R.; Aradóttir, E. S.; Gunnarsson, I. Reducing Emissions of Carbon Dioxide and Hydrogen Sulphide at Hellisheidi Power Plant in 2014−2017 and the Role of CarbFix in Achieving the 2040 Iceland Climate Goals. In *Energy Procedia*; 2018; Vol. *146*.

(51) Scott, J. H. *Computer Analysis of Digital Well Logs*; 1984.

(52) Helm-Clark, C. M.; Rodgers, D. W.; Smith, R. P. Borehole Geophysical Techniques to Define Stratigraphy, Alteration and Aquifers in Basalt. *J. Appl. Geophy* **2004**, *55* (1−2), 3.

(53) Helander, D. P. *Fundamentals of Formation Evaluation*; Oil & Gas Consultants Intl., 1983.

(54) Keller, G. V.; Frischknecht, F. C. *Electrical Methods in Geophysical Prospecting*; Pergamon Press, 1966.

(55) Revil, A.; Coperey, A.; Mao, D.; Abdulsamad, F.; Ghorbani, A.; Rossi, M.; Gasquet, D. Induced Polarization Response of Porous Media with Metallic Particles - Part 8: Influence of Temperature and Salinity. *Geophysics* **2018**, *83* (6), E435.

(56) Bairlein, K.; Bücker, M.; Hördt, A.; Hinze, B. Temperature Dependence of Spectral Induced Polarization Data: Experimental Results and Membrane Polarization Theory. *Geophys J. Int.* **2016**, *205* (1), 440.

(57) Telford, W. M.; Geldart, L. P.; Sheriff, R. E. *Applied Geophysics*, 2nd ed.; Cambridge University Press, 1990.

(58) Sumner, J. S. Theory of Induced Polarization. In *Principles of Induced Polarization for Geophysical Exploration, Developments in Economic Geology, 5*; Elsevier Scientific Publishing Company: Amsterdam, 1976; pp 47−80.

(59) Mao, D.; Revil, A. Induced Polarization Response of Porous Media with Metallic Particles - Part 3: A New Approach to Time-Domain Induced Polarization Tomography. *Geophysics* **2016**, *81* (4), D345.

(60) Mao, D.; Revil, A.; Hinton, J. Induced Polarization Response of Porous Media with Metallic Particles - Part 4: Detection of Metallic and Nonmetallic Targets in Time-Domain-Induced Polarization Tomography. *Geophysics* **2016**, *81* (4), D359.

(61) Parkhurst, D. L.; Appelo, C. A. J. Description of Input and Examples for PHREEQC Version 3 — A Computer Program for Speciation, Batch-Reaction, One-Dimensional Transport, and Inverse Geochemical Calculations; *Modeling techniques*. U.S. Geological Survey: Denver, CO, 2013.

(62) Voigt, M.; Marieni, C.; Clark, D. E.; Gíslason, S. R.; Oelkers, E. H. Evaluation and Refinement of Thermodynamic Databases for Mineral Carbonation. In *Energy Procedia*; Elsevier, 2018; Vol. *146*.

(63) Heřmanská, M.; Voigt, M. J.; Marieni, C.; Declercq, J.; Oelkers, E. H. A Comprehensive and Internally Consistent Mineral Dissolution Rate Database: Part I: Primary Silicate Minerals and Glasses. *Chem. Geol.* **2022**, *597*, 120807.

(64) Neveu, M.; Desch, S. J.; Castillo-Rogez, J. C. Aqueous Geochemistry in Icy World Interiors: Equilibrium Fluid, Rock, and Gas Compositions, and Fate of Antifreezes and Radionuclides. *Geochim. Cosmochim. Acta* **2017**, *212*, 324.

(65) Steefel, C. I.; DePaolo, D. J.; Lichtner, P. C. Reactive Transport Modeling: An Essential Tool and a New Research Approach for the Earth Sciences. *Earth Planet Sci. Lett.* **2005**, *240* (3−4), 539.

(66) Serra, O. *Fundamentals of Well Log Interpretation, 1. The Acquisition of Logging Data*, 1st ed.; Elsevier, 1984.

(67) Roy, A.; Dhar, R. L. Radius of Investigation in DC Resistivity Well Logging. *Geophysics* **1971**, *36* (4), 754.

(68) Přikryl, J.; Jha, D.; Stefánsson, A.; Stipp, S. Mineral Dissolution in Porous Media: An Experimental and Modeling Study on Kinetics, Porosity and Surface Area Evolution. *Appl. Geochem.* **2017**, *87*, 57.

(69) Galeczka, I. M.; Wolff-Boenisch, D.; Oelkers, E. H.; Gíslason, S. R. An Experimental Study of Basaltic Glass-H2O-CO2 Interaction at 22 and 50°C: Implications for Subsurface Storage of CO2. *Geochim. Cosmochim. Acta* **2014**, *126*, 123.

(70) Aradóttir, E. S. P.; Sonnenthal, E. L.; Björnsson, G.; Jónsson, H. Multidimensional Reactive Transport Modeling of CO2 mineral Sequestration in Basalts at the Hellisheidi Geothermal Field, Iceland. *International Journal of Greenhouse Gas Control* **2012**, *9*, 24.

(71) Gíslason, S.; Oelkers, E. H. Mechanism, Rates, and Consequences of Basaltic Glass Dissolution: II. An Experimental Study of the Dissolution Rates of Basaltic Glass as a Function of PH and Temperature. *Geochim. Cosmochim. Acta* **2003**, *67* (20), 3817.

(72) Seyfried, W. E.; Janecky, D. R. Heavy Metal and Sulfur Transport during Subcritical and Supercritical Hydrothermal Alteration of Basalt: Influence of Fluid Pressure and Basalt Composition and Crystallinity. *Geochim. Cosmochim. Acta* **1985**, *49* (12), 2545.

(73) GuÐbrandsson, S.; Wolff-Boenisch, D.; Gíslason, S. R.; Oelkers, E. H. An Experimental Study of Crystalline Basalt Dissolution from $2 \leqslant pH \leqslant 11$ and Temperatures from 5 to 75°C. *Geochim. Cosmochim. Acta* **2011**, *75* (19), 5496.

(74) Scott, S. W.; Lévy, L.; Covell, C.; Franzson, H.; Gibert, B.; Valfells, Á.; Newson, J.; Frolova, J.; Júlíusson, E.; GuÐjónsdóttir, M. S. ValgarÐur: A Database of the Petrophysical, Mineralogical, and Chemical Properties of Icelandic Rocks. *Earth Syst. Sci. Data* **2023**, *15* (3), 1165.

(75) Oelkers, E. H.; Gíslason, S. R. The Mechanism, Rates and Consequences of Basaltic Glass Dissolution: I. An Experimental Study of the Dissolution Rates of Basaltic Glass as a Function of Aqueous Al, Si and Oxalic Acid Concentration at 25°C and PH = 3 and 11. *Geochim. Cosmochim. Acta* **2001**, *65* (21), 3671−3681.

(76) Wolff-Boenisch, D.; Gíslason, S. R.; Oelkers, E. H.; Putnis, C. V. The Dissolution Rates of Natural Glasses as a Function of Their Composition at PH 4 and 10.6, and Temperatures from 25 to 74°C. *Geochim. Cosmochim. Acta* **2004**, *68* (23), 4843.

(77) Daux, V.; Christophe, G.; Advocat, T.; Crovisier, J. L.; Stille, P. Kinetic Aspects of Basaltic Glass Dissolution at 90°c: Role of Aqueous Silicon and Aluminium. *Chem. Geol.* **1997**, *142* (1−2), 109.

(78) Sonnenthal, E.; Ito, A.; Spycher, N.; Yui, M.; Apps, J.; Sugita, Y.; Conrad, M.; Kawakami, S. Approaches to Modeling Coupled Thermal, Hydrological, and Chemical Processes in the Drift Scale Heater Test at Yucca Mountain. *International Journal of Rock Mechanics and Mining Sciences* **2005**, *42* (5−6), 698−719.

(79) Beckingham, L. E.; Mitnick, E. H.; Steefel, C. I.; Zhang, S.; Voltolini, M.; Swift, A. M.; Yang, L.; Cole, D. R.; Sheets, J. M.; Ajo-Franklin, J. B.; DePaolo, D. J.; Mito, S.; Xue, Z. Evaluation of Mineral Reactive Surface Area Estimates for Prediction of Reactivity of a Multi-Mineral Sediment. *Geochim. Cosmochim. Acta* **2016**, *188*, 310.

(80) Hellevang, H.; Pham, V. T. H.; Aagaard, P. Kinetic Modelling of CO2-Water-Rock Interactions. *International Journal of Greenhouse Gas Control* **2013**, *15*, 3.

(81) Larsen, O.; Postma, D. Kinetics of Reductive Bulk Dissolution of Lepidocrocite, Ferrihydrite, and goethite. *Geochim. Cosmochim. Acta* **2001**, *65* (9), 1367.

(82) Gysi, A. P.; Stefánsson, A. Mineralogical Aspects of CO 2 Sequestration during Hydrothermal Basalt Alteration - An Experimental Study at 75 to 250°C and Elevated PCO 2. *Chem. Geol.* **2012**, *306−307*, 146.

(83) Franzson, H.; Gunnlaugsson, E. Formation of Clays and Chlorites in the Upper Icelandic Crust. In *Proceedings World Geothermal Congress 2020 + 1*; Reykjavík, 2020.

(84) Schiffman, P.; Fridleifsson, G. O. The Smectite−Chlorite Transition in Drillhole NJ-15, Nesjavellir Geothermal Field, Iceland: XRD, BSE and Electron Microprobe Investigations. *Journal of Metamorphic Geology* **1991**, *9* (6), 679.

(85) Kristmannsdóttir, H. Alteration of Basaltic Rocks by Hydrothermal-Activity at 100−300°C. *Developments in Sedimentology* **1979**, *27*(C), 359.

(86) Larsson, D.; Grönvold, K.; Oskarsson, N.; Gunnlaugsson, E. Hydrothermal Alteration of Plagioclase and Growth of Secondary Feldspar in the Hengill Volcanic Centre, SW Iceland. *Journal of Volcanology and Geothermal Research* **2002**, *114* (3−4), 275.

(87) Peterson, F. L.; Lao, C. Electric Well Logging of Hawaiian Basaltic Aquifers. *Groundwater* **1970**, *8* (2), 11.

(88) Franzson, H.; GuĐlaugsson, S. P.; FriĐleifsson, G. Ó. Petrophysical Properties of Icelandic Rocks. In *Proceedings of the 6th Nordic Symposium on Petrophysics*; 2001.

(89) Muñoz, A. Q. *Interpretation of Geophysical Well Logs from the Nesjavellir Geothermal Field, Iceland*; Reykjavík, Iceland, 1996.

(90) Gunnarsdóttir, S. H.; Helgadóttir, H. M.; Snaebjörnsdóttir, S. GECO: Geological Properties, Permeability and Porosity of the Nesjavellir High Temperature Area in Relation to the Re-Injection of Geothermal CO2 and H2S Gases. In *Proceedings World Geothermal Congress*; Reykjavik, Iceland, 2020.

(91) HafstaĐ, P. H. *NiĐurrennslisholurnar NN-3 Og NN-4 á Nesjavöllum*. ISOR*: PHH-03−06* 2003.

(92) Grant, M. A.; Garg, S. K.; Riney, T. D. Interpretation of Downhole Data and Development of a Conceptual Model for the Redondo Creek Area of the Baca Geothermal Field. *Water Resour Res.* **1984**, *20* (10), 1401.

(93) Sigfusson, B.; Gíslason, S. R.; Meharg, A. A. et al.. *Appl. Geochem.* **2011**, *26* (4), 553.

(94) Callow, B.; Falcon-Suarez, I.; Ahmed, S.; Matter, J. Assessing the Carbon Sequestration Potential of Basalt Using X-Ray Micro-CT and Rock Mechanics. *International Journal of Greenhouse Gas Control* **2018**, *70*, 146.

(95) Crovisier, J. L.; Honnorez, J.; Fritz, B.; Petit, J. C. Dissolution of Subglacial Volcanic Glasses from Iceland: Laboratory Study and Modelling. *Appl. Geochem.* **1992**, *7*, 55.

(96) Helgeson, H. C.; Delany, J. M.; Nesbitt, H. W.; Bird, D. K. Summary and Critique of the Thermodynamic Properties of Rock-Forming Minerals. *Am. J. Sci.* **1978**, *278-A*, 1−229.

(97) Marty, N. C. M.; Fritz, B.; Clément, A.; Michau, N. et al.. *Appl. Clay Sci.* **2010**, *47* (1−2), 82.

(98) Lévy, L.; Gibert, B.; Sigmundsson, F.; Flóvenz, O. G.; Hersir, G. P.; Briole, P.; Pezard, P. A. The Role of Smectites in the Electrical Conductivity of Active Hydrothermal Systems: Electrical Properties of Core Samples from Krafla Volcano, Iceland. *Geophys J. Int.* **2018**, *215* (3), 1558.

(99) Martin, T.; Weller, A. Superposition of Induced Polarization Signals Measured on Pyrite-Sand Mixtures. *Geophys. J. Int.* **2023**, *234* (1), 699.

(100) Franzson, H.; Zierenberg, R.; Schiffman, P. Chemical Transport in Geothermal Systems in Iceland. Evidence from Hydrothermal Alteration. *Journal of Volcanology and Geothermal Research* **2008**, *173* (3−4), 217.

(101) Lévy, L.; Ciraula, D.; Legros, B.; Martin, T.; Weller, A. Understanding the Fate of H2S Injected in Basalts by Means of Time-Domain Induced Polarization Geophysical Logging. *Journal of Geophysical Research: Solid Earth* **2024**, *129*, e2023JB028316.

(102) Percak-Dennett, E.; He, S.; Converse, B.; Konishi, H.; Xu, H.; Corcoran, A.; Noguera, D.; Chan, C.; Bhattacharyya, A.; Borch, T.; Boyd, E.; Roden, E. E. et al.. *Geobiology* **2017**, *15* (5), 690.

(103) Mielke, R. E.; Pace, D. L.; Porter, T.; Southam, G. A Critical Stage in the Formation of Acid Mine Drainage: Colonization of Pyrite by Acidithiobacillus Ferrooxidans under PH-Neutral Conditions. *Geobiology* **2003**, *1* (1), 81.

(104) Polites, E. G.; Schaef, H. T.; Horner, J. A.; Owen, A. T.; Holliman, J. E., Jr.; McGrail, B. P.; Miller, Q. R. S. Exotic Carbonate Mineralization Recovered from a Deep Basalt Carbon Storage Demonstration. *Environ. Sci. Technol.* **2022**, *56*, 14713−14722.

(105) McGrail, B. P.; Schaef, H. T.; Spane, F. A.; Cliff, J. B.; Qafoku, O.; Horner, J. A.; Thompson, C. J.; Owen, A. T.; Sullivan, C. E. Field Validation of Supercritical CO2 Reactivity with Basalts. *Environ. Sci. Technol. Lett.* **2017**, *4* (1), 6.

Supporting Information for:

Advanced monitoring of H_2S injection through the coupling of reactive transport models and geophysical responses

Daniel A. Ciraula[1,*], Barbara I. Kleine-Marshall[2], Iwona M. Galeczka[3,4], Léa Lévy[3,5]

[1]Nordic Volcanological Center, Institute of Earth Sciences, University of Iceland, 101 Reykjavík, Iceland
[2]GeoZentrum Nordbayern, Friedrich-Alexander-Universität, Schlossgarten 5, 91054 Erlangen-Nuremberg, Germany
[3]ÍSOR-Iceland Geosurvey, Urðarhvarf 8, 203 Kópavogur
[4]Carbfix, Höfðabakki 9D, 110 Reykjavík, Iceland
[5]Lund University, Engineering Geology, Lund Box 117, SE-221 00, Sweden
*Correspondence author at: Nordic Volcanological Center, Institute of Earth Sciences, University of Iceland, 101 Reykjavík, Iceland. E-mail address: danielac@hi.is (D.A. Ciraula).

Summary: 24 pages, 4 text descriptions, 5 tables, 9 figures

Supporting text (pages S2-S8) providing (Text S1) background on the wastewater produced and the injection system at Nesjavellir power station; (Text S2) details on the application of the weighed averaging function derived from the induced polarization logging tool sensitivity applied to the sulfide volume fraction over the 1-dimensional flow path; (Text S3) the derivation of the well mobility factor used to determine the volume rate of injection water entering each model layer; (Text S4) a complete description of the injection fluid and bulk rock chemical analysis methods.

Tables (pages S9-S13) include data on (Table S1) the NN-3 and NN-4 injection wells; (Table S2) measured basalt whole rock composition; (Table S3) basaltic glass formulas for the reactive transport models (RTMs); (Table S4) measured injection water chemistry; (Table S5) and the chemical compositions of the secondary alteration minerals allowed to precipitate in the RTMs.

Figures (pages S14-S22) displaying (Figure S1) The workflow outlining the joint application of geophysical methods and reactive transport modeling to study H_2S mineralization; (Figure S2) The volume fraction of all secondary minerals from the NN-3 and NN-4 RTMs; (Figure S3) relative source of S upon progressive basaltic glass dissolution; (Figure S4) basaltic glass dissolution rates for the various RTMs; (Figure S5) sulfide formation predicted by RTMs with homogeneous basalt composition; (Figure S6) percentage of total S mineralized upon basaltic glass alteration in reaction path models constructed for all measured basalt compositions in NN-3 and NN-4; (Figure S7) impact of advective transport flow schemes compared to advective-dispersive transport schemes on the change in sulfide volume fraction; (Figure S8) impact of pyrite kinetic precipitation rates on the expected change in sulfide volume fraction compared to RTMs that allow pyrite to mineralize to equilibrium; (Figure S9) changes in resistivity, neutron, and IP wireline response after 40 days of H_2S-charged water injection.

References for supporting information (pages S23-S24) (PDF)

Text S1: Nesjavellir Wastewater and Injection System

The Nesjavellir power plant produces three types of wastewater. First is separated geothermal water (SGW), which is the aqueous phase of the high enthalpy production fluid. Second is condensate water, which is the steam from the high enthalpy production fluid used to turn the turbines. Third is cooling water, which is cold groundwater used to condense the steam.

A controlled pressure decrease of the utilized geothermal fluid produces steam and separated geothermal water (SGW) at 195°C. The operation of all four turbines for electricity generation at Nesjavellir requires 240 kg/s of steam. To cool the steam, condensers require ~2,000 l/s of cold groundwater (5-7°C). The condensed steam forms the condensate wastewater, composed of dilute water with some dissolved gas (primarily CO_2 and H_2S). The cold groundwater leaves the condensers at around 55°C and is either sent to cooling towers in preparation for disposal or sent to heat exchanges for further usage. The heat exchangers use the 195°C SGW to heat the groundwater to 87°C, where it is then pumped 27 km to Reykjavík.

After steam production from the geothermal production fluid, the remaining SGW contains high concentrations of dissolved solids, posing a considerable risk of both thermal and chemical pollution of surface waters. For this reason, SGW is diluted with the condensate wastewater and injected into the subsurface, including the NN-3 and NN-4 injection wells investigated in this study. Excess SGW and condensate water is discharged at the surface. Much of the SGW is pumped through a delay tank before injection where the dissolved silica polymerizes limiting amorphous silica scaling formation within the injection well and the injection reservoir. However, some amount of untreated SGW is sent to the injection wells, except for NN-3 which only receives SGW from the delay tank.

H_2S and CO_2 gases are captured from the condensers at the power plant using liquid ring vacuum pumps. This differs from the CarbFix process, which uses scrubbing towers to dissolve CO_2 and H_2S. This results in larger concentrations of CO_2 and H_2S compared to the injection waters of CO_2 (1,220 ppm) and H_2S (481 ppm) compared to this study (CO_2 ~10 ppm, H_2S ~75 ppm) (Galeczka et al., 2022). Gas-charged water from the CarbFix process is sent to a deeper injection well at Nesjavellir (NJ-18) (Galeczka et al., 2022). In the shallow reinjection system studied here, the captured gases are dissolved into the vacuum pump seal water (lásvatn), composed of heated groundwater or condensate wastewater. Starting in January of 2021, the seal water has been mixed with the condensate and SGW, constituting the final, H_2S-charged injection fluid. Prior to January 2021, the injection fluid for NN-3 and NN-4 was composed of condensate and SGW only, and thus had lower concentrations of dissolved H_2S and CO_2.

Text S2: Calculations of Sulfide Volume Fraction and the Weighted Average

In the PHREEQC advection model, the user specifies the cell residence time rather than cell geometry and flow parameters (i.e., permeability). For each simulation, the chemical reactions are calculated relative to a representative volume (RV) that contains 1 L of water when fully saturated. PHREEQC returns the moles of secondary minerals mineralized per L of water. Therefore, since the volume of water in the system is fixed at 1L, changes in the porosity ($\emptyset$) change the representative volume. Additionally, the initial moles of solid reactants are scaled by the factor of (1-porosity)/porosity to account for porosity variability in the starting model.

$$RV = {}^{1{,}000\ cm^3}/_{\emptyset}$$

To recover the volumetric proportion of sulfide minerals in each cell (i.e., sulfide volume fraction SVF), we divide the volume of sulfides precipitated (pyrite and pyrrhotite) by the cell's representative porous-medium volume, which factors in porosity variability. This SVF term is equal to the change in SVF as we assume there are no sulfides in the host rock.

$$SVF = \frac{V_{sulfides}}{RV} = \frac{moles\ per\ L\ water_{sulfides} \times molar\ volume_{sulfides}}{RV}$$

To best compare the results of the reactive transport model to the IP wireline results, we average the change in sulfide volume fraction over the entire flow path after 40 days to obtain a single representative value for the given depth interval. We apply a weighted average to account for varying contributions to the measured IP signal based on the distance of H_2S mineralization away from the borehole. The contribution function is formulated in Roy & Dhar (1971), and considers electrostatic potentials of individual cylindrical shells of varying radii integrated to obtain the total contribution to the measured signal. For a normal sonde, as used in this study, the radial investigation characteristic (*RIC*) is defined as follows:

$$RIC = \frac{\rho I}{8\pi} dr \cdot \int_{-\infty}^{+\infty} \frac{r^3 + rz(z-L)}{(r^2+z^2)^{3/2}[r^2+(z-L)^2]^{3/2}} dz\ ,$$

where ρ is the resistivity, I is the current, dr is the thickness of the circular ground element, r is the average radius of the circular ground element, z is the cell height variable, and L is the electrode spacing (64”). Using the wireline resistivity and current measurements, we solve for the RIC relative contribution over 0.5 m bins from 0 to 3.5 m. The RIC values are normalized to 90% of the total signal, given that 90% of the signal is expected over 3.25 m (2 times the electrode spacing) (Roy & Dhar, 1971). These contributions are shown in the following figure. For every bin, *i*, ranging from x = a to b away from the borehole center, the SVF for all cells located within that bin (taking into consideration the radius of the borehole) are totaled and scaled by the relative contribution of the bin:

$$\Delta SVF_i = RIC_i \times \sum_{x=a}^{x=b} \Delta SVF.$$

Finally, the average change in sulfide volume fraction ($\bar{x}_{\Delta SVF}$) is calculated by multiplying each bin's SVF change by the volume of each 0.5 m bin, given the bin's width ($r_{i,2} - r_{i,1}$), relative to the volume of the total flow column away from the borehole (3.25 m + 0.2 m borehole radius). These resulting SVF contributions are summed over the flow path.

$$\bar{x}_{\Delta SVF} = \sum_{i=1}^{7} \Delta SVF_i \times \frac{{r_{i,2}}^2 - {r_{i,1}}^2}{3.45^2}.$$

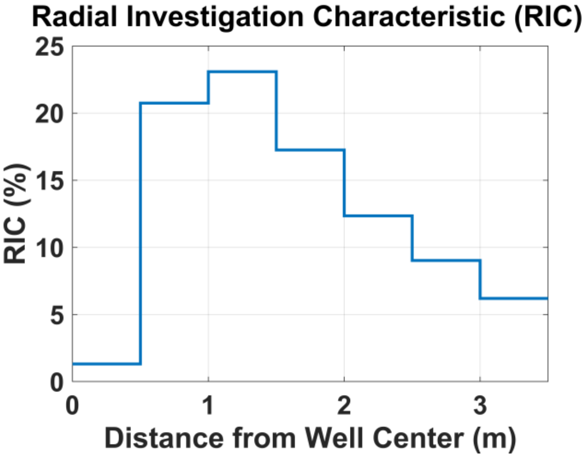

The radial investigation characteristic showing the relative contribution to the IP signal as a function of distance from the center of the borehole (Roy & Dhar, 1971). The signal is grouped into 0.5 m bins, and the total volume of sulfides that mineralize in the bin is scaled by the RIC of that bin.

Text S3: Injection Mobility Factor

The injection mobility factor (μ) is the relative proportion of the total injection fluid (Q_T) that enters each RTM layer (*i*) along the injection wells (Kipp, 1987). It is derived from Darcy's Law relating the volumetric fluid flux (Q) to the hydraulic conductivity (K), the cross-sectional flow area (A), and the hydraulic gradient ($\partial h/\partial x$). We solve for the relative volumetric fluid flux for *n* layers as

$$\mu_i = \frac{Q_i}{Q_T} = \frac{-K_i * A_i * \frac{\partial h_i}{\partial x}}{\sum_{i=1}^{n} -K_i * A_i * \frac{\partial h_i}{\partial x}} \, .$$

Given that all layers have equal cell height (h) and assuming the hydraulic gradient is uniform across all layers, the pressure differences are independent of depth, and the borehole has the same radius (r) across the entire domain, the relationship above simplifies as follows:

$$\mu_i = \frac{-K_i * 2\pi r h * \frac{\partial h_i}{\partial x}}{\sum_{i=1}^{n} -K_i * 2\pi r h * \frac{\partial h_i}{\partial x}} = \frac{K_i}{\sum_{i=1}^{n} K_i}$$

Further assuming that injection fluid density and dynamic viscosity are uniform across the entire well, the hydraulic conductivity ratio becomes equivalent to the ratio of permeability (k),

$$\mu_i = \frac{K_i}{\sum_{i=1}^{n} K_i} = \frac{k_i}{\sum_{i=1}^{n} k} \, .$$

Text S4: Injection fluid and bulk rock chemical analyses

The chemical composition of the injection fluid and bulk rock from drill cuttings was analyzed to investigate the chemical heterogeneity of the host rock and injection fluid as well as other physiochemical parameters (e.g., pH, injection rate, temperature) on the extent of H_2S mineralization upon injection.

Injection fluid samples (n = 2) were sampled at the wellhead of NN-3 and NN-4 injection wells in November 2022. The temperature and electrical conductivity were measured on-site. The pH of the fluid samples was analyzed at 21°C using a pH meter and electrode calibrated with commercial buffer solution (analytical precision ±0.1). Fluid samples for major anion and cation analyses were prepared as described in Arnórsson et al. (2006). Analyses were carried out at the Institute of Earth Sciences, University of Iceland, using an Inductively Coupled Plasma Optical Emission Spectroscopy (ICP-OES) instrument (ThermoFisher iCAP 7400 Duo) for cations and an ion chromatography (IC) instrument (Dionex ICS-2000) for anions. Dissolved sulfide (H_2S) concentrations were measured via mercury acetate titration with dithizone as the indicator (Arnórsson et al., 2006). Carbon dioxide (CO_2) concentrations were measured through modified alkalinity titration (Arnórsson et al., 2006; Jeffery et al., 1989; Stefánsson et al., 2007) as follows,

$$CO_2(ppm) = \frac{(mL\ HCl \times Molarity\ HCl - mL\ NaOH \times Molarity\ NaOH)}{mL\ sample} \times 44{,}000 - 1.182 \times H_2S(ppm).$$

The analytical precision of major elements was based on duplicate analysis of the samples and was found to be <5% at the 95% confidence level in all cases.

The injection fluids are found to be alkaline (pH > 7) for both NN-3 and NN-4, with the NN-4 fluid having a slightly higher pH than the NN-3 fluid (9.1 vs. 8.5). The NN-3 and NN-4 injection fluids have similar chemical compositions, particularly in measured H_2S concentration (NN-3 = 74.4 ppm and NN-4 = 76.8 ppm). Compared to meteoric water reported at the nearby Vellankatla natural spring (Gysi & Stefánsson, 2012), the injection fluids are generally dilute but with elevated H_2S (NN-3 = 74.4 ppm and NN-4 = 76.8 ppm), SiO_2 (NN-3 = 435 ppm and NN-4 = 428 ppm) and K (NN-3 = 20.3 ppm and NN-4 = 20.3 ppm) concentrations.

Bulk rock compositions from drill cuttings (n = 28) were collected from beneath the casing at the NN-3 and NN-4 injection wells. All samples were milled to a grain size of <150 μm. Total carbon (C) and sulfur (S) analyses of the drill cuttings were conducted using an ELTRA combustion infrared carbon and sulfur analyzer (www.actlabs.com/geochemistry). The data error range was taken from the detection limit of the equipment for all species analyzed (0.01 wt.%). For major component analyses (SiO_2, Al_2O_3, FeO, MnO, MgO, CaO, Na_2O, K_2O, TiO_2) via ICP-OES, a subset of the milled samples ($n = 10$) was fluxed with LiB_2 at 1,000°C for 30 min, and subsequently digested in a solution of 5.0 vol% nitric acid (16 molar), 1.3 vol% hydrochloric acid (12 molar), 1.3 vol% oxalic acid (0.8 molar). Accuracy and precision of the analyses were ensured by duplicate sample analyses and repeated analyses of the United States Geological Survey (USGS) standard reference material (BHVO-1 and W-2; Jochum et al., 2016). We interpolated the major element compositions at every total C and S measurement and renormalized the wt.% to account for the C and S compositions not measured via ICP-OES.

Table S1: NN injection well information

Table S1: Details on the Nesjavellir NN injection wells in this study.

Well ID	NN-3	NN-4
Coordinates[a]	64°06’38.23” N, 21°15’20.27” W	64°06’50.03” N, 21°15’0.06” W
Measured Depth (m)[b,c]	563	422
Deviation[b,c]	0°	0°
Casing Depth (m)[b,c]	205	201
Feed Zone Depths (m)[a]	390, 445, 535	280, 300, 330, 388
Flow Rate (kg/s)	12.5	149

[a] Gómez-Díaz et al. (2022), [b] Hafstað et al. (2015), [c] Hafstað (2003)

Table S2: Rock Chemistry

Table S2: Rock compositions measured via ICP-OES and IR-CSA for the NN-3 and NN-4 H_2S injection wells.

Depth (m)	SiO_2	Al_2O_3	FeO	MnO	MgO	CaO	Na_2O	K_2O	TiO_2	C[a]	S[a]
Well NN-3 (wt.%)											
206[b]	48.52	14.83	11.95	0.20	7.46	12.20	2.15	0.19	1.94	0.54	0.03
220	49.38	14.81	12.12	0.20	7.01	11.68	2.18	0.28	2.09	0.27	< 0.01
236	50.29	14.75	12.29	0.20	6.48	11.06	2.21	0.37	2.25	0.10	< 0.01
254	51.04	14.61	12.43	0.21	5.85	10.31	2.24	0.47	2.42	0.41	0.01
272[b]	52.04	14.54	12.62	0.21	5.25	9.60	2.28	0.58	2.60	0.24	0.03
290	52.36	14.44	12.61	0.22	4.95	9.19	2.53	0.69	2.61	0.37	0.04
310	52.84	14.36	12.62	0.23	4.64	8.75	2.81	0.82	2.63	0.26	0.05
332	53.26	14.25	12.60	0.25	4.28	8.25	3.12	0.95	2.65	0.35	0.05
348[b]	53.67	14.19	12.62	0.26	4.03	7.90	3.34	1.05	2.67	0.22	0.06
376	52.08	14.20	12.90	0.25	4.88	9.15	3.05	0.76	2.55	0.15	0.03
400	50.67	14.20	13.14	0.24	5.61	10.21	2.79	0.50	2.45	0.18	0.01
426[b]	49.17	14.20	13.40	0.23	6.40	11.36	2.51	0.23	2.34	0.15	< 0.01
452	48.83	14.37	13.05	0.23	6.50	11.64	2.52	0.28	2.30	0.27	< 0.01
480	48.47	14.56	12.68	0.23	6.61	11.94	2.52	0.33	2.26	0.41	< 0.01
510[b]	48.23	14.80	12.32	0.24	6.74	12.30	2.53	0.39	2.22	0.24	< 0.01
540	48.86	14.99	11.89	0.21	7.22	12.18	2.26	0.25	1.87	0.24	0.03
562[b]	49.34	15.14	11.58	0.20	7.57	12.11	2.07	0.14	1.61	0.22	0.03
Well NN-4 (wt.%)											
206[b]	50.06	16.41	10.13	0.16	5.96	12.54	2.34	0.20	2.02	0.17	< 0.01
220	49.90	16.32	10.02	0.16	6.33	12.75	2.26	0.18	1.83	0.25	< 0.01
236	49.86	16.26	9.92	0.16	6.78	13.02	2.17	0.15	1.62	0.05	< 0.01
254	49.64	16.14	9.77	0.16	7.26	13.28	2.06	0.12	1.37	0.17	0.01
272[b]	49.44	16.03	9.63	0.17	7.73	13.55	1.96	0.09	1.12	0.27	< 0.01
290	49.18	15.66	10.26	0.18	7.39	13.13	2.09	0.17	1.42	0.47	0.04
310	49.21	15.35	11.02	0.20	7.05	12.75	2.26	0.25	1.76	0.08	0.06
332	48.92	14.92	11.79	0.22	6.63	12.24	2.42	0.34	2.13	0.34	0.05
354[b]	48.81	14.54	12.60	0.24	6.24	11.79	2.60	0.43	2.50	0.23	0.02
376	49.11	14.51	12.22	0.23	6.54	12.19	2.45	0.36	2.27	0.12	0.01
388[b]	49.17	14.46	11.99	0.22	6.69	12.39	2.36	0.32	2.13	0.25	0.02

[a] Measured via IR-CSA.

[b] Samples measured with ICP-OES. Otherwise, interpolated between measurements and renormalized given IR-CSA measured C and S wt.%.

Table S3: Basaltic Glass Phases for RTM

Table S3: Basaltic glass compositions defining the primary phase of the RTMs for wells NN-3 and NN-4.

Depth (m)	Basaltic Glass Formula
Well NN-3	
200-225	$Si_{1.00}Al_{0.357}Fe_{0.2055}Mn_{0.00343}Mg_{0.221}Ca_{0.261}Na_{0.0857}K_{0.00612}Ti_{0.031}C_{0.0416}S_{0.00058}O_{3.45}$
225-250	$Si_{1.00}Al_{0.346}Fe_{0.2042}Mn_{0.00342}Mg_{0.192}Ca_{0.236}Na_{0.0854}K_{0.0094}Ti_{0.0336}C_{0.00995}S_{0.000}O_{3.32}$
250-275	$Si_{1.00}Al_{0.333}Fe_{0.2038}Mn_{0.00342}Mg_{0.161}Ca_{0.207}Na_{0.085}K_{0.0131}Ti_{0.0366}C_{0.0317}S_{0.000724}O_{3.30}$
275-300	$Si_{1.00}Al_{0.325}Fe_{0.2011}Mn_{0.00358}Mg_{0.141}Ca_{0.188}Na_{0.0936}K_{0.0168}Ti_{0.0375}C_{0.0354}S_{0.00143}O_{3.26}$
300-325	$Si_{1.00}Al_{0.32}Fe_{0.1996}Mn_{0.00376}Mg_{0.131}Ca_{0.177}Na_{0.103}K_{0.0197}Ti_{0.0375}C_{0.0246}S_{0.00177}O_{3.22}$
325-350	$Si_{1.00}Al_{0.314}Fe_{0.1978}Mn_{0.00403}Mg_{0.116}Ca_{0.162}Na_{0.117}K_{0.0239}Ti_{0.0374}C_{0.0267}S_{0.00193}O_{3.19}$
350-375	$Si_{1.00}Al_{0.317}Fe_{0.2023}Mn_{0.00409}Mg_{0.126}Ca_{0.173}Na_{0.117}K_{0.0218}Ti_{0.0371}C_{0.0175}S_{0.00159}O_{3.20}$
375-400	$Si_{1.00}Al_{0.321}Fe_{0.2071}Mn_{0.00407}Mg_{0.14}Ca_{0.188}Na_{0.113}K_{0.0185}Ti_{0.0368}C_{0.0144}S_{0.00108}O_{3.23}$
400-425	$Si_{1.00}Al_{0.33}Fe_{0.2173}Mn_{0.00404}Mg_{0.165}Ca_{0.216}Na_{0.107}K_{0.0127}Ti_{0.0363}C_{0.0178}S_{0.00037}O_{3.30}$
425-450	$Si_{1.00}Al_{0.34}Fe_{0.2279}Mn_{0.004}Mg_{0.194}Ca_{0.248}Na_{0.0991}K_{0.00595}Ti_{0.0358}C_{0.0153}S_{0.000}O_{3.38}$
450-475	$Si_{1.00}Al_{0.347}Fe_{0.2235}Mn_{0.00404}Mg_{0.198}Ca_{0.255}Na_{0.0999}K_{0.00729}Ti_{0.0355}C_{0.0277}S_{0.000}O_{3.42}$
475-500	$Si_{1.00}Al_{0.354}Fe_{0.2189}Mn_{0.00408}Mg_{0.203}Ca_{0.264}Na_{0.101}K_{0.00876}Ti_{0.0351}C_{0.0423}S_{0.000}O_{3.47}$
500-525	$Si_{1.00}Al_{0.362}Fe_{0.2132}Mn_{0.00413}Mg_{0.208}Ca_{0.273}Na_{0.102}K_{0.0104}Ti_{0.0347}C_{0.0249}S_{0.000}O_{3.45}$
525-550	$Si_{1.00}Al_{0.362}Fe_{0.2038}Mn_{0.0037}Mg_{0.22}Ca_{0.267}Na_{0.0898}K_{0.00648}Ti_{0.0288}C_{0.0246}S_{0.00115}O_{3.43}$
Well NN-4	
200-225	$Si_{1.00}Al_{0.386}Fe_{0.1692}Mn_{0.0027}Mg_{0.184}Ca_{0.271}Na_{0.0892}K_{0.00492}Ti_{0.029}C_{0.0211}S_{0.000}O_{3.38}$
225-250	$Si_{1.00}Al_{0.384}Fe_{0.1665}Mn_{0.00275}Mg_{0.203}Ca_{0.28}Na_{0.0844}K_{0.00396}Ti_{0.0244}C_{0.00502}S_{0.000}O_{3.36}$
250-275	$Si_{1.00}Al_{0.383}Fe_{0.1646}Mn_{0.00283}Mg_{0.226}Ca_{0.291}Na_{0.0787}K_{0.00283}Ti_{0.0189}C_{0.0222}S_{0.000189}O_{3.41}$
275-300	$Si_{1.00}Al_{0.375}Fe_{0.1742}Mn_{0.00313}Mg_{0.224}Ca_{0.286}Na_{0.0825}K_{0.00434}Ti_{0.0217}C_{0.0478}S_{0.00152}O_{3.47}$
300-325	$Si_{1.00}Al_{0.368}Fe_{0.1874}Mn_{0.00344}Mg_{0.214}Ca_{0.278}Na_{0.089}K_{0.00647}Ti_{0.027}C_{0.00813}S_{0.00229}O_{3.39}$
325-350	$Si_{1.00}Al_{0.359}Fe_{0.2012}Mn_{0.00378}Mg_{0.202}Ca_{0.268}Na_{0.0961}K_{0.00881}Ti_{0.0327}C_{0.0348}S_{0.00192}O_{3.44}$
350-375	$Si_{1.00}Al_{0.351}Fe_{0.216}Mn_{0.00413}Mg_{0.191}Ca_{0.259}Na_{0.103}K_{0.0112}Ti_{0.0386}C_{0.0236}S_{0.000768}O_{3.42}$

Table S4: Fluid Chemistry

Table S4: Injection fluid composition measured via ICP-OES and IC analysis. Fluids were sampled at the injection well heads.

Well no.	NN-3	NN-4
Fluid (ppm)		
pH	9.10	8.50
Cond. (µS/cm)[a]	637	678
Temperature (°C)[b]	64.0	85.0
H_2S	74.4	76.8
SO_4	8.56	10.4
CO_2	13.5	8.36
SiO_2	435	428
Na	97.3	97.4
K	20.3	20.3
Ca	0.420	0.420
Mg	0.100	0.0960
Fe	0.0150	0.0100
Al	1.13	1.13
B	1.11	1.12
Cl	88.4	88.1
F	0.760	0.760

[a] Measured in the field at the wellhead. Otherwise, measured in the lab at 21°C.

[b] Averaged from continuous measurements since start of H_2S injection

Table S5: Secondary RTM Phases

Table S5: Secondary minerals included in the geochemical RTMs for wells NN-3 and NN-4.

Minerals	Chemical Composition
Secondary Phases	
Analcime	$Na_{0.96}Al_{0.96}Si_{2.04}O_6{:}1H_2O$
Calcite	$CaCO_3$
Celadonite	$KMgAlSi_4O_{10}(OH)_2$
Dolomite	$CaMg(CO_3)_2$
Goethite	$FeOOH$
Magnesite	$MgCO_3$
Pyrite	FeS_2
Pyrrhotite	FeS
Vermiculite-Ca-Mg-Al	$Ca_{0.4}Mg_{2.5}Al_{1.8}Si_{2.7}O_{10}(OH)_2$
Vermiculite-Ca-Mg-Fe	$Ca_{0.4}Mg_{2.5}Fe_{0.5}Al_{1.3}Si_{2.7}O_{10}(OH)_2$
Vermiculite-K-Mg-Al	$K_{0.8}Mg_{2.5}Al_{1.8}Si_{2.7}O_{10}(OH)_2$
Vermiculite-K-Mg-Fe	$K_{0.8}Mg_{2.5}Fe_{0.5}Al_{1.3}Si_{2.7}O_{10}(OH)_2$
Vermiculite-Mg-Mg-Al	$Mg_{2.9}Al_{1.8}Si_{2.7}O_{10}(OH)_2$
Vermiculite-Mg-Mg-Fe	$Mg_{2.9}Fe_{0.5}Al_{1.3}Si_{2.7}O_{10}(OH)_2$
Vermiculite-Na-Mg-Al	$Na_{0.8}Mg_{2.5}Al_{1.8}Si_{2.7}O_{10}(OH)_2$
Vermiculite-Na-Mg-Fe	$Na_{0.8}Mg_{2.5}Fe_{0.5}Al_{1.3}Si_{2.7}O_{10}(OH)_2$
Saponite-Mg-Ca	$Ca_{0.175}Mg_3Al_{0.35}Si_{3.65}O_{10}(OH)_2$
Saponite-Mg-Na	$Na_{0.35}Mg_3Al_{0.35}Si_{3.65}O_{10}(OH)_2$
Siderite	$FeCO_3$
Thomsonite	$Ca_2NaAl_5Si_5O_{20}{:}6H_2O$

*Average composition of all measured samples

Figure S1: Study Workflow

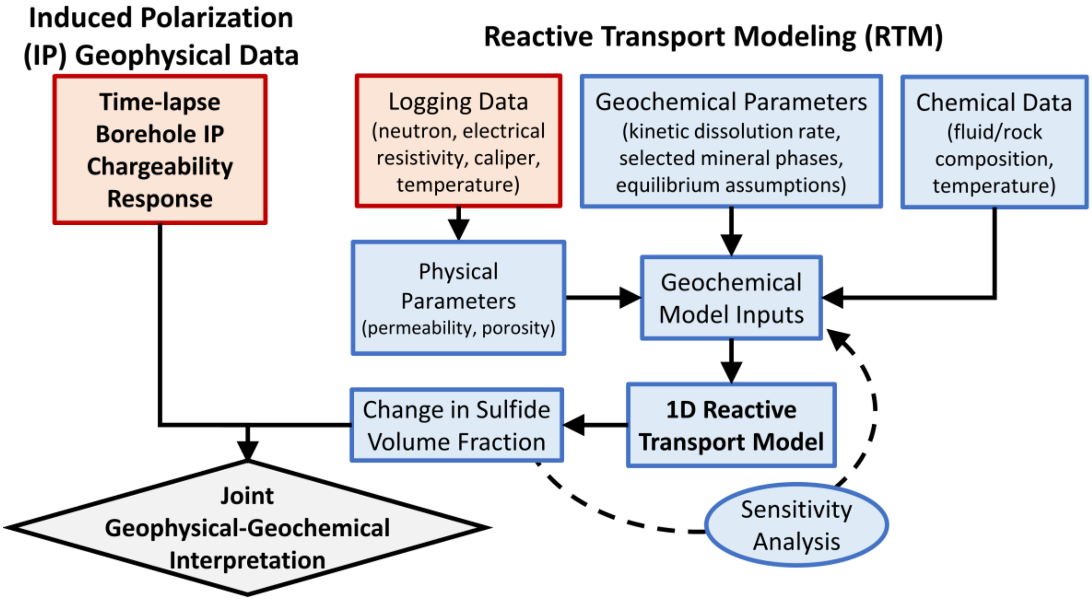

Figure S1. The workflow deployed in this study where the IP geophysical responses and reactive transport models were used to track the magnitude and distribution of H_2S mineralization upon injection. Geophysical and geochemical modeling methods are shown in red and blue boxes, respectively.

Figure S2: RTM Secondary Mineral Formation

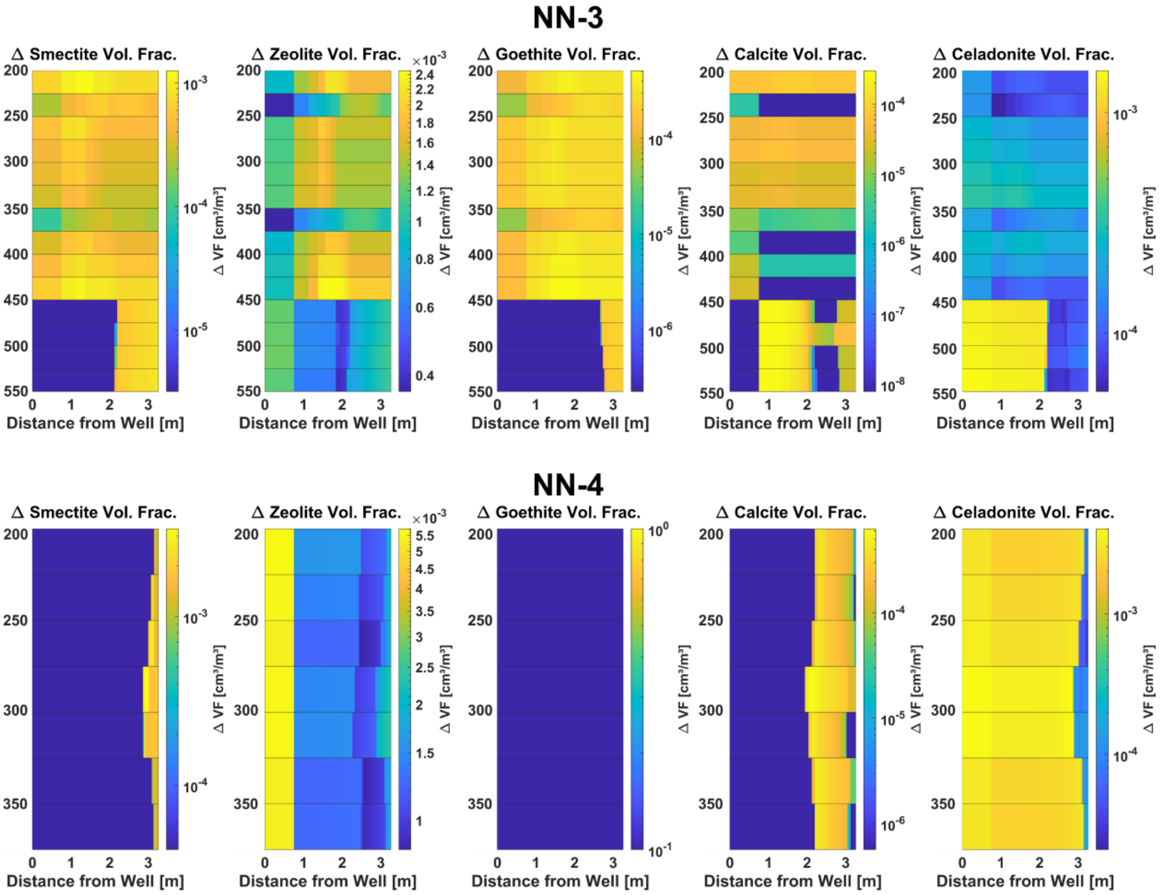

Figure S2: Magnitude and distribution of volume fraction change in secondary minerals of the NN-3 (top) and NN-4 (bottom) flow models. The models are parameterized as described in the main text for the RTM model results shown in Figure 4.

Figure S3: Source of Sulfur Upon Fluid-Rock Interaction

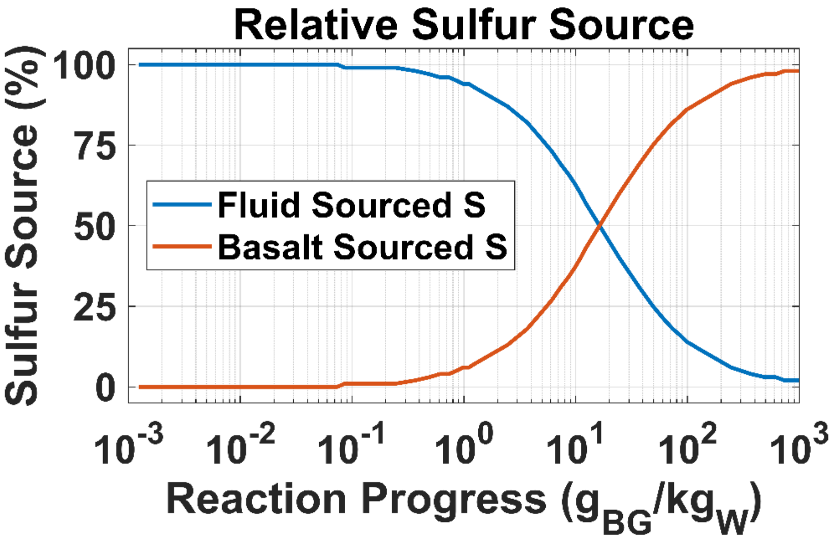

Figure S3: The percentage of S sourced from the H_2S *charged injection fluid compared to the percentage of S sourced from the basaltic glass upon progressive alteration. At high water-rock ratios (i.e., low values along the x-axis), the injection fluid is the primary source of S. Upon alteration of 16 g of basaltic glass in 1 kg of water (0.13* mol_{BG}/kg_{W}*), basalt sourced S becomes the dominant source of S. This modeling is done with NN-4 fluids and basaltic glass from 300-325 to establish an extreme case as this cell has the highest S mole ratio (0.00229* mol_{S}/mol_{BG}*) of all cells in the reactive transport model.*

Figure S4: Basaltic Glass Dissolution Rates

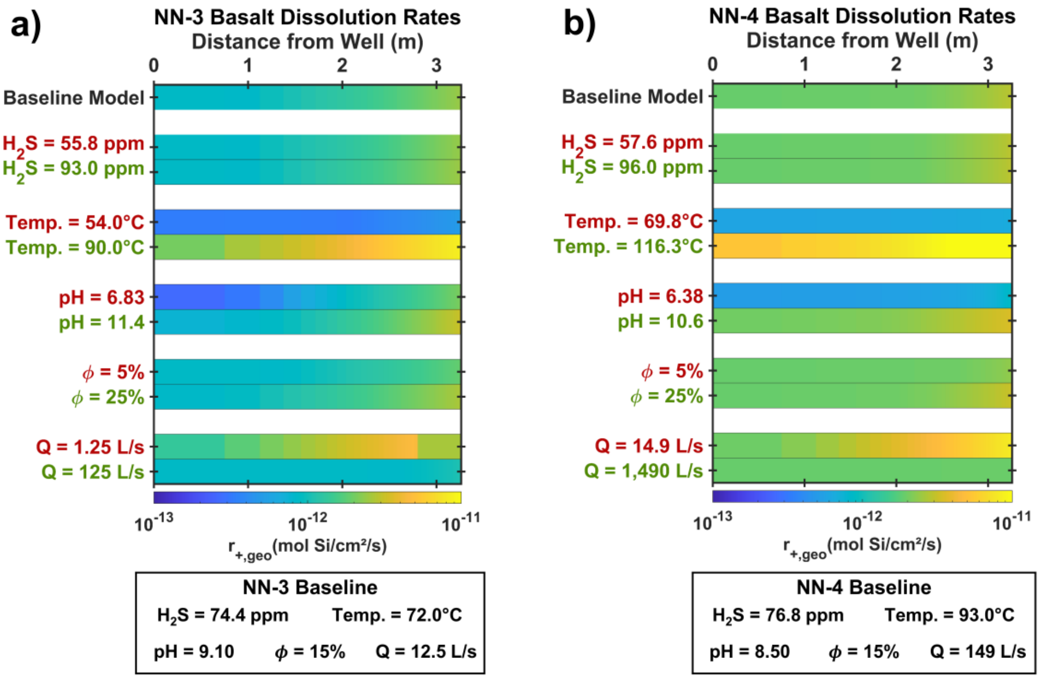

Figure S4: Compiled results of the surface area normalized basaltic glass dissolution rates for models of varying parameters in NN-3 and NN-4. The top row in both left and right figures is the basaltic glass dissolution rates given the measured fluid parameters (temperature, pH, H_2S *concentration). The low parameter and high parameter estimates are -25% and +25% of the measured values, respectively, mid-estimate porosity, and the true injection rates with even allocation of the injection fluid to each model layer. All models are run with the average basalt composition over their respective well, NN-3 and NN-4.*

Figure S5: Sulfide Formation Assuming Homogenous Porosity and Permeability

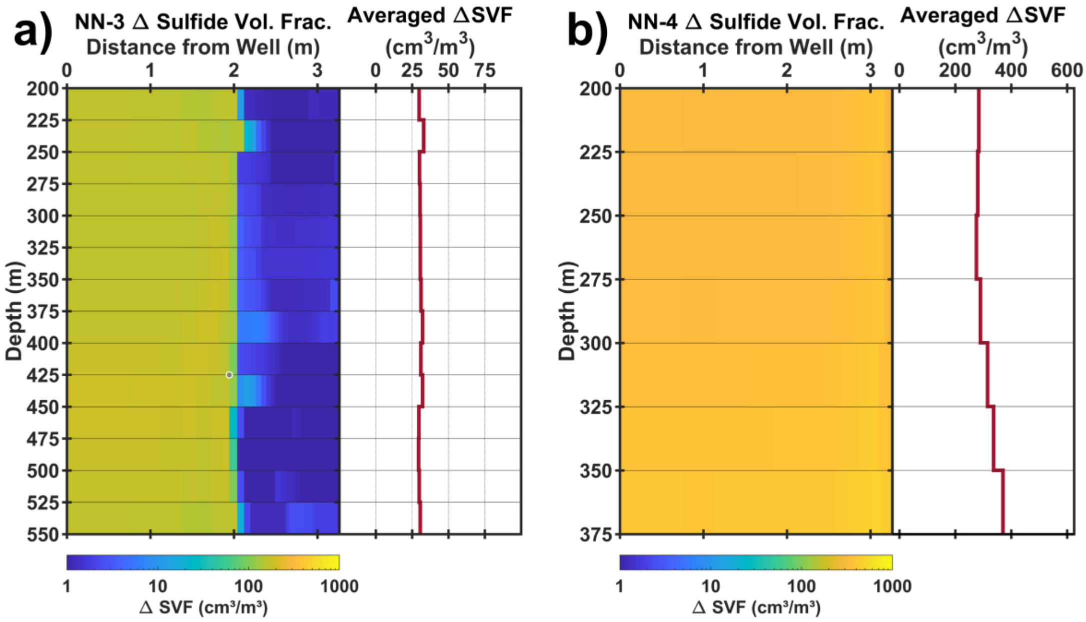

Figure S5: Change in sulfide volume fraction per cubic meter of basalt near the borehole after 40 days of injection in NN-3 (a) and NN-4 (b). The left panels show the distribution of change in sulfide volume fraction (SVF) as fluid flows laterally away from the injection wells. The right panels display the change in SVF at each depth as a weighted average over the flow path as described in Text S5. The models assume a homogeneous porosity of 15% and uniform volumetric flow allocation to each RTM layer, relative to each well's injection rate. The measured injection fluid compositions in wells NN-3 and NN-4 are used for each respective well mode (Table S4). The basaltic glass composition is defined from the measured whole rock compositions and are detailed in Table S3.

Figure S6: Sulfur Mineralization Efficiency

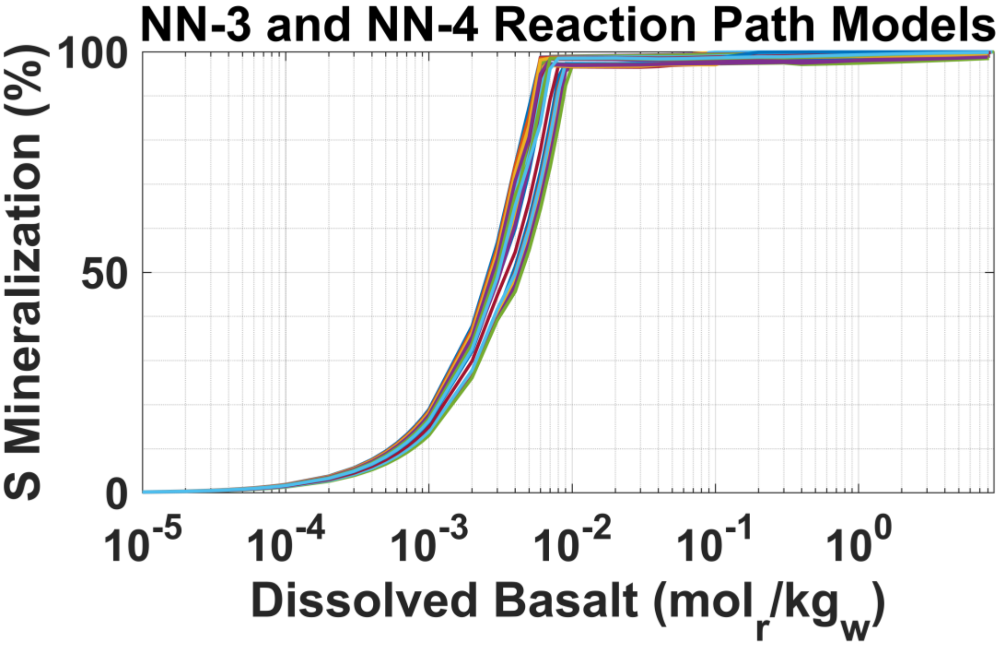

Figure S6: Reaction path models allowing secondary minerals (as listed in Table S5) to mineralize to equilibrium upon progressive basalt alteration in 1 kg of injection fluid. The percentage of S mineralized is calculated using the precipitated pyrite, pyrrhotite, and total S in the solution after each reaction step. A model is constructed for each of the basalt compositions measured in NN-3 and NN-4 to evaluate how basalt composition impacts S mineralization efficiency.

Figure S7: Comparison of Advective Transport to Advective-Dispersive Transport

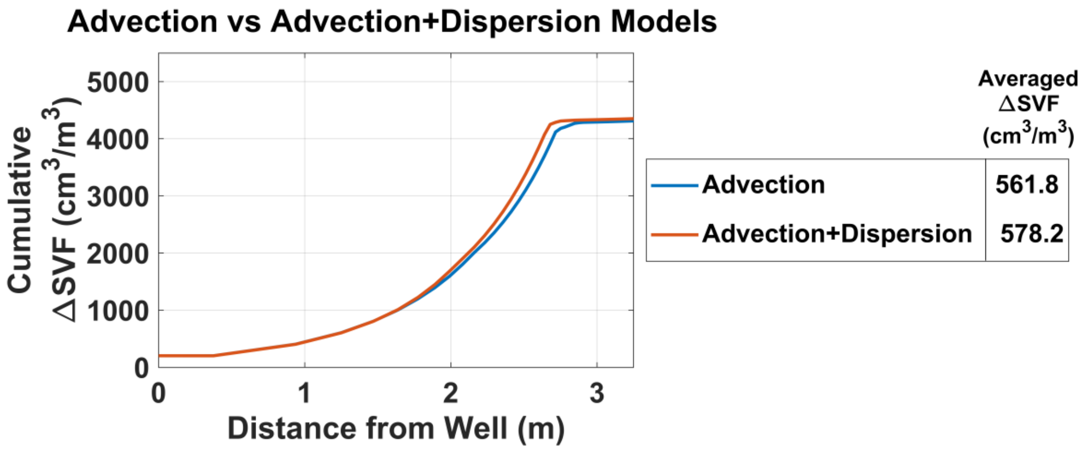

Figure S7: Change in the cumulative sulfide volume fraction for RTMs of NN-3, 525-550 m depth with advective transport compared to advective-dispersive transport with diffusion. Dispersity in each cell was set as 10% of the total flow distance (Appelo & Postma, 2004; Přikryl et al., 2018), and the diffusion coefficient is 0.3×10^{-9} m^2/s, the default value in PHREEQC (Parkhurst & Appelo, 2013).

Figure S8: Kinetic vs Equilibrium Precipitation

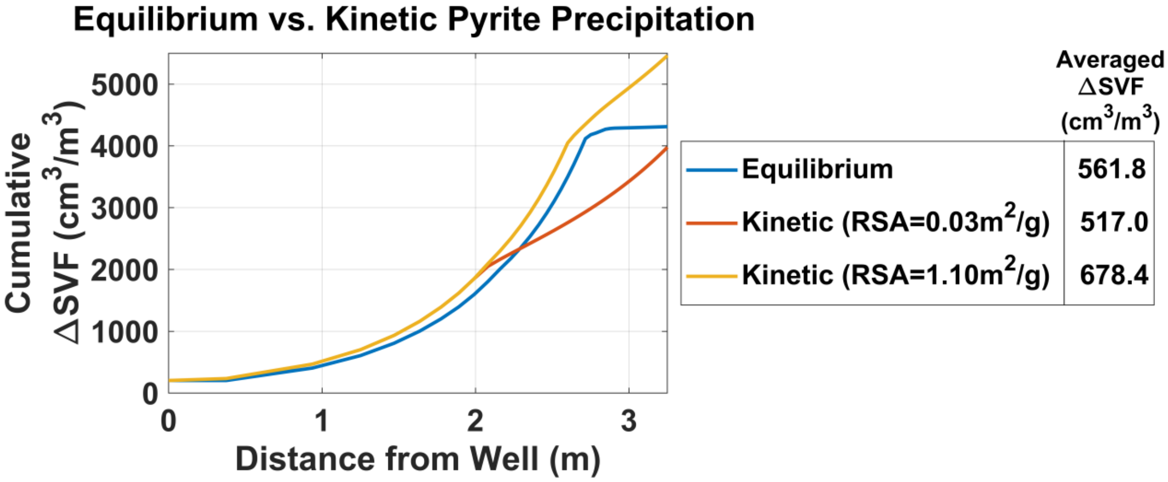

Figure S8: Cumulative change in sulfide volume fraction (SVF) for models where pyrite precipitation is either equilibrium driven (blue line), or kinetically controlled (yellow and orange lines). The kinetic rate constant for pyrite is 1.88×10^{-18} *mol/m*^{2}*/s (Marty et al., 2010). The pyrite reactive surface areas represent the highest (1.10 m*^{2}*/g) and lowest (0.03 m*^{2}*/g) values compiled from a literature search of measured pyrite reactive surface areas presented in Beckingham et al. (2016). By using the extremes values for the range of pyrite reactive surface area, we test the sensitivity of* H_2S *mineralization to the reactive surface area and evaluate the assumption of equilibrium precipitation. Pyrite is the only sulfide allowed to mineralize. The results are shown for the reactive transport model of NN-3, 525-550 m depth.*

Figure S9: Wireline Response Changes upon H_2S Injection

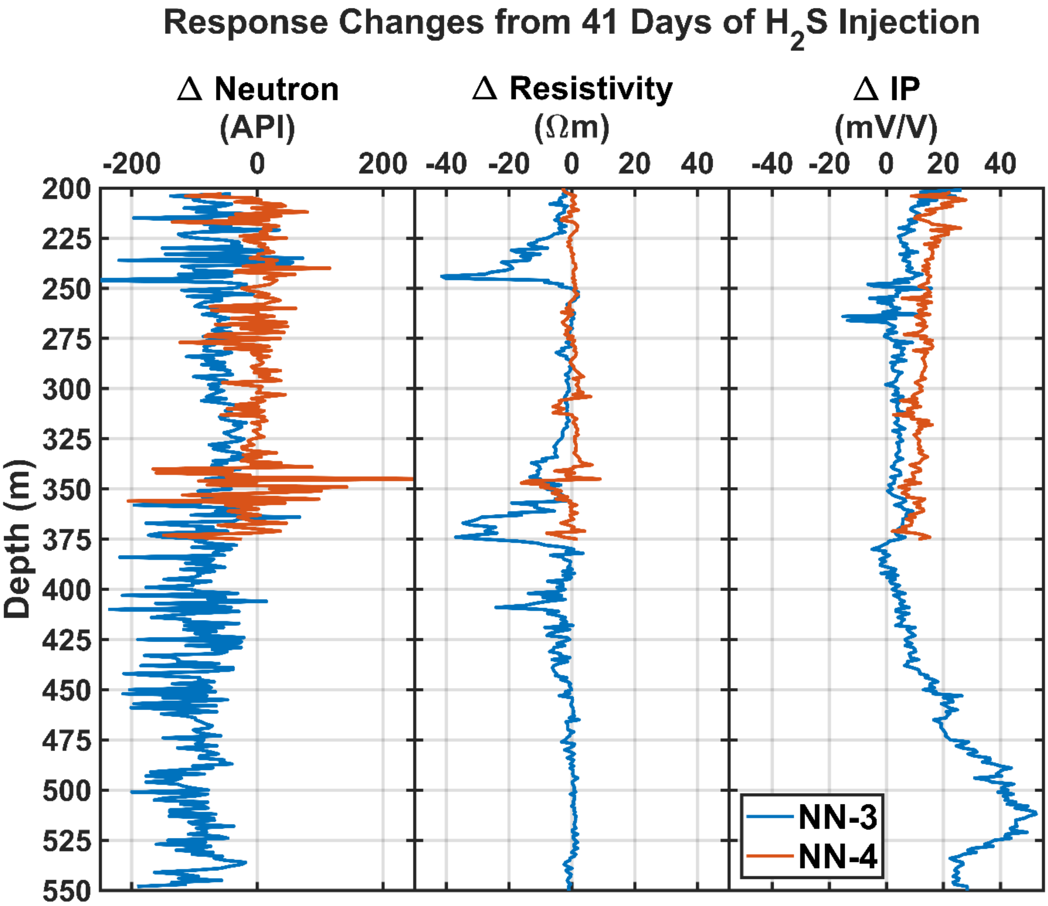

Figure S9: Wireline logging response changes after 40 days of H_2S injection at NN-3 and NN-4.

References (Supporting Information):

Appelo, C. A. J., & Postma, D. (2004). Geochemistry, groundwater and pollution, second edition. In *Geochemistry, Groundwater and Pollution, Second Edition*. https://doi.org/10.1201/9781439833544

Arnórsson, S., Bjarnason, J. Ö., Giroud, N., Gunnarsson, I., & Stefánsson, A. (2006). Sampling and analysis of geothermal fluids. *Geofluids*, *6*(3). https://doi.org/10.1111/j.1468-8123.2006.00147.x

Beckingham, L. E., Mitnick, E. H., Steefel, C. I., Zhang, S., Voltolini, M., Swift, A. M., Yang, L., Cole, D. R., Sheets, J. M., Ajo-Franklin, J. B., DePaolo, D. J., Mito, S., & Xue, Z. (2016). Evaluation of mineral reactive surface area estimates for prediction of reactivity of a multi-mineral sediment. *Geochimica et Cosmochimica Acta*, *188*. https://doi.org/10.1016/j.gca.2016.05.040

Galeczka, I. M., Stefánsson, A., Kleine, B. I., Gunnarsson-Robin, J., Snæbjörnsdóttir, S. Ó., Sigfússon, B., Gunnarsdóttir, S. H., Weisenberger, T. B., & Oelkers, E. H. (2022). A pre-injection assessment of CO2 and H2S mineralization reactions at the Nesjavellir (Iceland) geothermal storage site. *International Journal of Greenhouse Gas Control*, *115*. https://doi.org/10.1016/j.ijggc.2022.103610

Gómez-Díaz, E., Scott, S., Ratouis, T., & Newson, J. (2022). Numerical modeling of reinjection and tracer transport in a shallow aquifer, Nesjavellir Geothermal System, Iceland. *Geothermal Energy*, *10*(7). https://doi.org/10.1186/s40517-022-00217-3

Gysi, A. P., & Stefánsson, A. (2012). CO 2-water-basalt interaction. Low temperature experiments and implications for CO 2 sequestration into basalts. *Geochimica et Cosmochimica Acta*, *81*. https://doi.org/10.1016/j.gca.2011.12.012

Hafstað, Þ. H. (2003). Niðurrennslisholurnar NN-3 og NN-4 á Nesjavöllum. *ISOR: ÞHH-03-06*.

Hafstað, Þ. H., Stefánsson, H. Ö., & Franzson, H. (2015). Niðurrennsli á Nesjavöllum: Holur NN-6, NN-7 og NN-9. *ÍSOR-15035*.

Jeffery, G. H., Bassett, J., Mendham J, & Denney, R. C. J. (1989). *Vogel's textbook of quantitative chemical analysis* (5th ed.). Longman Scientific and Technical.

Jochum, K. P., Weis, U., Schwager, B., Stoll, B., Wilson, S. A., Haug, G. H., Andreae, M. O., & Enzweiler, J. (2016). Reference Values Following ISO Guidelines for Frequently Requested Rock Reference Materials. *Geostandards and Geoanalytical Research*, *40*(3). https://doi.org/10.1111/j.1751-908X.2015.00392.x

Kipp, K. L. (1987). HST3D—A computer code for simulation of heat and solute transport in three-dimensional ground-water flow systems. *U.S. Geological Survey Water-Resources Investigations Report 86–4095*.

Marty, N. C. M., Fritz, B., Clément, A., & Michau, N. (2010). Modelling the long term alteration of the engineered bentonite barrier in an underground radioactive waste repository. *Applied Clay Science*, *47*(1–2). https://doi.org/10.1016/j.clay.2008.10.002

Parkhurst, D. L., & Appelo, C. A. J. (2013). Description of input and examples for PHREEQC Version 3 — A computer program for speciation, batch-reaction, one-dimensional transport, and inverse geochemical calculations. In *U.S. Geological Survey Techniques and Methods, book 6, chapter A43*.

Přikryl, J., Marieni, C., Guðbrandsson, S., Aradóttir, E. S., Gunnarsson, I., & Stefánsson, A. (2018). H2S sequestration process and sustainability in geothermal systems. *Geothermics*, *71*. https://doi.org/10.1016/j.geothermics.2017.09.010

Roy, A., & Dhar, R. L. (1971). Radius of investigation in DC resistivity well logging. *Geophysics*, *36*(4). https://doi.org/10.1190/1.1440210

Stefánsson, A., Gunnarsson, I., & Giroud, N. (2007). New methods for the direct determination of dissolved inorganic, organic and total carbon in natural waters by Reagent-Free^{TM} Ion Chromatography and inductively coupled plasma atomic emission spectrometry. *Analytica Chimica Acta*, *582*(1). https://doi.org/10.1016/j.aca.2006.09.001

Paper 2

Quantifying H_2S Mineral Storage Processes in Fractured Basalt Using a Field-Scale Reactive Transport Model

D. A. Ciraula[1], S. W. Scott[1], E. L. Sonnenthal[2], E. Gómez-Díaz[3,4], B. I. Kleine-Marshall[5]

[1]Nordic Volcanological Center, Institute of Earth Sciences, University of Iceland, Reykjavík 101, Iceland.
[2]Lawrence Berkeley National Laboratory, Energy Geosciences Division, Berkeley, CA, 94720, USA.
[3]Geological Institute, Energy and Minerals Resources Group, RWTH Aachen University, Aachen, 52056, Germany.
[4]Geothermal Energy and Geofluids Group, Department of Earth Sciences, ETH Zurich, Zurich, 8092, Switzerland
[5]GeoZentrum Nordbayern, Friedrich-Alexander-Universität Erlangen-Nuremberg, Schlossgarten 5, 91054 Erlangen, Germany

Key Points:

- Over 25 years, 87% of injected H_2S mineralizes to pyrite before reaching Lake Thingvellir, resulting in minimal contamination of the lake
- Pyrite mainly forms in the rock matrix closest to the fractures, where slow, diffusion-controlled transport enables fluid-rock interactions
- Lithology plays an important role in H_2S mineralization, controlling the availability of iron for pyrite formation

---

Corresponding author: D. A. Ciraula, `danielac@hi.is`

Abstract

Hydrogen sulfide (H_2S) mineral storage in basalts offers an approach to reduce emissions from geothermal energy production. Laboratory-scale geochemical models indicate that the injected H_2S-charged water interacts with basalt to mineralize iron-sulfides. Understanding the processes controlling H_2S mineralization at the field-scale is essential to optimize industrial-scale mineral storage systems and mitigate environmental impacts. Existing models contain simplifying assumptions that reduce their ability to accurately capture real-world systems. To evaluate the efficacy of field-scale H_2S mineral storage, this study develops a novel, 3D multiple-porosity reactive transport model of H_2S re-injection into fractured basalts at the Nesjavellir geothermal site (SW Iceland). The multiple-porosity framework simulates fluid-rock interactions within both the advection-dominated fractures and the diffusion-dominated rock matrix. Overall, H_2S mineral storage is effective with 87% mineralizing as pyrite before reaching the nearby lake over 25 years of injection. This is consistent with estimates from fluid mass balance calculations of similar injection systems. However, the model reveals that such fluid mass balance calculations provide only a limited view of total mineralization. The high-permeability fracture network, calibrated to values between 10^{-12} and 10^{-10} m^2, efficiently transports H_2S and results in dispersed pyrite mineralization. Large vertical permeabilities in fault zones and non-isothermal fluid flow drive upward fluid migration, but H_2S concentrations remain below 2.5 µM at Lake Thingvellir. Approximately 90% of the mineralization occurs within the outer basalt matrix, where fluid-rock interactions are greatest, underscoring the importance of multiple-porosity frameworks in field-scale reactive transport modeling.

Plain Language Summary

Geochemical models provide a powerful tool to characterize how water interacts with rocks in the subsurface. However, implementing complex fluid-rock processes in models is challenging, leading to simplified models that lack the ability to accurately represent real-world subsurface processes. In this study, we develop a field-scale geochemical model that considers many of these complexities to better characterize hydrogen sulfide (H_2S) mineral storage at a geothermal site in Iceland. H_2S gas is emitted during geothermal power production and is toxic to humans and the environment. In the mineral storage approach, the H_2S is injected into the subsurface, where it interacts with the rock and mineralizes, thus sequestering the emissions. Complexities included in the model reveal that H_2S mineralization depends on the rock's chemical composition and how water and H_2S are transported through it. Water flows quickly through fractures in the rock, and thus, H_2S is transported away before it has a chance to interact with the rock. Deeper within the rock matrix, H_2S transport is controlled by slower processes, which provide time for the H_2S to react with the rock and mineralize. Most mineralization occurs when the rock contains minerals that readily react with water and are rich in iron. Overall, H_2S mineral storage at Nesjavellir is shown to be effective, as 87% of the H_2S injected over 25 years mineralizes before reaching the extent of the nearby lake, and contamination of the lake is minimal.

1 Introduction

Geothermal energy production has grown to a combined global capacity of 16,318 MW (Gutiérrez-Negrín, 2024), offering a stable alternative source of energy to fossil fuels. While geothermal energy generation represents a relatively clean source of energy, the industry emits an estimated 9.63 Mt of CO_2 and 0.13 Mt of H_2S per year (Marieni et al., 2018). These gases originate from the high-enthalpy geothermal production fluids and are released into the atmosphere upon energy production.

One approach to reduce these emissions is through mineral storage, where the gases are captured, dissolved into the geothermal wastewater, and re-injected into the subsurface (Matter et al., 2016; Gunnarsson et al., 2018). Basaltic rocks are a common injection target due to their high reactivity and high divalent cation content of up to 25 wt% Ca, Mg, and Fe (Matter et al., 2016). Laboratory experiments find that upon interaction with basalt at low temperatures (< 100°C), gases mineralize to carbonates (i.e. calcite, siderite, magnesite) and iron sulfides (i.e. pyrite, pyrrhotite), along with chalcedony, smectites, zeolites, Fe-Al hydroxides, and potentially elemental sulfur (Galeczka et al., 2022; A. Stefánsson et al., 2011; Přikryl et al., 2018; Schaef et al., 2013).

While laboratory studies suggest effective mineral storage in basalts, uncertainty still remains in the industrial-scale implementation of mineral storage approaches due to complex hydrologic, geologic, and engineering processes in the field (Liu et al., 2019). Previous studies have used methods such as pump tests (S. K. White et al., 2020), geophysical wire-line logging (Ciraula et al., 2024; Lévy et al., 2024), and mass balance calculations from borehole water samples (Clark et al., 2018, 2020; Gunnarsson et al., 2018) to evaluate field-scale mineral storage. The mass balance calculations suggest that 60% and 85% of the injected CO_2 and H_2S mineralize after 3.5 years, respectively (Clark et al., 2020). However, each of these methods is an indirect measurement, contains ambiguity in its interpretations, and its ability to characterize total mineralization across the entire reservoir remains uncertain.

Geochemical modeling is a powerful tool that complements field sampling methods by constraining the relevant fluid-rock interactions that govern mineral storage. Understanding these fluid-rock interactions is essential for optimizing field injection strategies and mitigating the environmental impacts of re-injection, such as acidification of the groundwater system, contamination of surface waters, and pore-clogging of the injection reservoir. This is particularly important in relation to H_2S mineral storage, as a recent study examining time-lapse changes in geophysical logs recorded in injection wells called into question the permanence of H_2S mineral storage (Lévy et al., 2024). Reactive transport models couple together complex hydrological (e.g., non-isothermal flow, fracture vs. matrix flow and transport), geochemical (e.g., variable lithology, heterogeneous porosity and permeability, mineral reaction kinetics), and engineering (e.g., variable injection rates and temperatures, injection fluid chemistry) processes that govern mineral storage systems over time (Steefel & Lasaga, 1994; Steefel et al., 2005; Aradóttir, Sonnenthal, Björnsson, & Jónsson, 2012).

Despite their utility, few studies have developed field-scale reactive transport models for mineral storage systems (Aradóttir, Sonnenthal, Björnsson, & Jónsson, 2012; Liu et al., 2019; Bacon et al., 2014; Ciraula et al., 2024; Přikryl et al., 2018). Significant technical challenges are faced when integrating complex geochemical and hydrological processes at the macroscopic, continuum scale (Carrera et al., 2022; Baqer & Chen, 2022). As a result, field-scale models often rely on simplifying assumptions that may reduce their accuracy, particularly over long time-scales. One such simplification is the effective porous medium approach, which assumes uniform flow and transport processes throughout the domain rather than explicitly modeling distinct processes in fractures and the rock matrix (i.e., multiple-porosity). This is a substantial limitation for mineral storage simulations, as laboratory-scale models indicate that contrasting flow and transport in fractures and the rock matrix strongly influence mineralization, which mainly occurs in diffusion-dominated zones where the reaction rates are large relative to flow rates (i.e., rock matrix with large Damköhler numbers) (Giammar et al., 2014; Adeoye et al., 2017; Luhmann et al., 2017; Xiong et al., 2017). Furthermore, Chen et al. (2024) demonstrated that permeability distributions influence the spatial distribution of various carbonate species, with magnesite forming sharp mineralization fronts while calcite and siderite exhibit more diffuse mineralization. Field-scale reactive transport simulations of mineral storage approaches have thus far followed the effective porous medium framework (i.e., single-porosity), and thus, they are less sensitive to these complex flow processes. These field-scale models are also simplified to 1D or 2D isothermal flow and transport, further limiting their ability to capture the full heterogeneities of real-world systems. Lastly, reactive transport models, such as those presented in Ciraula et al. (2024) and Přikryl et al. (2018), are often constructed with simplified mineralogy, potentially overlooking important fluid-rock interactions.

In this study, we develop a field-scale, 3D reactive transport model of the Nesjavellir H_2S mineral storage site. The model uniquely couples non-isothermal fluid flow and solute transport through a multiple-porosity medium with kinetically-controlled geochemical reactions to simulate H_2S mineral storage under real-world conditions. The main objectives of this model are to (1) evaluate the long-term effectiveness of H_2S mineral storage, (2) constrain geological controls on H_2S mineralization, (3) assess the risk of H_2S contamination of surface waters, and (4) validate the ability of fluid mass balance monitoring methods to constrain the total effectiveness of H_2S mineralization. Through the development of this integrated model, we aim to demonstrate how reactive transport can be used as a powerful tool to assess complex fluid-rock interactions at the field-scale and evaluate the performance of mineral storage strategies.

2 Site Description

2.1 Geologic Setting and Model

The Nesjavellir high-temperature geothermal field is located in southwest Iceland between the Hengill central volcano and Lake Thingvellir, Iceland's largest lake (Figure 1). Lake Thingvellir extends into Thingvellir National Park, a UNESCO World Heritage Site, and the lake and surrounding water catchment area are protected by Icelandic legislation (Iceland Ministry of the Environment & Climate, 2005).

The Hengill volcano is situated on a ridge-ridge-transform triple junction between the Reykjanes Rifting Zone, Southern Seismic Zone, and the Western Volcanic Zone (Foulger, 1988). The area is composed mainly of late Quaternary and post-glacial age volcanic rocks, primarily in basalt flows and hyaloclastites (Arnason et al., 1969; Foulger & Toomey, 1989). A roughly 10 km wide graben structure transverses the area and is oriented parallel to the hyaloclastite ridges at approximately N30°E (Arnason et al., 1969; Foulger, 1988). The Nesjavellir power station sits within an inner, 5 km wide graben that is the focus of much of the faulting and volcanism (Arnason et al., 1969).

The area of interest modeled in this study is the shallow groundwater system above the top of the geothermal clay cap, located at $\sim$500 m depth (Franzson, 1988). The shallow groundwater system is cold water with measured down-borehole water temperatures ranging from 10-25°C. Alteration is minimal at depths less than 400 m, underlain by an alteration zone of zeolites and smectites approaching the clay cap (Ciraula et al., 2024; Helgadóttir, 2021). Intrusions are not present at these shallow depths (Franzson, 1988).

In total, our geological model considers six lithological units informed from drill cuttings and well logging reports: (1) Grunnberg composite hyaloclastites, (2) Nesjahraun lava flow, (3) Hagavíkurhraun lava flow, (4) Stangarhólshraun lava flow, (5) a layer of deep lava flows, and (6) a layer bounding the bottom of the model near the geothermal clay cap (Franzson, 1988; Ciraula et al., 2024; Weisenberger & Snæbjörnsdóttir, 2021; Helgadóttir, 2021; Sigfusson et al., 2011). The Grunnberg composite hyaloclastites dominate the upper 500 m and are composed of vesicular hyaloclastite tuff, hyaloclastite breccia, and pillow basalt. Significant amounts of basaltic glass (>20%) have been identified in drill cuttings from this unit. The layer of deep lava flows is observed in boreholes at depths of 170-250 m. Grain size is variable in this layer, ranging from very fine- to medium-grained, and there is minimal basaltic glass present. Three Holocene lava flows are also present at the surface (0-50 m depth) northeast of the injection wells: Nesjahraun (2 ka), Hagavíkurhraun (5.5 ka), and Stangarhólshraun (8 ka) (Sigfusson et al., 2011).

The model also includes three near-vertical, NNE-SSW fault systems, identified through drilling and field mapping (Franzson, 1988; Hafstad et al., 2007). These faults are characterized by high horizontal and vertical permeabilities and play a critical role in fluid transport near the surface and at injection depths (Gómez-Díaz et al., 2022).

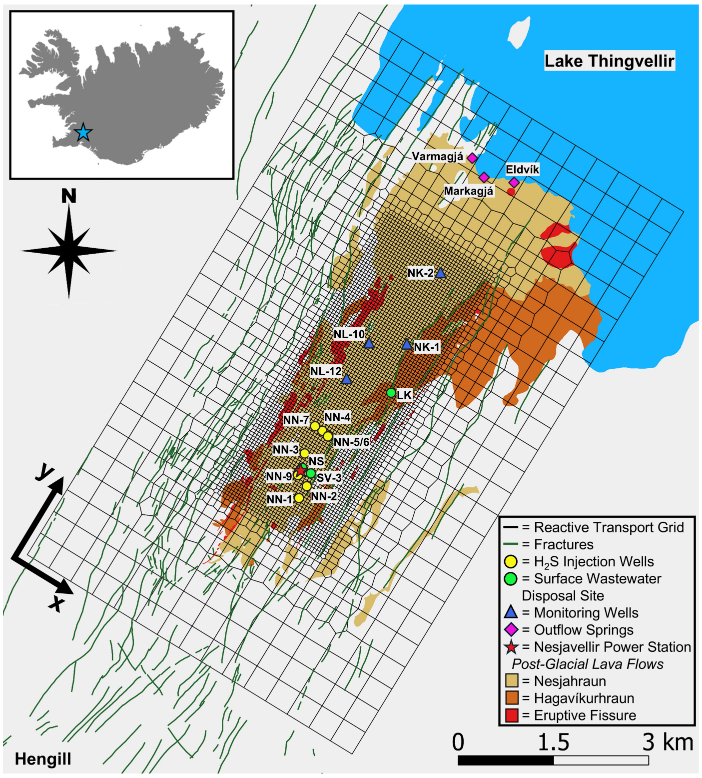

Figure 1. Map of the Nesjavellir injection site in southwest Iceland and the reactive transport grid. A simplified geological map of the surface lithology is shown, mapping the extents of the post-glacial lava flows considered in the reactive transport model. Uncolored areas within the grid extent are treated as Grunnberg composite hyaloclastites.

2.2 Geothermal Production, Wastewater Disposal, and Monitoring

The Nesjavellir power plant began operations in 1990 with the drilling of four boreholes for space heating. Electricity generation started in 1998 with two 30 MWe turbines, expanded to 90 MWe in 2001 with a third turbine, and reached the current 120 MWe capacity in 2005 with the addition of a fourth turbine. Nesjavellir produces an additional 300 MWth in the form of heated groundwater used for district heating in the Reykjavik area ∼30 km away (Snæbjörnsdóttir et al., 2021).

Energy and electricity production at Nesjavellir, detailed in Zarandi and Ivarsson (2010), is briefly outlined here to provide context for the wastewater injection. Three main types of wastewater are produced at Nesjavellir; (i) condensate wastewater formed when the steam that drives the turbines is condensed back to water, (ii) heated groundwater which is used to condense the steam and is sourced from shallow wells near Lake Thingvellir, and (ii) separated geothermal liquid remaining after flashing of the high-enthalpy fluid from the production boreholes.

Current operations at Nesjavellir produce roughly 240 kg/s of separated geothermal wastewater and 240 kg/s of condensate (Ívarsson, 2019). Various methods are utilized to dispose of the geothermal wastewater (Zarandi & Ivarsson, 2010; Ívarsson, 2019). Prior to 2004, shallow wells near the power plant and a disappearing stream (Laekjarhvarf) were used for wastewater disposal. Since 2004, injection wells ("NN wells") have been used for wastewater injection, in addition to shallow wells and surface disposal. In 2015, the NN-6, NN-7, and NN-9 wells were drilled to increase the injection capacity (Ívarsson, 2019). The injection wells, which are the focus of this study, receive most of the separated geothermal fluid and the condensate water, with excess being disposed of at the surface along with heated groundwater.

To monitor the Nesjavellir geothermal area, Reykjavik Energy and its subsidiary Orka Náttúrunnar, which own and operate the Nesjavellir power plant, collect samples twice per year in shallow monitoring boreholes in the Holocene lava flows and at springs at the shore of Lake Thingvellir (see Figure 1 for a few of these sites) (Zarandi & Ivarsson, 2010). Chemical and thermal pollution related to geothermal production has been observed in the springs since the start of the power production in 1990 (Gómez-Díaz et al., 2022; Zarandi & Ivarsson, 2010). Strategies recently implemented to reduce the chemical and thermal pollution include utilizing cooling towers, a retention tank to allow for silica polymerization before disposal (Zarandi & Ivarsson, 2010), hot water injection away from the Nesjavellir site (Mosfellsheidi), and utilization of deep injection wells (NJ-18 and NN-10) (Ívarsson, 2019; Zarandi & Ivarsson, 2010).

In addition to the subsurface pollution from wastewater disposal, geothermal energy production also results in atmospheric emissions, notably CO_2 and H_2S gases. These gases can be highly concentrated, with vapor phase concentrations measured at production well heads averaging around 3,200 ppm CO_2 and 800 ppm H_2S (Scott et al., 2014) at the nearby Hellisheidi power plant. At Nesjavellir, the yearly emissions are estimated to be 15,000-18,600 tons of CO_2 and 8,000-11,300 tons of H_2S (Marieni et al., 2018; Snæbjörnsdóttir et al., 2021). To reduce these emissions, a process was implemented at Nesjavellir in 2021 in which H_2S gas is dissolved into a mixture of separated geothermal wastewater and condensate wastewater using liquid ring vacuum pumps (Galeczka et al., 2022; Ciraula et al., 2024; Lévy et al., 2024). The H_2S-rich wastewater is then continuously injected into the shallow groundwater system through the NN wells.

3 Modeling Approach

The model developed in this study couples reactive chemistry to calibrated hydrological flow models of the H_2S-rich geothermal wastewater injection into the shallow groundwater system at Nesjavellir. The reactive transport simulations are performed using TOUGHREACT (Xu et al., 2006, 2011, https://tough.lbl.gov/software/toughreact_v4-13-omp), a numerical simulator that introduces chemical reactivity to the fluid and heat flow simulator, TOUGH2 (Pruess et al., 1999). The TOUGH suite of codes can incorporate non-isothermal and multi-component fluid and heat flow, multiple -porosity capabilities, feedback of porosity-permeability changes on fluid flow, three-dimensional capabilities, and parallelized computation (e.g., Aradóttir, Sonnenthal, Björnsson, and Jónsson (2012); Ratouis et al. (2022); Xu et al. (2006)).

3.1 Governing Flow and Transport Equations

TOUGHREACT performs the numerical modeling through the integral finite differences method (IFD), in which the model domain is spatially discretized based on integral statements of conservation of mass and energy:

$$\frac{d}{dt}\int_{V_n} M^k dV_n = \int_{A_n} \mathbf{F}^k \cdot \mathbf{n} dA_n + \int_{V_n} q^k dV_n \ , \tag{1}$$

where M_k represents the mass and energy density of component k within volume V_n, $\mathbf{F_k} \cdot \mathbf{n}$ is the flow term of flux of component k normal to surface A_n, and q_k represents the contribution of component k from sources and sinks. By introducing volume averages over V_n and surface averages over A_n, the conservation of mass and energy equation can be rewritten for an average mass density, M_k:

$$\frac{\partial M_k}{\partial t} = -\nabla \mathbf{F_k} + q_k \ . \tag{2}$$

This study considers non-isothermal flow of a single water in fully saturated conditions (TOUGH module EOS1), thus simplifying the number of components k in Equations 1 and 2. The q_k term becomes comprised of water sources and sinks (q_w), heat sources and sinks (q_h), and chemical component sources and sinks from the water ($q_{j,w}$) and reactions with the solid rock media ($q_{j,s}$). Mass density terms for water (M_w), heat (M_h), and chemical components (M_j) simplify to:

$$M_w = \phi\rho_w \ , \quad M_h = \phi\rho_w U_w + (1-\phi)\rho_s U_s \ , \quad M_j = \phi C_{j,w} \ , \tag{3}$$

where ϕ is porosity, ρ is density, U is internal energy, $C_{j,w}$ is the concentration of component j in the water, and subscripts w and s denote water and solid rock components, respectively. Finally, the average mass flux terms ($\nabla\mathbf{F_k}$) in the single-phase, fully saturated system become:

$$\mathbf{F_w} = \rho_w \mathbf{u_w} \ , \quad \mathbf{F_h} = h_w \rho_w \mathbf{u_w} - \lambda\nabla T \ , \quad \mathbf{F_j} = \mathbf{u_w} C_{j,w} - (\tau\phi D_w)\nabla C_{j,w} \ , \tag{4}$$

where $\mathbf{u_w}$ is the Darcy's velocity for the liquid phase, h_w is the specific enthalpy for the heat convection, λ is the thermal conductivity for heat conduction, T is the temperature, τ is tortuosity, and D_w is the diffusion coefficient, set here to 6×10^{-9} m^2/s (Ratouis et al., 2022). The Darcy velocity is given as:

$$\mathbf{u_w} = -\mathbf{k}\frac{k_{r,w}}{\mu_w}(\nabla P_w - \rho_w \mathbf{g}) \ , \tag{5}$$

comprised of the permeability in each dimension ($\mathbf{k}$), relative permeability ($k_{r,w}$), water viscosity (μ_w), fluid pressure field (P_w), and the gravity vector ($\mathbf{g}$).

TOUGHREACT solves flow, transport, and geochemical reactions using a sequential, non-iterative time-stepping scheme. First, the flow equations are solved using Newton-Raphson iterations at each time step to define the fluid velocity field. The fluid velocity field and diffusive flux terms are then used to solve chemical transport for each component, providing concentrations at each grid element. Local chemical reactions are then solved for each grid block via Newton–Raphson iterations, updating the fluid concentrations, and rock mineralogy. The individual flow, transport, and geochemical reaction processes are each solved with a fully implicit time-weighting scheme.

3.2 Fluid Flow and Transport

3.2.1 Grid Structure

We developed the IFD model grid using AMESH (Haukwa, 1998), PyTOUGH (Croucher, 2011), and TIM (Yeh et al., 2013) software. There are ∼72,500 elements with ∼204,000 connections, covering a total area of 60 km^2 (6×10 km) northeast of the Nesjavellir geothermal plant. The grid extends from the water table down to the top of the geothermal clay cap at ∼500 m depth and is vertically discretized into 16 ∼50 m-thick layers. We defined the water table using data from Reykjavik Energy (Gómez-Díaz et al., 2022) alongside a digital elevation model and measured depth-to-water values in various wells. A Gaussian filter was applied to the water table surface to smooth large gradients inherited from the high-resolution digital elevation model. We rotate the grid by 31.5° E of N to orient it parallel to the NNE-SSW rifting direction and associated normal faults. This orientation allows for the cross-rift permeability (x-dimension) and along-rift permeability (y-dimension) to be considered individually (Gómez-Díaz et al., 2022).

The grid is irregularly discretized in the x-y plane to increase the computational efficiency while preserving resolution in the main areas of interest. Grid refinement to 50×50 m cells is focused around the H_2S wastewater injection wells. Cells within the transition zone between the coarse and refined regions contain non-orthogonal connections, which can create mass balance errors in the IFD solution. To reduce these errors, the geometries of the elements within the transition zones were optimized via a nonlinear least-squares operation, considering connection angles and the degree of cell skewness (Croucher, 2011).

3.2.2 Multiple Interacting Continua (MINC)

To capture the complex fluid flow in the fractured basalt media, this model implements a multiple-porosity grid over the entire model extent based on the Multiple Interacting Continua (MINC) approach (Pruess & Narasimhan, 1985). This framework is built on the principle that changes in reservoir conditions propagate quickly through the interconnected fractures, while affecting the rock matrix more slowly. The MINC approach sub-discretizes the grid elements into individual fracture and matrix elements. Global flow in the model domain occurs exclusively through the fracture elements, which are modeled as an effective porous continuum representing the fracture network. The rock matrix is further discretized into nested volume elements such that the change in the thermodynamic conditions of the matrix block is controlled by the proximity of the matrix blocks to the nearest fracture. Local, transient interporosity flow occurs between the connected fracture and matrix elements and between the nested matrix elements. Overall, the MINC approach captures complex flow in the fracture domain and allows for distinguishing transport processes and chemical reactions occurring in the subsurface fractures and reservoir matrix.

This model considers a fracture continuum and two nested matrix continua with volume fractions of 5%, 25%, and 70%, respectively (Ratouis et al., 2022). We consider three perpendicular fracture sets (x, y, z) with a fracture spacing of 2 m (DePaolo et al., 2022).

Table 1. Porosity and calibrated permeability values for all rock types of the MINC model.

		Permeability (m^2)		
Rock Type	Porosity	k_x	k_y	k_z
Grunnberg Hyaloclastites				
- Fracture Network	0.60	1.01×10^{-12}	9.71×10^{-11}	1.29×10^{-13}
- Outer & Inner Matrix	0.25	1.00×10^{-14}	1.00×10^{-14}	1.00×10^{-14}
Holocene Lava Flows[a]				
- Fracture Network	0.60	5.06×10^{-12}	1.94×10^{-12}	1.49×10^{-12}
- Outer & Inner Matrix	0.10	1.00×10^{-15}	1.00×10^{-15}	1.00×10^{-15}
Deep Lava Flow Layer				
- Fracture Network	0.60	1.46×10^{-13}	1.56×10^{-11}	1.49×10^{-12}
- Outer & Inner Matrix	0.10	1.00×10^{-15}	1.00×10^{-15}	1.00×10^{-15}
Faulted Zone 1				
- Fracture Network[b]	0.60	3.00×10^{-11}	5.00×10^{-10}	5.00×10^{-13}
- Outer & Inner Matrix	0.10	1.00×10^{-14}	1.00×10^{-14}	1.00×10^{-14}
Faulted Zone 2				
- Fracture Network[b]	0.60	3.00×10^{-12}	5.00×10^{-11}	5.00×10^{-13}
- Outer & Inner Matrix	0.10	1.00×10^{-14}	1.00×10^{-14}	1.00×10^{-14}
Faulted Zone 3				
- Fracture Network[b]	0.60	3.00×10^{-12}	5.00×10^{-12}	5.00×10^{-13}
- Outer & Inner Matrix	0.10	1.00×10^{-14}	1.00×10^{-14}	1.00×10^{-14}
Bottom Boundary	0.26	1.00×10^{-14}	1.00×10^{-14}	1.00×10^{-14}

[a] Nesjahraun, Hagavíkurhraun, and Stangarhólshraun lava flows.

[b] Fracture permeability calibrated in Gómez-Díaz et al. (2022).

3.2.3 Porosity, Permeability, and Flow Model Calibration

The MINC porosity and permeability values are presented in Table 1. We assigned the matrix porosity and permeabilities based on typical values observed in fresh Icelandic basalts as reported in Scott et al. (2023). The hyaloclastite matrix has a porosity of 25% and x-, y-, and z-permeabilities of 1×10^{-14} m^2. Lava flows, which typically have lower porosity and permeability (Scott et al., 2023), are assigned a porosity of 10% and x-, y-, and z-permeabilities of 1×10^{-15} m^2. We estimate the MINC fracture porosity to be 60% following the method presented in Ratouis et al. (2022), where the fracture total porosity of the MINC model is the same as the porosity of a single, effective porous media model:

$$\phi_{eff} = \phi_f \times \theta_f + \phi_m \times \theta_m \, , \tag{6}$$

where θ_f is the fracture volume fraction (5%), θ_m is the matrix volume fraction (95%), and ϕ_{eff}, ϕ_f, and ϕ_m are the effective, fracture, and matrix porosities, respectively. Accounting for matrix porosity differences between hyaloclastites and lava flows and the relative volumes of hyaloclastites and lava flows within the model domain, equation 6 becomes:

$$\phi_{eff} = \phi_f \times \theta_f + \phi_{m,H} \times \theta_{m,H} + \phi_{m,L} \times \theta_{m,L} \, , \tag{7}$$

where the subscripts H and L denote the hyaloclastite and basalt lava lithologies, respectively. A fracture porosity of 60% results in an effective porous media porosity of 26%, which is in line with values measured in Nesjavellir wells and core samples (Muñoz, 1996; V. Stefánsson, 1991) and qualitative analysis of rock cuttings from NN-3 and NN-4 (Helgadóttir, 2021). Porosity and permeability changes are calculated using the abundance and molar volume of individual minerals along with a simplified Carman-Kozeny relationship (Bear, 1972), but feedback on flow and transport is not considered.

We utilized PEST software (Doherty & Hunt, 2010) to iteratively calibrate the fracture permeability values of the major lithological units to temperature data (n=21) measured from 2001-2013 in the NK-01, NL-10, and NL-12 monitoring boreholes. The model was fit to temperature measurements at grid cell centers for NL-12, and to the average temperature measured in the upper 50 m of NK-01 and NL-10, given the temperature fluctuations over the shallow depths of the NK wells. To reduce the high computational cost of 3D model calibration within the MINC domain, calibration was performed on a coarse (200×200×50 m) subset of the full model surrounding the injection wells. Additionally, the Holocene lavas are calibrated as a single anisotropic unit. The deep lava flow identified in the NN boreholes has the same z-permeability as the Holocene lavas, but the x- and y-permeabilities are treated as separate parameters. The permeabilities of major fault zones are adopted from values presented in Gómez-Díaz et al. (2022), who calibrated them using tracer tests and temperature data.

For all rock types listed in Table 1, the rock grain density is 2650 $\mathrm{kg\,m^{-3}}$, the thermal conductivity is set to 1.7 $\mathrm{W\,m^{-1}\,{}^{\circ}C^{-1}}$, and the rock grain specific heat is set to 900 $\mathrm{J\,kg^{-1}\,{}^{\circ}C^{-1}}$. We set the matrix and fracture tortuosity factors to 0.1 and 0.8, respectively. The fracture tortuosity and thermal conductivity are further scaled by the bulk fracture porosity to account only for fracture intersections.

3.2.4 Sources and Sinks

Sources and sinks within the model domain include various wastewater injection and fresh groundwater production wells. The sources, detailed in Table 2, include:

1. Surface wastewater disposal at shallow injection wells (SV-3 and NS) near the power station and Laekjarhvarf (LK), a disappearing stream near the Holocene lava field. To model infiltration of the surface disposal observed in NL-12, wastewater is supplied from the shallow injection wells to the upper 100 m of the water column.
2. Wastewater injection into the NN wells (NN-1, NN-2, NN-3, NN-4, NN-5, NN-6, NN-7, NN-9). Injection rates and temperatures were provided by Reykjavik Energy.
3. Cold groundwater production wells at the Grámelur pumping station.

3.3 Geochemical System

3.3.1 Fluid and Rock Chemistry

Chemical analyses of Nesjavellir waters presented in Ciraula et al. (2024) and Sigfusson et al. (2011) constrain the fluid chemistry of the reactive transport model. The background fluid for the model was sampled in 1991, before contamination from geothermal wastewater disposal (Sigfusson et al., 2011). Geothermal wastewater disposed of at the surface was measured by Sigfusson et al. (2011) at the Laekjarhvarf disappearing stream, at the power station outlet, and in the surface stream in 2008. The H_2S-rich injection waters were sampled by Ciraula et al. (2024) at the NN-3, NN-4, NN-5, and NN-7 boreholes in November 2021. Injection water chemistry of the NN-1, NN-2, NN-6, and NN-9 boreholes is defined as the average of the NN-4, NN-5, and NN-7 waters, given that similar water is sent to each of these wells (Ívarsson, 2019). Major cation and anion concentrations were measured using Inductively Coupled Plasma Optical Emission Spectroscopy (ICP-OES; ThermoFisher

Table 2. Reactive transport model source and sink locations, depths, and rates during the H_2S injection period.

Source/Sink Name	Coordinates (ISN-93)	Source/Sink Measured Depths[a,b] (m)	Avg. Rate[c] (kg/s)	Avg. Temp.[c] (°C)
NN-1	389,995; 402,110	295	43.5	88.9
NN-2	390,120; 402,300	415	43.5	88.9
NN-3	390,105; 402,775	390, 445, 535	10.5	68.3
NN-4	390,360; 403,170	280, 300, 330, 388	109.6	85.7
NN-5	390,460; 403,090	220, 320, 520	30.9	88.7
NN-6	390,450; 403,080	246, 280, 325, 425, 510	53.5	84.8
NN-7	390,240; 403,240	200, 220, 255, 280, 400, 440	32.4	88.6
NN-9	389,980; 402,470	310	43.5	88.9
SV-3 Shallow Well	390,195; 402,475	0-100	200.0[b]	40.0[b]
NS Shallow Well	390,055; 402,670	0-100	160.0[b]	40.0[b]
Laekjarhvarf (LK)	391,445; 403,750	0-50	200.0[b]	40.0[b]
Grámelur Pumping Wells	394,075; 406,445	0-50	-2020.0[b]	–

[a] Rates are allocated evenly over source/sink depths.

[b] Data estimates from Gómez-Díaz et al. (2022), Zarandi and Ivarsson (2010), Ívarsson (2019).

[c] Average rate and temperature from 01/2021-01/2024. Positive rates denote injection.

iCAP 7400 Duo) and Ion Chromatography (Dionex ICS-2000), respectively (Ciraula et al., 2024). Dissolved sulfide concentrations were determined by mercury acetate titrations with dithizone as the indicator (Arnórsson et al., 2006). A modified alkalinity titration was used to determine the dissolved carbon dioxide concentrations (Arnórsson et al., 2006; Jeffery et al., 1989; Stefánsson et al., 2007). Table 3 details the resulting fluid compositions.

Drill cuttings obtained from the NN-3, NN-4, and NN-7 boreholes constrain the mineralogy of the host rock (Ciraula et al., 2024; Helgadóttir, 2021). The bulk rock composition was measured using ICP-OES analysis of milled cuttings as presented in Ciraula et al. (2024). A linear least-squares fit to the average bulk rock composition, considering the primary minerals listed in Table 4, constrained the initial mineral abundances in the reactive transport model. Comparisons to field observations at Nesjavellir validate the resulting primary mineralogy (Vivanco et al., 2024). We defined the basaltic glass composition stochiometrically from the average bulk rock composition, and estimated the volume fraction to be 0.25 in the hyaloclastites and 0.05 in the lava flows, following observations of drill cuttings from the NN wells (Helgadóttir, 2021) and typical Icelandic basalts (Scott et al., 2023). The volume fractions of the other primary minerals are scaled to account for the addition of the basaltic glass (Table 4).

Secondary minerals are determined based on laboratory observations and results of previous geochemical models of basalt alteration in H_2S-charged fluids (see Ciraula et al. (2024) and references therein). Table 4 contains the primary and secondary minerals considered by the reactive transport simulations, and their elemental compositions are detailed in Table S1. We use the *carbfix.dat* thermodynamic database (Voigt et al., 2018; Heřmanská et al., 2022, 2023), based off the database described in Aradóttir, Sonnenthal, and Jónsson (2012) and the *core10.dat* database (Neveu et al., 2017), with redox conditions determined by the HS^-/SO_4^{2-} couple.

Table 3. Chemistry data of initial background fluid, the H_2S-rich injection fluid, and the surface disposal wastewater. Concentrations are given in mmol/L.

	Background Water[a]	H_2S-Rich Injection Wastewater[b]				Surface Wastewater[c]	
		NN-3	NN-4	NN-5	NN-7	SV-3/NS	LK
Sample Date	1991	11-2021	11-2021	11-2021	11-2021	3-2008	3-2008
pH/T_{pH}	7.71/25	9.1/21	8.5/21	8.7/21	8.9/21	8.03/17.7	8.64/22.5
Al	0.00248	0.0420	0.0419	0.0434	0.0418	0.00557	0.0322
B	0.0111[d]	0.103	0.103	0.103	0.104	0.00934	0.083
Ca	0.219	0.0105	0.0105	0.0103	0.0108	0.236	0.206
Cl	0.264	2.494	2.49	2.48	2.50	0.463	2.243
F	0.005	0.0402	0.0401	0.0401	0.0403	0.009	0.033
Fe_{Tot}[f]	0.00100	0.000269	0.000179	0.000591	0.000376	0.000218	0.000250
K	0.027	0.520	0.519	0.508	0.520	0.071	0.395
Mg	0.217	0.00424	0.00395	0.00420	0.00424	0.206	0.113
Mn	0.000050[b]	0.00226[e]	0.00226[e]	0.00226[e]	0.00226[e]	0.000382	0.000382
Na	0.46	4.24	4.24	4.20	4.24	0.864	3.712
SiO_2	0.39	7.25	7.13	7.13	7.21	0.792	5.77
$Ti(OH)_4$[g]	0.0280	1.41×10^{-6}	3.47×10^{-5}	1.67×10^{-6}	1.97×10^{-6}	4.02×10^{-6}	2.24×10^{-10}
HS^-	0.00	2.32	2.40	2.48	2.32	0.000546	0.002
SO_4	0.085	0.0892	0.108	0.106	0.127	0.168	0.486
HCO_3^-	0.70	0.222	0.103	0.000	0.164	1.45	0.826

[a] Groundwater data from Sigfusson et al. (2011), measured at Grámelur.

[b] NN-1/2/6/9 H_2S-rich wastewater composition defined from the average values of NN-4/5/7.

[c] Data from heated groundwater and Laekjarhvarf samples in Sigfusson et al. (2011).

[d] Value from 2007 at Grámelur from Sigfusson et al. (2011).

[e] Value from 2008 sample of wastewater at power plant outlet in Sigfusson et al. (2011).

[f] Fe^{2+}/Fe^{3+} ratio measured for background water and surface wastewater in Sigfusson et al. (2011). Ratio in H_2S-rich wastewater determined via speciation considering the S^{2-}/S^{6+} redox couple (PHREEQC; Parkhurst and Appelo (2013)).

[g] $Ti(OH)_4$ concentrations defined through equilibrium with ilmenite.

Table 4. Initial basalt mineral composition, secondary minerals, and kinetic parameters used for mineral precipitation and dissolution rates.

	Vol. % of basalt	Surf. Area $[\mathrm{cm}^2\mathrm{g}^{-1}]^g$	Acidic Mechanism			Neutral Mechanism		Basic Mechanism		
			$\log(k_{25})$	E_a	$n(H^+)$	$\log(k_{25})$	E_a	$\log(k_{25})$	E_a	$n(H^+)$
Primary Phases:										
Plagioclase										
Albite[a]	22.96	0.1	-10.30	58.0	0.3	-11.19	60.0	-13.6	50.0	-0.3
Anorthite[b]	21.84	0.1	-5.17	58.0	1.22	-11.34	60.0	-13.6	50.0	-0.3
Sanidine[a]	2.59	0.1	-10.4	51.7	0.5	-12.48	60.0	-20.8	62.0	-0.8
Pyroxenes										
Diopside[a]	9.69	0.1	-9.80	32.7	0.3	-11.00	43.9	–	–	–
Hedenbergite[a]	7.84	0.1	-9.80	32.7	0.3	-11.00	43.9	–	–	–
Enstatite[a]	1.94	0.1	-8.30	46.1	0.5	-11.90	89.5	–	–	–
Ferrosilite[a]	1.29	0.1	-8.30	46.1	0.5	-11.90	89.5	–	–	–
Olivines										
Fayalite[b]	1.57	0.1	-6.25	70.4	0.4	–	–	-7.39	60.9	0.2
Forsterite[b]	2.22	0.1	-7.16	70.4	0.4	–	–	-8.33	60.9	0.2
Iron Oxides										
Ilmenite[c]	1.84	1.0	-8.35	37.9	0.421	-11.16	37.9	–	–	–
Magnetite[c]	1.22	1.0	-8.59	18.6	0.279	-10.78	18.6	–	–	–
Basaltic Glass[a]	25.00	0.2	$\log(k_{25})$=-7.564, E_a=25.5, $n(H^+)$=1.00, $n(Al^{3+})$=-0.33							
Alteration Phases:										
Zeolites										
Analcime[b]	–	1000.0	-3.3	63.0	1.0	-11.3	58.5	-14.3	58.0	-0.4
Chabazite[b]	–	1000.0	-6.56	33.7	0.82	-11.55	44.2	-12.05	44.2	-0.2
Heulandite[b]	–	1000.0	-7.51	33.7	0.82	-12.6	44.2	-13.2	44.2	-0.2
Thomsonite[b]	–	1000.0	-5.61	33.7	0.82	-10.7	44.2	-11.0	44.2	-0.2
Carbonates										
Calcite[c]	–	100.0	-0.30	14.4	1.00	-5.81	23.5	–	–	–
Dolomite[c]	–	100.0	-3.76	56.7	0.500	-8.60	95.3	-5.37	45.7	0.500
Magnesite[c]	–	100.0	-6.38	14.4	1.000	-9.34	23.5	-5.22	62.8	1.000
Siderite[d]	–	100.0	-3.799	45.0	0.9	-8.900	62.76	-15.600	71.0	-0.572
Clays										
Celadonite[b]	–	10000.0	-11.68	32.3	0.37	-13.53	37.5	–	–	–
Montmorillonite[b]	–	10000.0	-11.7	50.8	0.55	-14.3	30.0	-17.2	48.0	-0.3
Nontronite[b]	–	10000.0	-11.7	50.8	0.55	-14.3	30.0	-17.2	48.0	-0.3
Saponite[b]	–	10000.0	-11.7	50.8	0.55	-14.3	30.0	-17.2	48.0	-0.3
Iron Oxides										
Goethite[c]	–	100.0	–	–	–	-7.94	86.5	–	–	–
Sulfides										
Pyrite[c]	–	100.0	-7.52	56.9	-0.50	-4.55	56.9	–	–	–
Pyrrhotite[c]	–	100.0	-8.04	50.8	-0.597	–	–	–	–	–
Sulfates										
Anhydrite[c]	–	100.0	–	–	–	-3.19	14.3	–	–	–
Gypsum[c]	–	100.0	–	–	–	-2.79	0.00	–	–	–
SiO_2(am)[a,c,e]	–	1000.0	-10.6	41.6	0.3	-12.23	74.5	-14.2	73.0	-0.4
Elemental sulfur[f]	–	–	–	–	–	–	–	–	–	–

[a] Heřmanská et al. (2022)
[b] Heřmanská et al. (2023)
[c] Palandri and Kharaka (2004)
[d] Knauss et al. (2005)
[e] SiO_2(am) precipitation occurs under the free energy rate law from Carrol et al. (1998); $\log(k_{25})$ = -9.29.
[f] Elemental sulfur precipitation occurs under equilibrium.
[g] Matrix continua surface area (Aradóttir, Sonnenthal, Björnsson, & Jónsson, 2012; Berndsen et al., 2024).
Fracture surface area = Volume $\text{Fraction}_{mineral}$ × 2.8×10^{-3} $\mathrm{m}^2/\mathrm{m}^3$.
Rate of enstatite is used for ferrosilite, diopside for hedenbergite, saponite for nontronite, glauconite for celadonite.
Units: $\log(k_{25})$=mol m^{-2} s^{-1}; E_a=kJ mol^{-1}

3.3.2 Mineral Precipitation and Dissolution Kinetics

Kinetic constraints are applied to the precipitation of secondary phases and the dissolution of the primary and secondary phases. The kinetic rates are modeled based on transition state theory defined by a rate constant (k), reactive surface area (A), and the saturation conditions specified by the equilibrium constant (K), the reaction quotient (Q), and two exponential terms (θ, η) which are often assumed to be 1:

$$r = kA\left[1-\left(\frac{Q}{K}\right)^{\theta}\right]^{\eta} . \tag{8}$$

The rates are implemented in TOUGHREACT, accounting for additional mechanisms of dissolution and precipitation catalyzed by specific species as:

$$r = \ k_{25}^{nu}\exp\left[\frac{-E_a^{nu}}{R}\left(\frac{1}{T}-\frac{1}{298.15}\right)\right] + \sum_i k_{25}^{i}\exp\left[\frac{-E_a^{i}}{R}\left(\frac{1}{T}-\frac{1}{298.15}\right)\right]\prod_j a_{ij}^{n_{ij}} . \tag{9}$$

For each mineral, the values for the rate constants (k_{25}), the activation energies (E_a), the activity power term (n), and mineral reactive surface areas (A_i) are compiled from literature values and are reported in Table 4 (Aradóttir, Sonnenthal, Björnsson, & Jónsson, 2012; Berndsen et al., 2024; Heřmanská et al., 2022, 2023; Palandri & Kharaka, 2004; Knauss et al., 2005).

The dissolution and precipitation of all minerals are catalyzed by H^+ (acid mechanism) and OH^- (base mechanism), aside from the basaltic glass. The rate law for basaltic glass dissolution was established in Gíslason and Oelkers (2003) at far from equilibrium conditions, temperatures from 6-300 °C, and pH ranging from 1-11 as follows:

$$r_{geo} = \ kA\exp\left[\frac{-E_a}{RT}\right]\left(\frac{a_{H^+}^3}{a_{Al^{3+}}}\right)^{1/3}\left(1-\frac{Q}{K}\right) . \tag{10}$$

This rate law is implemented into TOUGHREACT, accounting for the mechanisms of Al and acid concentrations through the parameters listed in Table 4.

To calculate the equilibrium constants for basaltic glass dissolution, we consider the glass to be a mixture of oxides (Paul, 1977). This method has been shown to successfully model basaltic glass dissolution under similar temperature conditions (Aradóttir, Sonnenthal, & Jónsson, 2012; Aradóttir, Sonnenthal, Björnsson, & Jónsson, 2012; Aradóttir et al., 2013; Techer et al., 2001). In this approach, the equilibrium constant for the basaltic glass phase is determined by the solubility products (K_i) and mole fractions (x_i) of the glass-constituting oxides:

$$log\ K_{BG} = \sum_i x_i log\ K_i + \sum_i x_i log\ x_i . \tag{11}$$

The mole fractions are determined based on the measured oxide weight percents presented in the basaltic glass in Table S1. The equilibrium constants for the various oxides and further description of the method can be found in Aradóttir, Sonnenthal, and Jónsson (2012).

To better capture fluid-rock interactions in the MINC fracture continuum, the mineral reactive surface areas within each fracture continuum element differ from those presented in Table 4. Instead, these reactive surface areas are geometrically derived from the product of the surface area of the fracture-matrix interface for the grid element ($A_{interface}$) normalized to 1 m^3, found to be 2.85 $m^2 \cdot m^{-3}$, and the mineral volume fractions ($V_{frac,i}$):

$$A_i = \frac{A_{interface}}{V_{Elem,frac}+V_{Elem,matrix1}+V_{Elem,matrix2}} * V_{frac,i} . \tag{12}$$

While kinetic rates and mineral reactive surface areas can be constrained through literature values, these values are uncertain and can often be two to four orders of magnitude lower in the field compared to experimentally-derived values (e.g., Aradóttir, Sonnenthal, Björnsson, and Jónsson (2012); A. F. White et al. (1996); A. F. White and Brantley (2003)). To address this uncertainty, we calibrated the reactive surface areas to match fluid compositions measured in the NL-12 monitoring borehole near the start of H_2S injection (Figure S1). Fit to the measured fluid values was achieved by reducing the reactive surface area of the primary minerals within the rock matrix by two orders of magnitude (Table 4) from the values reported in Aradóttir, Sonnenthal, Björnsson, and Jónsson (2012) and Berndsen et al. (2024). This reduction aligns with findings from reactive transport models produced at the nearby Hellisheidi power plant (Aradóttir, Sonnenthal, Björnsson, & Jónsson, 2012). Reactive surface areas within the fracture domain were not reduced.

3.4 Boundary and Initial Conditions

We define the boundary conditions for this model based on the geological and hydrological settings. Constant temperature-pressure-concentration boundaries are assigned to the following: (1) the southern and northern model edges to capture the inflow and outflow along the principal flow direction aligned with rifting in the region, (2) the top surface to simulate an atmosphere layer and maintain fully-saturated fluid flow conditions within the model, and (3) shallow model elements that intersect Lake Thingvellir at the northern extent of the model. No-flow conditions are assigned to the following boundaries: (4) the eastern and western extents of the grid, as the NNE-SSW trending eruptive fissures act as barriers to east-west oriented fluid flow, and (5) the bottom layer of the model domain approaching the clay cap isolating the shallow groundwater from the deeper geothermal system. The bottom layer's temperature is fixed throughout the simulation.

We performed a series of simulations to establish the initial conditions for the H_2S-rich wastewater injection model. First, 10,000 years of steady-state flow were simulated to establish steady-state temperature and pressure conditions. Reactive transport under steady-state flow conditions was then simulated for 200 years to achieve a chemical pseudo-steady-state before wastewater injection. Water samples collected in 1991 (Sigfusson et al., 2011) and the mineralogy presented in Tables 4 and S1 define the initial groundwater chemistry and basalt composition for the pseudo-steady-state reactive transport model. Next, the steady-state temperature, pressure, and geochemical conditions were used as initial conditions in a reactive transport simulation of wastewater disposal and injection at Nesjavellir from 1990 to 2021, prior to the introduction of H_2S injection in January 2021. Finally, the resulting temperature, pressure, and geochemical conditions were used as initial conditions for the reactive transport model of H_2S injection presented here.

3.5 Mineralization Percent from Mass Balance Calculations

Previous studies have utilized down-hole fluid samples collected from monitoring boreholes and mass balance calculations to determine the fate of injected CO_2 and H_2S into Icelandic basalts (Clark et al., 2020; Gunnarsson et al., 2018; Matter et al., 2016). As related to H_2S mineralization, the method involves co-injecting H_2S with a non-reactive tracer and measuring the concentrations of both species at a monitoring borehole. By comparing the H_2S and tracer molar ratios and concentrations between the injection and monitoring fluids, H_2S mineralization can be estimated. Additional information on the mass balance calculations and derivation of the equations can be found in Text S1 and Clark et al. (2020).

While this method provides a practical estimate, previous studies offer limited context for interpreting the reported mineralization percentages and the factors that influence the estimates (e.g., fluid recovery). The 3D reactive transport model presented here offers a means to evaluate how the fluid mass balance estimates relate to actual mineralization in a heterogeneous, multiple-porosity reservoir. From the simulation output, we calculated mineralization percentages using the fluid mass balance equations at various locations away from the borehole and compared them to the overall mineralization calculated from total sulfide mineralization. Boric acid ($B(OH)_3(aq)$) is used as the tracer as it is contained in the injection fluid, but is non-reactive with the primary and secondary rock phases considered in this model.

4 Results

4.1 Flow Model Calibration

Temperature increases due to the wastewater disposal at Nesjavellir are well reproduced through the model calibration (Figure 2). Temperatures in NL-12 are largest in the upper 150 m of the system, but decrease from 25-20 °C from 2006 to 2013 following the installation of wastewater cooling towers and changes to the wastewater disposal system. The model captures this trend well. Temperatures in the fresh lava field range from 20-33 °C, reflecting the fluid temperatures measured in the nearby disappearing stream (Laekjarhvarf). The model generally reproduces the measured temperatures to within a few degrees. The largest temperature discrepancy ($\sim$10°C) occurs in the NK-01 well in October 2001 and April 2003. NK-01 is strongly influenced by wastewater disposal at the disappearing stream, which varies by 10-20 °C. This variation, along with complex flow channels in the fresh lava identified in Gómez-Díaz et al. (2022), likely explains the early-time discrepancy in the NK-01 calibration.

Overall, the calibration recovers highly permeable, fractured basalts in the shallow subsurface at the Nesjavellir site (Table 1). The largest permeabilities are perpendicular to the main extensional rifting direction, with fracture permeabilities up to 9.7×10^{-11} m^2 in the hyaloclastites and 1.9×10^{-11} m^2 in the lava flows. Larger hyaloclastite permeabilities agree with trends observed in fresh Icelandic basalts (Scott et al., 2023). Cross-rift permeability values are roughly 1-2 orders of magnitude less than those perpendicular to the rifting direction. This trend and the overall highly permeable shallow groundwater system agree with findings from previous flow model calibrations done in Gómez-Díaz et al. (2022), and the permeability values align with the upper limits for matrix permeabilities of fresh Icelandic basalts (Scott et al., 2023).

4.2 Fluid-Rock Interactions

Near the injection wells, host-rock alteration depends on the rock domain (fracture vs. matrix) and geology (hyaloclastite vs. lava flow). Hyaloclastites are more reactive than the basalt lava flows, with 21 times more dissolution in the fracture domain and 5 times more dissolution in the matrix domain (Figure 3). Alteration in the fractures is primarily attributed to olivine dissolution, followed by basaltic glass, feldspars, pyroxenes, and then primary iron oxides. Within the rock matrix, dissolution of basaltic glass, olivine, and feldspars is the greatest, followed by pyroxenes and iron oxides.

Alteration of the host rock by the injection fluids results in the formation of smectite clays, zeolites, carbonates, sulfides, iron oxides, and amorphous silica. Smectite clays are the most abundant minerals to precipitate, followed by zeolites, sulfides, carbonates, and iron oxides. No amorphous silica precipitates in the rock matrix. In the fracture domain, secondary mineralization is dominated by zeolite formation, followed by sulfides and minor amounts of carbonates, amorphous silica, iron oxides, and clays.

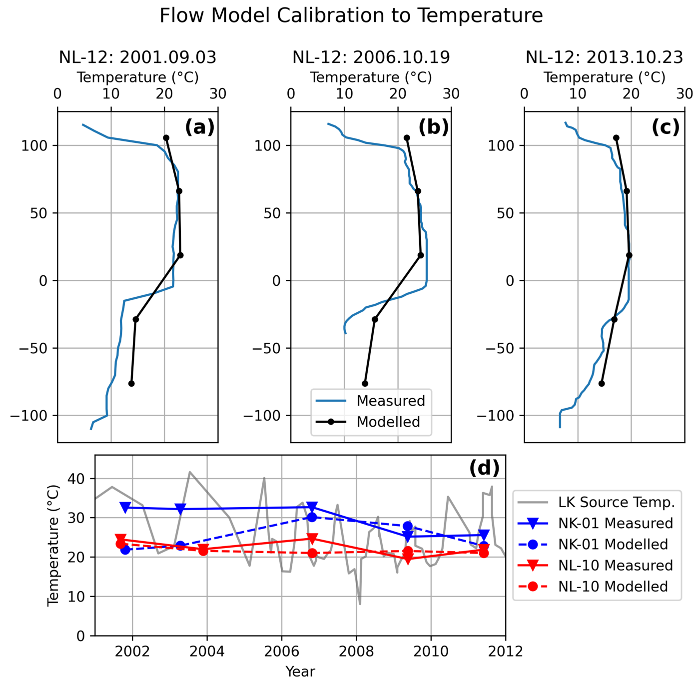

Figure 2. Results of the hyaloclastite and lava flow fracture permeability calibration. The calibration is fit to data points from NL-12 (a-c), NK-01 (blue line in plot d), and NL10 (red line in plot d).

Regarding H_2S mineral storage at Nesjavellir, all H_2S mineralization occurs as pyrite precipitation, and sulfates do not precipitate within the model domain. Pyrite mineralization is more extensive in the rock matrix than in the fracture domain. Within the matrix, hyaloclastites exhibit greater pyrite precipitation (0.0014%) than lava flows (0.0002%), due to their higher reactivity with enhanced iron supply from basaltic glass and olivine dissolution. While enhanced fluid-rock interactions in the matrix drive pyrite precipitation, they also promote clay (e.g., smectite) formation, which competes with pyrite for available iron. In contrast, reduced fluid-rock interactions in fractures limit clay formation, resulting in less competition for iron but also less pyrite formation overall. Larger volumes of pyrite mineralization are also observed in the hyaloclastites compared to lava flows, owing to the increased reactivity and permeability values (i.e., larger supply of H_2S-charged fluid from the injection well feed zones).

After 25 years of injection, the increase in secondary mineral volume percent is roughly two times greater than the decrease in primary mineral volume percent in the rock matrix. However, the absolute difference between mineralization and dissolution equates to only 0.016% in the hyaloclastites and 0.0029% in the lava flows. In the fractures, volume percent changes between the total mineralization and dissolution are also small at 0.0005% in lava flows and 0.032% in hyaloclastites. These small magnitude differences between changes in volume percent of primary and secondary minerals indicate little change in porosity and permeability throughout the near-borehole reservoir. Over the 25 year injection duration, the largest porosity and permeability reductions within 75 m of the injection borehole are observed in the hyaloclastites, with an average porosity decrease (i.e., $\phi - \phi_0$) of 0.22%, 0.06%, and 0.002% and an average permeability percent decrease (i.e., k/k_0) of 1.1%, 0.75%, 0.03% in the fracture, outer matrix, and inner matrix, respectively.

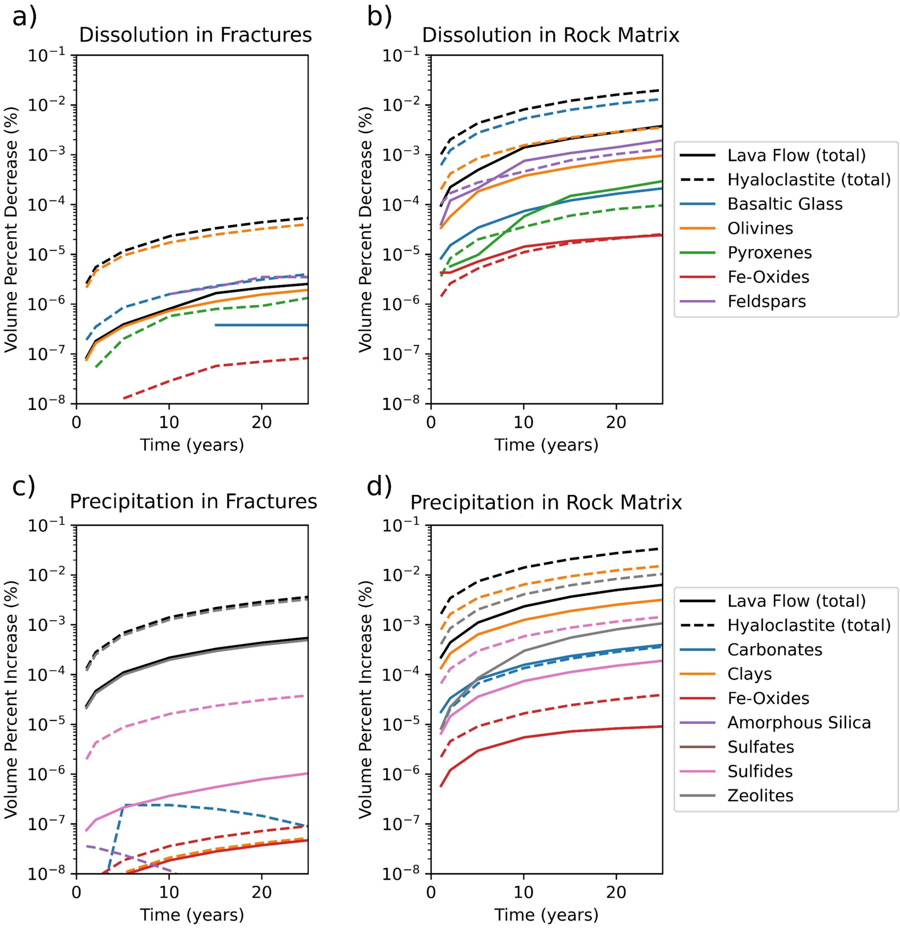

Figure 3. Alteration in the fractures (a and c) and the basalt matrix (b and d) within 75 m of the NN-4 H_2S injection well. The top row shows dissolution of the primary minerals, and the bottom row shows precipitation of secondary minerals. Changes in volume percent within the lava flows (solid lines) and hyaloclastites (dashed lines) are calculated separately, relative to the total volume of each respective lithologic unit.

4.3 H_2S Mineralization at Nesjavellir

The simulations show that 83% of the injected H_2S mineralizes before reaching the extent of Lake Thingvellir during the first 5 years of injection (Figure 4). H_2S mineralization is sustained throughout the 25 years of injection, remaining constant at 87%. Most mineralization (89-92%) occurs in the outer matrix, followed by the inner matrix (4-8%) and the fracture network (3-4%) (Figure 4). Throughout the 25 years of injection, roughly 10% of the total injected H_2S is transported out of the model domain to the northeast.

The depth at which pyrite mineralizes depends mainly on the borehole feed zones as illustrated in Figure 5(a-c). The profile A-A' in Figure 5(a) shows limited pyrite mineralization above the injection zones, and the mineralization occurs primarily in the hyaloclastites beneath the lava flow layer. Conversely, profile B-B' in Figure 5b along a major fault zone shows pyrite mineralization at shallower depths as the H_2S-charged fluid migrates vertically along the fault. The profile C-C' in

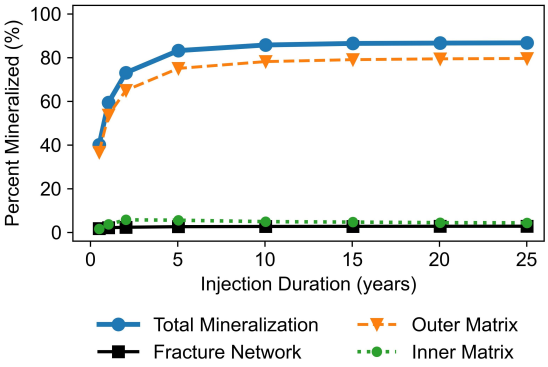

Figure 4. Percentage of the injected H_2S that mineralizes within the model domain and the proportion of H_2S mineralization occurring in each MINC domain (fracture, outer matrix, and inner matrix).

Figure 5(c) shows the sulfide mineralization across the rift valley at injection wells NN-4, NN-5, NN-6, and NN-7. The lateral extent of pyrite mineralization is limited across the rifting direction, following the reduced permeabilities normal to the rift direction (NW-SE) compared to the along-rift permeabilities.

The lateral distribution of pyrite mineralization is further visualized in Figure 5(d) by summing the total pyrite volume within each vertical column of the model grid. The pyrite mineralization follows the transport of the H_2S-charged fluid from the injection wells towards the northeast (model y dimension), following the primary direction of regional groundwater flow towards Lake Thingvellir. Pyrite mineralization is greatest near the injection boreholes, further supporting the rapid mineralization of H_2S. The pyrite mineralization remains confined to the Nesjavellir rift valley due to the highly permeable fault zones that bound the valley. These fault zones efficiently channel the groundwater towards the northeast, following the main rifting direction. The pyrite mineralization slightly broadens as the H_2S-charged fluid reaches the lake, but remains aligned with the primary SE-NE flow direction.

4.3.1 H_2S Concentration

The H_2S dissolved in geothermal wastewater is a weak acid, which exists primarily as hydrogen sulfide anion (HS^-) at pH values greater than 7 (Steudel, 1996). Similar to the pyrite formation, the aqueous HS^- remains within the Nesjavellir rift valley, primarily transported along the fault zone extending northeast from the injection wells towards Lake Thingvellir (Figure S2). The fault zone, with large vertical permeability, also contributes to the upwelling of the hot geothermal wastewater as the water approaches the NK-2 monitoring borehole (Figure S3). After 25 years of injection, aqueous sulfur remains in its reduced sulfide state, as H_2S oxidation to sulfate is not observed; the pH remains basic (> 7.5, Figure S4) and sulfate concentrations remain minimal (< 0.17 mmol/L, Figure S5).

Since the start of geothermal wastewater disposal at Lake Thingvellir in the 1990s, three surface springs have shown evidence of thermal pollution: Varmagjá, Markagjá, and Eldvík. After 25 years of injection, HS^- concentrations remain minimal at these springs, with concentrations of 0.013 µmol/L, 0.0087 µmol/L, and 0.0012 µmol/L at Varmagjá, Markagjá, and Eldvík, respectively (Figure 6). However, HS^- concentrations increase with depth, particularly at Varmagjá, where HS^- concentrations are 2.55 µmol/L at 75 m depth and 234 µmol/L at 250 m depth. To a lesser extent, HS^- concentrations at Markagjá and Eldvík also increase with depth, reaching 8.54 and 7.30 µmol/L at 250 m depth, respectively.

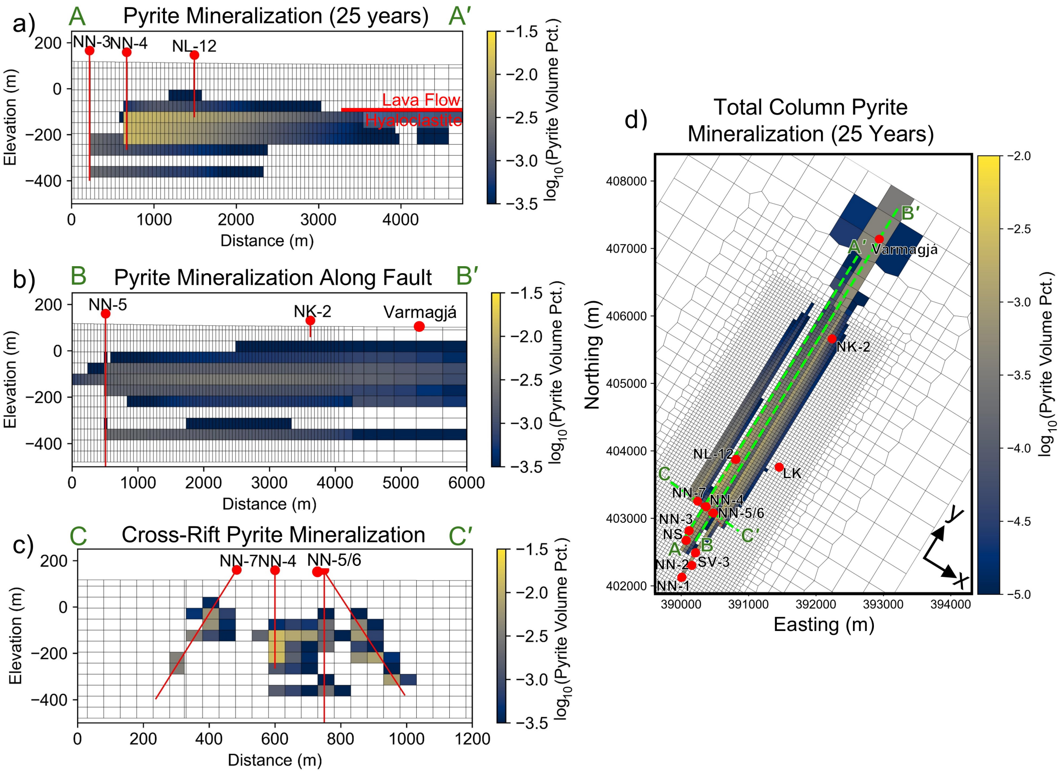

Figure 5. (a-c) Profiles of the volume of sulfide mineralized following 25 years of H_2S injection. The red dashed arrows highlight the trends of pyrite mineralization away from the injection wells, with a larger vertical distribution of pyrite in the fault zone. (d) Sum of the sulfide volume in each column of the reactive transport grid. Wastewater disposal sites, injection wells, and key monitoring boreholes are displayed as red dots. The dashed green indicates the locations of the profiles shown in the left subplots (A-A', B-B', and C-C').

4.4 Mineralization Percent from Mass Balance Monitoring

We perform the mass balance calculations of H_2S mineralization on a reactive transport model that considers injection only into well NN-4 to simplify the calculations. The results obtained using the mass balance Equation S1.3 suggest effective H_2S mineralization, in agreement with the mineralization percentages calculated from sulfide mineralization (Figure 4). At the injection depths beneath Lake Thingvellir, the calculated mineralization percentage exceeds 95% over the 25 years of continuous H_2S injection.

However, the mineralization percentage of H_2S, calculated using a mass balance approach, is strongly influenced by both the distance from the injection well and the hydrologic connection between the injection and monitoring locations. This is particularly the case for sampling locations near the injection well. At the injection depth interval along the primary southwest-northeast oriented flow path originating from well NN-4, H_2S mineralization after five years of injection is estimated to be 28% at 500 m, 51% at 1000 m, 83% at 2000 m, and 97% at 3000 m. In contrast, along a flow path shifted 100 m southeast of the primary flow path originating from well NN-4 and at depths 100 m shallower than the injection interval, mineralization percentages are larger at shorter distances; 68% at 500 m, 83% at 1000 m, 93% at 2000 m, and 97% at 3000 m. These results are plotted in Figure S6.

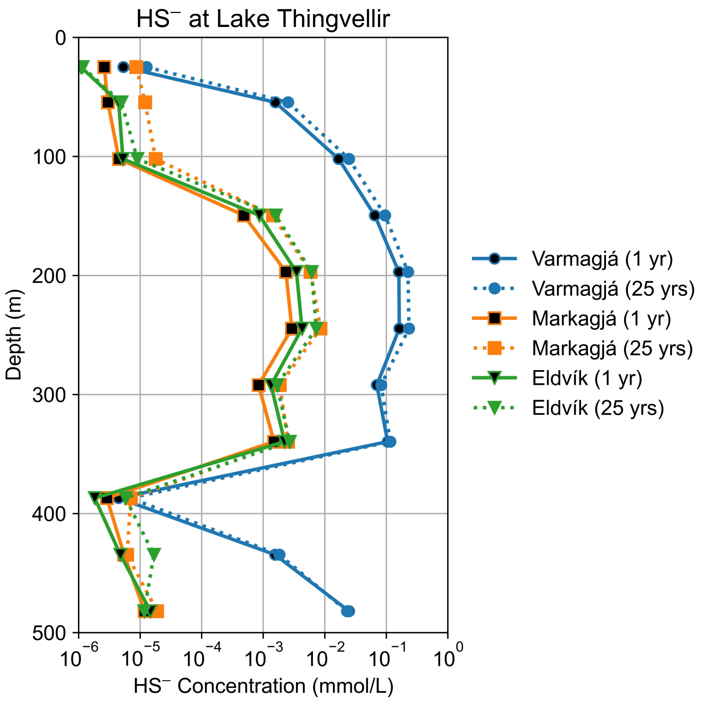

Figure 6. HS^- concentrations at three surface springs along the shoreline of Lake Thingvellir after 1 year (solid lines) and 25 years (dashed lines) of hydrogen sulfide injection.

5 Discussion

5.1 Effectiveness of H_2S Mineral Storage

The reactive transport modeling suggests that 87% of the injected H_2S mineralizes to pyrite before reaching Lake Thingvellir throughout 25 years of injection at the Nesjavellir site. This mineralization percentage aligns with values suggested by borehole fluid sampling of a similar H_2S injection system in Icelandic basalts (Clark et al., 2020). Pyrite mineralization is rapid and greatest near the injection boreholes, which agrees with laboratory flow-through column experiments that found sulfide mineralization is greatest on the inlet side of the column (Přikryl et al., 2018; Marieni et al., 2018). In long-term simulations of injection for 25 years, pyrite mineralization remains stable regardless of the interactions with the shallow groundwater. While laboratory studies of H_2S mineralization suggest that elemental sulfur may mineralize (Přikryl et al., 2018), the reactive transport model finds that sulfides are the only sulfur-bearing alteration phase, suggesting that the groundwater system is sufficiently reduced to maintain sulfide mineralization.

In this field model, the H_2S mineralization percent is limited by the high permeability fracture network that transports H_2S outside the model domain. This agrees with previous modeling approaches that found that the permeability distribution plays a key role in determining the spatial distribution of H_2S mineralization (Ciraula et al., 2024). While the large permeabilities, identified here through temperature and tracer calibrations in Gómez-Díaz et al. (2022) and through temperature calibrations, enhance the supply of H_2S-rich fluid, they also reduce fluid residence times. As a result, the H_2S-basalt interactions within a single reaction volume over a given time are limited, and pyrite formation becomes more dispersed.

Where lateral permeabilities are large relative to vertical permeability, the H_2S disperses laterally but remains near the injection depth. However, non-isothermal flow and the large vertical permeabilities of the fault zones identified in Gómez-Díaz et al. (2022) result in upwelling of the H_2S-charged wastewater (Figure S3) and shallower pyrite formation (Figure 5b). Vertical migration of the injected wastewater at Nesjavellir has been previously suggested based on tracer tests and a high temperature anomaly around the NK-2 borehole (Gómez-Díaz et al., 2022; Ívarsson, 2019). The degree of this vertical transport could result in contamination of Lake Thingvellir, which extends to depths of 50-60 m at the northeast edge of the model boundary (Stevenson et al., 2012). However, the model indicates that after 25 years of injection, the maximum hydrogen sulfide concentration at the lake is only 2.5 µmol/L (Figure 6). Nonetheless, the shallow boreholes and surface springs near the lake should be consistently sampled to ensure that contamination from vertical migration of the injected wastewater is minimal. Additionally, injection can be reduced or stopped in the boreholes nearest the faulted zones (NN-5 and NN-6), and injection boreholes with deeper casing, such as the recently drilled NN-10 borehole and the nearby NJ-18 borehole, can be utilized to reduce the risk of injected wastewater reaching the lake.

In addition to tracking H_2S transport, the reactive transport model also provides insight into the potential oxidation of the injected H_2S to sulfuric acid. Sulfuric acid is a strong acid that can significantly lower the pH of the groundwater, enhancing basalt dissolution and metal mobility (Sigfusson et al., 2011; A. Stefánsson et al., 2011). The simulations find that after 25 years of injection, the groundwater pH remains basic (Figure S4) and the sulfate concentrations are minimal (Figure S5), further supporting the effectiveness of H_2S mineral storage in the shallow groundwater system at Nesjavellir. These results agree with findings from A. Stefánsson et al. (2011) that considerable amounts of H_2S need to be oxidized ($\sim 40\%$ for 5 mmol/kg S at 100 °C) to reach pH values below 4.

5.2 Lithologic Controls on H_2S Mineral Storage

Previous laboratory experiments and geochemical models often attribute iron availability to basaltic glass, and frequently simplify the system to consider basaltic glass as the only primary rock phase (Ciraula et al., 2024; Přikryl et al., 2018; A. Stefánsson et al., 2011; Galeczka et al., 2022). Our model shows that olivine, and to a lesser extent pyroxenes, also play an essential role in supplying iron for H_2S mineral storage (Figure 3). In fact, Fe-rich olivine dissolution supplies the most iron, given its high iron content and fast kinetic rates (Heřmanská et al., 2022). However, the relative iron supply depends on the relative proportion in the starting mineralogy, which is uncertain in this model. The composition of olivine and the abundance of basaltic glass can be highly variable within Icelandic basalts (see Scott et al. (2023) and references therein), thus impacting the supply of iron. Nonetheless, these results suggest that the starting mineralogy is essential to consider for H_2S mineral storage, and that field-scale mineralization can be optimized by targeting hyaloclastites containing abundant basaltic glass and fresh lava flows containing abundant Fe-rich olivine.

5.3 Alteration Trends in the Fracture Network and Rock Matrix

In addition to evaluating H_2S mineral storage at the Nesjavellir site, this field-scale, multiple-porosity reactive transport model is also uniquely positioned to provide insights into the general alteration trends observed within fractured basalts. During 25 years of H_2S injection, fluid-rock interactions are most significant in the rock matrix, resulting from the prolonged fluid residence times from diffusion-controlled flow in the lower permeability matrix (Dávila et al., 2016; Cao et al., 2024; Adeoye et al., 2017). Within the rock matrix, pyrite formation is largest in the outer matrix closest to the fracture network, reflecting the rapid H_2S mineralization upon interaction with the basalt. In the fracture network, H_2S is abundant but iron is limited, while the inner matrix has abundant iron but limited H_2S; both processes limit pyrite formation. Recent studies have shown a similar mechanism for CO_2 mineral storage in basalts (Adeoye et al., 2017; Xiong et al., 2017, 2018), where the location of carbonate formation reflects the opposing chemical gradients between the primary fractures (high CO_2 concentration, low pH, low cation concentration) and the deeper rock matrix and fracture network (low CO_2 concentration, high pH, high cation concentrations). These results highlight the importance of interporosity, diffusion-controlled flow in mineral storage approaches (Adeoye et al., 2017). In fact, decreasing the diffusion coefficient of aqueous species to 1.23×10^{-9} m^2/s in the reactive transport model, indicative of hydrogen sulfide diffusion at low temperatures (10 °C) (Halmour & Sandall, 1984; Tamimi et al., 1994; Huang et al., 2022), reduces the total mineralization efficiency from 87% to 59% (Figure S7). This further illustrates the importance of multiple-porosity frameworks considering diffusion-limited zones for accurate field-scale modeling of mineral storage.

While the largest volumes of secondary mineral precipitation occur in the rock matrix, changes in porosity and permeability are minimal due to protolith dissolution. Basalt alteration models presented in Thien et al. (2015) suggest that this balance of precipitation and dissolution allows for rock alteration to continue, potentially to complete alteration, as fluid circulation is maintained and sufficient water is available to react with the host rock (i.e., large water-rock ratio). In the basalt around the NN-4 injection well, where temperatures average to 30°C, secondary minerals comprise only 0.034% of the hyaloclastite volume after 25 years of H_2S injection. However, extrapolating the alteration to the age of the recent heating episode in the Nesjavellir system (∼5 ka) results in 7% alteration of the protolith by volume. Extrapolating the alteration further recovers 100% alteration after 73,000 years, which aligns with the age of the oldest episode of the Nesjavellir system (∼80 ka). Overall, assessing the alteration rate over geological time-scales provides context for the minimal alteration observed on the shorter, engineering time-scales of H_2S injection.

In contrast to the large residence times that promote fluid-rock interactions in the rock matrix, the advection-controlled flow through permeable fractures limits the water-rock interactions within the fracture network (Luhmann et al., 2017; Deng & Spycher, 2019; Dávila et al., 2016; Singurindy & Berkowitz, 2005; Ciraula et al., 2024) and efficiently transports the H_2S-rich wastewater throughout the domain. Dissolution is minimal in the fracture domain, and precipitation is dominated by zeolites and sulfides, which are supersaturated in the injection wastewater. Because precipitation drives alteration in the fracture domain, decreases in pore and fracture space are observed following injection. This mechanism is in contrast to findings of CO_2 injection systems, where high CO_2 concentrations decrease pH, promoting dissolution and limiting precipitation of carbonates and secondary aluminosilicates near the injection sites and major fracture inlets (Aradóttir, Sonnenthal, Björnsson, & Jónsson, 2012; Xiong et al., 2017; Adeoye et al., 2017).

While permeability of the fracture network is expected to decrease at the Nesjavellir injection system, the model suggests that permeability decreases by only 4.5% after 100 years of injection, estimated by a cubic law relationship between the permeability and expected porosity changes (Steefel & Lasaga, 1994). These estimates are, however, highly uncertain as porosity and permeability evolution is a challenging phenomenon to capture accurately on the continuum scale (Baqer & Chen, 2022; Berre et al., 2019), and macroscopic porosity-permeability relationships have shown variable success in capturing true changes in heterogeneous rocks (see Sabo and Beckingham (2021) and references therein). Future studies should incorporate field observations (e.g., step-rate tests, side-wall core, etc.) with finer-scale reactive transport modeling to investigate field-scale porosity and permeability evolution for mineral storage in fractured basalts.

5.4 Validating the Mass Balance Monitoring Method

The reactive transport model developed in this study provides a tool to assess the ability of the mass balance method, as defined in Gunnarsson et al. (2018) and Clark et al. (2020), to quantify the success of H_2S mineral storage. Effective H_2S mineralization (87-97% after 25 years) recovered by both the mass balance calculations (Figure S6) and the total pyrite mineralization (Figure 4) suggests that the method can be used to indicate H_2S mineralization. However, the mass balance method is found to be highly sensitive to the degree of injection fluid recovery in the monitoring borehole (i.e., the degree of hydrologic connection between the injection and monitoring locations) (Figure S6). If monitoring wells are near the injection wells or injection fluid recovery is large, lower estimates of the mineralization percentages are obtained from the mass balance calculations. In this case, insufficient fluid-rock interactions occur over the short flow distances given the elevated supply of H_2S-charged fluids. Likewise, higher estimates of the mineralization percent are obtained if the monitoring wells are far from the injection well or if injection fluid recovery is low. In this case, long flow paths and limited H_2S-charged fluid supply provide ample water-rock interactions to mineralize the H_2S. This illustrates that the mass balance method quantifies mineralization along the flow path between the injection and monitoring locations, but not over the entire reservoir. An accurate assessment of H_2S mineral storage requires collecting samples throughout the injection reservoir, which can be a limiting factor at sites like Nesjavellir, where monitoring wells are sparse.

5.5 Model Uncertainties

While this model indicates that H_2S mineralizes upon injection at Nesjavellir, the predicted magnitude and distribution of H_2S mineralization are subject to uncertainties inherent to reactive transport modeling. These uncertainties are associated with both under-constrained site-specific parameters and incomplete knowledge of geochemical reaction rates. Physical model parameters such as permeability, porosity, diffusivity, and lithology are challenging to constrain in all groundwater flow models (Aradóttir, Sonnenthal, Björnsson, & Jónsson, 2012). To reduce these uncertainties in this study, we have integrated geological data from surface mapping and borehole cuttings (Franzson, 1988; Ciraula et al., 2024; Helgadóttir, 2021), utilized Iceland-specific rock property databases (Scott et al., 2023), and incorporated flow model calibration (Gómez-Díaz et al., 2022). While steps are taken to reduce uncertainty, field-scale models are never exact. Nevertheless, the model provides useful information on the dynamics of field-scale H_2S mineralization.

Regarding uncertainty in the flow model calibration, the PEST calibration recovers an acceptable fit to the borehole temperature data, with a weighted root mean squared error of only 1.3 °C. Additionally, the recovered permeabilities agree with expected values of Icelandic hyaloclastites (Scott et al., 2023) and previous model calibration results (Gómez-Díaz et al., 2022). However, the permeability of fresh Icelandic basalts can vary by up to six orders of magnitude (Scott et al., 2023). The best constrained unit from the PEST calibration (hyaloclastites along the primary flow direction) reflects this variability, recovering a 95% confidence interval of $1.3\times10^{-11} - 7.9 \times 10^{-10}$ m^2). Constraints on this lithology is critical for the accuracy of this model as the hyaloclastites receive the majority of the injected H_2S-rich water. The other permeabilities are less constrained in the PEST simulation and do not have meaningful confidence intervals, which may be due to limitations in the linearity assumptions applied to logarithmically scaled permeability parameters with large uncertainties. Manual calibration in Gómez-Díaz et al. (2022) revealed complex permeability distribution and channelized groundwater flow within the basalt lava flows at Nesjavellir. The coarse grid required for this model calibration to reduce the computational cost of each 3D simulation on the MINC grid reduces the resolution of the calibrated values in these heterogeneous basalts and introduces uncertainty. Additional uncertainties arise from a limited number of calibration temperature data points collected from the limited monitoring boreholes. The monitoring boreholes are shallow and do not extend through the entire model depth, reducing certainty in the z-axis permeability. The monitoring boreholes are also primarily located along a single flow direction from the injection wells (y-axis), reducing the constraints on the x-axis permeabilities. Future modeling efforts of the Nesjavellir system should continue to improve upon the calibration presented here and in Gómez-Díaz et al. (2022) by incorporating additional temperature data, constructing more detailed geologic models, and utilizing borehole logging to constrain local parameters.

Regarding uncertainty in geochemical reactions, kinetic parameters are also a significant source of uncertainty in reactive transport modeling (Carrera et al., 2022). These parameters are typically derived from laboratory experiments on end-member species, and translating them to the field-scale introduces challenges. In particular, reactive surface areas in the field are often orders of magnitude lower than those in laboratory experiments and exhibit considerable spatial and temporal variability (Beckingham et al., 2017). Moreover, most rates are developed for dissolution mechanisms, and further work is required to constrain precipitation mechanics. Biogeochemical processes can further complicate kinetic rate laws (Carrera et al., 2022) and potentially impact the stability of pyrite formation (Lévy et al., 2024; Mielke et al., 2003; Percak-Dennett et al., 2017). In the model presented here, some of the uncertainty associated with kinetic parameters is mitigated by using thermodynamic databases (Voigt et al., 2018; Aradóttir, Sonnenthal, & Jónsson, 2012) and rate laws (Gíslason & Oelkers, 2003) tailored to Icelandic fluid-rock interactions, and by calibrating the reactive surface areas to match observed fluid compositions.

6 Conclusions

A fully coupled, field-scale reactive transport model was developed in this study to evaluate the effectiveness of the H_2S mineral storage approach at the Nesjavellir geothermal site. The fluid flow parameters of the model were calibrated against down-hole temperature measurements in nearby monitoring boreholes, revealing very high fracture permeabilities ranging from 1.01×10^{-12} to 9.71×10^{-11} m^2 in the shallow basalt units. The chemical reaction rates were calibrated to historical groundwater data and samples collected near the start of H_2S injection.

The results indicate that H_2S mineral storage is an effective long-term strategy to reduce H_2S at the Nesjavellir injection site, with 87% of the injected H_2S mineralizing to pyrite before reaching the extent of Lake Thingvellir over 25 years of injection. Hyaloclastites with abundant basaltic glass and lava flows with abundant Fe-rich olivine offer a suitable reservoir for H_2S mineral storage. No sulfates or elemental sulfur precipitates throughout the 25 years of injection, indicating that the redox conditions remain favorable for pyrite formation throughout the reservoir. The alteration assemblage agrees with trends observed in low-temperature alteration of Icelandic basalts. Smectite clays are the most abundant alteration mineral and compete with pyrite for iron availability.

The multiple-porosity framework is found to be an essential consideration for field-scale modeling of H_2S mineral storage, enabling rapid transport through basalt fractures and diffusion-aided reaction with the rock matrix. Diffusive transport between the fracture network and the rock matrix is essential for H_2S mineralization, as most of the pyrite mineralizes in the rock matrix near the fracture network. Within the rock matrix, longer residence times increase the fluid-rock interactions that control iron availability. Conversely, advective-controlled transport in the highly permeable fracture network limits fluid-rock interactions necessary for pyrite formation and transports H_2S away from the injection wells. Within the fractures, alteration is dominated by mineral precipitation from injection-fluid supersaturation, which decreases permeability near the injection wells by 4.5% over 100 years of injection.

The model predicts that the injected H_2S at Nesjavellir does not oxidize to sulfuric acid, and therefore the injection is not expected to acidify the shallow groundwater system. Additionally, minimal contamination of Lake Thingvellir after 25 years of injection, with HS^- concentrations remaining below 2.5 µmol/L. However, the model also illustrates the risk of contamination when injection occurs in faulted zones with high vertical permeabilities, such as around wells NN-5 and NN-6. Therefore, continued groundwater sampling should be carried out near the fracture systems and at the lake's natural springs. Mass balance calculations on fluid samples are also effective for monitoring the performance of mineral storage. However, the method does not reflect total mineralization within the host reservoir and only quantifies the mineralization along the fluid flow path between the injection and sampling sites.

Open Research Section

Rock composition data for this research are included in this paper (and its supplementary information files): Ciraula, D. A., Kleine-Marshall, B. I., Galeczka, I. M., Lévy, L. (2024). Advanced monitoring of H_2S injection through the coupling of reactive transport models and geophysical responses. Environmental Science and Technology. https://doi.org/10.1021/acs.est.3c10139. Fluid composition and injection data are provided in the text (Table 3). Borehole temperature data is available for download from the Icelandic National Energy Authority's (Orkustofnun) map resource (https://www.map.is/os/).

TOUGHREACT software (Xu et al., 2011) supporting this research (version 4.13) is available with the appropriate licensing agreement upon purchase, and it is not openly accessible to the public or research community. TOUGHREACT software is available for purchase at the Berkeley Lab Marketplace (https://tough.lbl.gov/licensing-download/toughreact-licensing-download/). The reactive transport model grid was developed using AMESH software version 1.0 (Haukwa, 1998), which is openly accessible to the public (https://tough.lbl.gov/licensing-download/free-software-download/). PyTOUGH software version 1.6.5 (Croucher, 2011) was used to modify the grid, perform data analysis, and visualize simulation output. All code and functions can be downloaded from GitHub (https://github.com/acroucher/PyTOUGH.git) and from the PyPI repository (https://pypi.org/project/PyTOUGH/) under the LGPL-3.0 license. PEST software version 18 (Doherty & Hunt, 2010) was used to calibrate flow model parameters and is accessible for download (https://pesthomepage.org/programs).

Acknowledgments

Reykjavik Energy is thanked for providing wastewater injection data and facilitating the fluid sampling efforts. Léa Lévy, Íris Eva Einarsdóttir, and Thorsteinn Ari Thorgeirsson are thanked for their contributions to the fluid sampling at Nesjavellir. Thanks also to Helga Margrét Helgadóttir for assistance in collecting well cutting samples. Funding critical to this research was provided by the Nordic Volcanological Center (NordVulk), Landsvirkjun Energy Research Fund, the VOR - Reykjavik Energy Research and Innovation Fund, and the EEGS Foundation.

References

Adeoye, J. T., Menefee, A. H., Xiong, W., Wells, R. K., Skemer, P., Giammar, D. E., & Ellis, B. R. (2017). Effect of transport limitations and fluid properties on reaction products in fractures of unaltered and serpentinized basalt exposed to high pCO_2 fluids. *International Journal of Greenhouse Gas Control*, *63*. doi: 10.1016/j.ijggc.2017.06.003

Aradóttir, E. S., Sigfússon, B., Sonnenthal, E. L., Björnsson, G., & Jónsson, H. (2013). Dynamics of basaltic glass dissolution - Capturing microscopic effects in continuum scale models. *Geochimica et Cosmochimica Acta*, *121*. doi: 10.1016/j.gca.2013.04.031

Aradóttir, E. S., Sonnenthal, E. L., Björnsson, G., & Jónsson, H. (2012). Multidimensional reactive transport modeling of CO_2 mineral sequestration in basalts at the Hellisheidi geothermal field, Iceland. *International Journal of Greenhouse Gas Control*, *9*. doi: 10.1016/j.ijggc.2012.02.006

Aradóttir, E. S., Sonnenthal, E. L., & Jónsson, H. (2012). Development and evaluation of a thermodynamic dataset for phases of interest in CO_2 mineral sequestration in basaltic rocks. *Chemical Geology*, *304-305*. doi: 10.1016/j.chemgeo.2012.01.031

Arnason, B., Theodorsson, P., Björnsson, S., & Saemundsson, K. (1969). Hengill, a high temperature thermal area in Iceland. *Bulletin Volcanologique*, *33*. doi: 10.1007/BF02596720

Bacon, D. H., Ramanathan, R., Schaef, H. T., & McGrail, B. P. (2014). Simulating geologic co-sequestration of carbon dioxide and hydrogen sulfide in a basalt formation. *International Journal of Greenhouse Gas Control*, *21*. doi: 10.1016/j.ijggc.2013.12.012

Baqer, Y., & Chen, X. (2022). A review on reactive transport model and porosity evolution in the porous media. *Environmental Science and Pollution Research*, *29*.

Bear, J. (1972). *Dynamics of fluids in porous media.* Elsevier. doi: 10.1097/00010694-197508000-00022

Beckingham, L. E., Steefel, C. I., Swift, A. M., Voltolini, M., Yang, L., Anovitz, L. M., ... Xue, Z. (2017). Evaluation of accessible mineral surface areas for improved prediction of mineral reaction rates in porous media. *Geochimica et Cosmochimica Acta*, *205*. doi: 10.1016/j.gca.2017.02.006

Berndsen, M., Erolc, S., Akınd, T., Akıne, S., Nardinib, I., Immenhausera, A., & Nehlerb, M. (2024). Experimental study and kinetic modeling of high temperature and pressure CO_2 mineralization. *International Journal of Greenhouse Gas Control*, *132*. doi: 10.1016/j.ijggc.2023.104044

Berre, I., Doster, F., & Keilegavlen, E. (2019). Flow in fractured porous media: A review of conceptual models and discretization approaches. *Transport in Porous Media*, *130*. doi: 10.1007/s11242-018-1171-6

Cao, X., Li, Q., Xu, L., & Tan, Y. (2024). A review of in situ carbon mineralization in basalt. *Journal of Rock Mechanics and Geotechnical Engineering*, *16*. Retrieved from `https://www.sciencedirect.com/science/article/pii/S1674775523003372` doi: 10.1016/J.JRMGE.2023.11.010

Carrera, J., Saaltink, M. W., Soler-Sagarra, J., Jingjing, W., & Valhondo, C. (2022). Reactive Transport: A Review of Basic Concepts with Emphasis on Biochemical Processes. *Energies*, *15*. doi: 10.3390/en15030925

Chen, Y., Clennell, B., Zhang, J., Tang, M., & Ahmed, S. (2024). Reactive transport modelling of in-situ co_2 mineralization in basalt formations. *Capillarity*, *13*. doi: 10.46690/capi.2024.11.02

Ciraula, D. A., Kleine-Marshall, B. I., Galeczka, I. M., & Lévy, L. (2024). Advanced monitoring of H_2S injection through the coupling of reactive transport models and geophysical responses. *Environmental Science Technology*. doi: 10.1021/acs.est.3c10139

Clark, D. E., Gunnarsson, I., Aradóttir, E. S., Arnarson, M. T., Thorgeirsson, T. A., Sigurdardóttir, S. S., ... Gíslason, S. R. (2018). The chemistry and potential reactivity of the CO_2-H_2S charged injected waters at the basaltic CarbFix2 site, Iceland. In *Energy procedia* (Vol. 146). doi: 10.1016/j.egypro.2018.07.016

Clark, D. E., Oelkers, E. H., Gunnarsson, I., Sigfússon, B., Snæbjörnsdóttir, S., Aradóttir, E. S., & Gíslason, S. R. (2020). CarbFix2: CO_2 and H_2S mineralization during 3.5 years of continuous injection into basaltic rocks at more than 250°C. *Geochimica et Cosmochimica Acta*, *279*. doi: 10.1016/j.gca.2020.03.039

Croucher, A. (2011). PyTOUGH: a python scripting library for automating TOUGH2 simulations. *New Zealand Geothermal Workshop 2011 Proceedings*. Retrieved from `https://pypi.org/project/PyTOUGH/`

Deng, H., & Spycher, N. (2019). Modeling reactive transport processes in fractures. *Reviews in Mineralogy and Geochemistry*, *85*. doi: 10.2138/rmg.2019.85.3

DePaolo, D. J., Sonnenthal, E. L., & Pester, N. J. (2022). Thermo-Hydro-Chemical Simulation of Mid-Ocean Ridge Hydrothermal Systems: Static 2D Models and Effects of Paleo-Seawater Chemistry. *Geochemistry, Geophysics, Geosystems*, *23*. doi: 10.1029/2022GC010524

Doherty, J., & Hunt, R. (2010). Approaches to highly parameterized inversion: a guide to using PEST for groundwater-model calibration. *U. S. Geological Survey Scientific Investigations Report 2010-5169*.

Dávila, G., Luquot, L., Soler, J. M., & Cama, J. (2016). Interaction between a fractured marl caprock and co_2-rich sulfate solution under supercritical co_2 conditions. *International Journal of Greenhouse Gas Control*, *48*. doi: 10.1016/j.ijggc.2015.11.005

Foulger, G. R. (1988). Hengill Triple Junction, SW Iceland: 1. Tectonic structure and the spatial and temporal distribution of local earthquakes. *Journal of Geophysical Research*, *93*. doi: 10.1029/jb093ib11p13493

Foulger, G. R., & Toomey, D. R. (1989). Structure and evolution of the Hengill-Grensdalur volcanic complex, Iceland: geology, geophysics, and seismic tomography. *Journal of Geophysical Research*, *94*. doi: 10.1029/jb094ib12p17511

Franzson, H. (1988). Nesjavellir-Borholujardfrædi, vatnsgengd í jardhitageymi. *Orkustofnun, Report No. OS-88046/JHD-09*.

Galeczka, I. M., Stefánsson, A., Kleine, B. I., Gunnarsson-Robin, J., Ósk Snæbjörnsdóttir, S., Sigfússon, B., ... Oelkers, E. H. (2022). A pre-injection assessment of CO_2 and H_2S mineralization reactions at the Nesjavellir (Iceland) geothermal storage site. *International Journal of Greenhouse Gas Control*, *115*. doi: 10.1016/j.ijggc.2022.103610

Giammar, D. E., Wang, F., Guo, B., Surface, J. A., Peters, C. A., Conradi, M. S., & Hayes, S. E. (2014). Impacts of diffusive transport on carbonate mineral formation from magnesium silicate-co_2-water reactions. *Environmental Science and Technology*, *48*. doi: 10.1021/es504047t

Gunnarsson, I., Aradóttir, E. S., Oelkers, E. H., Clark, D. E., Arnarson, M. T., Sigfússon, B., ... Gíslason, S. R. (2018). The rapid and cost-effective capture and subsurface mineral storage of carbon and sulfur at the CarbFix2 site. *International Journal of Greenhouse Gas Control*, *79*. doi: 10.1016/j.ijggc.2018.08.014

Gutiérrez-Negrín, L. (2024). Evolution of worldwide geothermal power 2020–2023. *Geothermal Energy*, *12*. doi: 10.1186/s40517-024-00290-w

Gíslason, S., & Oelkers, E. H. (2003). Mechanism, rates, and consequences of basaltic glass dissolution: II. An experimental study of the dissolution rates of basaltic glass as a function of pH and temperature. *Geochimica et Cosmochimica Acta*, *67*. doi: 10.1016/S0016-7037(00)00176-5

Gómez-Díaz, E., Scott, S., Ratouis, T., & Newson, J. (2022). Numerical modeling of reinjection and tracer transport in a shallow aquifer, Nesjavellir Geothermal System, Iceland. *Geothermal Energy*, *10*. doi: 10.1186/s40517-022-00217-3

Hafstad, T., Vilmundardóttir, E., & Kristjánsson, B. (2007). *Rannsóknarborholur í hraununum á affallssvæi virkjunarinnar.*

Halmour, N., & Sandall, O. C. (1984). Molecular diffusivity of hydrogen sulfide in water. *Journal of Chemical and Engineering Data*, *29*. doi: 10.1021/je00035a009

Haukwa, C. (1998, 08). *AMESH A mesh creating program for the integral finite difference method: A User's Manual.* Retrieved from `https://www.osti.gov/biblio/892927` doi: 10.2172/892927

Helgadóttir, H. M. (2021). *NN-03 and NN-04 in Nesjavellir: Drill cuttings analysis.*

Heřmanská, M., Voigt, M. J., Marieni, C., Declercq, J., & Oelkers, E. H. (2022). A comprehensive and internally consistent mineral dissolution rate database: Part I: Primary silicate minerals and glasses. *Chemical Geology*, *597*. doi: 10.1016/j.chemgeo.2022.120807

Heřmanská, M., Voigt, M. J., Marieni, C., Declercq, J., & Oelkers, E. H. (2023). A comprehensive and consistent mineral dissolution rate database: Part II: Secondary silicate minerals. *Chemical Geology*, *636*. doi: 10.1016/j.chemgeo.2023.121632

Huang, Y., Wu, C., Chen, Y., Chou, I. M., & Jiang, L. (2022). Measurement of diffusion coefficients of hydrogen sulfide in water and brine using in-situ raman spectroscopy. *Fluid Phase Equilibria*, *556*. doi: 10.1016/j.fluid.2022.113381

Iceland Ministry of the Environment, E., & Climate. (2005, 5). *Act on the Conservation of Lake Thingvallavatn and its Catchment Area.*

Knauss, K. G., Johnson, J. W., & Steefel, C. I. (2005). Evaluation of the impact of CO_2, co-contaminant gas, aqueous fluid and reservoir rock interactions on the geologic sequestration of CO_2. *Chemical Geology*, *217*. doi: 10.1016/j.chemgeo.2004.12.017

Liu, D., Agarwal, R., Li, Y., & Yang, S. (2019). Reactive transport modeling of mineral carbonation in unaltered and altered basalts during co_2 sequestration. *International Journal of Greenhouse Gas Control*, *85*. doi: 10.1016/j.ijggc.2019.04.006

Luhmann, A. J., Tutolo, B. M., Bagley, B. C., Mildner, D. F., Seyfried, W. E., & Saar, M. O. (2017). Permeability, porosity, and mineral surface area changes in basalt cores induced by reactive transport of co_2-rich brine. *Water Resources Research*, *53*. doi: 10.1002/2016WR019216

Lévy, L., Ciraula, D., Legros, B., Martin, T., & Weller, A. (2024). Understanding the fate of H_2S injected in basalts by means of time-domain induced polarization geophysical logging. *Journal of Geophysical Research: Solid Earth*, *129*. doi: 10.1029/2023JB028316

Marieni, C., Prikryl, J., Aradóttir, E. S., Gunnarsson, I., & Stefánsson, A. (2018). Towards 'green' geothermal energy: Co-mineralization of carbon and sulfur in geothermal reservoirs. *International Journal of Greenhouse Gas Control*, *77*. doi: 10.1016/j.ijggc.2018.07.011

Matter, J. M., Stute, M., Snæbjörnsdóttir, S., Oelkers, E. H., Gíslason, S. R., Aradóttir, E. S., . . . Broecker, W. S. (2016). Rapid carbon mineralization for permanent disposal of anthropogenic carbon dioxide emissions. *Science*, *352*. doi: 10.1126/science.aad8132

Mielke, R. E., Pace, D. L., Porter, T., & Southam, G. (2003). A critical stage in the formation of acid mine drainage: Colonization of pyrite by Acidithiobacillus ferrooxidans under pH-neutral conditions. *Geobiology*, *1*. doi: 10.1046/j.1472-4669.2003.00005.x

Muñoz, A. Q. (1996). *Interpretation of Geophysical Well Logs from the Nesjavellir Geothermal Field, Iceland.*

Neveu, M., Desch, S. J., & Castillo-Rogez, J. C. (2017). Aqueous geochemistry in icy world interiors: Equilibrium fluid, rock, and gas compositions, and fate of antifreezes and radionuclides. *Geochimica et Cosmochimica Acta*, *212*. doi: 10.1016/j.gca.2017.06.023

Palandri, J. L., & Kharaka, Y. K. (2004). *A compilation of rate parameters of water-mineral interaction kinetics for application to geochemical modeling* (Vol. 2004-1068).

Parkhurst, D. L., & Appelo, C. (2013). *Description of input and examples for PHREEQC Version 3 — A computer program for speciation, batch-reaction, one-dimensional transport, and inverse geochemical calculations.*

Paul, A. (1977). Chemical durability of glasses; a thermodynamic approach. *Journal of Materials Science*, *12*. doi: 10.1007/BF00552247

Percak-Dennett, E., He, S., Converse, B., Konishi, H., Xu, H., Corcoran, A., ... Roden, E. E. (2017). Microbial acceleration of aerobic pyrite oxidation at circumneutral pH. *Geobiology*, *15*. doi: 10.1111/gbi.12241

Pruess, K., & Narasimhan, T. N. (1985). A Practical Method for Modeling Fluid and Heat Flow in Fractured Porous Media. *Society of Petroleum Engineers Journal*, *25*. doi: 10.2118/10509-pa

Pruess, K., Oldenburg, C., & Moridic, G. (1999). *TOUGH2 User's Guide Version 2.0.*

Přikryl, J., Marieni, C., Gudbrandsson, S., Aradóttir, E. S., Gunnarsson, I., & Stefánsson, A. (2018). H_2S sequestration process and sustainability in geothermal systems. *Geothermics*, *71*. doi: 10.1016/j.geothermics.2017.09.010

Ratouis, T. M., Snæbjörnsdóttir, S., Voigt, M. J., Sigfússon, B., Gunnarsson, G., Aradóttir, E. S., & Hjörleifsdóttir, V. (2022). Carbfix 2: A transport model of long-term CO_2 and H_2S injection into basaltic rocks at Hellisheidi, SW-Iceland. *International Journal of Greenhouse Gas Control*, *114*. doi: 10.1016/j.ijggc.2022.103586

Sabo, M. S., & Beckingham, L. E. (2021). Porosity-permeability evolution during simultaneous mineral dissolution and precipitation. *Water Resources Research*, *57*. doi: 10.1029/2020WR029072

Schaef, H. T., McGrail, B. P., Owen, A. T., & Arey, B. W. (2013). Mineralization of basalts in the CO_2-H_2O-H_2S system. *International Journal of Greenhouse Gas Control*, *16*. doi: 10.1016/j.ijggc.2013.03.020

Scott, S., Gunnarsson, I., Arnórsson, S., & Stefánsson, A. (2014). Gas chemistry, boiling and phase segregation in a geothermal system, Hellisheidi, Iceland. *Geochimica et Cosmochimica Acta*, *124*. doi: 10.1016/j.gca.2013.09.027

Scott, S., Lévy, L., Covell, C., Franzson, H., Gibert, B., Ágúst Valfells, ... Gudjónsdóttir, M. S. (2023). Valgardur: a database of the petrophysical, mineralogical, and chemical properties of Icelandic rocks. *Earth System Science Data*, *15*. doi: 10.5194/essd-15-1165-2023

Sigfusson, B., Gíslason, S. R., & Meharg, A. A. (2011). A field and reactive transport model study of arsenic in a basaltic rock aquifer. *Applied Geochemistry*, *26*. doi: 10.1016/j.apgeochem.2011.01.013

Singurindy, O., & Berkowitz, B. (2005). The role of fractures on coupled dissolution and precipitation patterns in carbonate rocks. *Advances in Water Resources*, *28*. doi: 10.1016/j.advwatres.2005.01.002

Snæbjörnsdóttir, S. , Galeczka, I. M., Sigfússon, B., & Oelkers, E. H. (2021). Injection of geothermal CO_2 and H_2S gases at the Nesjavellir site, SW Iceland: A pre-injection overview. In *Proceedings world geothermal congress 2021.*

Steefel, C. I., DePaolo, D. J., & Lichtner, P. C. (2005). Reactive transport modeling: An essential tool and a new research approach for the earth sciences. *Earth and Planetary Science Letters*, *240*. doi: 10.1016/j.epsl.2005.09.017

Steefel, C. I., & Lasaga, A. C. (1994). A coupled model for transport of multiple chemical species and kinetic precipitation/dissolution reactions with application to reactive flow in single phase hydrothermal systems. *American Journal of Science*, *294*. doi: 10.2475/ajs.294.5.529

Stefánsson, A., Arnórsson, S., Gunnarsson, I., Kaasalainen, H., & Gunnlaugsson, E. (2011). The geochemistry and sequestration of H2S into the geothermal system at Hellisheidi, Iceland. *Journal of Volcanology and Geothermal Research*, *202*. doi: 10.1016/j.jvolgeores.2010.12.014

Stefánsson, V. (1991). *Fordafrædistudlar : poruhluti bergs.*

Steudel, R. (1996). Mechanism for the Formation of Elemental Sulfur from Aqueous Sulfide in Chemical and Microbiological Desulfurization Processes. *Industrial and Engineering Chemistry Research*, *35*. doi: 10.1021/ie950558t

Stevenson, J. A., Mitchell, N. C., Mochrie, F., Cassidy, M., & Pinkerton, H. (2012). Lava penetrating water: The different behaviours of pāhoehoe and 'a'ā at the nesjahraun, thingvellir, iceland. *Bulletin of Volcanology*, *74*. doi: 10.1007/s00445-011-0480-1

Tamimi, A., Rinker, E. B., & Sandall, O. C. (1994). Diffusion coefficients for hydrogen sulfide, carbon dioxide, and nitrous oxide in water over the temperature range 293–368 k. *Journal of Chemical and Engineering Data*, *39*. doi: 10.1021/je00014a031

Techer, I., Advocat, T., Lancelot, J., & Liotard, J. M. (2001). Dissolution kinetics of basaltic glasses: Control by solution chemistry and protective effect of the alteration film. *Chemical Geology*, *176*. doi: 10.1016/S0009-2541(00)00400-9

Thien, B. M., Kosakowski, G., & Kulik, D. A. (2015). Differential alteration of basaltic lava flows and hyaloclastites in icelandic hydrothermal systems. *Geothermal Energy*, *3*. doi: 10.1186/s40517-015-0031-7

Vivanco, D. I. T., Kleine-Marshall, B. I., Smit, M. J., Gunnarsdóttir, S. H., Franzson, H., & Stefánsson, A. (2024). Lithogeochemistry of the nesjavellir geothermal field, sw iceland—implications for elemental mass movement in active geothermal systems. *Geothermics*, *120*. Retrieved from `https://www.sciencedirect.com/science/article/pii/S0375650524001020` doi: 10.1016/J.GEOTHERMICS.2024.103013

Voigt, M., Marieni, C., Clark, D. E., Gíslason, S. R., & Oelkers, E. H. (2018). Evaluation and refinement of thermodynamic databases for mineral carbonation. In *Energy procedia* (Vol. 146). doi: 10.1016/j.egypro.2018.07.012

Weisenberger, T. B., & Snæbjörnsdóttir, S. (2021). *Report on Integrated Geological and Reservoir Models and Injection Modelling.*

White, A. F., Blum, A. E., Schulz, M. S., Bullen, T. D., Harden, J. W., & Peterson, M. L. (1996). Chemical weathering rates of a soil chronosequence on granitic alluvium: I. Quantification of mineralogical and surface area changes and calculation of primary silicate reaction rates. *Geochimica et Cosmochimica Acta*, *60*. doi: 10.1016/0016-7037(96)00106-8

White, A. F., & Brantley, S. L. (2003). The effect of time on the weathering of silicate minerals: Why do weathering rates differ in the laboratory and field? *Chemical Geology*, *202*. doi: 10.1016/j.chemgeo.2003.03.001

White, S. K., Spane, F. A., Schaef, H. T., Miller, Q. R., White, M. D., Horner, J. A., & McGrail, B. P. (2020). Quantification of CO_2 Mineralization at the Wallula Basalt Pilot Project. *Environmental Science and Technology*, *54*. doi: 10.1021/acs.est.0c05142

Xiong, W., Wells, R. K., Horner, J. A., Schaef, H. T., Skemer, P. A., & Giammar, D. E. (2018). Co_2 mineral sequestration in naturally porous basalt. *Environmental Science and Technology Letters*, *5*. doi: 10.1021/acs.estlett.8b00047

Xiong, W., Wells, R. K., Menefee, A. H., Skemer, P., Ellis, B. R., & Giammar, D. E. (2017). Co_2 mineral trapping in fractured basalt. *International Journal of Greenhouse Gas Control*, *66*. doi: 10.1016/j.ijggc.2017.10.003

Xu, T., Sonnenthal, E., Spycher, N., & Pruess, K. (2006). TOUGHREACT - A simulation program for non-isothermal multiphase reactive geochemical transport in variably saturated geologic media: Applications to geothermal injectivity and CO_2 geological sequestration. *Computers and Geosciences*, *32*. doi: 10.1016/j.cageo.2005.06.014

Xu, T., Spycher, N., Sonnenthal, E., Zhang, G., Zheng, L., & Pruess, K. (2011). TOUGHREACT version 2.0: A simulator for subsurface reactive transport under non-isothermal multiphase flow conditions. *Computers and Geosciences*, *37*. doi: 10.1016/j.cageo.2010.10.007

Yeh, A., Croucher, A. E., & O'sullivan, M. J. (2013). TIM- Yet Another Graphical Tool for TOUGH2. *35th New Zealand Geothermal Workshop*.

Zarandi, S., & Ivarsson, G. (2010). *A Review on Waste Water Disposal at the Nesjavellir Geothermal Power Plant.*

Ívarsson, G. (2019). *Nidurrennsli á Nesjavöllum.*

Water Resources Research

Supporting Information for

Quantifying H_2S Mineral Storage Processes in Fractured Basalt Using a Field-Scale Reactive Transport Model

D. A. Ciraula[1], S. W. Scott[1], E. L. Sonnenthal[2], E. Gómez-Díaz[3,4], B. I. Kleine-Marshall[5]

[1]Nordic Volcanological Center, Institute of Earth Sciences, University of Iceland, Reykjavík, Iceland
[2]Lawrence Berkeley National Laboratory, Energy Geosciences Division, Berkeley, CA, USA
[3]Geological Institute, Energy and Minerals Resources Group, RWTH Aachen University, Aachen, Germany
[4]Geothermal Energy and Geofluids Group, Department of Earth Sciences, ETH Zurich, Zurich, Switzerland
[5]GeoZentrum Nordbayern, Friedrich-Alexander-Universität Erlangen-Nuremberg, Erlangen, Germany

Contents of this file

Introduction

Supporting information contains additional information on the . Additional figures include geochemical calibration results (S1), simulated groundwater HS^- concentration (S2-S3), groundwater pH (S4), sulfate concentration (S5), an evaluation of the mass balance method for estimating H_2S mineralization percent (S6), and the sensitivity of the reactive transport model to the diffusion coefficient (S7). Table S1 details the minerals considered in the reactive transport model and their chemical compositions.

Text S1. Mass Balance Calculations to Estimate Mineralization Percent

Gunnarsson et al. (2018) and Clark et al. (2020) present a method to estimate the mineralization percent via fluid sampling with the injected species at concentration $C_{\mathrm{H2S,inj.}}$ and a non-reactive tracer at concentration $C_{\mathrm{tracer,inj.}}$. Following injection, the concentration of both species is measured at a monitoring borehole ($C_{\mathrm{H2S,meas.}}$ and $C_{\mathrm{tracer,meas.}}$).

Using the measured tracer concentration in the monitoring borehole, the concentration of the tracer and H_2S in the background water ($C_{\mathrm{tracer,bkg.}}$ and $C_{\mathrm{H2S,bkg.}}$), and the molar ratio between the H_2S and the tracer in the injection fluid (A), the concentration of H_2S if no H_2S mineralization occurred can be predicted as follows:

$$C_{H2S,pred.} = \frac{C_{H2S,bkg.} \cdot \left(C_{tracer,inj.} - C_{tracer,meas.}\right) + A \cdot C_{tracer,inj.} \cdot \left(C_{tracer,meas.} - C_{tracer,bkg.}\right)}{C_{tracer,inj.} - C_{tracer,bkg.}}, \quad \text{(S1.1)}$$

$$A = \frac{C_{H2S,inj.}}{C_{tracer,inj.}} \, . \quad \text{(S1.2)}$$

The H_2S concentration predicted by the mass balance calculations can then be compared to the measured H_2S concentration to determine the mineralization percent:

$$H_2S\ Mineralization\ \% = \frac{C_{H2S,pred.} - C_{H2S,meas.}}{C_{H2S,pred.} - C_{H2S,bkg.}} \times 100 \, . \quad \text{(S1.3)}$$

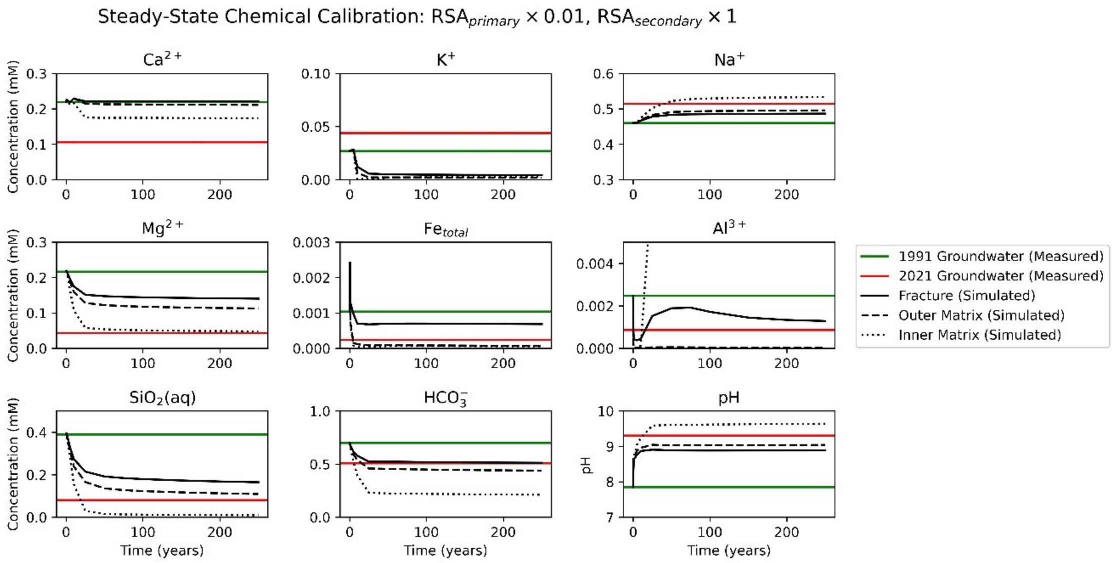

Figure S1. Simulations of "pseudo" steady-state chemistry were performed to calibrate the reactive surface area parameters. The resulting concentrations largely fall within measured values from groundwater samples collected in 1991 (green line; Sigfusson et al. (2011)) and 2021 (red line; NL-12), when the primary mineral reactive surface areas are reduced by two orders of magnitude relative to the values reported by Aradóttir, Sonnenthal, Björnsson, and Jónsson (2012) and Berndsen et al. (2024).

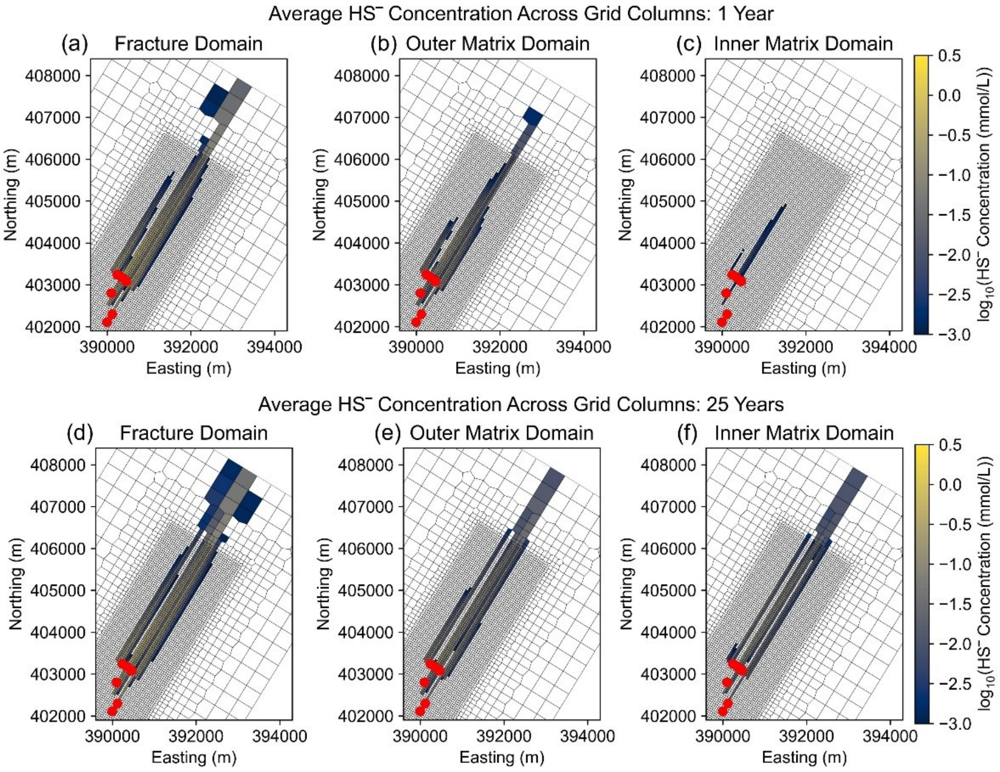

Figure S2. Average HS$^-$ concentration across the grid columns after 1 year (a-c) and 25 years (d-f) of injection.

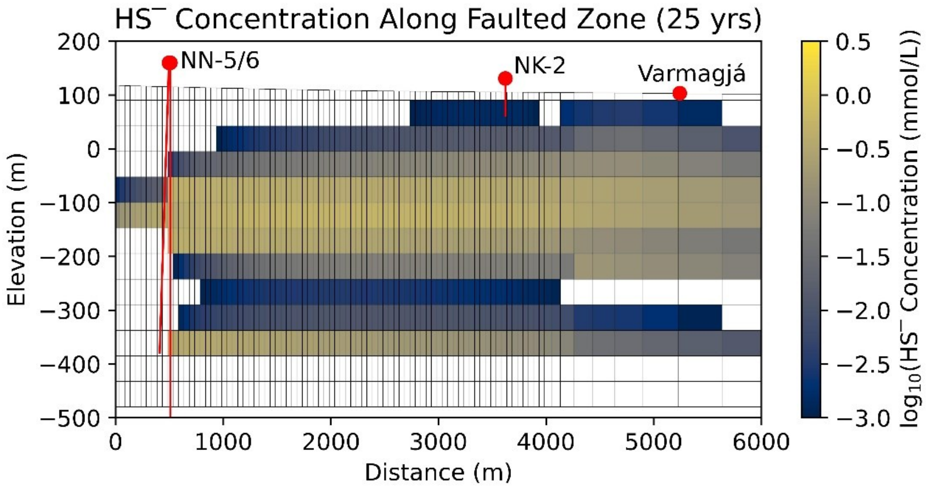

Figure S3. HS$^-$ concentration along the fault zone extending to Lake Thingvellir from the NN-5 and NN-6 injection wells after 25 years of injection.

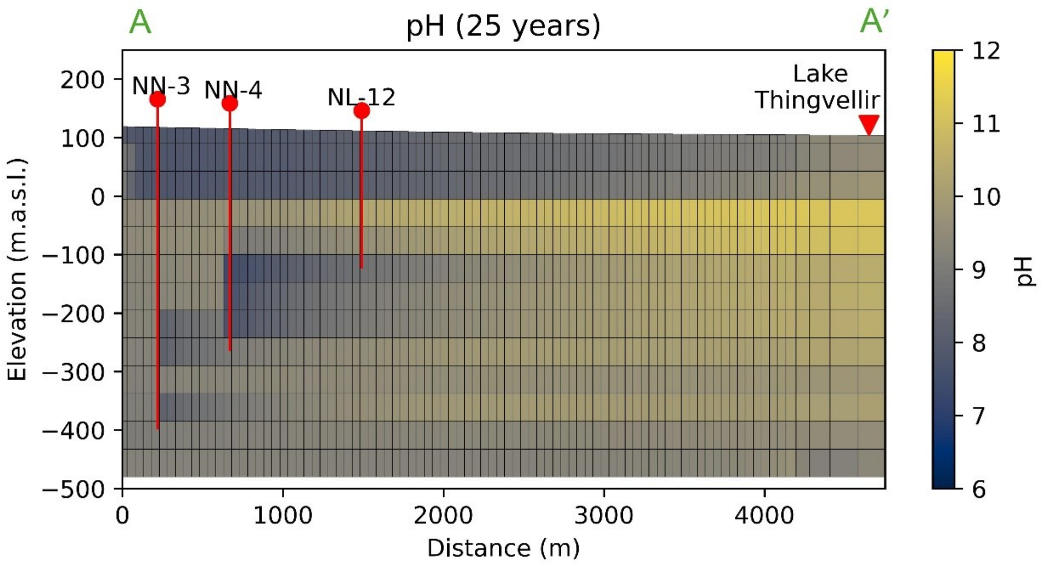

Figure S4. Groundwater pH after 25 years of H_2S injection. The profile is shown from A-A' in Figure 5(d) in the main text.

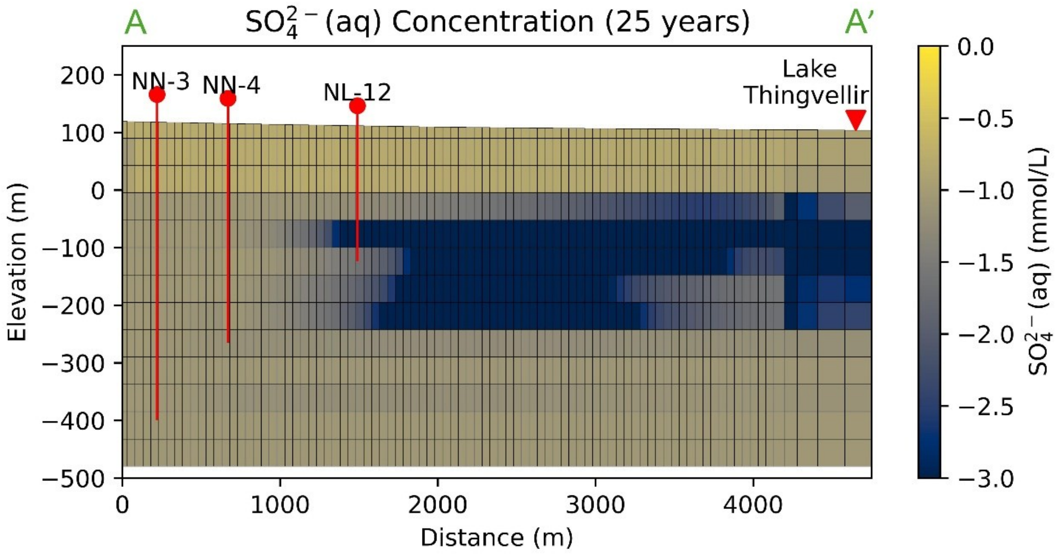

Figure S5. Aqueous sulfate concentration after 25 years of H_2S injection. The profile is shown from A-A' in Figure 5(d) in the main text.

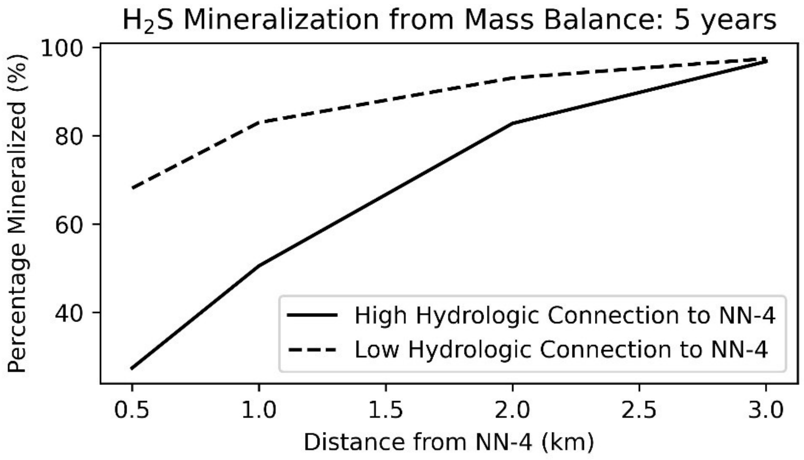

Figure S6. Percentage of the injected H_2S that mineralizes after 5 years of continuous injection as a function of distance from injection well NN-4. The calculations follow the mass balance approach described Text S1 from Gunnarsson et al. (2018) and Clark et al. (2020). The solid line indicates sampling locations along the primary flow path originating from NN-4 at the injection depth. The dashed lines indicate sampling locations with less hydrologic connection to the NN-4 injection well, taken along a flow path parallel to the primary flow path but shifted 100 m southeast and at depths 100 m shallower than the injection interval.

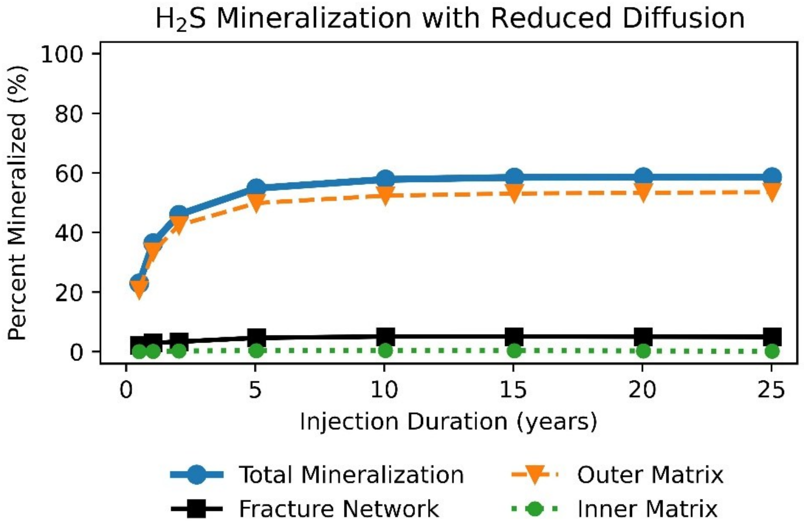

Figure S7. HS^- concentration along the fault zone extending to Lake Thingvellir from the NN-5 and NN-6 injection wells after 25 years of injection.

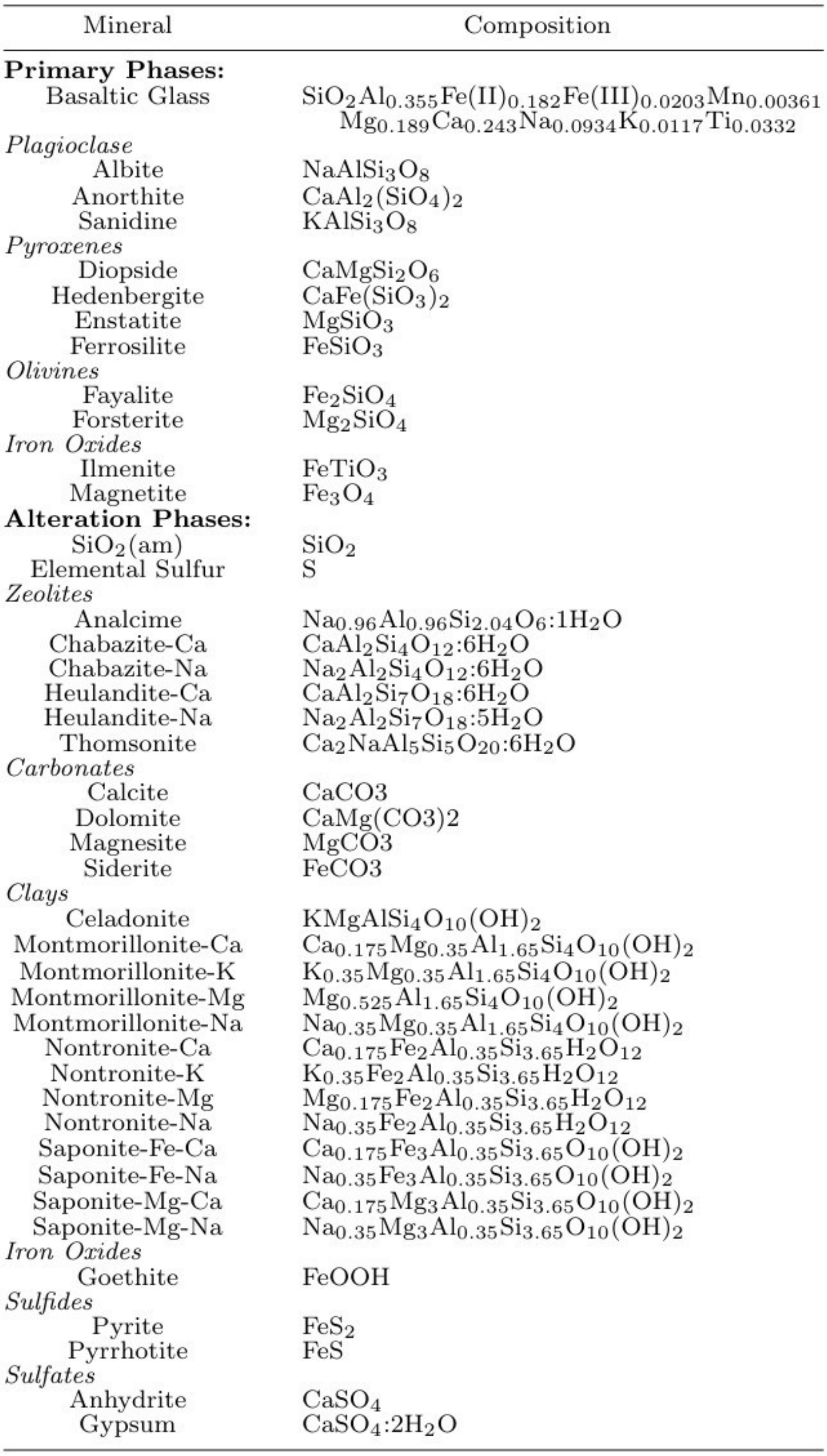

Mineral	Composition
Primary Phases:	
Basaltic Glass	$SiO_2Al_{0.355}Fe(II)_{0.182}Fe(III)_{0.0203}Mn_{0.00361}$ $Mg_{0.189}Ca_{0.243}Na_{0.0934}K_{0.0117}Ti_{0.0332}$
Plagioclase	
Albite	$NaAlSi_3O_8$
Anorthite	$CaAl_2(SiO_4)_2$
Sanidine	$KAlSi_3O_8$
Pyroxenes	
Diopside	$CaMgSi_2O_6$
Hedenbergite	$CaFe(SiO_3)_2$
Enstatite	$MgSiO_3$
Ferrosilite	$FeSiO_3$
Olivines	
Fayalite	Fe_2SiO_4
Forsterite	Mg_2SiO_4
Iron Oxides	
Ilmenite	$FeTiO_3$
Magnetite	Fe_3O_4
Alteration Phases:	
SiO_2(am)	SiO_2
Elemental Sulfur	S
Zeolites	
Analcime	$Na_{0.96}Al_{0.96}Si_{2.04}O_6$:$1H_2O$
Chabazite-Ca	$CaAl_2Si_4O_{12}$:$6H_2O$
Chabazite-Na	$Na_2Al_2Si_4O_{12}$:$6H_2O$
Heulandite-Ca	$CaAl_2Si_7O_{18}$:$6H_2O$
Heulandite-Na	$Na_2Al_2Si_7O_{18}$:$5H_2O$
Thomsonite	$Ca_2NaAl_5Si_5O_{20}$:$6H_2O$
Carbonates	
Calcite	CaCO3
Dolomite	CaMg(CO3)2
Magnesite	MgCO3
Siderite	FeCO3
Clays	
Celadonite	$KMgAlSi_4O_{10}(OH)_2$
Montmorillonite-Ca	$Ca_{0.175}Mg_{0.35}Al_{1.65}Si_4O_{10}(OH)_2$
Montmorillonite-K	$K_{0.35}Mg_{0.35}Al_{1.65}Si_4O_{10}(OH)_2$
Montmorillonite-Mg	$Mg_{0.525}Al_{1.65}Si_4O_{10}(OH)_2$
Montmorillonite-Na	$Na_{0.35}Mg_{0.35}Al_{1.65}Si_4O_{10}(OH)_2$
Nontronite-Ca	$Ca_{0.175}Fe_2Al_{0.35}Si_{3.65}H_2O_{12}$
Nontronite-K	$K_{0.35}Fe_2Al_{0.35}Si_{3.65}H_2O_{12}$
Nontronite-Mg	$Mg_{0.175}Fe_2Al_{0.35}Si_{3.65}H_2O_{12}$
Nontronite-Na	$Na_{0.35}Fe_2Al_{0.35}Si_{3.65}H_2O_{12}$
Saponite-Fe-Ca	$Ca_{0.175}Fe_3Al_{0.35}Si_{3.65}O_{10}(OH)_2$
Saponite-Fe-Na	$Na_{0.35}Fe_3Al_{0.35}Si_{3.65}O_{10}(OH)_2$
Saponite-Mg-Ca	$Ca_{0.175}Mg_3Al_{0.35}Si_{3.65}O_{10}(OH)_2$
Saponite-Mg-Na	$Na_{0.35}Mg_3Al_{0.35}Si_{3.65}O_{10}(OH)_2$
Iron Oxides	
Goethite	FeOOH
Sulfides	
Pyrite	FeS_2
Pyrrhotite	FeS
Sulfates	
Anhydrite	$CaSO_4$
Gypsum	$CaSO_4$:$2H_2O$

Table S1. Elemental composition of the primary and secondary phases considered in the reactive transport model. Compositions are based on the *carbfix.dat* database (Voigt et al., 2018).

Paper 3

submitted to *Geophys. J. Int.*

Constraining Time-lapse Geophysical Responses with Reactive Transport Modeling: An Approach to Monitor H_2S Mineral Storage

Daniel A. Ciraula[1], Gianluca Fiandaca[2], Jian Chen[2], Samuel Scott[1], Léa Lévy[3],

[1]*NordVulk, Institute of Earth Sciences, University of Iceland, Reykjavík 101, Iceland. Email: danielac@hi.is*

[2]*Department of Earth Sciences "Ardito Desio", University of Milano, 20133, Italy*

[3]*CNRS-INSU, Géosciences Rennes UMR 6118, Rennes, France*

SUMMARY

Geothermal energy production emits significant amounts of hydrogen sulfide (H_2S). A strategy to mitigate the emissions is to reinject the H_2S into basaltic formations, where it reacts with the rock to form pyrite. Due to the polarization properties of pyrite, the direct current resistivity (DC) and induced polarization (IP) geophysical method (i.e., DCIP) has shown the potential for monitoring H_2S mineral storage. However, field applications of DCIP monitoring have been limited by the low spatial coverage of wireline logging and by the ambiguity in interpreting IP signals due to multiple processes that contribute to the polarization response. This study integrates DCIP with field-scale reactive transport modeling, utilizing both synthetic modeling and field investigations, to assess the ability of surface and cross-hole DCIP to monitor H_2S mineral storage at the Nesjavellir study site in Iceland. Two surface DCIP datasets were collected at Nesjavellir, with six months of continuous H_2S injection between them. Time-lapse inversions, performed using a novel gridding scheme that accounts for electrode misplacement between the two DCIP surveys, recover no significant IP changes beyond data noise. Interpreting these results alongside the reactive transport results finds that pyrite mineralization during the six-month injection period is too small and too deep to be resolved by surface DCIP time-lapse surveying, highlighting the benefit of a joint geophysical-geochemical interpretation approach.

Conversely, joint DCIP-reactive transport synthetic modeling shows the potential of cross-hole DCIP for monitoring long-term H_2S mineral storage, provided that data noise is low and sufficient H_2S is injected. The reactive transport models also provide insight into the mechanisms contributing to the polarization response, demonstrating that pyrite mineralization is the primary contributor to the polarization response, with minimal contribution from other minerals such as smectites and iron oxides. However, existing petrophysical relationships are simplistic, which adds uncertainty to the interpretation of the DCIP signal and the quantification of pyrite mineralization. Additionally, smectite formation has been shown to decrease both the polarization signals and the quality of the IP data due to its electrically conductive properties. At Nesjavellir, a decrease in the DC resistivity from 1925 to 325 Ωm is observed, attributed to the disposal of warm wastewater. This decrease is identified by comparing resistivity data collected in this study to historical vertical electrical sounding data collected prior to geothermal development. Lastly, petrophysical relationships linking DC resistivity, smectite content, and permeability suggest a high basalt fracture permeability of 7.9×10^{-12} m^2, which agrees with values recovered through flow model calibrations. This result demonstrates the value of geophysical surveying not only for monitoring but also for constraining key parameters in reactive transport simulations.

Key words: Induced polarization, Hydrogeophysics, Inverse theory, Hydrothermal systems

1 INTRODUCTION

Geothermal energy is a key component of the Icelandic energy grid, accounting for 65% of the nation's electricity and heating production (Government of Iceland 2016). While geothermal energy provides a stable and clean source of energy, the flash steam geothermal production in Iceland emits roughly 30,000 tons of H_2S per year (Marieni et al. 2018). These gases are naturally occurring in the high-enthalpy geothermal production fluids, where concentrations are generally in the hundreds of parts per million (Arnórsson 1995; Galeczka et al. 2022). H_2S gases are toxic to humans and the environment, and their emissions are regulated within Iceland (Government of Iceland 2010).

To reduce H_2S emissions from geothermal energy production, gas is dissolved into geothermal wastewater and injected into the subsurface in a mineral storage sequestration approach. Upon injection, the H_2S-charged wastewater interacts with the basaltic host reservoir, binding fluid-sourced sulfide with iron released upon basalt alteration to mineralize iron sulfides (e.g., pyrite).

Geochemical models, laboratory experiments, and field geochemical sampling indicate that this H_2S mineral storage approach in basalts is an effective method to reduce atmospheric H_2S emissions (Ciraula et al. 2024; Clark et al. 2018; Clark et al. 2020; Galeczka et al. 2022; Marieni et al. 2021; Prikryl et al. 2018; Snæbjörnsdóttir et al. 2017; Snæbjörnsdóttir et al. 2021; Stefánsson et al. 2011). However, the H_2S injection system must be monitored to mitigate potential environmental impacts, including groundwater acidification, chemical and thermal contamination of fresh surface and water systems, and pore-clogging of the storage reservoir (Callow et al. 2018; Ciraula et al. 2024). Current monitoring approaches are primarily limited to geochemical approaches with low spatial resolution, such as mass balance calculations based on fluid sampling of monitoring wells (Clark et al. 2020; Gunnarsson et al. 2018; Matter et al. 2016; Snæbjörnsdóttir et al. 2017).

Geophysical surveying, aided by recent advancements in data acquisition and time-lapse inversion software, has been established as a reliable tool to improve the spatial and temporal resolution of environmental monitoring efforts (e.g., Singha et al. 2015; Binley et al. 2015). Electrical geophysical methods have been particularly beneficial for hydrological and environmental monitoring due to their sensitivity to relevant hydrogeological parameters, such as pore fluid conductivity, pore space geometry, and electrochemical interactions at the fluid-rock interface (Singha et al. 2015). By constraining these parameters, electrical geophysical data can be integrated with process-based models, such as flow and transport models and reactive transport models, to assist in hydrogeological mapping (Üner, Ağaçgözgü, and Doğan 2019), hydrological parameter estimation (e.g., Pleasants et al. 2022; Camporese et al. 2015; Commer et al. 2020; Hinnell et al. 2010; Pollock and Cirpka 2012; Deiana et al. 2008; Scheibe and Chien 2003; Tran et al. 2016; Cheng and Hsu 2021), and hydrological monitoring (e.g., Briggs et al. 2013; Kemna, Kulessa, and Vereecken 2002; Rubin and Hubbard 2005; Chen, Hubbard, and Williams 2013; Flores-Orozco et al. 2011). Likewise, process-based models can provide information on geophysical inversion parameters (e.g., Commer, Gasperikova, and Doughty 2022) and the underlying processes controlling the geophysical response (e.g., Ahmmed et al. 2020; Wu et al. 2011). Therefore, integrating the two approaches presents a mutual benefit between the geophysical methods and process-based models (Wu et al. 2014).

Induced polarization (IP) is an electrical geophysical method that measures the transfer and reversible accumulation of charges in a porous medium (e.g. Wong 1979; Revil, Florsch, and Mao 2015). The IP method is sensitive to multiple reactive processes, making it a potentially powerful tool for monitoring environmental applications (e.g., Slater and Lesmes 2002; Kessouri et al. 2019), including secondary mineral precipitation associated with bioremediation (e.g., Ntarlagiannis et al. 2005; Williams et al. 2005; Williams et al. 2009; Flores-Orozco et al. 2011; Flores-Orozco, Williams, and Kemna 2013), microbially induced calcite precipitation (e.g., Wu et al. 2011; Saneiyan et al. 2018; Saneiyan et al. 2019), geothermal alteration (e.g., Revil et al. 2017a; Revil and Gresse 2021; Ghorbani et al. 2018), and mineral storage approaches (e.g., Ciraula et al. 2024; Lévy et al. 2024b). However, the IP signature is often a result of confounding processes, leading to ambiguity in the interpretation of the complex IP response. As detailed in Kessouri et al. (2019), a growing number of laboratory studies have integrated IP with reactive models (e.g., reactive experiments and numerical simulations) to help de-couple the underlying reactive processes. Critically, these studies have found that integrating IP with reactive models serves to monitor the rates of reactive processes (Williams et al. 2005; Mellage et al. 2018a; Saneiyan et al. 2018), enhance the conceptual understanding of the reactions (Wu et al. 2010; Mellage et al. 2018a; Rembert 2021), constrain hydrogeologic parameters essential for numerical modeling (Wu et al. 2014), and de-convolve the multiple contributions to the measured IP signal (Wu et al. 2010; Wu et al. 2011; Hubbard et al. 2013; Mellage et al. 2018a; Mellage et al. 2018b; Peshtani et al. 2025).

While integrating IP with reaction models has shown utility in laboratory settings, the integration of IP surveying with reactive models in the field remains underutilized (Kessouri et al. 2019). For example, Williams et al. (2009) corroborated the field IP bioremediation monitoring surveys with laboratory column experiments and analysis of fluids and sediments to attribute the

IP response to iron and sulfate reduction and identify other IP mechanisms that should be investigated in future work. Saneiyan et al. (2019) combined geochemical monitoring and laboratory sample analyses with field IP data to monitor microbially induced carbonate precipitation. More recently and of particular relevance to the work presented here, Ciraula et al. (2024) integrated reactive transport modeling with the direct current resistivity (DC) and time-domain IP electrical methods, commonly referred to together as DCIP, to evaluate pyrite formation in field-scale H_2S mineral storage. The semiconducting properties of pyrite generates a strong IP response which can indicate alteration zones and provide a direct measure of H_2S mineralization (Ciraula et al. 2024; Lévy et al. 2024b). Through qualitative integration of wireline DCIP with reactive transport modeling, Ciraula et al. (2024) identified the key hydrogeological parameters (i.e., porosity, permeability, temperature, and injection rate) controlling the degree of pyrite mineralization and its associated DCIP response. However, Lévy et al. (2024b) brought into question the long-term stability of H_2S mineral storage at Nesjavellir and highlighted further ambiguities in the interpretation of the IP changes. Additionally, the wireline DCIP logging survey provided limited spatial extent for monitoring H_2S mineralization.

This study quantitatively integrates time-lapse DCIP geophysics with field-scale reactive transport models to better characterize H_2S mineralization at the Nesjavellir injection site in SW Iceland. We utilize a novel time-lapse inversion software and flexible gridding approach to recover changes in full waveform, surface DCIP data collected at Nesjavellir in 2020, prior to H_2S injection, and in 2021 following six months of continuous H_2S injection. We compare the time-lapse inversion results to the expected DCIP changes from reactive transport simulations in a joint approach to constrain interpretations of the H_2S mineral storage. The reactive transport models are also used for joint geochemical-geophysical synthetic modeling to evaluate the cross-hole DCIP survey configuration, enhancing the monitoring of H_2S mineral storage at the Nesjavellir site. Lastly, reactive transport models are utilized alongside historical electric geophysical data to better understand the underlying processes contributing to the DCIP response associated with H_2S mineral storage. Specifically, there are three main aims of this study: (1) evaluate the ability of DCIP to monitor H_2S mineral storage through field surveying and joint reactive transport-DCIP synthetic modeling; (2) reduce ambiguity in geophysical DCIP interpretations by constraining the underlying processes contributing to geophysical responses; (3) explore how time-lapse DCIP can be used to validate reactive transport model parameters.

2 DCIP GEOPHYSICS BACKGROUND

2.1 DCIP Methodology

The DCIP method expands upon the Ohmic conduction measured in conventional DC electrical resistivity surveys by considering induced polarization (IP), a low-frequency capacitive effect in the subsurface (e.g., Pelton et al. 1978; Wong 1979; Lesmes and Frye 2001). IP describes the ability of a material to store electrical charges, and the response is largely driven by the reorganization of charges of the electrical double layer at the pore fluid-rock interface during the current injection (e.g., Shuey 1975; Vinegar and Waxman 1984; Bücker, Flores-Orozco, and Kemna 2018). The IP effect is frequency-dependent; thus, IP considers a complex resistivity that is the sum of the real (ρ') and imaginary (ρ'') parts of resistivity (e.g., Fiandaca et al. 2015):

$$\rho^* = \rho' + i\rho'' \, . \tag{1}$$

This study utilizes time-domain IP, where a sequence of direct current pulses of alternating polarity is injected through two grounded electrodes (A and B) to build up charge in the subsurface. The build-up of charges creates a time-dependent voltage that is measured at two additional electrodes (M and N). The current and voltage electrodes are commonly placed along lines at the surface (surface DCIP) or down neighboring boreholes (cross-hole DCIP). In both the surface and cross-hole DCIP approaches, the A-B-N-M electrodes make up a single quadrapole and represent a single geoelectrical measurement called the complex apparent resistivity (ρ_a^*) (Martin et al. 2021):

$$\rho_a^* = k \times \frac{2\pi \Delta V_{MN}^*}{I^*} \, , \tag{2}$$

where ΔV_{MN}^* is the measured time-varying voltage difference between the M and N electrodes and I^* is the time-varying current injected. The term k is a geometric factor related to the distances between the various electrodes (AM, AM, BM, BN), defined as:

$$k = \frac{1}{\frac{1}{AM} - \frac{1}{AN} - \frac{1}{BM} + \frac{1}{BN}} \ . \tag{3}$$

The time-varying voltage response between the M and N electrodes (ΔV^{*}_{MN}) contains the static (DC) voltage response and an IP voltage response which arises as residual charges, accumulated during current injection, return to equilibrium (voltage decay). In this study, we use a 100% duty-cycle with no off-time between the injection current polarity switch (Olsson et al. 2015). The 100% duty-cycle ($+I_{on}, -I_{on}$) is preferred in this study over the the 50% duty-cycle ($+I_{on}, I_{off}, -I_{on}, I_{off}$) because data acquisition is twice as fast and the signal strength is approximately doubled (Olsson et al. 2015).

2.2 IP Relaxation Model

A common relaxation model used to describe the IP voltage response curve is the complex resistivity Cole-Cole model (Pelton et al. 1978; Weller and Slater 2022). The Cole-Cole model describing complex resistivity (RCC) can be defined by the resistivity (ρ_0), chargeability (m), relaxation time (τ_σ), and frequency exponent (C):

$$RCC\left\{\rho_0, m, \tau_\sigma, C\right\} = \rho_0 \left[1 - m\left(1 - \frac{1}{1 + (i\omega\tau_\sigma)^C}\right)\right] \ . \tag{4}$$

In this study, we invert the complex resistivity for maximum phase angle model parameters (MPA) (Fiandaca, Madsen, and Maurya 2018), a re-parameterization of the RCC model. We utilize this re-parameterization as it has been shown to decrease model parameter correlation and improve model resolution, particularly in data with low signal-to-noise ratios (Fiandaca, Madsen, and Maurya 2018). In the MPA model, the model domain is re-parameterized to $MPA\{\rho_0, \phi_{max}, \tau_\phi, C\}$. The relaxation time, τ_ϕ, is defined in terms of the Cole-Cole parameters m, τ_ϕ, and C:

$$\tau_\phi = \tau_\sigma \times (1 - m)^{-1/2C} \ . \tag{5}$$

The phase of the Cole-Cole complex resistivity, $\phi(\omega)$, is maximized at an angular frequency of $\omega_\phi = 1/\tau_\phi$. Thus, the maximum phase, ϕ_{max}, can be described as:

$$\phi_{max} = -tan^{-1}\left(\frac{\rho''(1/\tau_\phi)}{\rho'(1/\tau_\phi)}\right) \ . \tag{6}$$

After the inversion, we calculate the RCC parameters from the MPA parameters following the iterative approach outlined in Appendix A of Fiandaca et al. (2018). The routine calculates the chargeability m by matching the phase reponse of the MPA and RCC models; $m = \frac{tan(-\phi_{max})}{(1-a)\cdot tan(-\phi_{max})+b}$, where a and b are the real and imaginary part of $\frac{1}{1+(i\omega\tau_\rho)^C}$, calculated at the frequency $\omega = \frac{1}{\tau_\phi}$ at which the maximum phase is reached. The chargeability m and relaxation time τ_ρ are computed iteratively through these equations using the relation $\tau_\rho = \tau_\phi \cdot (1-m)^{-1/2C}$, starting with $m = 0$ and $\tau_\rho = \tau_\phi$ and minimizing $\Delta m = \frac{|m(n)-m(n-1)|}{m(n)}$ over n iterations. This procedure yields the RCC parameter set, including the chargeability used in the petrophysical relationship discussed in the following section.

2.3 Petrophysical IP Relationship

It is well established that disseminated metallic minerals, such as iron sulfides and some iron oxides, have a large impact on the polarization characteristics of the subsurface (e.g., Wong 1979; Abdulsamad, Florsch, and Camerlynck 2017; Gurin et al. 2013; Gurin et al. 2015; Hupfer et al. 2016; Revil, Florsch, and Mao 2015). Revil, Florsch, and Mao (2015) presents a polarization model for disseminated metallic particles, based on the effective medium theory, where the semiconducting properties of metallic minerals allow for electron mobility within the minerals themselves, accumulating additional charge at the mineral-electrolyte interface when an external electric field is applied. The model from Revil, Florsch, and Mao (2015) used in this study follows a similar approach to the models produced in Wong (1979) and Gurin et al. (2015), relating the the chargeability parameter, m, to the sum of the background chargeability (m_b) and the volume fraction of semiconducting metallic particles in the porous media, $\theta_{metallic}$:

$$m = \frac{9}{2} \times \theta_{metallic} + m_b \, . \tag{7}$$

Analysis of core samples of altered Icelandic volcanic rocks in Lévy et al. (2019b) confirmed the linear relationship between the IP response and the volume content of metallic particles, thereby supporting the use of eq. 7 to serve as a first-order approximation to link H_2S mineralization to the expected chargeability response.

Ghorbani et al. 2018 shows that the background chargeability term (m_b) is constant when fluid salinity is low, independent of temperature and saturation. Additionally, the metallic minerals are comprised of iron oxides and iron sulfides, which are expected to have similar influences on the chargeability based on derivations of the chargeability from the effective medium theory (Revil, Florsch, and Mao 2015). Similarly, laboratory studies of sand-metallic particle mixtures in Gurin et al. (2015) found that the mineral composition has minimal impact on chargeability. Therefore, the chargeability change simplifies to reflect only the change in volume fraction of iron sulfides (pyrite and pyrrhotite) from precipitation and primary iron oxides (magnetite and ilmenite) from dissolution:

$$\Delta m = \frac{9}{2} \times \left(\Delta\theta_{iron-sulfides} + \Delta\theta_{iron-oxides}\right). \tag{8}$$

Chargeability in eq. 8 is not anticipated to be influenced by temperature, as it depends on the ratio of high-frequency conductivity to direct current conductivity, which shares the same temperature relationship (Ghorbani et al. 2018). Fluid conductivity effects are also not considered in eq. 8 as previous studies have shown that chargeability is independent of the pore fluid conductivity over a similar range of values as observed at Nesjavellir (∼0.01-0.07 S/m) (Gurin et al. 2015; Hupfer et al. 2016; Lévy et al. 2019b). Furthermore, major temperature and fluid conductivity changes between the time-lapse measurements are not expected as hot wastewater injection began at Nesjavellir two decades before introducing H_2S.

3 METHODS

3.1 DCIP Field Data

3.1.1 Nesjavellir Field Site

The dataset used to test the DCIP monitoring approach developed in this paper was collected at the Nesjavellir high-temperature geothermal field. Nesjavellir is located north of the Hengill central volcano in southwest Iceland, situated on a ridge-ridge-transform triple junction (Foulger 1988). The area is composed mainly of late Quaternary and post-glacial age volcanic rocks, primarily in basalt lava flows and hyaloclastites (Arnason et al. 1969; Foulger and Toomey 1989).

The power plant produces 120 MWe of electricity and 290 MWth as thermal energy for district heating (Gómez-Díaz et al. 2022). Since 2004, warm geothermal wastewater produced as a byproduct of energy production has been injected into shallow wells (”NN wells”, 200-500 m deep) or discharged at the surface into $\sim$25 m deep wells near the power plant and into a nearby disappearing stream. At the NN well injection depths, the groundwater system is cold (10 °C) and the basalt is unaltered, comprised of highly porous and permeable hyaloclastites and basalt lava flows (Helgadóttir 2021; Gómez-Díaz et al. 2022; Ciraula et al. 2024). The groundwater table is measured at 50-60 m depth.

Starting January 29, 2021, H_2S from the geothermal production fluid is dissolved into the geothermal wastewater and injected into the NN wells located 250-750 m northeast of the Nesjavellir power station (Fig. 1). The injection water temperature ranges from 60-90 °C and H_2S concentrations are $\sim$75 ppm. Injection is continuous at each well at rates ranging from 15-150 L/s. Additional information on the Nesjavellir geothermal site can be found in Lévy et al. (2024b) and Ciraula et al. (2024).

3.1.2 Time-lapse DCIP Data Acquisition During H_2S Injection

Time-domain, full waveform surface DCIP data were acquired at the Nesjavellir field site in July 2020 and 2021 (Fig. 1) using the ABEM Terrameter LS2 with a maximum injection current of 500 mA at 600 V. In the field, injection currents averaged $\sim$350 mA. Stainless steel electrodes were used in this survey, which can introduce background drift to the data due to the electrochemical and current-induced electrode polarization of the stainless steel electrodes (e.g., Dahlin, Leroux, and Nissen 2002; Olsson et al. 2016). However, we utilize the full-waveform drift model presented in Olsson et al. (2016), which has been shown to effectively remove the background drift from data collected with stainless steel electrodes. Data were collected along seven survey lines in both years with a multiple gradient array acquisition. Five of the lines, Lines 1-5, were 1200 m long and oriented at roughly 33°E of N, parallel to the Nesjavellir rift valley and along the principal direction of groundwater flow. The other lines, Lines 6 and 7, were 800 m long and were collected transecting the 1200 m lines.

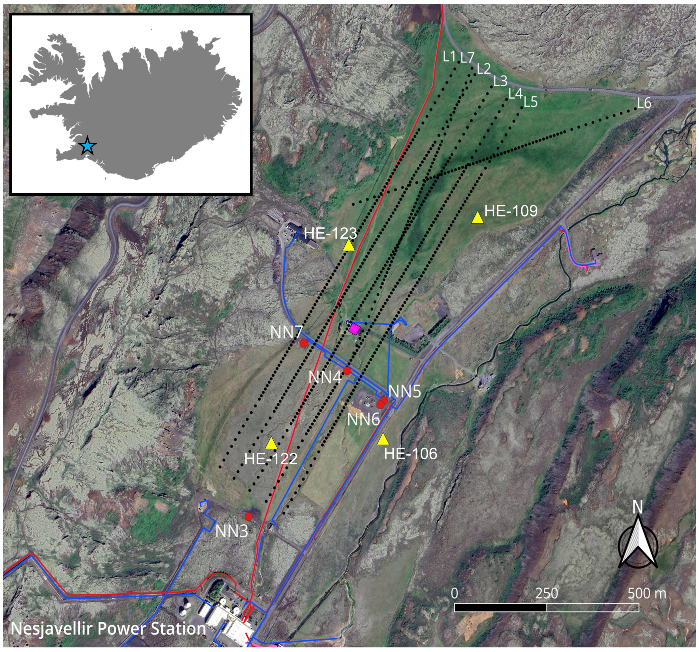

Figure 1. Map of the Nesjavellir geothermal field site. The H_2S injection wells are shown as red circles. The approximate electrode locations along the DCIP survey lines are displayed as black dots, and the locations of the vertical electrical soundings collected in 1985 are shown as yellow triangles. Red lines indicate buried power lines, the pink square is the location of a residential building, and the blue lines indicate hot water and steam pipes.

Lines 1-5 consisted of 101 electrodes at 10 m spacing in the center of the line (200-1000 m) and 20 m spacing along the edges (0-200 m and 1000-1200 m). Surveys were collected using two line configurations: (1) a roll-along approach where 1200 m long lines are composed of three, 800 m overlapping lines, and (2) a single line approach that utilized the ES10-64C Electrode Selector to increase the electrode capacity and collect along the entire 1200 m line. When available, we use data collected using the roll-along approach. Although this survey configuration has a shorter maximum electrode spacing than the single-line approach with the ES10-64C, the roll-along configuration increases the data density without significantly limiting the depth of investigation recovered by the inversions.

Lines 6 and 7 consisted of 81 electrodes with 10 m spacing in the center of the line (200-600 m) and 20 m spacing along the line edges (0-200 m and 600-800 m). The ES10-64C or roll-along approaches were not required to image these shorter, 800 meter-long lines.

3.1.3 Historical Vertical Electrical Sounding Field Data

Electrical data collected at the Nesjavellir site in 1985 for geothermal resource characterization provide insight into the subsurface electrical properties before geothermal development and wastewater disposal at Nesjavellir (Árnason et al. 1986). The data were collected using the vertical electrical sounding (VES) method with a Schlumberger array configuration. Four sounding locations were collected within the area of this study, HE-106, HE-109, HE-122, and HE-123 (Fig. 1). The VES method provides a 1D sounding of the subsurface resistivity and follows a similar methodology as the DC method outlined earlier, where current is injected through two surface electrodes (A and B) and the resulting electrical field is determined by measuring the voltage between another pair of electrodes (M and N). The current electrodes remained fixed around the central sounding location, and the spacing was gradually increased from 4 to 3560 m, with larger spacing probing deeper into the subsurface. The potential electrodes also remain centered around the sounding location, but the electrode spacing remains small (1-200 m) and is increased to preserve the signal-to-noise ratio at large AB spacings.

In the 1D soundings, near-surface heterogeneities can cause shifts in the apparent resistivity measured at similar AB spacings but with varying MN spacings. Following the method detailed in Hersir, Gudnason, and Flóvenz (2022), the apparent resistivity measurements at the various MN spacings are corrected by a multiplication factor to minimize misfit to the apparent resistivities measured by the largest MN electrode spacing. The largest MN electrode spacing remains fixed because it is assumed to be least impacted by local heterogeneities. For this data, the multiplication factors range from 0.85 to 1.6. To obtain a 1D resistivity model, the corrected data were inverted using pyGIMLi software using a smoothness-constrained inversion that minimizes the L2-norm of the data misfit on a logarithmic scale (Rücker, Günther, and Wagner 2017).

3.2 Synthetic Cross-hole DCIP

This study also explores the potential of cross-hole DCIP to monitor H_2S mineralization through synthetic experiments. Cross-hole electrical surveying can be advantageous for monitoring deep subsurface processes, improving the spatial resolution of wireline surveying. Monitoring implementations include tracking CO_2 injection systems (Carrigan et al. 2013; Jia et al. 2024; Schmidt-Hattenberger et al. 2011), tracer migration (Singha and Gorelick 2005; Wilkinson et al. 2010), and groundwater remediation (Lévy et al. 2022; Lévy et al. 2024a; Bording et al. 2019; Nivorlis et al. 2019).

The survey design utilizes two boreholes spaced 100 m apart. Each borehole has 31 electrodes, spaced 10 m apart from 150 to 450 m depth. Following a similar approach as Lévy et al. (2022), the synthetic model is imaged by combining four different aquisition geometries; (1) individual gradient array down the injection borehole, (2) second individual gradient array down the monitoring borehole, (3) AB-MN array configuration with the current dipole (A and B) in the injection borehole and potential dipole (M and N) in the monitoring borehole, and (4) AM-BN configuration with the current and potential dipoles split across the two boreholes.

The DCIP starting model for the cross-hole study is constructed by extracting the MPA parameters along NN-4 from the inversion of field data collected in 2020. The time-lapse chargeability changes due to H_2S injection are estimated through reactive transport simulations, where the change in the volume fraction of metallic particles (iron sulfides and iron oxides) is converted to a synthetic chargeability response through eq. 8 (further discussed in Section 3.5).

3.3 Time-Lapse DCIP Data Processing and Inversion

The DCIP geophysical modeling and data inversions are performed utilizing a novel electric and electromagnetic geophysical software, EEMverter (Fiandaca et al. 2023). The data were manually processed by removing outliers in EEMstudio (Sullivan, Viezzoli, and Fiandaca 2023). Sources of noise can be high contact resistances ($\sim$0.7-1.5 kΩ in our data), polarization of the stainless steel electrodes, and capacitive and inductive coupling between cables and the ground. Cultural noise from nearby infrastructure is also a consideration at this field site due to a buried power line and a residential building located within the survey area (Fig. 1). The impact of the surrounding infrastructure on data noise can be observed in the standard deviations mapped in SI Fig. S1.

EEMverter models the full voltage decay, accounting for the effects of the current waveform and receiver transfer function in the IP forward response (Fiandaca et al. 2012; Fiandaca et al.

2013). The 2D DCIP forward response follows the method presented in Fiandaca et al. (2013) and builds off the 1D response outlined in Fiandaca et al. (2012). The time-lapse inversion scheme, as presented in Xiao et al. (2022), simultaneously inverts two datasets to obtain the corresponding geophysical models. The time-lapse inversion is solved iteratively utilizing the Levenberg-Marquardt adaptive minimization scheme (Auken et al. 2015; Menke 2018). The time-lapse models are constrained through the asymmetric minimum support norm, which penalizes large time-lapse changes to favor the smallest model changes consistent with the data (Fiandaca et al. 2015). Minimum support parameter values of $\alpha = 0.01$, $\sigma = 0.1$, $p_1 = 1.35$, $p_2 = 2.0$ were found to minimize both the data and time-lapse model misfits and are used in the inversion of the field DCIP data. Additional details on the forward response time-lapse inversion scheme are included in Supporting Information.

The inversion utilizes a multimesh approach where the model meshes are decoupled from the forward and constraint meshes (Fig. 2) (Xiao et al. 2022; Zhang et al. 2021). In the multimesh approach, the values on the inversion model mesh are mapped to the forward mesh utilizing an inverse distance weighting interpolation (Madsen, Fiandaca, and Auken 2020). A separate set of constraint meshes connects the model parameters of individual models, applying horizontal and vertical smoothness, and different models against one another through time-lapse constraints. These constraint meshes share the same geometry as the model mesh and are vertically discretized with a log-increasing spacing. The horizontal discretization of the forward meshes is derived from the electrode placement (x, y, and z). It is further subdivided horizontally into four cells to improve the resolution of the forward response without increasing the size of the model space (Fiandaca et al. 2013). Nonuniform electrode spacing along the survey lines (20 m along the survey edges vs 10 m near the center) results in mesh cells with variable widths. To avoid numerical artifacts resulting from uneven cell widths, the larger mesh cells (20 m width) were subdivided into two cells of equal widths (10 m).

As the forward meshes are defined by electrode locations, differences in electrode placement between datasets $\mathbf{d}_1$ and $\mathbf{d}_2$ result in misalignment between the meshes. Since the values along each forward mesh are only compared to their respective dataset ($\mathbf{d}_1$ or $\mathbf{d}_2$), misalignment between

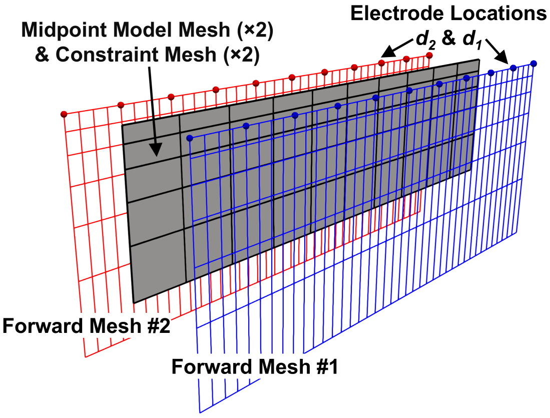

Figure 2. Schematic of the multimesh inversion approach with decoupled forward, constraint, and model meshes. The forward meshes (red and blue grid) are determined based on the electrode locations of the two surveys (red and blue spheres). The identical inversion model meshes (midpoint model meshes) and corresponding constraint meshes are calculated from the average electrode positions and displayed as a black grid with grey-filled cells.

the forward meshes does not pose any issues. However, each of the model and constraint meshes must be spatially aligned to correctly constrain the difference between the models $\mathbf{m}_1$ and $\mathbf{m}_2$. This presents a challenge for time-lapse surveys collected with electrodes that are subject to movement between datasets or that are not permanently installed, such as the datasets collected in this study. To construct two spatially identical model meshes, referred to here as midpoint model meshes, the electrode positions (x, y, and z) of datasets $\mathbf{d}_1$ and $\mathbf{d}_2$ are averaged. Each time-lapse inversion model presented in this study is solved on midpoint model meshes to limit the effects of variable electrode placement between the baseline and monitoring datasets ($\mathbf{d}_1$ and $\mathbf{d}_2$).

The effectiveness of the midpoint model mesh approach in managing electrode offset is evaluated through a synthetic test using the resistivity model recovered from the inversion of 2020 field data along Line 4. In this test, the resistivity forward response is simulated along lines with electrodes that are systematically shifted by 2, 4, 6, and 8 m along the line. The resulting offset data are then inverted alongside the unshifted dataset using two different inversion approaches: (1) two model meshes that are offset based on the electrode placement of each line and (2) two identical midpoint model meshes (Fig. 2). Since the datasets are generated from the same resistivity model and noise is not added in this synthetic test, time-lapse variability is related to electrode offset.

The depth of investigation (DOI) is determined using a cumulated approximate analysis approach (Fiandaca, Christiansen, and Auken 2015; Maurya et al. 2018). In this method, the sensitivities at each model layer, defined by the Jacobian matrix elements and covariance matrix, are summed upwards for each column of the model matrix. This provides a sensitivity value for each layer, expressing the cumulative sensitivity of the inversion from that layer to the deepest layer. A threshold sensitivity value, selected here as 5.0 (Fiandaca, Christiansen, and Auken 2015; Maurya et al. 2018), defines the DOI, below which each of the recovered model parameters is no longer data-driven.

3.4 Geochemical Analysis

The reactive transport models are parameterized with geochemical data collected from groundwater, injection water, and basalt cuttings sampled at the Nesjavellir site. Groundwater samples were collected throughout the area in 1991, 2007, and 2008 (Sigfusson, Gíslason, and Meharg 2011), and at the NL-12 borehole in November 2021 (Ciraula et al. 2024). Injection water samples were collected at the injection boreholes in November 2021 (Ciraula et al. 2024). The groundwater and injection water compositions were constrained through Ion Chromatography (IC) and inductively coupled plasma optical emission spectroscopy (ICP-OES) analysis (Ciraula et al. 2024). Additionally, H_2S concentrations were measured via mercury acetate titration (Arnórsson et al. 2006), and CO_2 concentrations were measured through modified alkalinity titration using 0.1 M HCl and 0.1 M NaOH (Jeffery et al. 1989; Stefánsson, Gunnarsson, and Giroud 2007).

The rock composition was determined from borehole cuttings from injection wells NN-3, NN-4, and NN-7, and whole-rock composition of the basalt was constrained through ICP-OES analysis (Ciraula et al. 2024). The primary minerals in the basaltic host rock were estimated using a linear regression approach, which determined the relative mineral proportions based on the mineral compositions and the measured oxide weight percentages of the whole rock (Ciraula et al. 2025). Further details on the chemical methods and the fluid and rock composition utilized in the reactive transport models can be found in Ciraula et al. (2024).

3.5 Integrating DCIP with Reactive Transport Modeling

3.5.1 *Principles of Reactive Transport*

Reactive transport simulators couple chemical reactions with fluid and heat transport (Steefel and Lasaga 1994; Steefel, DePaolo, and Lichtner 2005; Molins and Knabner 2019). Simulations solve the advection-dispersion equation, a partial differential equation that satisfies the conservation of mass and momentum, considering advective fluid flow, dispersion processes (molecular diffusion and mechanical dispersion), fluid sources and sinks, and chemical reactions (e.g., Carrera et al. 2022). Through this coupled simulation, reactive transport predicts how geochemical and hydrological systems evolve over space and time, enabling a better understanding of the subsurface processes that control these changes. The reactive transport simulation outputs of particular relevance in this study are the mineral abundances. Further details on reactive transport modeling are beyond the scope of this paper; readers are referred to Steefel, DePaolo, and Lichtner (2005) and Carrera et al. (2022) for additional background on the methodology, and to Aradóttir et al. (2012) and Ciraula et al. (2025) for reactive transport modeling of mineral storage approaches in Iceland.

3.5.2 *3D Reactive Transport Integration with Surface DCIP*

In this study, reactive transport models predict the degree of H_2S mineralization to (1) guide interpretation of the geophysical inversion models, (2) evaluate the sensitivity of the DCIP monitoring to H_2S mineralization, and (3) constrain the underlying processes controlling H_2S mineralization and impacting the IP response. A full description of the reactive transport model is presented in Ciraula et al. (2025), but a brief description is included here to provide context for the integration with DCIP. The reactive transport models are constructed in TOUGHREACT (Xu et al. 2011) using calibrated flow and chemical parameters based on borehole temperature, tracer, and water chemistry measurements prior to integration with the DCIP geophysical surveying. The development and calibration of the reactive transport model are done independently of geophysical field data to ensure that the simulations serve as an independent method for interpreting the geophysical responses. The model is constructed using a 3D, multiple interacting continua (MINC) framework (Pruess and Narasimhan 1985), considering non-isothermal fluid flow.

The reactive transport model simulates surface disposal of the geothermal wastewater, pumping of shallow freshwater wells, and the injection of H_2S-rich water into the shallow groundwater system. The Nesjavellir operator, Reykjavik Energy, provided the injection rates and water temperature. Shallow well pumping rates, surface wastewater disposal rates, and wastewater temperatures are estimated from values in Gómez-Díaz et al. (2022). The geological model considers variable host rock geology, featuring a sequence of hyaloclastite and lava flow lithologic units. The geology builds on the model presented in Gómez-Díaz et al. (2022), and was constructed using surface geological maps, borehole cuttings (Helgadóttir 2021; Ciraula et al. 2024), and borehole data from internal reports of the Nesjavellir operator, Reykjavik Energy (SI Fig. S2). The hyaloclastites are characterized by larger porosity and permeability values than the lava flows (Supporting Information Table 1), and contain more abundant basaltic glass, as observed in typical Icelandic basalts (e.g., Scott et al. 2023).

The primary minerals considered in the study consist of plagioclase, pyroxenes, olivine, iron oxides (magnetite and ilmenite), and basaltic glass. Alteration minerals available to precipitate include zeolites, carbonates, smectite clays, iron oxide (goethite), iron sulfides (pyrite and pyrrhotite), amorphous silica, and elemental sulfur. Dissolution and precipitation of primary and alteration minerals are kinetically controlled. They are modeled based on transition state theory, which considers the phase's rate constant, reactive surface area, saturation conditions considering the thermodynamic conditions, and additional acid- and base-catalyzed mechanisms (e.g., Palandri and Kharaka 2004; Xu et al. 2011). A complete list of the primary and alteration minerals, along with their kinetic rate parameters, is included in Supporting Information Tables 2 and 3. The thermodynamic constants are provided in the *carbfix.dat* thermodynamic database (Voigt et al. 2018) with redox conditions determined by the S(-2)/S(6) couple. The reactive surface areas of each mineral, a value often uncertain in reactive transport models, were calibrated by simulating 250 years of ambient groundwater reactive transport and ensuring a match to groundwater fluid compositions.

To integrate the reactive transport model with the DCIP inversion results, we calculate IP chargeability changes from the simulated iron sulfide precipitation and iron oxide dissolution using eq. 8. We simulate H_2S injection for two durations: 6 months to compare with the field geophysical data, and 25 years to evaluate the long-term changes in the geophysical response. The chargeability changes are then added to the 2020 baseline DCIP models to construct predicted 2021 models along the survey lines.

3.5.3 2D Radial Reactive Transport integration with Cross-hole DCIP

Reactive transport modeling also produces synthetic geophysical responses to evaluate cross-hole DCIP as a monitoring method for H_2S mineral storage. For the cross-hole synthetic modeling, a 2D radial reactive transport model is developed in TOUGHREACT (Xu et al. 2011) with the same geochemical parameterization as the 3D model. The 2D model has cells refined to 5×5 m around the injection borehole (SI Fig. S3) to enhance the simulation's resolution of the near-borehole processes that the cross-hole DCIP seeks to image. The refined radial geometry captures the flow and transport near the injection boreholes while ensuring computational efficiency. Two separate long-term (25 year) simulations of H_2S injection are performed using different injection fluids: (1) the H_2S-rich water measured at the NN-4 wellhead and (2) a higher-concentration H_2S-rich water that is injected into the deeper NJ-18 borehole (2136 m deep) at Nesjavellir (Galeczka et al. 2022). We simulate both scenarios to gain insight into the implementation of cross-hole monitoring of deep H_2S injection. The NJ-18 injection well receives wastewater from the ”Carbfix” emission reduction method, which uses scrubbing towers to increase the concentration of H_2S and CO_2 dissolved into the injection water. At Nesjavellir, these higher-concentration fluids are designated for deeper injection, where the risk for surface water contamination is reduced. For an overview of the Carbfix method and its implementation at Nesjavellir, readers are referred to the work by Matter et al. (2016) and Galeczka et al. (2022).

Similar to the integration of the 3D reactive transport model and surface DCIP, the change in volume fraction of metallic particles (iron sulfides and iron oxides) calculated through the 2D radial reactive transport simulations is used in eq. 8 to generate synthetic chargeability response changes. Random Gaussian noise is added to the synthetic DC voltages and the polarization curves with a standard deviation of 2% of the data values to better represent field conditions.

4 RESULTS

4.1 Reactive Transport Modeling

The results of the reactive transport model are first detailed to provide relevant context for the interpretation of the geophysics and the joint geochemical-geophysical integration. Relevant to the IP response in this study, the model indicates that iron released upon the alteration, primarily from basaltic glass and iron-bearing olivine, results in pyrite formation. H_2S mineralization is effective, with roughly 70% of the injected H_2S anticipated to mineralize as pyrite within the first year of injection, and 87% over 25 years of continuous injection. Based on the injection fluid compositions, the average injection rates, and a mineralization rate of 87%, we estimate that 284 m^3 of pyrite forms each year. However, the reactive transport simulations show that the high-permeability fractured basalt effectively transports the H_2S-rich fluid from the injection wells, leading to pyrite mineralization distributed throughout the subsurface. This distribution, along with the limited total mass of injected H_2S, yields minute pyrite volume fractions observed after the first six months of injection ($< 1 \times 10^{-4}\%$ of the porous media volume within 75 m of the injection well).

In addition to pyrite formation, alteration minerals include zeolites, smectite clays, carbonates, amorphous silica, and minor Fe(III)-oxides. These alteration products are consistent with the mineralogical changes expected during the alteration of Icelandic basalts in warm water (e.g., Scott et al. 2023). Within the basalt (hyaloclastite) rock matrix, zeolites and smectite clays comprise the majority of the alteration minerals after six months of injection, approaching $\sim 5 \times 10^{-4}\%$ and $\sim 1 \times 10^{-3}\%$ of total volume within 75 m of the injection well, respectively. Given the small volumes of alteration products, absolute changes in the rock porosity and permeability over long-term injection (25 years) are low ($\phi_{25} - \phi_0 = -0.06\%,\ \kappa_{25}/\kappa_0 = 0.75\%$). Additional reactive transport model results that extend beyond the scope of this paper can be found in Ciraula et al. (2025).

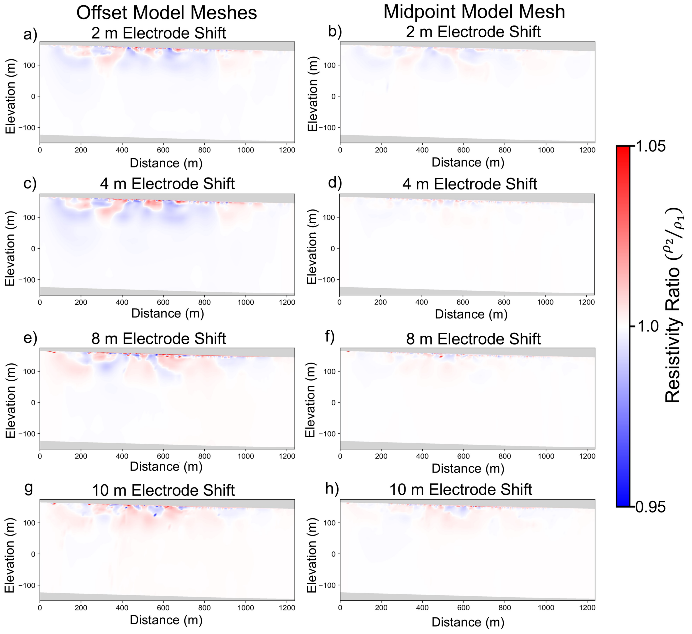

Figure 3. Time-lapse inversion results obtained using model meshes offset from one another (left column) and identical, midpoint model meshes (right column). The magnitude of the electrode misplacement (shift) is shown from a range of 2-8 m.

4.2 Validating Midpoint Model Mesh

The time-lapse inversions utilizing the shared midpoint model mesh are found to reduce erroneous time-lapse changes due to electrode misplacement in synthetic data as compared to inversions where the individual model meshes are offset (Fig. 3). This is essential for this study as the field campaigns were carried out a year apart, and the H_2S injection site did not offer the opportunity to install electrodes permanently. Given a 4 m shift in the electrode placement, the midpoint model mesh approach recovers an average absolute change (i.e., $\bar{x} = \frac{1}{n}\sum_{i=1}^{n}\left|\frac{m_{2,i}-m_{1,i}}{m_{1,i}} \times 100\right|$) of 0.1$\%$ compared to 2.1$\%$ for the offset mesh approach. The midpoint model mesh approach also recovers better inversion misfit than the offset model mesh approach: time-lapse misfit norm = 0.3 vs 2.1, first dataset L2 norm misfit = 1.2 vs 3.6, second dataset L2 norm misfit = 1.4 vs 3.9. Similar misfits are observed for the other offsets.

4.3 Integrating Surface DCIP and Reactive Transport Modeling

4.3.1 1985 vs 2020 Resistivity to Validate Reactive Transport Parameters

Changes between the resistivity model from 2020 DCIP lines and the 1985 VES model are compared to subsurface changes predicted by the reactive transport modeling. Between 1985 and 2020, resistivities decreased in the shallow groundwater system, as can be seen at the location of soundings HE-109 and HE-123, in the elevation range 0-100 meters above sea level (m.a.s.l.) (Fig. 4). Within this depth interval, the 2020 model recovers an average resistivity of $\sim$325 Ωm compared to an average resistivity of 1925 Ωm in the 1985 model. These soundings are located northeast of the injection boreholes, along the primary direction of groundwater flow. Soundings HE-122 and HE-106, located southeast of the injection wells away from the main groundwater flow direction, do not exhibit the same resistivity decreases and capture similar resistivity trends as the 2020 models. Here, we utilize the reactive transport model to provide a comprehensive understanding of the factors contributing to the resistivity decrease.

Variations in the total resistivity reflect changes happening in three parallel conduction pathways: electrolytic conduction, surface conduction in the electrical-double layer at the fluid-grain interface, and intra-solid conduction paths within the smectite clay sheets (e.g., Wyllie and Southwick 1954; McKelvey et al. 1955; Waxman and Smits 1968; Lévy et al. 2018). This is expressed by eq. 9 (Lévy et al. 2018),

$$\frac{1}{\rho_{tot}} = \sigma_{tot} = \frac{\sigma_w}{F} + \sigma_s + \frac{\frac{\sigma_w}{F'}}{1 + \frac{\sigma_w}{F' X_{smect} \sigma_{smect}}} \, , \tag{9}$$

where σ_w is the fluid conductivity (Sm^{-1}), σ_s is the surface conductivity pathway (Sm^{-1}), F is the formation factor from Archie's Law (Archie 1942) that depends on the porosity (ϕ) and the cementation factor (m) of the rock ($F = \phi^{-m}$), F' is the formation factor of the intra-solid conduction pathway, X_{smect} is the volume fraction of smectite in the bulk rock, and σ_{smect} is the intrinsic conduction of the solid smectite (Sm^{-1}).

The measured resistivity in 1985 is expected to be controlled by electrolytic and surface conduction because smectite clays are not identified in the shallow unaltered basalts at these depths prior to geothermal wastewater injection (Ciraula et al. 2024; Helgadóttir 2021). The reactive trans-

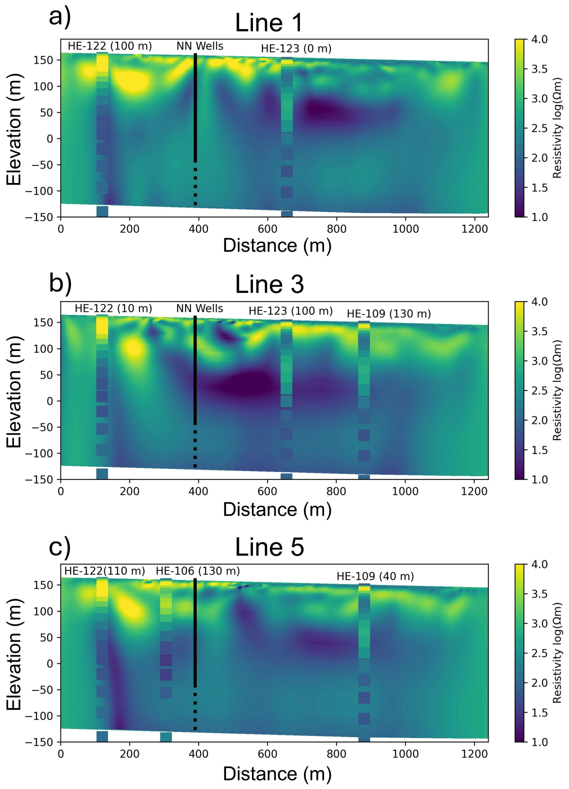

Figure 4. Results of the VES inversions of the 1985 data (HE-106, HE-109, HE-122, HE-123) plotted over the 2020 DC resistivity model for Lines 1, 3, and 5. The distance from the sounding to the line is included with the sounding labels. The black lines indicate the location of the NN injection wells, with the solid and dashed segments representing the cased and open intervals, respectively.

port model considers changes to the fluid chemistry and temperature (McCleskey et al. 2012) and predicts a fluid conductivity increase from 0.009 to 0.034 Sm^{-1} in 2020 near the 1985 sounding locations. These fluid conductivities align with field measurements of fresh groundwater (6×10^{-3} Sm^{-1}) and groundwater mixed with geothermal wastewater (0.037-0.046 Sm^{-1}) observed in NL-12 between 2001 and 2021. To determine the impact of the warm, conductive geothermal wastewater on the total resistivity, we first solve for the surface conductivity term using the field resistivity measured in 1985 ($\rho_{field,1985} = 1925\ \Omega m$), $\sigma_{freshwater} = 6 \times 10^{-3}\ Sm^{-1}$ (Zarandi and Ivarsson 2010; Ívarsson 2019), $\phi = 25\%$ (Muñoz 1996; Stefánsson 1991), and $m = 2.06$, indicative of minimally altered basalts (alteration < 10 wt.$\%$) from Lévy et al. (2018) and similar to values observed in Revil et al. (2017b). We identify a surface conductivity of $2 \times 10^{-4}\ Sm^{-1}$, similar to laboratory values recovered for minimally altered basalts in Lévy et al. (2018). Substituting the fresh water conductivity with the more conductive 2020 fluids ($4 \times 10^{-2}\ Sm^{-1}$) in eq. 9, we find the total resistivity decreases from 1925 to 400 Ωm, constituting most of the measured resistivity change.

While the majority of the resistivity decrease from 1985 to 2020 can be attributed to the presence of warm, conductive geothermal wastewater in the shallow groundwater system, smectite clay mineralization upon basalt alteration may also contribute to decreasing the resistivity (e.g., Lévy et al. 2018). The reactive transport model predicts the precipitation of smectite, with final volume fractions in the range 0.02-0.15$\%$ in the region of the field resistivity decrease. Using average values from basalt samples containing smectite measured in Lévy et al. (2018), we assign $F' = 29.1$ and $\sigma_{smect} = 0.65\ Sm^{-1}$ in the intra-solid conduction term contained in eq. 9. This range of predicted smectite abundance further decreases the estimated 2020 resistivity from 400 Ωm to 330-385 Ωm. These values are similar to the resistivities observed in 2020 ($\rho_{field,2020} = 325$ Ωm), and provide a process-based explanation for the field changes measured using geophysics.

To further explore how the resistivity measurements can validate the reactive transport model, we utilize a relationship established in Lévy et al. (2020) between the electrical conductivity, smectite volume fraction ($\theta_{smectite}$), and permeability (k) at low ($< 0.5\ Sm^{-1}$), uniform fluid conductivity, following:

$$\frac{1}{\rho} = \sigma = \frac{B\,\theta_{smectite}}{a\,k^{-\beta}}\ . \tag{10}$$

In this empirical relationship, the denominator defines a formation factor (i.e., how much the rock matrix impedes electrical current, Archie (1942)) and the constants have values a=14.4, B=8.4 S/m, and β=0.25. This relationship does not inform changes observed in the field resistivity from 1985 to 2020, but provides a means to assess the permeability values used in the reactive transport model using the average smectite abundance predicted by the reactive transport model in 2020 (0.06$\%$) and the resistivity values measured in 2020 (325 Ωm). We find that a high permeability value of 7.9 $\times 10^{-12}$ m^2 is required to capture the resistivity decrease observed in this alteration zone. This permeability is consistent with the x- and y-permeabilities assigned to the fractured hyaloclastite in the reactive transport model (1.0 $\times 10^{-12}$ m^2 and 9.7 $\times 10^{-11}$ m^2, respectively), which were calibrated to temperature logs in nearby monitoring boreholes (Ciraula et al. 2025).

Furthermore, these values align with values expected for permeable basalts (Freeze and Cherry 1979), and with the upper limit of values observed in unaltered, Icelandic hyaloclastites (Scott et al. 2023).

Overall, this integration establishes a framework in which electrical resistivity geophysical surveys can validate field-scale reactive transport models. While the integration presented here serves only to support for the general fluid conductivity changes, smectite mineralization, and high permeabilities of the present model, future studies with better resolution of the time-lapse geophysics could utilize these relationships between resistivity, fluid conductivity, smectite content, and permeability, alongside field samples quantifying fluid chemistry, smectite abundance, and permeability, to explore high-resolution calibration of reactive transport parameters (chemical and physical) to resistivity data.

4.3.2 Synthetic IP from Reactive Transport

The expected change in chargeability due to H_2S injection between the baseline and monitoring DCIP surveys is predicted by the reactive transport model along each of the DCIP survey lines and is shown in Fig. 5. The chargeability changes extend beyond the injection wells to larger distances along the lines, reflecting the regional groundwater flow direction towards Lake Thingvellir (from southwest to northeast). The changes are expected to be very small, at less than 0.02 mV/V during the six months of injection. Additionally, the changes are limited to depths greater than 280 m (elevation = -120 m.a.s.l.) due to the 200 m of borehole casing. The largest increase in volume fraction of metallic particles and chargeability values is closest to the NN-4 injection borehole along Line 4, as NN-4 had one of the highest injection rates of H_2S charged water over the survey period at 105 kg/s (total) compared to 11-43 kg/s at the other injection wells. Along Line 4, deep chargeability changes are observed as a result of injection into NN-3. However, injection rates average only 15 kg/s into NN-3, resulting in chargeability changes with smaller magnitudes (0.005 mV/V) at depths greater than 360 m (elevation = -200 m.a.s.l.). Injection into NN-4 also produces chargeability changes along Line 3, but the changes occur further along the line as the fluid laterally migrates from the NN-4 feed zones. Changes along Line 5 result from fluid injection near

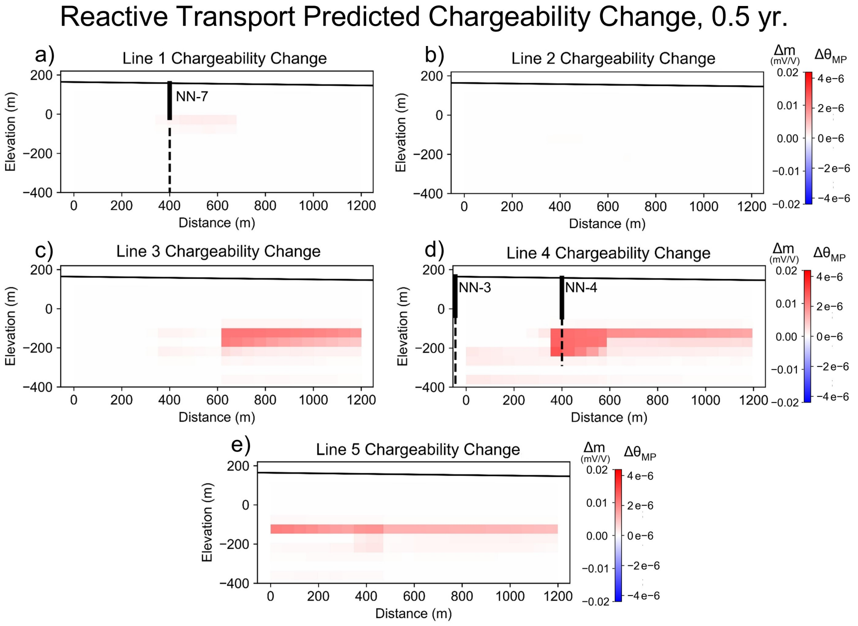

Figure 5. Results of the reactive transport model extracted along the field DCIP survey lines showing the minute expected change in metallic particles ($\Delta\theta_{MP}$= iron sulfides and iron oxides) and the corresponding chargeability change (Δm) following six months of H_2S injection. The NN-3, NN-4, and NN-7 injection wells that intersect the survey lines are displayed as black lines (solid = casing, dashed = open interval).

the power plant, with small contributions at a distance of 400 m along the line from H_2S injection through the NN-5 and NN-6 boreholes, located 80 m southeast of the line. Minimal changes are seen along Lines 1 and 2, as the nearby NN-7 injection borehole is deviated away from these lines.

The expected chargeability changes are also calculated for long-term injection (25 years) of H_2S at Nesjavellir (SI Fig. S4). After 25 years of injection, the expected chargeability anomaly remains small, at less than 0.5 mV/V along Line 4.

4.4 Time-Lapse Inversions of 2020-2021 Field Data

The time-lapse inversions recovered a sufficient fit to the data, with an average DC L2-norm misfit (δd_{DC}) of $\delta d_{DC,2020}$ =3.4, $\delta d_{DC,2021}$ =3.6, and an average IP L2-norm misfit (δd_{IP}) of $\delta d_{IP,2020}$ =2.0, $\delta d_{IP,2021}$ =1.5. The largest data misfits are observed near infrastructure, such as the buried power line, the house, and the injection boreholes/hot water pipes.

The results of the time-lapse IP inversions are shown in Fig. 6 as the change in the chargeability and the equivalent change in volume fraction of metallic particles (iron sulfides and iron oxides). The results are trimmed to the DOI and at the water table (elevation = 110 m.a.s.l.) to focus on changes occurring within the fully saturated subsurface. The DC inversion resolves down to 200-250 m depth (elevation = $\sim$0 to -100 m.a.s.l.). However, the center of Line 3, which is next to the house, only images to $\sim$100 m depth. The IP DOI reaches 100 m depth (elevation = $\sim$50 m.a.s.l.) along the southern extent of the survey and 150 m depth (elevation = $\sim$0 m.a.s.l.) towards the northern extent of the survey. Similar to the decreased DC DOI at the center of Line 3, the IP DOI at the center of Lines 2-5 near the house and injection infrastructure falls above the water table, limiting the IP data within 100 m of the house. Overall, the DOI values are roughly 50 m deeper along the northern extent of the line (away from the injection wells) compared to the southern extent (near the injection wells) for both the DC and IP inversions.

The time-lapse inversions reveal little change between the 2020 and 2021 DC and IP models. Aside from a few isolated nodes, changes in the chargeability and resistivity are negligible (Fig. 6, SI Fig. S5). The large range of chargeability magnitude plotted on the colorscale of Fig. 6 compared to the chargeability change expected from the reactive transport model (Fig. 5) highlights the magnitude of the noise in the surface DCIP field data relative to the predicted signal. This resolution limitation is further discussed Section 5.2.2. The large (>450 mV/V) isolated chargeability change at the southern extent of Line 4 aligns with the intersection of the buried power line. Similarly, the large changes observed along Line 3, beyond the residential building, align with areas of large data misfit and are near the DOI. Most DC resistivity changes are also isolated near infrastructure, aside from a broad increase in the DC resistivity along Line 5 near the NN-5 injection borehole (SI Fig. S5). However, the 2021 Line 5 data is notably noisy (SI Fig. S1) and the inversion misfit is large compared to the other lines (6.1 vs. 3-4), suggesting that this increase could be due to noise, such as coupling. Interestingly, the average injection rate of warm wastewater into NN-5 in the six months leading up to the 2020 survey was 62 L/s, compared to 38 L/s preceding the 2021 survey, which could also contribute to the increase in resistivity. Overall, the time-lapse inversions show agreement with the results of the reactive transport models and do not indicate systematic increases or decreases in chargeability or resistivity due to H_2S injection.

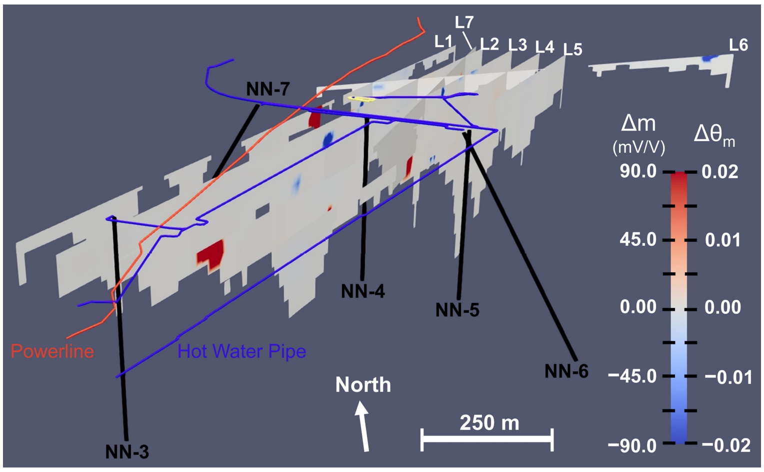

Figure 6. Results of the time-lapse IP inversion recovering changes in chargeability (m) and volume fraction of metallic particles (θ_m) following six months of H_2S injection. The casings of the NN injection wells (~200 m depth) are displayed as black lines and indicate the minimum depth that H_2S-charged water enters the subsurface. Beneath the casing, the wells are open and extend another 200-350 m. The results are trimmed to the water table at ~110 m depth and to the depth of investigation. Infrastructure in the survey area is displayed along the ground surface (yellow outline = house, blue line = hot water/steam pipes, red line = buried power line).

4.5 Integrating Cross-hole DCIP and Reactive Transport Modeling

Similar to the integration with surface DCIP, reactive transport modeling is integrated with cross-hole DCIP to evaluate the method's sensitivity to expected response changes. In the 5×5 m cells within the near-borehole environment, the radial reactive transport model predicts minor chargeability increases of 0.6 mV/V and 1.9 mV/V after 25 years of injection of the NN-4 and NJ-18 H_2S-charged waters, respectively (Fig. 7(a)/(c)). These chargeability increases coincide with the NN-4 feed zones at -120, -140, -170, and -228 m above sea level.

The time-lapse inversion results for the synthetic datasets from 25 years of H_2S injection with 2% Gaussian noise added are shown in Fig. 7(b) and 7(d). For the NN-4 injection fluid, chargeability increases at the depth intervals are partially recovered within 25 m of the boreholes. However, the spatial resolution is severely impacted by the background noise. Moreover, chargeability decreases of equivalent magnitude to the predicted increase (i.e., -0.5 mV/V) are introduced due to the background noise, making the interpretation of pyrite mineralization highly uncertain. Compared to NN-4, the larger predicted anomaly from the injection of NJ-18 fluids is better recovered.

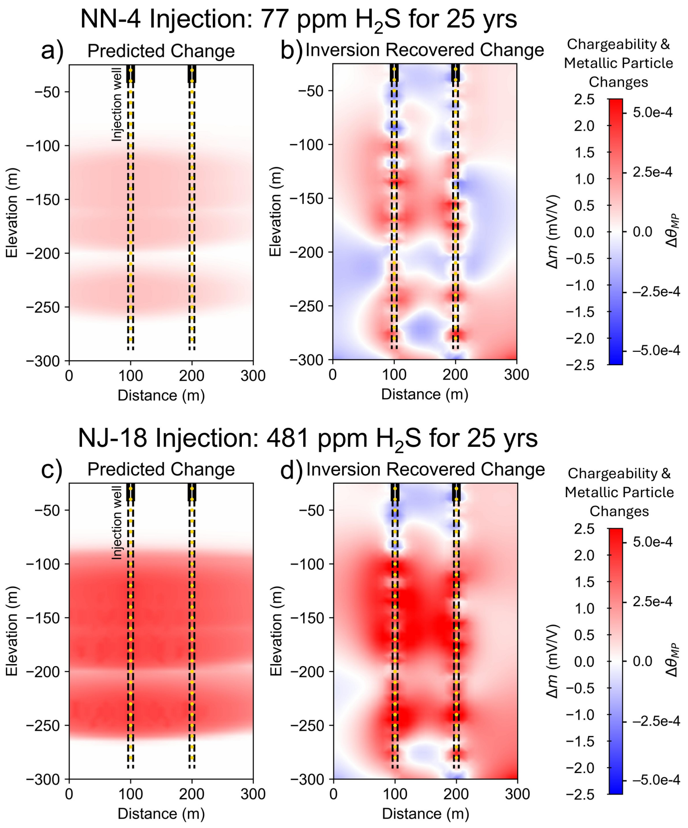

Figure 7. Results of the synthetic cross-hole modeling showing expected chargeability (m) change and the corresponding change in volume fraction of metallic particles (θ_{MP}) following 25 years of injection into NN-4 (top row) and NJ-18 (bottom row). The NN-4 and NJ-18 injection fluids have H_2S concentrations of 77 ppm (Ciraula et al. 2024) and 481 ppm (Galeczka et al. 2022), respectively. The right plots show the time-lapse inversion results of the predicted synthetic data with 2% Gaussian noise added to the IP decays and the DC voltages. Solid black lines indicate borehole casing, dashed black lines indicate the open boreholes, and yellow dots indicate the electrode locations.

The inversion reconstructs the magnitude and spatial extent of the changes within 25-75 m from the boreholes, and extends the full 100 m between the boreholes near the feed zones. Beyond 75 m from the boreholes, the inversion resolution diminishes, and the background noise dominates the response changes.

The ability of cross-hole DCIP to resolve chargeability changes from shorter injection durations is also tested through time-lapse inversions of synthetic data from five years of H_2S injection (SI Fig. S6). The inversion does not recover the minimal expected chargeability changes (0.15 mV/V) from the injection of NN-4 fluids. The chargeability changes from five years of H_2S injection into NJ-18 (0.5 mV/V) are slightly better resolved compared to NN-4 due to larger anomalies from the highly concentrated H_2S injection fluids. However, the changes are limited to 10-20 meters from the boreholes, and the data noise reduces the vertical resolution down the borehole.

5 DISCUSSION

5.1 Reducing Artifacts from Variable Electrode Placement

The synthetic modeling of the flexible inversion grid approach presented here improves the resolution of time-lapse inversions. The midpoint model mesh approach, constructed considering the average location among the electrodes, represents a simple yet effective approach to minimize artifacts introduced by variable electrode placement between time-lapse electrical surveys. Ultimately, this promotes higher resolution time-lapse imaging and allows for more flexible field implementation of time-lapse electrical surveys. Furthermore, this method could be applied alongside other approaches that further decrease artifacts, such as implementing array configurations that are less sensitive to variable electrode placement (Zhou and Dahlin 2003), correcting electrode location based on changes in apparent resistivity (Wilkinson et al. 2010; Wilkinson et al. 2015), and simultaneously inverting for electrode displacement and geoelectrical parameters (Loke et al. 2017; Kim et al. 2014).

5.2 DCIP Monitoring of H_2S Mineral Storage at Nesjavellir

5.2.1 Joint Interpretation of Reactive Transport and Field DCIP

In agreement with previous laboratory (Prikryl et al. 2018; Marieni et al. 2018) and field studies (Clark et al. 2020; Gunnarsson et al. 2018), the reactive transport model recovers effective H_2S mineralization with 70% of the total injected H_2S mineralizing during the first year of H_2S injection. However, the expected geophysical response from the H_2S mineralization resulting from the current injection system at Nesjavellir is minimal, suggesting that it cannot be detected with surface DCIP. The results of the time-lapse IP collected at the Nesjavellir injection site confirm these findings, as the method does not recover changes indicative of H_2S mineralization following six months of H_2S injection. The few observed changes are large and isolated, with metallic particle volume fractions $> 10\%$, far greater than the maximum volume changes of iron sulfides and iron oxides predicted by the reactive transport model. Thanks to the joint interpretation of the time-lapse IP changes with the reactive transport model, the infrastructure effects on the data can be distinguished from the mineralogical changes.

In this study, the reactive transport is used a-poseriori to interpret the results of field data. Such integrated approaches could be used a-priori in future studies to optimize survey design and evaluate the method's sensitivity to the subsurface processes of interest. This idea is explored further in the integration with cross-hole DCIP monitoring, discussed in the following section.

5.2.2 Surface DCIP Detection Limit Analysis

To assess the resolution of the surface DCIP survey to H_2S mineralization in a more quantitative manner, we calculate signal-to-noise ratios (SNR) resulting from various degrees of pyrite mineralization at different depths throughout the model. The signal-to-noise ratios are calculated utilizing the inversion sensitivity (Jacobian) matrix ($J_{i,j}$), the data standard deviation σ_i, the inversion model chargeability (m_j), and chargeability changes (Δm_j) in eq. 11.

$$SNR_i = \frac{J_{i,j}}{\sigma_i} \cdot \frac{\Delta m_j}{m_j} = \frac{\Delta d_i(\Delta m_j)}{\sigma_i} \ , \tag{11}$$

where the Jacobian is computed in the logarithmic parameter space (i.e., $J_{i,j} = \frac{\partial d_i}{\partial log(m_j)}$) and $\Delta d_i(\Delta m_j)$ is the data variation due to the model variation. The SNR vector is defined for each time gate of the IP decay curve, and the root mean square is calculated across the individual decay curves to provide a single amplitude value for each quadrapole. SNR values greater than one indicate that the chargeability signal, which is attributed only to pyrite mineralization in this analysis, is greater than the noise.

The analysis shows a clear decrease in the SNR with decreasing pyrite volume and increasing pyrite depth. The surface DCIP lacks resolution for bodies of pyrite with volume percentages $\leq 1\%$ at depths greater than 100 m. Smaller anomalies comprising 0.1 $vol.\%$ pyrite does not produce a surface DCIP signal magnitude greater than the noise at any depth. For larger anomalies

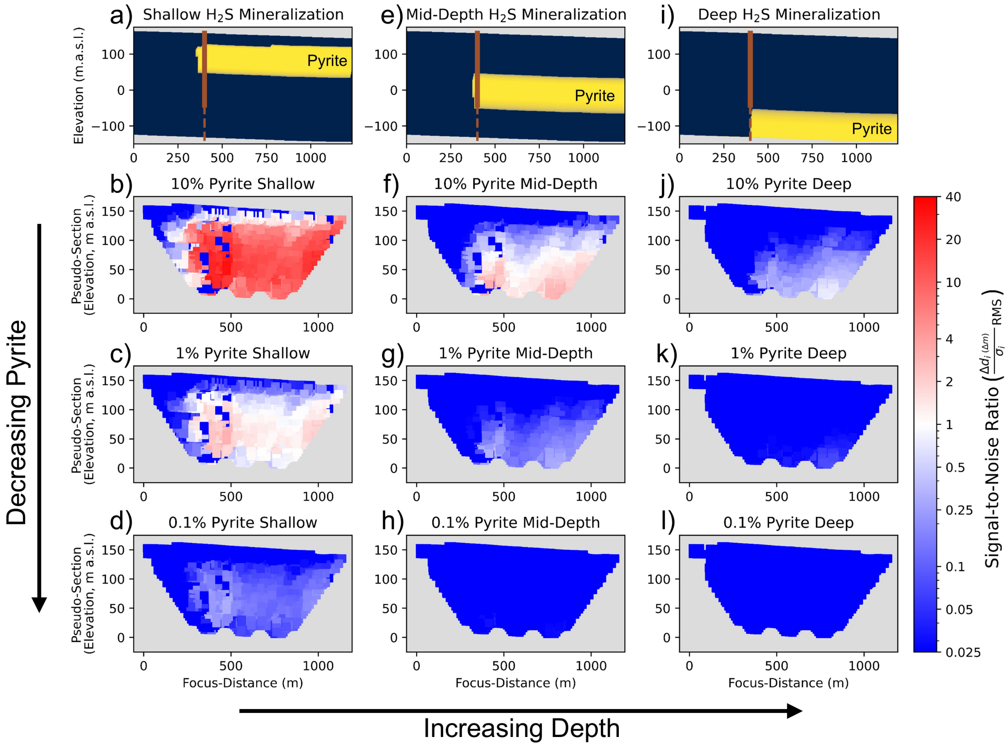

Figure 8. Signal-to-noise ratios of the surface DCIP data to pyrite mineralization at variable depth and abundance. Each column represents the resolution of shallow (a-d), mid-depth (e-h), and deep (i-l) H_2S mineralization, as indicated by the yellow anomaly extent in the top row. The second, third, and fourth rows are pseudo-sections of the signal-to-noise ratios for chargeability anomalies resulting from 10%, 1%, and 0.1% pyrite by volume, respectively. The signal-to-noise ratio is calculated as the root mean square (RMS) of the data variation (Δd_i) across the full IP decay due to the model variation (Δm_j), relative to the data standard deviation (σ_i).

comprising 10 $vol.\%$ pyrite, the SNR slightly exceeds one for the mid-depth anomaly from 100-200 m depth (elevation -50-50 m.a.s.l.) and greatly exceeds one for shallow anomaly depths from 50-150 m depth (elevation 25-125 m.a.s.l.). The surface DCIP data struggles to resolve signals greater than the noise for all pyrite anomalies at the deep injection depth ($>$ 200 m depth, elevation $<$ -50 m.a.s.l.).

These results quantitatively demonstrate the surface DCIP method's lack of resolution of the minute pyrite abundances ($< 4 \times 10^{-4}\%$) predicted by the reactive transport model over the six months of H_2S injection. The analysis supports the interpretation that the lack of change in the time-lapse DCIP survey does not directly indicate unsuccessful H_2S mineralization, but rather could indicate insignificant signal change, as suggested by the reactive transport model. Based on the resolution of the surface DCIP from the detection limit analysis and the rate of pyrite mineralization at the Nesjavellir injection site from the reactive transport simulations, monitoring long-term injection with surface DCIP remains unfeasible.

5.2.3 Cross-hole DCIP Monitoring

The synthetic 2D reactive transport models presented in Fig. 7 suggest that cross-hole monitoring could be implemented to monitor long-term H_2S mineralization of highly-concentrated H_2S-charged fluids like those injected using the Carbfix method. The downhole electrode configuration in cross-hole surveying enables the imaging of deeper H_2S mineralization that is below the imaging depth of the surface DCIP monitoring. Thus, the method could be applied to enhance the spatial coverage of surface and down-borehole monitoring efforts for H_2S mineral storage (Ciraula et al. 2024; Lévy et al. 2024b), particularly between the injection and monitoring boreholes.

However, challenges associated with the cross-hole method limit the practicality of cross-hole monitoring for H_2S mineral storage. First, background noise limits the method's ability to quantitatively capture the expected response change at distances greater than 25-50 meters from the borehole. While low noise levels (2%) are modeled in this idealized synthetic study, cross-hole surveys can be impacted by complex noise sources that mask the polarization signal, such as geologic noise (Zhao, Rijo, and Ward 1986), electrode geometric errors (Wilkinson et al. 2008), electromagnetic coupling (Gruszka and Wait 1989; Zhao et al. 2015), and cylindrical borehole and casing effects (Schenkel and Morrison 1994; Singer and Strack 1998; Osiensky, Nimmer, and Binley 2004). In the case of injection fluid into NN-4 with lower H_2S concentrations, relative to the NJ-18 Carbfix injection, smaller magnitude anomalies make interpretation unreliable and further limit the spatial resolution of the cross-borehole imaging (< 25 m). Second, implementing cross-hole surveying can be impractical in the field as it requires nearby boreholes, and the injection infrastructure at the wellhead can impede the ability to place down-hole electrodes. Third, shorter time-scales, such as monitoring 5 years of injection (SI Fig. S6), do not produce a large enough magnitude response change to be resolved by the geophysical inversions, limiting the temporal resolution of cross-hole DCIP monitoring of H_2S mineralization. Lastly, factors other than the pyrite volumetric fraction can potentially impact the field IP response. While many studies show that the chargeability is primarily a function of the metallic particle content (e.g., Pelton et al. 1978; Gurin et al. 2013; Gurin et al. 2015; Revil, Florsch, and Mao 2015; Hupfer et al. 2016), recent studies have shown varying dependencies of the polarization response of metallic particles on the size of the mineral grains (Martin and Weller 2023), geometry and orientation of the mineral grains (Izumoto 2023), and state of mineral surfaces (Gurin, Titov, and Ilyin 2019). These dependencies may impact the polarization response in the field, as laboratory experiments of H_2S mineralization in basalts recovered various manners of pyrite mineralization (e.g., surface coatings, discrete nodules, intergrowths within other secondary minerals, and in fractures within the basaltic glass) (Schaef et al. 2013). Moreover, Lévy et al. (2024b) observed polarization decreases following an initial increase in wireline DCIP response upon continuous H_2S injection over 540 days at the Nesjavellir site. The author's speculated that this decrease could be caused by a variety of factors, including passivation of the pyrite minerals due to the formation of other secondary minerals (e.g., Gurin, Titov, and Ilyin 2019), corrosion of the pyrite surfaces (e.g., Placencia-Gómez et al. 2013), or connectivity of pyrite grains. Ultimately, these contributions are poorly constrained in the field, and by not considering their potential degradation to the DCIP response, the synthetic cross-hole modeling represents an idealized field scenario. Further processes contributing to the IP response are discussed in the following section.

5.3 Underlying Processes Contributing to the DCIP Response

The results of the DC resistivity and reactive transport modeling can be used to better understand the IP response by detangling the underlying processes that contribute to the IP response in this field setting. The IP resolution is controlled by the signal strength, which depends on the measured subsurface voltages relative to background noise and the magnitude of the chargeability response change. In terms of the IP signal, the reactive transport model and DC resistivity data reveal key factors contributing to weak IP chargeability responses associated with H_2S mineral storage in fractured basalts; (1) the depth at which the mineralization occurs, (2) the widespread distribution of H_2S mineralization, and (3) the geological changes occurring alongside H_2S mineralization.

5.3.1 IP Noise Sources

Since data quality is a function of the signal-to-noise ratio, characterizing data noise is essential to evaluating IP as a monitoring method. The noise distribution is assessed by mapping the average measurement standard deviation along the survey lines, as shown in SI Fig. S1. The average standard deviations are largest near the infrastructure noise sources, including the buried power line, injection pipes and wells, and buildings. The DOI of the DCIP inversions also provides an indirect assessment of data noise, as shallow DOI values indicate data removal and lower parameter sensitivity relative to the noise. As shown in Fig. 6, the DOI values are severely impacted by the infrastructure at the field site. Since this infrastructure is associated with geothermal energy production and H_2S injection, these inherent noise sources potentially limit the broad use of surface DCIP for monitoring H_2S mineral storage at geothermal sites.

5.3.2 H_2S Mineralization Depth

The depth at which most H_2S mineralization occurs falls well below the DOI recovered in the field data inversions. The induced electrical field is weaker at greater depths, resulting in less current flow and smaller voltage responses. Additionally, the sensitivity to deep structures and the total number of deep data points are limited by the survey line length, requiring large electrode dipole spacings. Large injection currents and long survey lines can be difficult and impractical to implement in the field. This ultimately limits the applicability of surface DCIP as a monitoring tool for H_2S mineralization at Icelandic geothermal reinjection sites, as injection occurs at similar or greater depths than the Nesjavellir wells studied here.

5.3.3 Distribution of H_2S mineralization

The reactive transport model suggests that most of the injected H_2S mineralizes and that mineralization is widespread throughout the injection reservoir. The highly permeable fractured basalt host rock, identified through model calibrations (Gómez-Díaz et al. 2022; Ciraula et al. 2024) and validated by changes in resistivity observed from 1985 to 2020, is responsible for the widespread distribution of sulfide formation. Since the chargeability is proportional to the volume fraction of metallic minerals (eq. 8), more dilute pyrite mineralization over large total volumes limits the magnitude of the chargeability signal and is one of the largest challenges to using IP as a monitoring tool at Nesjavellir.

5.3.4 Non-Sulfide Mineral Influences on the IP Response

Since the petrophysical relationship in this study relates the chargeability change to the change in metallic particles (iron sulfides and iron oxides), the dissolution of primary iron oxides could mask the chargeability increase from H_2S mineralization. However, the magnetite and ilmenite dissolution is minimal, decreasing the chargeability by less than 0.01 mV/V over 25 years (SI Fig. S4). This suggests that these processes are unlikely to influence the measured signal and thus help clarify the geophysical monitoring in terms of reactive processes.

The reactive transport model also suggests that smectite clays precipitate upon basalt alteration. However, the impact of smectite clays on the chargeability response of volcanic rocks is an active area of research (e.g., Lévy et al. 2018; Lévy et al. 2019b; Lévy et al. 2019a; Lévy, Weller, and Gibert 2019; Ghorbani et al. 2018; Revil et al. 2017a; Revil, Florsch, and Mao 2015; Revil et al. 2018). One polarization model presented by Ghorbani et al. (2018) suggests that smectite clays contribute to the background chargeability (m_b) in eq. 7 by:

$$m_b = \frac{D_g \times \lambda \times CEC}{(\phi \times \sigma_w) + (D_g \times B \times CEC)} , \tag{12}$$

where D_g denotes the grain density (2900 kg/m^3), ϕ is the porosity, σ_w is the fluid conductivity (measured injection fluid conductivity = 0.07 S/m at 25 °C), and B and λ denotes two effective ionic mobilities for conduction and polarization (B(Na+, 25°C) = 3.1×10^{-9} m^2/s/V and λ(Na+, 25°C) = 3.0×10^{-10} m^2/s/V) (Ghorbani et al. 2018; Revil and Gresse 2021). Lévy et al. (2018) provides a relationship between the weight fraction of smectites and the CEC measured of $CEC = 90.6 \times Wt.Fract._{smect.}$. Using this relationship in eq. 12, the change in smectite content is transformed to an expected chargeability response following 0.5 and 25 years of H_2S injection. The results find little contribution to the chargeability response from the CEC of smectite clays (SI Fig. S4), as anticipated for a system with low-salinity pore fluids and minor smectite content (Ghorbani et al. 2018).

Alternative polarization models suggest that smectite reduces the IP response due to an increase in electrical conduction through interfoliar current paths in the smectite crystals, reducing the polarization at the fluid-mineral interface (Lévy et al. 2019b; Lévy, Weller, and Gibert 2019). This model is supported by laboratory measurements on geothermally-altered Icelandic volcanic rocks, which found that for a given pyrite content, the polarization response (MPA) decreased with increasing smectite content (Lévy et al. 2019b). Additionally, field DCIP surveys in Lévy et al. (2019a) found that lower overall resistivities due to smectite clays reduce the measured voltage signals, thereby lowering the signal-to-noise ratio and impeding the collection of quality IP data. At Nesjavellir, decreased resistivity values due to warm wastewater injection and subsequent smectite precipitation are apparent between the 1985 and 2020 resistivity datasets. This presents further challenges to resolving H_2S mineralization due to the low signal-to-noise ratios of the surface DCIP survey and the higher temperatures (90°C) and increased alteration near the injection wells for cross-hole DCIP surveying.

5.4 Petrophysical Relationships: Uncertainties and Assumptions

Integrating process-based models with geophysical methods, such as the reactive transport models presented here, relies on the validity of petrophysical relationships. As such, uncertainty in these relationships presents a key challenge to the effective integration of these approaches. For resistivity, future research should focus on refining the relationship between the smectite content, permeability, and electrical conductivity (i.e., eq. 10). Laboratory studies on samples with a broader range of permeabilities and degrees of alteration are needed to validate this relationship, particularly for its extrapolation to low smectite contents and high permeabilities, as observed in this study.

For the IP method, numerous studies have demonstrated near-linear relationships, similar to eq. 8, that effectively captures the influence of the concentration of metallic particles on the chargeability (Pelton et al. 1978; Gurin et al. 2013; Gurin et al. 2015; Revil, Florsch, and Mao 2015; Lévy et al. 2019b; Nordsiek and Weller 2008; Hupfer et al. 2016). However, as discussed previously regarding challenges implementing and interpreting cross-hole DCIP monitoring (see the discussion in Section 5.2.3), studies have also suggested a dependency of chargeability on other factors such as the grain size of the metallic particles, mineral type, and surface characteristics (e.g., Martin and Weller 2023; Lévy et al. 2019b; Gurin, Titov, and Ilyin 2019). These additional factors impacting the polarization response, along with uncertainties surrounding the influence of smectite on the polarization response, underscore the need to better constrain the petrophysical relationships associated with the IP geophysical method. Strengthening these relationships and working towards a unified theory of the polarization mechanisms (e.g., Bücker, Flores-Orozco, and Kemna 2018) will enhance the coupling between the IP responses at the field-scale and the subsurface processes driving them.

6 CONCLUSIONS

This study investigated how field-scale reactive transport modeling can be integrated with electrical geophysics to better understand the process of H_2S mineral storage with both synthetic modeling and a specific application case at the Nesjavellir study site. Through the integration, we assessed, in particular, the ability of time-lapse DCIP to monitor H_2S mineral storage. Time-lapse surface DCIP, collected over 6 months of continuous H_2S injection, did not recover chargeability changes that would indicate H_2S mineralization. The joint interpretation with the reactive transport modeling and the detection limit analysis of the surface DCIP resolution provides insights into the lack of observable chargeability change and reveals that the absence of chargeability change does not necessarily indicate unsuccessful H_2S mineralization at Nesjavellir. Factors contributing to the inability of surface DCIP to monitor H_2S mineralization include total pyrite volume fractions that are too small to produce detectable IP responses, pyrite mineralization occurring too deep ($>$ 200 m) for the surface DCIP survey to resolve changes, decreased IP resolution from low resistivities caused by the warm injection water and smectite formation, and high fracture permeability leading to dispersed pyrite formation. While the surface DCIP method cannot monitor H_2S mineralization at the Nesjavellir site, joint reactive transport-DCIP synthetic modeling suggests that cross-borehole DCIP surveying is sensitive to H_2S mineralization at the field-scale. However, the synthetic cross-hole DCIP modeling presented here represents an idealized case (i.e., low data noise, polarization controlled entirely by metallic particle volume content, and no degradation of the polarization response from smectite mineralization, pyrite grain geometry, or mineral surface passivation), and field implementation of cross-hole DCIP monitoring would require highly concentrated H_2S-rich injection waters (i.e., Carbfix fluids) and long injection durations.

This study also demonstrates how reactive transport modeling can improve the geophysical characterization of the subsurface by constraining the processes underlying the geophysical response. In the low-salinity system at Nesjavellir, the reactive transport model suggests that the polarization response is primarily driven by pyrite mineralization, and the impact of other mineralogical changes associated with basalt alteration, such as iron oxide dissolution and smectite precipitation, is secondary. However, the ability to accurately quantify the impact of smectite formation on the chargeability is limited by uncertainty in the underlying petrophysical relationships. Future studies should prioritize further constraining these relationships and the underlying polarization mechanisms in order to improve the integration of process-based models with IP geophysics.

Since the start of geothermal wastewater disposal at the Nesjavellir site, resistivity decreases from 1925 Ωm to 325 Ωm have been identified in the vicinity of the injection wells. These larger conductivities have the potential to further reduce the ability to resolve chargeable structures, such as pyrite mineralization, due to decreased voltage build-up and decreased current density.

Lastly, the observed decrease in resistivity due to warm wastewater disposal was utilized in a petrophysical relationship alongside smectite formation predicted by the reactive transport model to validate the high fracture permeability of 7.9×10^{-12} m^2 in the shallow basaltic reservoir. This integration demonstrates the value that time-lapse geophysics can add to validating reactive transport parameters.

ACKNOWLEDGMENTS

We first thank our editor, Lindsey Heagy, and two anonymous reviewers for their time and constructive feedback that greatly contributed to the presentation and conclusions of this research. Reykjavik Energy and, in particular, Íris Eva Einarsdóttir and Thorsteinn Ari Thorgeirsson, are thanked for providing data on wastewater injection and their support in facilitating and collecting water samples at Nesjavellir. Pradip Maurya, Muhammad Rizwan Asif, Asdis Benediktsdottir, and Sigurdur Ymir Richter are thanked for their help with DCIP data collection during the 2020 and 2021 field campaigns. Lydie Gailler and Svetlana Byrdina are also thanked for their participation in the 2019 geophysical field campaign at Nesjavellir, which helped improve the acquisition strategy for the following years. The Iceland GeoSurvey (ÍSOR) and Sveinborg Hlíf Gunnarsdóttir are thanked for providing the historical vertical electrical sounding data. DC thanks Gylfi Páll Hersir for providing valuable insight into the vertical electrical sounding data and data processing. DC also thanks Eric Sonnenthal for help with developing the reactive transport models. Alessandro Signora, Nicole Sullivan, and Stefano Galli are thanked for their input and guidance on the use of EEMverter and EEMstudio. General revisions to sentence structure and grammar were supported by AI tools ChatGPT (OpenAI 2025) and Grammarly (Inc. 2025). This project has received funding from the Nordic Volcanological Center (NordVulk), Landsvirkjun Energy Research Fund, the VOR - Reykjavik Energy Research and Innovation Fund, and the EEGS Foundation. Funding for the field data collection was provided by the Icelandic Centre for Research (Rannís) to Léa Lévy.

DATA AVAILABILITY

All geophysical data presented in this study, including the 2020 and 2021 DCIP datasets and the 1985 vertical electrical soundings, will be made available upon publication on the following repository: 10.5281/zenodo.15770067 with Creative Commons Attribution 4.0 International license. Geochemical data utilized in the reactive transport modeling can be found at Ciraula et al. (2024) and Ciraula et al. (2025).

References

Abdulsamad, F., N. Florsch, and C. Camerlynck (2017). “Spectral induced polarization in a sandy medium containing semiconductor materials: Experimental results and numerical modelling of the polarization mechanism”. In: *Near Surface Geophysics* 15 (6). ISSN: 15694445. DOI: `10.3997/1873-0604.2017052`.

Ahmmed, B. et al. (2020). “PFLOTRAN-SIP: A PFLOTRAN module for simulating spectral-induced polarization of electrical impedance data”. In: *Energies* 13 (24). ISSN: 19961073. DOI: `10.3390/en13246552`.

Aradóttir, E. S. et al. (2012). “Multidimensional reactive transport modeling of CO2 mineral sequestration in basalts at the Hellisheidi geothermal field, Iceland”. In: *International Journal of Greenhouse Gas Control* 9. ISSN: 17505836. DOI: `10.1016/j.ijggc.2012.02.006`.

Archie, G. E. (1942). “The electrical resistivity log as an aid in determining some reservoir characteristics”. In: *Transactions of the AIME* 146 (01).

Arnason, B. et al. (1969). “Hengill, a high temperature thermal area in Iceland”. In: *Bulletin Volcanologique* 33 (1). ISSN: 14320819. DOI: `10.1007/BF02596720`.

Árnason, K. et al. (1986). *Report OS-87018 (In Icelandic): Nesjavellir - Ölkelduháls Yfirbordsrannsóknir 1986*. Tech. rep. Orkustofnun.

Arnórsson, S. (1995). “Geothermal systems in Iceland: Structure and conceptual models-I. High-temperature areas”. In: *Geothermics* 24 (5-6). ISSN: 03756505. DOI: `10.1016/0375-6505(95)00025-9`.

Arnórsson, S. et al. (2006). “Sampling and analysis of geothermal fluids”. In: *Geofluids* 6 (3). ISSN: 14688115. DOI: `10.1111/j.1468-8123.2006.00147.x`.

Auken, E. et al. (2015). “An overview of a highly versatile forward and stable inverse algorithm for airborne, ground-based and borehole electromagnetic and electric data”. In: *Exploration Geophysics* 46 (3). ISSN: 18347533. DOI: `10.1071/EG13097`.

Binley, A. et al. (2015). *The emergence of hydrogeophysics for improved understanding of subsurface processes over multiple scales*. DOI: `10.1002/2015WR017016`.

Bording, T. S. et al. (2019). “Cross-borehole tomography with full-decay spectral time-domain induced polarization for mapping of potential contaminant flow-paths”. In: *Journal of Contaminant Hydrology* 226. ISSN: 18736009. DOI: `10.1016/j.jconhyd.2019.103523`.

Briggs, M. A. et al. (2013). “Simultaneous estimation of local-scale and flow path-scale dual-domain mass transfer parameters using geoelectrical monitoring”. In: *Water Resources Research* 49 (9). ISSN: 19447973. DOI: `10.1002/wrcr.20397`.

Bücker, M., A. Flores-Orozco, and A. Kemna (2018). “Electrochemical polarization around metallic particles - Part 1: The role of diffuse-layer and volume-diffusion relaxation”. In: *Geophysics* 83 (4). ISSN: 19422156. DOI: `10.1190/geo2017-0401.1`.

Callow, B. et al. (2018). “Assessing the carbon sequestration potential of basalt using X-ray micro-CT and rock mechanics”. In: *International Journal of Greenhouse Gas Control* 70. ISSN: 17505836. DOI: `10.1016/j.ijggc.2017.12.008`.

Camporese, M. et al. (2015). “Coupled and uncoupled hydrogeophysical inversions using ensemble Kalman filter assimilation of ERT-monitored tracer test data”. In: *Water Resources Research* 51 (5). ISSN: 19447973. DOI: `10.1002/2014WR016017`.

Carrera, J. et al. (2022). “Reactive Transport: A Review of Basic Concepts with Emphasis on Biochemical Processes”. In: *Energies* 15 (3). ISSN: 19961073. DOI: `10.3390/en15030925`.

Carrigan, C. R. et al. (2013). “Electrical resistance tomographic monitoring of CO2 movement in deep geologic reservoirs”. In: *International Journal of Greenhouse Gas Control* 18. ISSN: 17505836. DOI: `10.1016/j.ijggc.2013.04.016`.

Chen, J., S. S. Hubbard, and K. H. Williams (2013). “Data-driven approach to identify field-scale biogeochemical transitions using geochemical and geophysical data and hidden Markov models: Development and application at a uranium-contaminated aquifer”. In: *Water Resources Research* 49 (10). ISSN: 00431397. DOI: `10.1002/wrcr.20524`.

Cheng, S. Y. and K. C. Hsu (2021). “Bayesian Integration Using Resistivity and Lithology for Improving Estimation of Hydraulic Conductivity”. In: *Water Resources Research* 57 (3). ISSN: 19447973. DOI: `10.1029/2020WR027346`.

Ciraula, D. A. et al. (2025). “Quantifying H_2S Mineral Storage Processes in Fractured Basalt Using a Field-Scale Reactive Transport Model”. In: *In prep.*

Ciraula, D. A. et al. (2024). “Advanced monitoring of H2S injection through the coupling of reactive transport models and geophysical responses”. In: *Environmental Science & Technology*. DOI: `10.1021/acs.est.3c10139`.

Clark, D. E. et al. (2018). “The chemistry and potential reactivity of the CO2-H2S charged injected waters at the basaltic CarbFix2 site, Iceland”. In: *Energy Procedia*. Vol. 146. DOI: `10.1016/j.egypro.2018.07.016`.

Clark, D. E. et al. (2020). “CarbFix2: CO2 and H2S mineralization during 3.5 years of continuous injection into basaltic rocks at more than 250C”. In: *Geochimica et Cosmochimica Acta* 279. ISSN: 00167037. DOI: `10.1016/j.gca.2020.03.039`.

Commer, M., E. Gasperikova, and C. Doughty (2022). “Improved geophysical monitoring of carbon sequestration through parameter linkage to reservoir modeling”. In: *International Journal of Greenhouse Gas Control* 119. ISSN: 17505836. DOI: `10.1016/j.ijggc.2022.103717`.

Commer, M. et al. (2020). “Imaging of a fluid injection process using geophysical data - A didactic example”. In: *Geophysics* 85 (2). ISSN: 19422156. DOI: `10.1190/geo2018-0787.1`.

Dahlin, T., V. Leroux, and J. Nissen (2002). “Measuring techniques in induced polarisation imaging”. In: *Journal of Applied Geophysics* 50 (3). ISSN: 09269851. DOI: `10.1016/S0926-9851(02)00148-9`.

Deiana, R. et al. (2008). “Calibration of a Vadose Zone Model Using Water Injection Monitored by GPR and Electrical Resistance Tomography”. In: *Vadose Zone Journal* 7 (1). ISSN: 1539-1663. DOI: `10.2136/vzj2006.0137`.

Fiandaca, G., A. V. Christiansen, and E. Auken (2015). “Depth of investigation for multi-parameters inversions”. In: *Near Surface Geoscience*.

Fiandaca, G., L. M. Madsen, and P. K. Maurya (2018). “Re-parameterisations of the Cole-Cole model for improved spectral inversion of induced polarization data”. In: *Near Surface Geophysics* 16 (4). ISSN: 15694445. DOI: `10.3997/1873-0604.2017065`.

Fiandaca, G. et al. (2012). “Time-domain-induced polarization: Full-decay forward modeling and 1D laterally constrained inversion of Cole-Cole parameters”. In: *Geophysics* 77 (3). ISSN: 00168033. DOI: `10.1190/geo2011-0217.1`.

Fiandaca, G. et al. (2013). “Resolving spectral information from time domain induced polarization data through 2-D inversion”. In: *Geophysical Journal International* 192 (2). ISSN: 1365246X. DOI: `10.1093/gji/ggs060`.

Fiandaca, G. et al. (2015). “Generalized focusing of time-lapse changes with applications to direct current and time-domain induced polarization inversions”. In: *Geophysical Journal International* 203 (2). ISSN: 1365246X. DOI: `10.1093/gji/ggv350`.

Fiandaca, G. et al. (2023). “Closing the gap between galvanic and inductive methods: EEMverter, a new 1D/2D/3D inversion tool for electric and electromagnetic data with focus on induced polarisation”. In: *AEM 2023: Short abstracts, Preview, 2023:225*, pp. 52–66. DOI: `10.1080/14432471.2023.2236352`.

Flores-Orozco, A., K. H. Williams, and A. Kemna (2013). “Time-lapse spectral induced polarization imaging of stimulated uranium bioremediation”. In: *Near Surface Geophysics* 11 (5). ISSN: 15694445. DOI: `10.3997/1873-0604.2013020`.

Flores-Orozco, A. et al. (2011). “Using complex resistivity imaging to infer biogeochemical processes associated with bioremediation of an uranium-contaminated aquifer”. In: *Journal of Geophysical Research: Biogeosciences* 116 (3). ISSN: 01480227. DOI: `10.1029/2010JG001591`.

Foulger, G. R. (1988). “Hengill Triple Junction, SW Iceland: 1. Tectonic structure and the spatial and temporal distribution of local earthquakes”. In: *Journal of Geophysical Research* 93 (B11). ISSN: 01480227. DOI: `10.1029/jb093ib11p13493`.

Foulger, G. R. and D. R. Toomey (1989). “Structure and evolution of the Hengill-Grensdalur volcanic complex, Iceland: geology, geophysics, and seismic tomography”. In: *Journal of Geophysical Research* 94 (B12). ISSN: 01480227. DOI: `10.1029/jb094ib12p17511`.

Freeze, R. A. and J. A. Cherry (1979). *Groundwater*. Prentice-Hall, Inc.

Galeczka, I. M. et al. (2022). “A pre-injection assessment of CO2 and H2S mineralization reactions at the Nesjavellir (Iceland) geothermal storage site”. In: *International Journal of Greenhouse Gas Control* 115. ISSN: 17505836. DOI: `10.1016/j.ijggc.2022.103610`.

Ghorbani, A. et al. (2018). “Complex conductivity of volcanic rocks and the geophysical mapping of alteration in volcanoes”. In: *Journal of Volcanology and Geothermal Research* 357. ISSN: 03770273. DOI: `10.1016/j.jvolgeores.2018.04.014`.

Gómez-Díaz, E. et al. (2022). “Numerical modeling of reinjection and tracer transport in a shallow aquifer, Nesjavellir Geothermal System, Iceland”. In: *Geothermal Energy* 10 (7). ISSN: 2195-9706. DOI: `10.1186/s40517-022-00217-3`.

Government of Iceland (2010). *Regulation no. 5/14/2010*.

Government of Iceland (2016). *Energy*. URL: `https://www.government.is/topics/business-and-industry/energy/`.

Gruszka, T. P. and J. R. Wait (1989). “Interaction of induced polarization and electromagnetic effects in borehole probing”. In: *Geoexploration* 25 (4). ISSN: 00167142. DOI: `10.1016/0016-7142(89)90001-X`.

Gunnarsson, I. et al. (2018). “The rapid and cost-effective capture and subsurface mineral storage of carbon and sulfur at the CarbFix2 site”. In: *International Journal of Greenhouse Gas Control* 79. ISSN: 17505836. DOI: `10.1016/j.ijggc.2018.08.014`.

Gurin, G., K. Titov, and Y. Ilyin (2019). “Induced Polarization of Rocks Containing Metallic Particles: Evidence of Passivation Effect”. In: *Geophysical Research Letters* 46 (2). ISSN: 19448007. DOI: `10.1029/2018GL080107`.

Gurin, G. et al. (2013). “Time domain spectral induced polarization of disseminated electronic conductors: Laboratory data analysis through the Debye decomposition approach”. In: *Journal of Applied Geophysics* 98. ISSN: 09269851. DOI: `10.1016/j.jappgeo.2013.07.008`.

Gurin, G. et al. (2015). “Induced polarization of disseminated electronically conductive minerals: A semi-empirical model”. In: *Geophysical Journal International* 200 (3). ISSN: 1365246X. DOI: `10.1093/gji/ggu490`.

Helgadóttir, H. M. (2021). *NN-03 and NN-04 in Nesjavellir Drill cuttings analysis*. Tech. rep. ÍSOR Short Report 21001.

Hersir, G. P., E. Á. Gudnason, and Ó. G. Flóvenz (2022). "Geophysical Exploration Techniques". In: *Comprehensive Renewable Energy*. Ed. by T. M. Letcher. 2nd ed. Vol. 7. Elsevier.

Hinnell, A. C. et al. (2010). "Improved extraction of hydrologic information from geophysical data through coupled hydrogeophysical inversion". In: *Water Resources Research* 46 (4). ISSN: 00431397. DOI: `10.1029/2008WR007060`.

Hubbard, C. G. et al. (2013). "Laboratory study of spectral induced polarization responses of magnetite - Fe2+ redox reactions in porous media". In: *Geophysics* 79 (1). ISSN: 19422156. DOI: `10.1190/GEO2013-0079.1`.

Hupfer, S. et al. (2016). "Polarization effects of unconsolidated sulphide-sand-mixtures". In: *Journal of Applied Geophysics* 135. ISSN: 09269851. DOI: `10.1016/j.jappgeo.2015.12.003`.

Inc., G. (2025). *Grammarly*. URL: `https://www.grammarly.com`.

Ívarsson, G. (2019). *Nidurrennsli á Nesjavöllum*. Orkuveita Reykjavíkur - Report 2019-0011.

Izumoto, S. (2023). "Induced Polarization of Metal Grains: Simulations of Three-Dimensional Electric Fields". In: *Journal of Geophysical Research: Solid Earth* 128 (9). ISSN: 21699356. DOI: `10.1029/2023JB026757`.

Jeffery, G. H. et al. (1989). *Vogel's textbook of quantitative chemical analysis*. 5th ed. Longman Scientific and Technical. ISBN: 0-582-44693-7.

Jia, N. et al. (2024). "Cross-Borehole ERT Monitoring System for CO2 Geological Storage: Laboratory Development and Validation". In: *Energies* 17 (3). ISSN: 19961073. DOI: `10.3390/en17030710`.

Kemna, A., B. Kulessa, and H. Vereecken (2002). "Imaging and characterisation of subsurface solute transport using electrical resistivity tomography (ERT) and equivalent transport models". In: *Journal of Hydrology* 267 (3-4). ISSN: 00221694. DOI: `10.1016/S0022-1694(02)00145-2`.

Kessouri, P. et al. (2019). “Induced polarization applied to biogeophysics: recent advances and future prospects”. In: *Near Surface Geophysics* 17 (6). ISSN: 15694445. DOI: `10.1002/nsg.12072`.

Kim, J. H. et al. (2014). “Simultaneous inversion of resistivity structure and electrode locations in ERT”. In: *Near Surface Geoscience 2014 - 20th European Meeting of Environmental and Engineering Geophysics*. DOI: `10.3997/2214-4609.20142057`.

Lesmes, D. P. and K. M. Frye (2001). “Influence of pore fluid chemistry on the complex conductivity and induced polarization responses of Berea sandstone”. In: *Journal of Geophysical Research: Solid Earth* 106 (B3). ISSN: 21699356. DOI: `10.1029/2000jb900392`.

Lévy, L. et al. (2018). “The role of smectites in the electrical conductivity of active hydrothermal systems: Electrical properties of core samples from Krafla volcano, Iceland”. In: *Geophysical Journal International* 215 (3). ISSN: 1365246X. DOI: `10.1093/gji/ggy342`.

Lévy, L. et al. (2019a). “Electrical resistivity tomography and time-domain induced polarization field investigations of geothermal areas at Krafla, Iceland: Comparison to borehole and laboratory frequency-domain electrical observations”. In: *Geophysical Journal International* 218 (3). ISSN: 1365246X. DOI: `10.1093/gji/ggz240`.

Lévy, L. et al. (2019b). “Tracking Magmatic Hydrogen Sulfur Circulations Using Electrical Impedance: Complex Electrical Properties of Core Samples at the Krafla Volcano, Iceland”. In: *Journal of Geophysical Research: Solid Earth* 124 (3). ISSN: 21699356. DOI: `10.1029/2018JB016814`.

Lévy, L. et al. (2022). “Quantifying Reagent Spreading by Cross-Borehole Electrical Tomography to Assess Performance of Groundwater Remediation”. In: *Water Resources Research* 58 (9).

Lévy, L., A. Weller, and B. Gibert (2019). “Influence of smectite and salinity on the imaginary and surface conductivity of volcanic rocks”. In: *Near Surface Geophysics* 17 (6). ISSN: 15694445. DOI: `10.1002/nsg.12069`.

Lévy, L. et al. (2020). “Relationships between Lithology, Permeability, Clay Mineralogy and Electrical Conductivity in Icelandic Altered Volcanic Rocks”. In: *World Geothermal Congress*.

Lévy, L. et al. (2024a). “Managing the remediation strategy of contaminated megasites using field-scale calibration of geo-electrical imaging with chemical monitoring”. In: *Science of the Total Environment* 920. ISSN: 18791026. DOI: `10.1016/j.scitotenv.2024.171013`.

Lévy, L. et al. (2024b). “Understanding the fate of H2S injected in basalts by means of time-domain induced polarization geophysical logging”. In: *Journal of Geophysical Research: Solid Earth* 129 (6). DOI: `10.1029/2023JB028316`.

Loke, M. H. et al. (2017). “Rapid inversion of data from 2D resistivity surveys with electrode displacements”. In: *Geophysical Prospecting* 66 (3), pp. 579–594. DOI: `10.1111/1365-2478.12522`.

Madsen, L. M., G. Fiandaca, and E. Auken (2020). “3-D time-domain spectral inversion of resistivity and full-decay induced polarization data - full solution of Poisson’s equation and modelling of the current waveform”. In: *Geophysical Journal International* 223 (3). ISSN: 1365246X. DOI: `10.1093/gji/ggaa443`.

Marieni, C. et al. (2018). “Towards ‘green’ geothermal energy: Co-mineralization of carbon and sulfur in geothermal reservoirs”. In: *International Journal of Greenhouse Gas Control* 77. ISSN: 17505836. DOI: `10.1016/j.ijggc.2018.07.011`.

Marieni, C. et al. (2021). “Mineralization potential of water-dissolved CO2 and H2S injected into basalts as function of temperature: Freshwater versus Seawater”. In: *International Journal of Greenhouse Gas Control* 109. ISSN: 17505836. DOI: `10.1016/j.ijggc.2021.103357`.

Martin, T. and A. Weller (2023). “Superposition of induced polarization signals measured on pyrite-sand mixtures”. In: *Geophysical Journal International* 234 (1). ISSN: 1365246X. DOI: `10.1093/gji/ggad091`.

Martin, T. et al. (2021). “Spectral induced polarization: Frequency domain versus time domain laboratory data”. In: *Geophysical Journal International* 225 (3). ISSN: 1365246X. DOI: `10.1093/gji/ggab071`.

Matter, J. M. et al. (2016). “Rapid carbon mineralization for permanent disposal of anthropogenic carbon dioxide emissions”. In: *Science* 352 (6291). ISSN: 10959203. DOI: `10.1126/science.aad8132`.

Maurya, P. K. et al. (2018). “Field-scale comparison of frequency- and time-domain spectral induced polarization”. In: *Geophysical Journal International* 214 (2). ISSN: 1365246X. DOI: `10.1093/GJI/GGY218`.

McCleskey, R. B. et al. (2012). “A new method of calculating electrical conductivity with applications to natural waters”. In: *Geochimica et Cosmochimica Acta* 77. ISSN: 00167037. DOI: `10.1016/j.gca.2011.10.031`.

McKelvey, J. G. et al. (1955). “The application of a three-element model to the S.P. and resistivity phenomena evinced by dirty sands”. In: *Geophysics* 20 (4). ISSN: 0016-8033. DOI: `10.1190/1.1438201`.

Mellage, A. et al. (2018a). “Linking Spectral Induced Polarization (SIP) and Subsurface Microbial Processes: Results from Sand Column Incubation Experiments”. In: *Environmental Science and Technology* 52 (4). ISSN: 15205851. DOI: `10.1021/acs.est.7b04420`.

Mellage, A. et al. (2018b). “Sensing Coated Iron-Oxide Nanoparticles with Spectral Induced Polarization (SIP): Experiments in Natural Sand Packed Flow-Through Columns”. In: *Environmental Science and Technology* 52 (24). ISSN: 15205851. DOI: `10.1021/acs.est.8b03686`.

Menke, W. (2018). *Geophysical data analysis: Discrete inverse theory*. 3rd ed. Elsevier. DOI: `10.1016/0040-1951(86)90212-x`.

Molins, S. and P. Knabner (2019). “Multiscale Approaches in Reactive Transport Modeling”. In: *Reviews in Mineralogy and Geochemistry* 85. ISSN: 19432666. DOI: `10.2138/rmg.2019.85.2`.

Muñoz, A. Q. (1996). *Interpretation of Geophysical Well Logs from the Nesjavellir Geothermal Field, Iceland*. The United Nations University, Geothermal Training Program (13).

Nivorlis, A. et al. (2019). “Multidisciplinary characterization of chlorinated solvents contamination and in-situ remediation with the use of the direct current resistivity and time-domain induced polarization tomography”. In: *Geosciences (Switzerland)* 9 (12). ISSN: 20763263. DOI: `10.3390/geosciences9120487`.

Nordsiek, S. and A. Weller (2008). “A new approach to fitting induced-polarization spectra”. In: *Geophysics* 73 (6). ISSN: 00168033. DOI: `10.1190/1.2987412`.

Ntarlagiannis, D. et al. (2005). “Low-frequency electrical response to microbial induced sulfide precipitation”. In: *Journal of Geophysical Research: Biogeosciences* 110 (G2). DOI: `10.1029/2005jg000024`.

Olsson, P. I. et al. (2015). “Measuring time-domain spectral induced polarization in the on-time: Decreasing acquisition time and increasing signal-to-noise ratio”. In: *Journal of Applied Geophysics* 123. ISSN: 09269851. DOI: `10.1016/j.jappgeo.2015.08.009`.

Olsson, P. I. et al. (2016). “Doubling the spectrum of time-domain induced polarization by harmonic de-noising, drift correction, spike removal, tapered gating and data uncertainty estimation”. In: *Geophysical Journal International* 207 (2). ISSN: 1365246X. DOI: `10.1093/gji/ggw260`.

OpenAI (2025). *ChatGPT*. URL: `https://chat.openai.com`.

Osiensky, J. L., R. Nimmer, and A. M. Binley (2004). “Borehole cylindrical noise during hole-surface and hole-hole resistivity measurements”. In: *Journal of Hydrology* 289 (1-4). ISSN: 00221694. DOI: `10.1016/j.jhydrol.2003.11.003`.

Palandri, J. L. and Y. K. Kharaka (2004). *A compilation of rate parameters of water-mineral interaction kinetics for application to geochemical modeling*.

Pelton, W. H. et al. (1978). “Mineral discrimination and removal of inductive coupling with multifrequency IP”. In: *Geophysics* 43 (3). ISSN: 19422156. DOI: `10.1190/1.1440839`.

Peshtani, K. et al. (2025). “Investigating Soil Organic Matter Complexation in Natural Analog Systems Using Geoelectrical Methods”. In: *Environmental Science & Technology* 59.34, pp. 18203–18212. DOI: `10.1021/acs.est.5c08323`.

Placencia-Gómez, E. et al. (2013). “Laboratory SIP signatures associated with oxidation of disseminated metal sulfides”. In: *Journal of Contaminant Hydrology* 148. ISSN: 01697722. DOI: `10.1016/j.jconhyd.2013.02.007`.

Pleasants, M. S. et al. (2022). “Hydrogeophysical Inversion of Time-Lapse ERT Data to Determine Hillslope Subsurface Hydraulic Properties”. In: *Water Resources Research* 58 (4). ISSN: 19447973. DOI: `10.1029/2021WR031073`.

Pollock, D. and O. A. Cirpka (2012). “Fully coupled hydrogeophysical inversion of a laboratory salt tracer experiment monitored by electrical resistivity tomography”. In: *Water Resources Research* 48 (1). ISSN: 00431397. DOI: `10.1029/2011WR010779`.

Prikryl, J. et al. (2018). “H2S sequestration process and sustainability in geothermal systems”. In: *Geothermics* 71. ISSN: 03756505. DOI: `10.1016/j.geothermics.2017.09.010`.

Pruess, K. and T. N. Narasimhan (1985). “A Practical Method for Modeling Fluid and Heat Flow in Fractured Porous Media”. In: *Society of Petroleum Engineers Journal* 25 (1). ISSN: 01977520. DOI: `10.2118/10509-pa`.

Rembert, F. (2021). “Development of geo-electrical methods to characterize dissolution and precipitation processes in a carbonate context”. PhD thesis. Sorbonne Université.

Revil, A. et al. (2017a). “Alteration of volcanic rocks: A new non-intrusive indicator based on induced polarization measurements”. In: *Journal of Volcanology and Geothermal Research* 341. ISSN: 03770273. DOI: `10.1016/j.jvolgeores.2017.06.016`.

Revil, A. et al. (2017b). “Induced polarization of volcanic rocks - 1. Surface versus quadrature conductivity”. In: *Geophysical Journal International* 208 (2). ISSN: 1365246X. DOI: `10.1093/gji/ggw444`.

Revil, A. et al. (2018). “Electrical conductivity and induced polarization investigations at Kilauea volcano, Hawai’i”. In: *Journal of Volcanology and Geothermal Research* 368. ISSN: 03770273. DOI: `10.1016/j.jvolgeores.2018.10.014`.

Revil, A. and M. Gresse (2021). *Induced polarization as a tool to assess alteration in geothermal systems: A review*. DOI: `10.3390/min11090962`.

Revil, A., N. Florsch, and D. Mao (2015). “Induced polarization response of porous media with metallic particles -Part 1: A theory for disseminated semiconductors”. In: *Geophysics* 80 (5). ISSN: 19422156. DOI: `10.1190/GEO2014-0577.1`.

Rubin, Y. and S. S. Hubbard (2005). *Hydrogeophysics*. Vol. 50. Springer. DOI: `10.1007/1-4020-3102-5_1`.

Rücker, C., T. Günther, and F. M. Wagner (2017). “pyGIMLi: An open-source library for modelling and inversion in geophysics”. In: *Computers and Geosciences* 109. ISSN: 00983004. DOI: `10.1016/j.cageo.2017.07.011`.

Saneiyan, S. et al. (2018). “Geophysical methods for monitoring soil stabilization processes”. In: *Journal of Applied Geophysics* 148. ISSN: 09269851. DOI: `10.1016/j.jappgeo.2017.12.008`.

Saneiyan, S. et al. (2019). “Induced polarization as a monitoring tool for in-situ microbial induced carbonate precipitation (MICP) processes”. In: *Ecological Engineering* 127. ISSN: 09258574. DOI: `10.1016/j.ecoleng.2018.11.010`.

Schaef, H. T. et al. (2013). “Mineralization of basalts in the CO2-H2O-H2S system”. In: *International Journal of Greenhouse Gas Control* 16. ISSN: 17505836. DOI: `10.1016/j.ijggc.2013.03.020`.

Scheibe, T. D. and Y. J. Chien (2003). “An evaluation of conditioning data for solute transport prediction”. In: *Ground Water* 41 (2). ISSN: 0017467X. DOI: `10.1111/j.1745-6584.2003.tb02577.x`.

Schenkel, C. J. and H. F. Morrison (1994). “Electrical resistivity measurement through metal casing”. In: *Geophysics* 59 (7). ISSN: 00168033. DOI: `10.1190/1.1443663`.

Schmidt-Hattenberger, C. et al. (2011). “Application of a Vertical Electrical Resistivity Array (VERA) for monitoring CO2 migration at the Ketzin site: First performance evaluation”. In: *Energy Procedia*. Vol. 4. DOI: `10.1016/j.egypro.2011.02.258`.

Scott, S. W. et al. (2023). “Valgardur: a database of the petrophysical, mineralogical, and chemical properties of Icelandic rocks”. In: *Earth System Science Data* 15 (3). ISSN: 18663516. DOI: `10.5194/essd-15-1165-2023`.

Shuey, R. T. (1975). *Semiconducting Ore Minerals*. Vol. 4. Elsevier Scientific Publishing Company.

Sigfusson, B., S. R. Gíslason, and A. A. Meharg (2011). “A field and reactive transport model study of arsenic in a basaltic rock aquifer”. In: *Applied Geochemistry* 26 (4). ISSN: 08832927. DOI: `10.1016/j.apgeochem.2011.01.013`.

Singer, B. S. and K. M. Strack (1998). “New aspects of through-casing resistivity theory”. In: *Geophysics* 63 (1). ISSN: 00168033. DOI: `10.1190/1.1444327`.

Singha, K. et al. (2015). “Advances in interpretation of subsurface processes with time-lapse electrical imaging”. In: *Hydrological Processes* 29 (6). ISSN: 10991085. DOI: `10.1002/hyp.10280`.

Singha, K. and S. M. Gorelick (2005). “Saline tracer visualized with three-dimensional electrical resistivity tomography: Field-scale spatial moment analysis”. In: *Water Resources Research* 41 (5). ISSN: 00431397. DOI: `10.1029/2004WR003460`.

Slater, L. D. and D. Lesmes (2002). “IP interpretation in environmental investigations”. In: *Geophysics* 67 (1). ISSN: 00168033. DOI: `10.1190/1.1451353`.

Snæbjörnsdóttir, S. Ó. et al. (2017). “The chemistry and saturation states of subsurface fluids during the in situ mineralisation of CO2 and H2S at the CarbFix site in SW-Iceland”. In: *International Journal of Greenhouse Gas Control* 58. ISSN: 17505836. DOI: `10.1016/j.ijggc.2017.01.007`.

Snæbjörnsdóttir, S. Ó. et al. (2021). “Injection of geothermal CO2 and H2S gases at the Nesjavellir site, SW Iceland: A pre-injection overview”. In: *Proceedings World Geothermal Congress 2021*.

Steefel, C. I. and A. C. Lasaga (1994). “A coupled model for transport of multiple chemical species and kinetic precipitation/dissolution reactions with application to reactive flow in single phase hydrothermal systems”. In: *American Journal of Science* 294 (5). ISSN: 00029599. DOI: `10.2475/ajs.294.5.529`.

Steefel, C. I., D. J. DePaolo, and P. C. Lichtner (2005). “Reactive transport modeling: An essential tool and a new research approach for the Earth sciences”. In: *Earth and Planetary Science Letters* 240 (3-4). ISSN: 0012821X. DOI: `10.1016/j.epsl.2005.09.017`.

Stefánsson, A., I. Gunnarsson, and N. Giroud (2007). “New methods for the direct determination of dissolved inorganic, organic and total carbon in natural waters by Reagent-Free™ Ion Chromatography and inductively coupled plasma atomic emission spectrometry”. In: *Analytica Chimica Acta* 582 (1). ISSN: 00032670. DOI: `10.1016/j.aca.2006.09.001`.

Stefánsson, A. et al. (2011). “The geochemistry and sequestration of H2S into the geothermal system at Hellisheidi, Iceland”. In: *Journal of Volcanology and Geothermal Research* 202 (3-4). ISSN: 03770273. DOI: `10.1016/j.jvolgeores.2010.12.014`.

Stefánsson, V. (1991). *Fordafrædistudlar : poruhluti bergs*. Orkustofnun Report VS-91/02.

Sullivan, N. A. L., A. Viezzoli, and G. Fiandaca (2023). “EEMstudio: an open-source freeware QGIS plugin for processing, modelling and inversion of electric and electromagnetic data”. In: *AEM 2023: Short abstracts, Preview, 2023:225*, pp. 52–66. DOI: `10.1080/14432471.2023.2236352`.

Tran, A. P. et al. (2016). “Quantifying shallow subsurface water and heat dynamics using coupled hydrological-thermal-geophysical inversion”. In: *Hydrology and Earth System Sciences* 20 (9). ISSN: 16077938. DOI: `10.5194/hess-20-3477-2016`.

Üner, S., G. Ö. Ağaçgözgü, and D. D. Doğan (2019). “Hydrogeophysical modelling of Hisarcik (Kütahya) geothermal field, western Turkey”. In: *Geophysical Prospecting* 67 (8). ISSN: 13652478. DOI: `10.1111/1365-2478.12826`.

Vinegar, H. J. and M. H. Waxman (1984). “Induced Polarization of Shaly Sands”. In: *Geophysics* 49 (8). ISSN: 00168033. DOI: `10.1190/1.1441755`.

Voigt, M. et al. (2018). “Evaluation and refinement of thermodynamic databases for mineral carbonation”. In: *Energy Procedia*. Vol. 146. DOI: `10.1016/j.egypro.2018.07.012`.

Waxman, M. H. and L. J. Smits (1968). “Electrical Conductivities in Oil-Bearing Shaly Sands”. In: *Soc. Pet. Eng. J.* (8). ISSN: 08910901. DOI: `10.2118/1863-a`.

Weller, A. and L. Slater (2022). “Ambiguity in induced polarization time constants and the advantage of the Pelton model”. In: *Geophysics* 87 (6). ISSN: 19422156. DOI: `10.1190/geo2022-0158.1`.

Wilkinson, P. B. et al. (2010). “High-resolution Electrical Resistivity Tomography monitoring of a tracer test in a confined aquifer”. In: *Journal of Applied Geophysics* 70 (4). ISSN: 09269851. DOI: `10.1016/j.jappgeo.2009.08.001`.

Wilkinson, P. B. et al. (2008). “Extreme sensitivity of crosshole electrical resistivity tomography measurements to geometric errors”. In: *Geophysical Journal International* 173 (1). ISSN: 0956540X. DOI: `10.1111/j.1365-246X.2008.03725.x`.

Wilkinson, P. B. et al. (2015). “Development and testing of displacement inversion to track electrode movements on 3-D electrical resistivity tomography monitoring grids”. In: *Geophysical Journal International* 200 (3). ISSN: 1365246X. DOI: `10.1093/gji/ggu483`.

Williams, K. H. et al. (2005). “Geophysical imaging of stimulated microbial biomineralization”. In: *Environmental Science and Technology* 39 (19). ISSN: 0013936X. DOI: `10.1021/es0504035`.

Williams, K. H. et al. (2009). “Geophysical monitoring of coupled microbial and geochemical processes during stimulated subsurface bioremediation”. In: *Environmental Science and Technology* 43 (17). ISSN: 0013936X. DOI: `10.1021/es900855j`.

Wong, J. (1979). “An electrochemical model of the induced-polarization phenomenon in disseminated sulfide ores.” In: *Geophysics* 44 (7). ISSN: 00168033. DOI: `10.1190/1.1441005`.

Wu, Y. et al. (2010). “On the complex conductivity signatures of calcite precipitation”. In: *Journal of Geophysical Research: Biogeosciences* 115 (G2). DOI: `10.1029/2009jg001129`.

Wu, Y. et al. (2011). “Geophysical monitoring and reactive transport modeling of ureolytically-driven calcium carbonate precipitation”. In: *Geochemical Transactions* 12. ISSN: 14674866. DOI: `10.1186/1467-4866-12-7`.

Wu, Y. et al. (2014). “Geophysical monitoring and reactive transport simulations of bioclogging processes induced by Leuconostoc mesenteroides”. In: *Geophysics* 79 (1). ISSN: 19422156. DOI: `10.1190/GEO2013-0121.1`.

Wyllie, M. and P. Southwick (1954). “An Experimental Investigation of the S.P. and Resistivity Phenomena in Dirty Sands”. In: *Journal of Petroleum Technology* 6 (02). ISSN: 0149-2136. DOI: `10.2118/302-g`.

Xiao, L. et al. (2022). “Three-dimensional time-lapse inversion of transient electromagnetic data, with application at an Icelandic geothermal site”. In: *Geophysical Journal International* 231 (1). ISSN: 1365246X. DOI: `10.1093/gji/ggac206`.

Xu, T. et al. (2011). “TOUGHREACT version 2.0: A simulator for subsurface reactive transport under non-isothermal multiphase flow conditions”. In: *Computers and Geosciences* 37 (6). ISSN: 00983004. DOI: `10.1016/j.cageo.2010.10.007`.

Zarandi, S. and G. Ivarsson (2010). *A Review on Waste Water Disposal at the Nesjavellir Geothermal Power Plant.*

Zhang, B. et al. (2021). “3D inversion of time-domain electromagnetic data using finite elements and a triple mesh formulation”. In: *Geophysics* 86 (3). ISSN: 19422156. DOI: `10.1190/geo2020-0079.1`.

Zhao, J. X., L. Rijo, and S. H. Ward (1986). “Effects of geologic noise on cross-borehole electrical surveys.” In: *Geophysics* 51 (10). ISSN: 00168033. DOI: `10.1190/1.1442053`.

Zhao, Y. et al. (2015). “Phase correction of electromagnetic coupling effects in cross-borehole EIT measurements”. In: *Measurement Science and Technology* 26 (1). ISSN: 13616501. DOI: `10.1088/0957-0233/26/1/015801`.

Zhou, B. and T. Dahlin (2003). “Properties and effects of measurement errors on 2D resistivity imaging surveying”. In: *Near Surface Geophysics* 1 (3). ISSN: 15694445. DOI: `10.3997/1873-0604.2003001`.

Supporting Information for:
Constraining Time-lapse Geophysical Responses with Reactive Transport Modeling: An Approach to Monitor H_2S Mineral Storage

Daniel A. Ciraula[1], Gianluca Fiandaca[2], Jian Chen[2], Samuel Scott[1], Léa Lévy[3],

[1]NordVulk, Institute of Earth Sciences, University of Iceland, Reykjavík 101, Iceland.
Email: danielac@hi.is
[2]Department of Earth Sciences “Ardito Desio”, University of Milano, 20133, Italy
[3]CNRS-INSU, Géosciences Rennes UMR 6118, Rennes, France

Contents

1 Text: DCIP Forward Response Additional Details

The DCIP forward response follows the approach presented in Fiandaca et al. (2013) where the complex resistivities are calculated for each cell in the finite element mesh for a set of frequencies and the corresponding forward responses are transformed to the time domain through a sine transformation. In particular, the time domain switch-off step response, V_{STEP}, is computed as follows:

$$V_{STEP}(m, t, q_{ABMN}) = \begin{cases} Z(\sigma(m, \omega = 0), q_{ABMN}) & , t \leq 0 \\ Z(\sigma(m, \omega = 0), q_{ABMN}) - K & , t > 0 \end{cases} , \tag{1}$$

$$K = \frac{2}{\pi} \int_0^\infty \mathrm{Im}\left(\frac{-Z^*(\sigma^*(m, \omega), q_{ABMN})}{i\omega} \right) \sin(\omega t)\, d\omega \; . \tag{2}$$

where $Z^*(\sigma^*(m, \omega), q_{ABMN})/i\omega$ represents the transfer function for a specific quadruple q_{ABMN}. The integral of the frequency domain transfer function in eq. 2 is computed using a fast Hankel transform for fixed, log-spaced t values, and cubic spline interpolation is used to obtain the necessary sampling frequency required by the fast Hankel transform.

2 Text: Time-lapse Inversion Scheme Additional Details

The time-lapse inversion scheme utilized in this study simultaneously inverts two datasets, solved iteratively to minimize the objective function:

$$\Phi = \Phi_d(\delta\mathbf{d}) + \Phi_{TL}(\delta\mathbf{m}) + \Phi_{Rm}(\mathbf{r}) \; . \tag{3}$$

The data difference measure (Φ_d) is a function of the difference between the forward response and the observed data ($\delta\mathbf{d} = \mathbf{d} - \mathbf{d}_{obs}$). The Φ_{Rm} regularization term is a measure of the model roughness ($\mathbf{r} = -\mathbf{R}_m\mathbf{m}$). The measure of the time-lapse model differences ($\delta\mathbf{m} = \mathbf{m}_2 - \mathbf{m}_1$) contributes to the overall inversion objective function through the regularization term Φ_{TL}. While datasets $\mathbf{d}_1$ and $\mathbf{d}_2$ can have variable sizes, the models $\mathbf{m}_1$ and $\mathbf{m}_2$ have identical sizes to obtain the model difference $\delta\mathbf{m}$. The Φ_{TL} term is defined by the asymmetric minimum support norm presented in Fiandaca et al. (2015); Xiao et al. (2022), whereas Φ_d, and Φ_{Rm} are L2-norm based. The asymmetric minimum support norm penalizes the number of components $\delta\mathbf{m}_i$ where $\mathbf{m}_{2,i}$ varies significantly from $\mathbf{m}_{1,i}$, thus, favoring compact time-lapse changes.

3 Nesjavellir Porosity and Permeability Values

Table 1: Porosity and calibrated permeability values utilized in the reactive transport model presented in presented in Ciraula et al. (2025). Values are provided for fracture and matrix domains of the MINC model.

		Permeability (m^2)		
Rock Type	**Porosity**	k_x	k_y	k_z
Hyaloclastites				
- Fracture Network	0.60	1.01×10^{-12}	9.71×10^{-11}	1.29×10^{-13}
- Outer & Inner Matrix	0.25	1.00×10^{-14}	1.00×10^{-14}	1.00×10^{-14}
Shallow Lava Flows[a]				
- Fracture Network	0.60	5.06×10^{-12}	1.94×10^{-12}	1.49×10^{-12}
- Outer & Inner Matrix	0.10	1.00×10^{-15}	1.00×10^{-15}	1.00×10^{-15}
Deep Lava Flows				
- Fracture Network	0.60	1.46×10^{-13}	1.56×10^{-11}	1.49×10^{-12}
- Outer & Inner Matrix	0.10	1.00×10^{-15}	1.00×10^{-15}	1.00×10^{-15}
Faulted Zone 1				
- Fracture Network[b]	0.60	3.00×10^{-11}	5.00×10^{-10}	5.00×10^{-13}
- Outer & Inner Matrix	0.10	1.00×10^{-14}	1.00×10^{-14}	1.00×10^{-14}
Faulted Zone 2				
- Fracture Network[b]	0.60	3.00×10^{-12}	5.00×10^{-11}	5.00×10^{-13}
- Outer & Inner Matrix	0.10	1.00×10^{-14}	1.00×10^{-14}	1.00×10^{-14}
Faulted Zone 3				
- Fracture Network[b]	0.60	3.00×10^{-12}	5.00×10^{-12}	5.00×10^{-13}
- Outer & Inner Matrix	0.10	1.00×10^{-14}	1.00×10^{-14}	1.00×10^{-14}
Model Bottom Boundary	0.26	1.00×10^{-14}	1.00×10^{-14}	1.00×10^{-14}

[a] Nesjahraun, Hagavíkurhraun, and Stangarhólshraun lava flows (Sigfusson et al., 2011).

[b] Fracture permeability calibrated in Gómez-Díaz et al. (2022).

4 Table: Primary Mineral Kinetic Parameters

Table 2: Initial basalt mineral composition, secondary minerals, and kinetic parameters used for mineral precipitation and dissolution rates.

	Vol. %	Surf. Area	**Acidic**	**Mechanism**		**Neutral**	**Mechanism**	**Basic**	**Mechanism**	
	of basalt	$[\mathrm{cm}^2\mathrm{g}^{-1}]^d$	$\log(k_{25})$	E_a	$n(H^+)$	$\log(k_{25})$	E_a	$\log(k_{25})$	E_a	$n(H^+)$
Albite[a]	22.96	0.1	-10.30	58.0	0.3	-11.19	60.0	-13.6	50.0	-0.3
Anorthite[b]	21.84	0.1	-5.17	58.0	1.22	-11.34	60.0	-13.6	50.0	-0.3
Sanidine[a]	2.59	0.1	-10.4	51.7	0.5	-12.48	60.0	-20.8	62.0	-0.8
Diopside[a]	9.69	0.1	-9.80	32.7	0.3	-11.00	43.9	–	–	–
Hedenbergite[a]	7.84	0.1	-9.80	32.7	0.3	-11.00	43.9	–	–	–
Enstatite[a]	1.94	0.1	-8.30	46.1	0.5	-11.90	89.5	–	–	–
Ferrosilite[a]	1.29	0.1	-8.30	46.1	0.5	-11.90	89.5	–	–	–
Fayalite[b]	1.57	0.1	-6.25	70.4	0.4	–	–	-7.39	60.9	0.2
Forsterite[b]	2.22	0.1	-7.16	70.4	0.4	–	–	-8.33	60.9	0.2
Ilmenite[c]	1.84	1.0	-8.35	37.9	0.421	-11.16	37.9	–	–	–
Magnetite[c]	1.22	1.0	-8.59	18.6	0.279	-10.78	18.6	–	–	–
Basaltic Glass[a]	25.00	0.2	$\log(k_{25})$=-7.564, E_a=25.5, $n(H^+)$=1.00, $n(Al^{3+})$=-0.33							

[a] Heřmanská et al. (2022)

[b] Heřmanská et al. (2023)

[c] Palandri and Kharaka (2004)

[d] Matrix continua surface area Aradóttir et al. (2012); Berndsen et al. (2024).

Fracture surface area = Volume Fraction$_{mineral}$ × 2.8×10^{-3} $\mathrm{m}^2/\mathrm{m}^3$.

Rate of enstatite is used for ferrosilite, diopside for hedenbergite

Units: $\log(k_{25})$=mol m^{-2} s^{-1}; E_a=kJ mol^{-1}

5 Table: Secondary Mineral Kinetic Parameters

Table 3: Alteration minerals and their kinetic precipitation and dissolution parameters.

	Surf. Area	**Acidic Mechanism**			**Neutral Mechanism**		**Basic Mechanism**		
Mineral	$[\mathrm{cm}^2\mathrm{g}^{-1}]^g$	$\log(k_{25})$	E_a	$n(H^+)$	$\log(k_{25})$	E_a	$\log(k_{25})$	E_a	$n(H^+)$
Analcime[b]	1000.0	-3.3	63.0	1.0	-11.3	58.5	-14.3	58.0	-0.4
Chabazite[b]	1000.0	-6.56	33.7	0.82	-11.55	44.2	-12.05	44.2	-0.2
Heulandite[b]	1000.0	-7.51	33.7	0.82	-12.6	44.2	-13.2	44.2	-0.2
Thomsonite[b]	1000.0	-5.61	33.7	0.82	-10.7	44.2	-11.0	44.2	-0.2
Calcite[c]	100.0	-0.30	14.4	1.00	-5.81	23.5	–	–	–
Dolomite[c]	100.0	-3.76	56.7	0.500	-8.60	95.3	-5.37	45.7	0.500
Magnesite[c]	100.0	-6.38	14.4	1.000	-9.34	23.5	-5.22	62.8	1.000
Siderite[d]	100.0	-3.799	45.0	0.9	-8.900	62.76	-15.600	71.0	-0.572
Celadonite[b]	10000.0	-11.68	32.3	0.37	-13.53	37.5	–	–	–
Montmorillonite[b]	10000.0	-11.7	50.8	0.55	-14.3	30.0	-17.2	48.0	-0.3
Nontronite[b]	10000.0	-11.7	50.8	0.55	-14.3	30.0	-17.2	48.0	-0.3
Saponite[b]	10000.0	-11.7	50.8	0.55	-14.3	30.0	-17.2	48.0	-0.3
Goethite[c]	100.0	–	–	–	-7.94	86.5	–	–	–
Pyrite[c]	100.0	-7.52	56.9	-0.50	-4.55	56.9	–	–	–
Pyrrhotite[c]	100.0	-8.04	50.8	-0.597	–	–	–	–	–
Anhydrite[c]	100.0	–	–	–	-3.19	14.3	–	–	–
Gypsum[c]	100.0	–	–	–	-2.79	0.00	–	–	–
SiO_2(am)[a,c,e]	1000.0	-10.6	41.6	0.3	-12.23	74.5	-14.2	73.0	-0.4
Elemental sulfur[f]	–	–	–	–	–	–	–	–	–

[a] Heřmanská et al. (2022)

[b] Heřmanská et al. (2023)

[c] Palandri and Kharaka (2004)

[d] Knauss et al. (2005)

[e] SiO_2(am) precipitation dictated by the free energy rate law from Carrol et al. (1998); $\log(k_{25}) = -9.29$.

[f] Elemental sulfur precipitation occurs under equilibrium.

[g] Matrix continua surface area Aradóttir et al. (2012); Berndsen et al. (2024).

Fracture surface area = Volume $\mathrm{Fraction}_{mineral} \times 2.8\times10^{-3}\ \mathrm{m}^2/\mathrm{m}^3$.

Rate of saponite is used for nontronite, glauconite for celadonite.

Units: $\log(k_{25})=\mathrm{mol\ m^{-2}\ s^{-1}}$; $E_a=\mathrm{kJ\ mol^{-1}}$

6 Figure: Field DCIP Data Standard Deviation

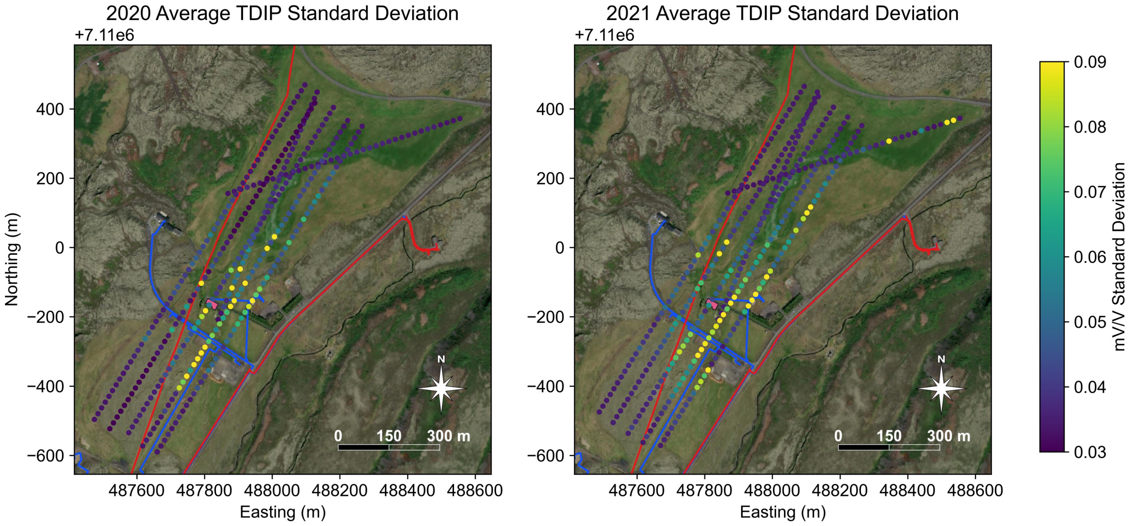

Figure S1: Average time-domain IP standard deviations as a function of location along the survey lines for data collected in 2020 (left) and 2021 (right). Each average value considers standard deviations grouped into 20 m bins along the line distance (x-y plane) from all pseudodepths (z-dimension). Red lines indicate power lines, blue lines indicate hot water/steam pipes, and the pink polygon near the center of the survey area is a residential building.

7 Figure: Nesjavellir Surface Geological Map and 3D Reactive Transport Grid

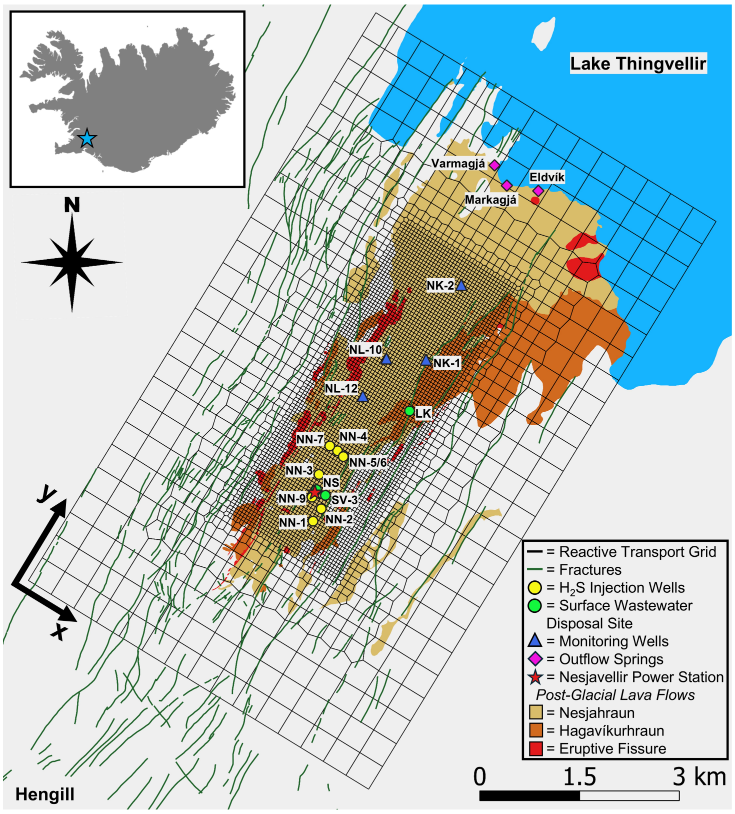

Figure S2: Map of the 3D reactive transport model grid (taken from Ciraula et al. (2025)).

8 Figure: 2D Reactive Transport Grid

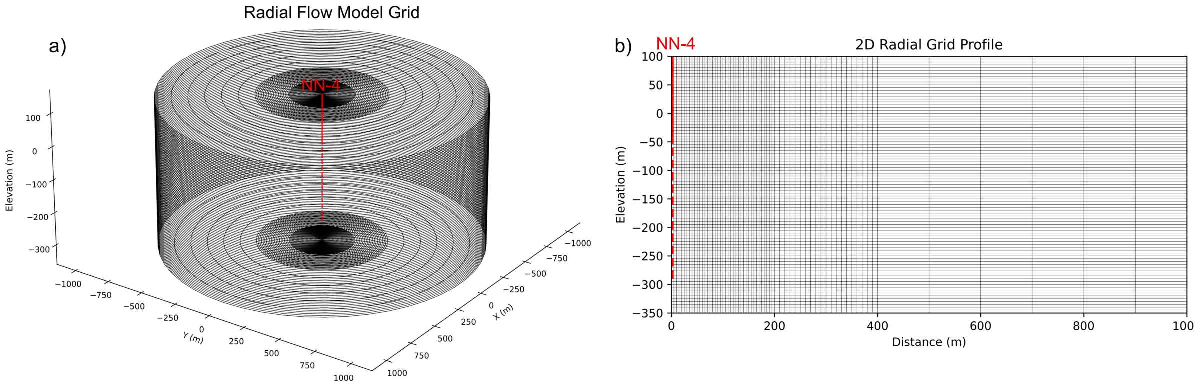

Figure S3: 3D representation of the radial grid (a) and 2D profile of the radial grid (b) used for simulating 2D radial flow from injection through NN-4 (red line). The solid red line indicates casing of NN-4 and the dashed red line indicates the open interval. The grid extends another 2 km, not shown here, to limit edge effects.

9 Figure: Expected Contributions to DCIP Response

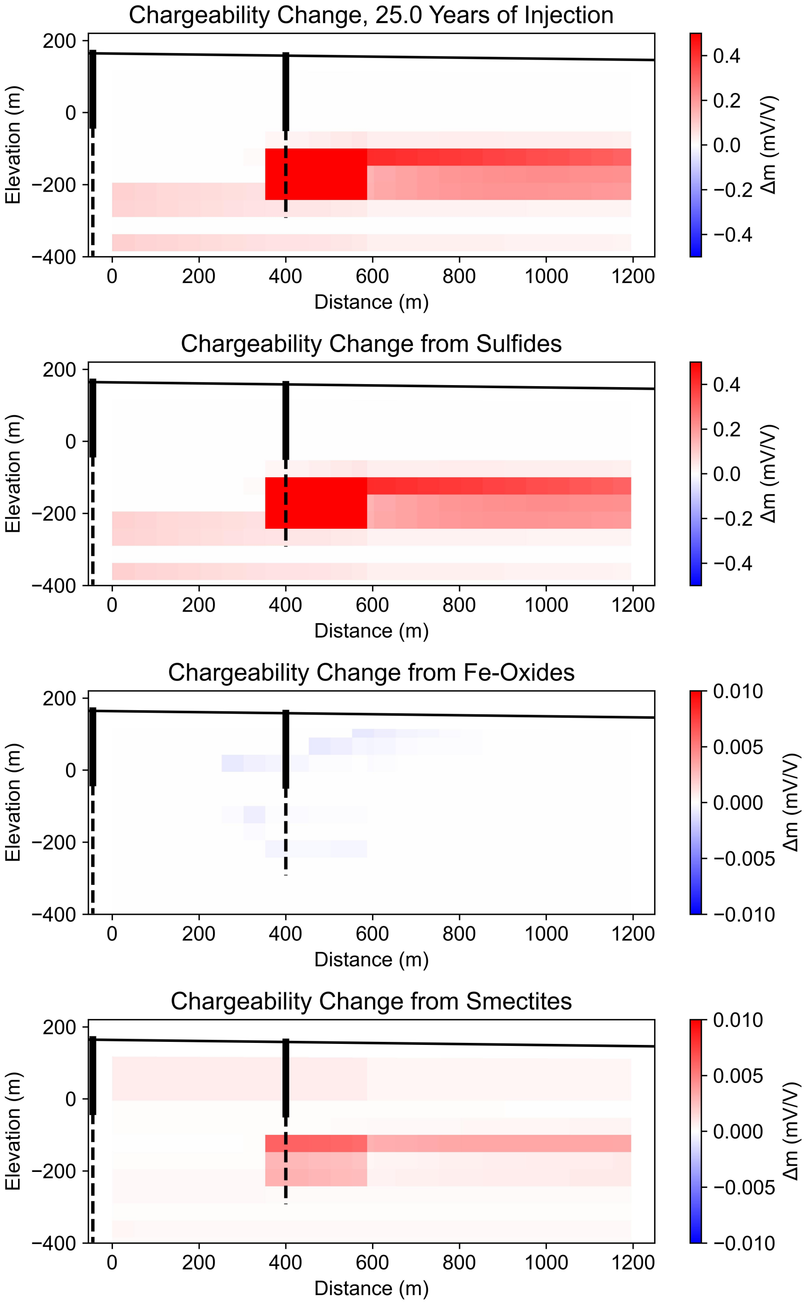

Figure S4: Expected chargeability changes from sulfide mineralization, iron-oxide dissolution, and smecite mineralization predicted by reactive transport simulations of 25 years of continuous H_2S injection.

10 Figure: Time-lapse DC Resistivity Results

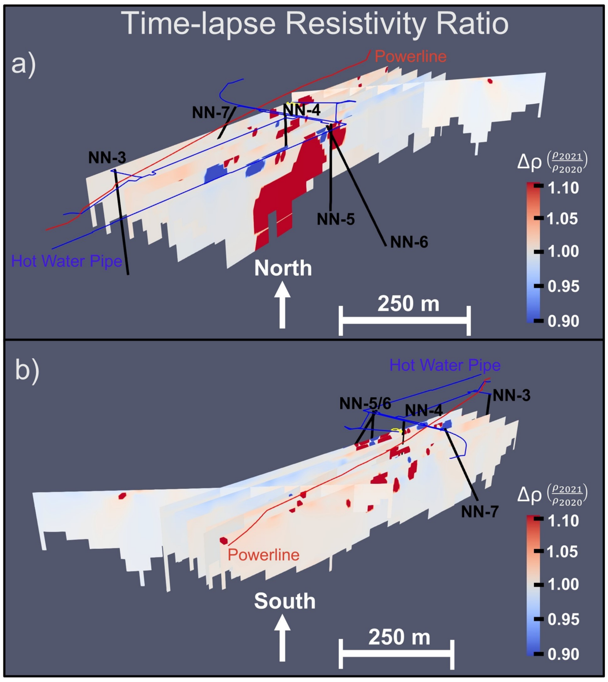

Figure S5: Time-lapse DCIP inversion results showing the change in the DC resistivity following six months of H_2S injection.

11 Figure: Cross-hole DCIP Response for 5 years of H_2S Injection

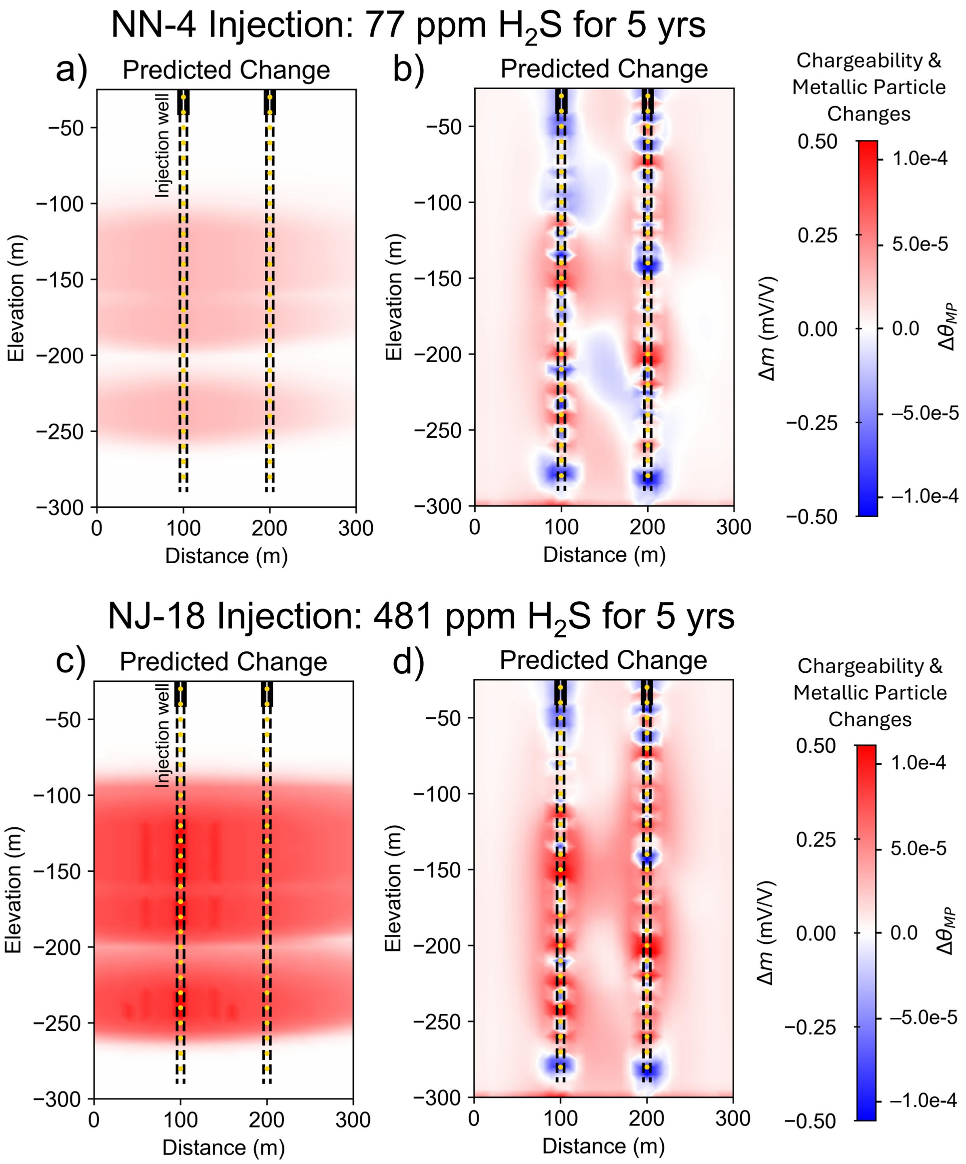

Figure S6: Results of the synthetic cross-hole modeling showing expected chargeability (m) change and the corresponding change in volume fraction of metallic particles (θ_{MP}) following 5 years of injection into NN-4 (top row) and NJ-18 (bottom row). The NN-4 and NJ-18 injection fluids have H_2S concentrations of 77 ppm and 481 ppm, respectively. The right plots show the time-lapse inversion results of the predicted synthetic data with 2% Gaussian noise added to the IP decays and the DC voltages. Solid black lines indicate borehole casing, dashed black lines indicate the open boreholes, and yellow dots indicate the electrode locations.

References

Aradóttir, E. S., E. L. Sonnenthal, G. Björnsson, and H. Jónsson (2012). Multidimensional reactive transport modeling of CO_2 mineral sequestration in basalts at the Hellisheidi geothermal field, Iceland. *International Journal of Greenhouse Gas Control 9.*

Berndsen, M., S. Erolc, T. Akınd, S. Akıne, I. Nardinib, A. Immenhausera, and M. Nehlerb (2024). Experimental study and kinetic modeling of high temperature and pressure CO_2 mineralization. *International Journal of Greenhouse Gas Control 132.*

Ciraula, D. A., S. W. Scott, B. I. Kleine-Marshall, E. Gómez-Díaz, and E. L. Sonnenthal (2025). Quantifying H_2S Mineral Storage Processes in Fractured Basalt Using a Field-Scale Reactive Transport Model. *In prep.*.

Fiandaca, G., J. Doetsch, G. Vignoli, and E. Auken (2015). Generalized focusing of time-lapse changes with applications to direct current and time-domain induced polarization inversions. *Geophysical Journal International 203.*

Fiandaca, G., J. Ramm, A. Binley, A. Gazoty, A. V. Christiansen, and E. Auken (2013). Resolving spectral information from time domain induced polarization data through 2-D inversion. *Geophysical Journal International 192.*

Gómez-Díaz, E., S. Scott, T. Ratouis, and J. Newson (2022). Numerical modeling of reinjection and tracer transport in a shallow aquifer, Nesjavellir Geothermal System, Iceland. *Geothermal Energy 10.*

Heřmanská, M., M. J. Voigt, C. Marieni, J. Declercq, and E. H. Oelkers (2022). A comprehensive and internally consistent mineral dissolution rate database: Part I: Primary silicate minerals and glasses. *Chemical Geology 597.*

Heřmanská, M., M. J. Voigt, C. Marieni, J. Declercq, and E. H. Oelkers (2023). A comprehensive and consistent mineral dissolution rate database: Part II: Secondary silicate minerals. *Chemical Geology 636.*

Knauss, K. G., J. W. Johnson, and C. I. Steefel (2005). Evaluation of the impact of CO_2, co-contaminant gas, aqueous fluid and reservoir rock interactions on the geologic sequestration of CO_2. *Chemical Geology 217.*

Palandri, J. L. and Y. K. Kharaka (2004). A compilation of rate parameters of water-mineral interaction kinetics for application to geochemical modeling.

Sigfusson, B., S. R. Gíslason, and A. A. Meharg (2011). A field and reactive transport model study of arsenic in a basaltic rock aquifer. *Applied Geochemistry 26.*

Xiao, L., G. Fiandaca, P. K. Maurya, A. V. Christiansen, and L. Lévy (2022). Three-dimensional time-lapse inversion of transient electromagnetic data, with application at an icelandic geothermal site. *Geophysical Journal International 231.*